

Chromophores within the Jovian atmosphere;

using ground-based observations to constrain atmospheric properties of Jupiter.

Charlotte Lauren Barbara Alexander

Linacre College

University of Oxford

DPhil in Atmospheric, Oceanic and Planetary Physics

2025

Abstract

The atmosphere of Jupiter is highly variable, both spatially and temporally. The belted regions evolve constantly from white to red hues, and all shades in between. These visible cloud top appearances are also linked to processes occurring deeper in the atmosphere, most notably with the changes to aerosol properties of the troposphere and lower stratosphere. Within these cloud and haze layers we find the cloud colouring chromophore material, which produces the colourful appearance of Jupiter. The creation of aerosol models allows us to characterise the atmosphere through spectral fits of observations using radiative transfer models. In this work we have used the NEMESIS radiative transfer algorithm for all modelling. Variations of the retrieved parameter values allow us to see how the atmosphere has changed between observations taken from 2018 to 2023.

In the visible and near infrared wavelengths, for which we have used VLT/MUSE observations, there is sensitivity to the aerosol profile as well as ammonia and methane in the atmosphere, but there is also a large amount of degeneracy within the parameter space. This can make it difficult to determine which models are most representative of the atmosphere. In this work we have reduced the scope of the degeneracy within our model by fixing parameters before the final retrievals. We have also applied further constraint by fitting to dual viewing angle spectra simultaneously, which have been produced using the Minnaert approximation. This has incorporated limb darkening affects into our retrievals, and provided more vertical constraint on our parameters.

Our parameterisation scheme has been able to fit dual angle spectra from 40°N – 40°S, for the observations taken. The parameterisation has also successfully retrieved a realistic distribution of cloud and haze opacities, chromophore properties adapting to visual changes, as well as deep ammonia mixing ratios which match radio observations. Alongside our ability to reproduce the belted regions we have also applied our parameterisation scheme to dual spectra observations of the Great Red Spot, extracted with the Minnaert approximation. These results showcase the abilities of the parameterisation scheme to adapt and reproduce observations across a wide range of latitudes in the Jovian atmosphere, allowing us to determine changes occurring over multiple years on Jupiter.

Acknowledgements

I would like to start by giving my upmost thanks to my supervisor Patrick Irwin. Throughout you have guided me and provided excellent advice and support. Thank you. To our group (Jingxuan, Shubham, AJ, Jack, Joe, Jake & Juan) thank you for joining me on this journey of learning the beast of a code which is NEMESIS and for answering all my stupid questions when they arose. Thank you to Emma Dahl and Ashwin Braude for understanding the joys of modelling Jupiter and the help you gave through discussions of our work. Thank you Emma and Glenn Orton for helping organise my trip to JPL and welcoming me into your group. To the wider NEMESIS team who have helped expand my scientific knowledge and also for helping me find the best pubs in every city. Thank you to Lucy for joining me on our fantastic CA to TX DPS road trip, fuelled with tortilla chips and margaritas. Having an office next to the kitchen and common room in AOPP has provided me with ample opportunity to know many faces in the department. I have enjoyed our time drinking lots of coffee and catching the sun on the balcony. Thank you to Rosie and Katherine for always saying yes to a break to debrief on life, work and everything else. To my friends near and far, I have been grateful for the fun we have had over my DPhil, providing me with needed (and superfluous) breaks from work over the years, thank you. Angus and Hannah, thank you for being the best housemates I could have asked for, my time in Oxford would not have been the same without you.

This final year did not turn out how I expected it would when I first started writing my thesis. The support of the people around me has provided me with the strength and positivity which has allowed me to complete my thesis alongside my recovery. The unexpected diagnosis of a rather large tumour in February and its removal a month later, made me feel so disconnected with the work I had been so consumed with finishing just before. Only with the continual support of those around me, have I made it here today.

To Jack, you have brought joy into every day we have been together and have helped me in so many ways. Thank you for everything, I love you so much. Onwards to our next adventure.

To my parents, thank you for your unwavering support and love in everything I have ever done in my life. You love me to bits, I love you together. Thank you.

Contents

1 Introduction **1**

1.1 History of Jupiter Observations . . . 2

1.1.1 Appearance . . . 2

1.1.2 Missions . . . 6

1.2 Atmospheric Composition . . . 8

1.2.1 Major constituents . . . 8

1.2.2 Minor Species . . . 10

1.2.3 Chromophores . . . 16

1.3 Visible changes of Jupiter . . . 22

1.3.1 Zone and Belt cyclic trends . . . 22

1.4 Determining Vertical Cloud Structure . . . 25

1.4.1 Equilibrium Cloud Condensation Models (ECCM) . . . 27

1.4.2 Galileo Descent Probe . . . 30

1.5 Radiative Transfer Derived Models . . . 34

1.5.1 Overview of previous models . . . 34

1.5.2 Post Carlson et al. (2016) chromophore models . . . 38

1.6 Research goals . . . 50

2 Observations **53**

2.1 VLT/MUSE . . . 54

2.1.1 Telescope Overview . . . 54

2.1.2 Juno Support . . . 57
2.2 Juno Mission . . . 57
2.2.1 Instruments onboard of Juno . . . 58
2.3 HST Observations . . . 60
2.4 Calibration and Data Processing . . . 61
2.4.1 Image processing . . . 61
2.4.2 Formatting MUSE observations for NEMESIS retrievals . . . 63
2.5 Spectra . . . 65
2.5.1 Observing Jupiter from Ultraviolet to Radio wavelengths . . . 66
2.5.2 Extracting Spectra from VLT/MUSE Observations . . . 71
2.5.3 Limb Darkening . . . 74
2.6 List of Observations . . . 76

3 NEMESIS Retrieval Algorithm 78

3.1 Radiative Transfer . . . 79
3.1.1 Line-by-line Model . . . 83
3.1.2 Correlated-k Method . . . 83
3.2 Retrieval of a Spectra . . . 87
3.3 Parameterisation of atmospheric profiles with NEMESIS . . . 92
3.3.1 Degeneracy of atmospheric retrievals . . . 92
3.4 Set-ups of NEMESIS specific to this work . . . 94
3.4.1 Layering Scheme . . . 94
3.4.2 Reference Atmosphere . . . 95
3.4.3 Temperature Profile . . . 96
3.4.4 Absorption Line Data . . . 97
3.4.5 Scattering Phase Functions . . . 98
3.4.6 Parameterisation profiles in NEMESIS . . . 99

4 Minnaert Approximation 103

4.1 Introducing the parameterisation . . . 103

4.1.1 Advantages to the Minnaert approximation . . . 107
4.2 Calibration with HST data . . . 108
4.3 Extracting spectra . . . 111
4.3.1 Dual viewing angle GRS spectra . . . 112
4.4 Testing previous works with the Minnaert Fit . . . 115

5 Parameterising Jupiter's clouds 118
5.1 Why is a simplified model needed? . . . 119
5.2 Determining the vertical location of clouds . . . 122
5.2.1 Snippet and Bracket Methods . . . 122
5.3 Investigation of the further parameter space . . . 126
5.3.1 Shape of aerosol layers . . . 127
5.3.2 Isolating haze characteristics . . . 129
5.3.3 Determining cloud radius . . . 130
5.3.4 Ammonia profile parameterisation . . . 131
5.3.5 Information about chromophore drawn from spectra . . . 132
5.3.6 Refractive indices for cloud and haze . . . 133
5.3.7 Final Parameterisation . . . 137

6 Application of the parameterised retrieval scheme to MUSE observations of Jupiter 139
6.1 2018 . . . 140
6.1.1 Appearance and spectral fits . . . 140
6.1.2 Cloud and haze opacity . . . 143
6.1.3 Ammonia distribution . . . 147
6.1.4 Imaginary refractive index . . . 148
6.2 2019 . . . 150
6.2.1 Appearance and spectral fits . . . 150
6.3 2020 . . . 153

6.3.1 Appearance and spectral fits . . . 153
6.4 2021 . . . 155
6.4.1 Appearance and spectral fits . . . 155
6.5 2022 . . . 158
6.5.1 Appearance and spectral fits . . . 158
6.6 2023 . . . 161
6.6.1 Appearance and spectral fits . . . 161
6.7 Inter-annual variability of parameters . . . 163
6.7.1 Appearance . . . 164
6.7.2 Ammonia distribution . . . 166
6.7.3 Opacity . . . 171
6.7.4 Imaginary Refractive Index . . . 176
6.7.5 Fixed parameters . . . 185
6.8 Great Red Spot Minnaert Retrievals . . . 189
6.9 Implication of Results for Jupiter's Atmosphere . . . 194

7 Conclusions and Future Work **199**

7.1 Summary . . . 199
7.2 Conclusions . . . 202
7.3 Further Work . . . 207
7.3.1 Observational . . . 207
7.3.2 Spectra extraction . . . 209
7.3.3 Parameterisation Scheme . . . 210
7.3.4 Laboratory Improvements . . . 212

Chapter 1

Introduction

Second only to the Sun, as a dominating player within our Solar System, Jupiter lurks over 600 million kilometres away. Despite this distance, Jupiter keeps its place in our night sky and scientific endeavours due to its bright appearance in our sky for most of the year, it has been a target for many to turn their eyes to. Due to its size, atmospheric characteristics have been discernible since the 17^{th} Century and have provided us with a long-standing record of atmospheric features as they appear and diminish over time. Over time observations of this planet have developed, moving from a pictorial record to being able to determine the more complex processes deeper within the atmosphere. As technology has advanced we have sent more orbiters to the Jovian system alongside improved ground-based telescope capabilities, allowing us to determine more about Jupiter than ever before. Therefore we have been able to deepen our understanding of the atmospheric system and begin to link together processes occurring on the planet. However, the atmospheric system is complex and not fully understood. Building a full picture of the atmosphere requires large amounts of data and analysis time, therefore piecing together information about the entire system in a snapshot of time is complex. Linking together multiple observations requires navigating ever more complex issues. Endeavouring to produce a contemporaneous analysis of the entirety of the atmospheric system is something we can look to the future to provide in due course. However, as part of this process, the work we do now to better understand the atmosphere, with both spatial and temporal links, will help eventually achieve this goal of understanding the gas giant which is Jupiter. At present, the many

unknowns at Jupiter creates a huge hurdle that prevents us from fully understanding its atmospheric system. Fortunately, observations are not sparse, and with a range of wavelengths probing the planet, we can begin to link together different processes at work. However, due to the complexity involved, providing an overview of the processes occurring at Jupiter is not straightforward.

Throughout this thesis we will set out the work done to model one aspect of this vast system, the vertical clouds structure, constructing a model which is able to reproduce observations of the planet. Through this work we will be using schemes to more rigorously fit the data and simultaneously reduce the number of parameters in the system, creating the most simplistic model possible whilst still maintaining a robust observational fit. By simplifying the cloud model we can more easily see the changing parameters, which link cloud top appearance and deeper structure changes over time.

1.1 History of Jupiter Observations

1.1.1 Appearance

Varying over a dramatic range of colours and shades, from pure white to brick red, Jupiter has a beautiful cloud-top appearance, with swirling filament regions interacting on the outskirts of strong striped belt and zone regions. Further interactions occur from storm features across the globe. Combined these showcase the dynamic nature of Jupiter's atmosphere. Each snapshot observation we acquire of Jupiter contains a wealth of information about the system. However, Jupiter is rapidly varying, as each of its regions and features interacts with each other. The rapid rotation rate of Jupiter leads to banded jets forming around the planet. They bring large differing wind speeds between regions leading to interactions through the shear between each region's alternating wind direction. These interactions can be monitored at the cloud tops, through their often regionally distinct, but changing, appearances. These zonal interactions reach deeper within the atmosphere, through convection, with regions of up-welling and down-welling across the globe, associated with each zonal feature. Therefore what can be observed from the cloud tops is the cumulative outcome from a multitude of interactions across the entirety of the belts and zones. However, as more can be discovered about the vertical profiles of these zones and belts, such as the staggering depths to

which they reach down into the planet, we begin to expose the huge complexity residing in the fluid dynamics of the cloud-hosting regions on Jupiter.

Parameter	Value
Equatorial Radius (1 bar level) [km]	71,492
Polar radius [km]	66,854
Ellipticity	0.06487
Gravity (mean, 1 bar) $[m/s^2]$	25.9
Mean Semimajor axis [AU]	5.20
Perihelion [AU]	5.035
Aphelion [AU]	5.367
Sidereal orbit period [years]	11.86
Rotation period [hours]	9.93
V-band magnitude	-9.40
Mean Apparent diameter [arc seconds ”]	46.9
Max. apparent diameter [arc seconds ”]	50.1
Min. apparent diameter [arc seconds ”]	30.5
Scale height [km]	27
Mean molecular weight $[g/m^3]$	2.22
GRS mean latitude	23.6°S
GRS mean width [°]	8

Table 1.1.1: Typical values for Jupiter and its Great Red Spot. Values from NASA Jupiter factsheet and for the GRS – Sánchez-Lavega et al. (2024)

The striped appearance of Jupiter, which can be seen in Figure 1.1.1, is caused by the cloud-top appearance of the zones and belts which are alternating prograde (westerly) and retrograde (easterly) moving bands (Atkinson et al., 1998). However, we must consider that the coloured appearance is located in a limited altitude range of the troposphere, unlike the belts and zones which extend beyond this, both above and below (Fletcher et al., 2020). Instead of colour, vorticity and temperature characterises each region. The hemispheres consist of 6-7 eastward moving jets, separated by westward jets (Fletcher et al., 2020). This difference in the wind direction and therefore vorticity of the jets leads to a vorticity gradient which prevents mixing and keeps the jets stable (Read et al., 2006). If we define through vorticity, belts have cyclonic vorticity and zones are anti-cyclonic (Fletcher et al., 2020). It is seen from Juno observations that these winds extend to depths of 3000km (Kaspi et al., 2018), indicating that the zone/belt structure is more complex than only the colour difference seen at the cloud tops. Considering the temperature variation of these regions in the upper troposphere above the cloud tops, we find that the cyclonic belts are typically

warmer, leading to depleted aerosol and gases in these regions, unlike anti-cyclonic zones which are colder leading to an enhancement of aerosols, suggesting of up-welling moist air (Fletcher et al., 2020). It is a combination of these factors which may lead to the colour variation of these regions as observed at their cloud tops, suggesting a link between a lack of cloud at the belts and a redder hue (Ingersoll et al., 2004), alongside a lack of aerosols higher in the troposphere (Fletcher et al., 2009). Therefore, throughout this work, we will refer to the colour differences of zones/belts whilst noting the greater depths to which these regions extend and the potential coupling between the visible cloud top changes and the rest of the region.

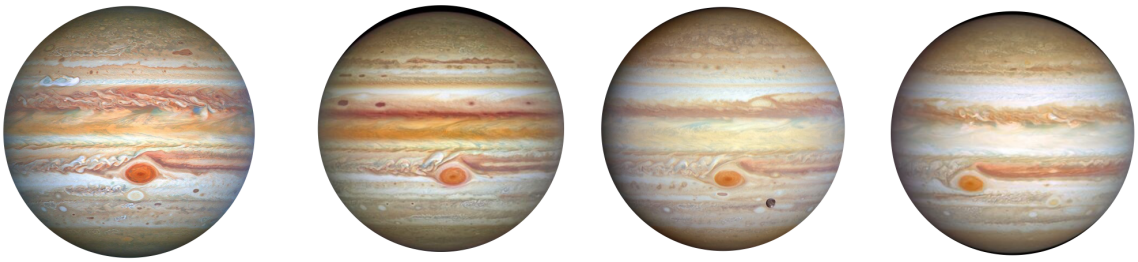


Figure 1.1.1: HST images of Jupiter as part of the OPAL legacy programme (Simon et al., 2015). From left to right: 21st August 2020, 4th September 2021, 6th January 2023, 5th January 2024. During this span, we can see the Equatorial zone both with and without a red revival, plus the North Equatorial Belt recover from an expansion event. Images NASA, ESA, A. Simon (NASA-GSFC), and M. H. Wong (UC Berkeley); Image Processing: J. DePasquale and A. Pagan (STScI)

Typically, the low contrast of the paler zones gives the appearance that they are more uniform, additionally, the features of the zones are often longer lived and more gradual when changing (Ingersoll et al., 2004). Such features include $5\mu m$ hot spots; holes in the cloud deck allowing radiation (strongest at $5\mu m$) from below to be sensed (Ortiz et al., 1998). However, the belts have a range of additional features, such as convective outbreaks which appear as great plumes, spilling out over the entire region of each belt (Simon-Miller et al., 2001). Therefore neither type of region should be considered stable, instead being dynamic in their shape, size, colour as well as interactions with the other features present on Jupiter. One of these such features is the Great Red Spot (GRS), seen in Figure 1.1.2, a huge, long-lived, deeply coloured anticyclone which resides in Jupiter's southern hemisphere. Several thousand kilometres across, several times the diameter of Earth, the storm resides around 20° South. It often interacts with smaller features which can be seen through filamenting of

its red material after an interaction with smaller storms. It is a dynamic storm undergoing changes over time including shrinking and colour changes alongside constant procession around the globe (but remaining fixed in latitude). As with the rest of the globe and its colouration, what makes the GRS its striking red colour is not known, and adds to the wider unknowns of the planet.

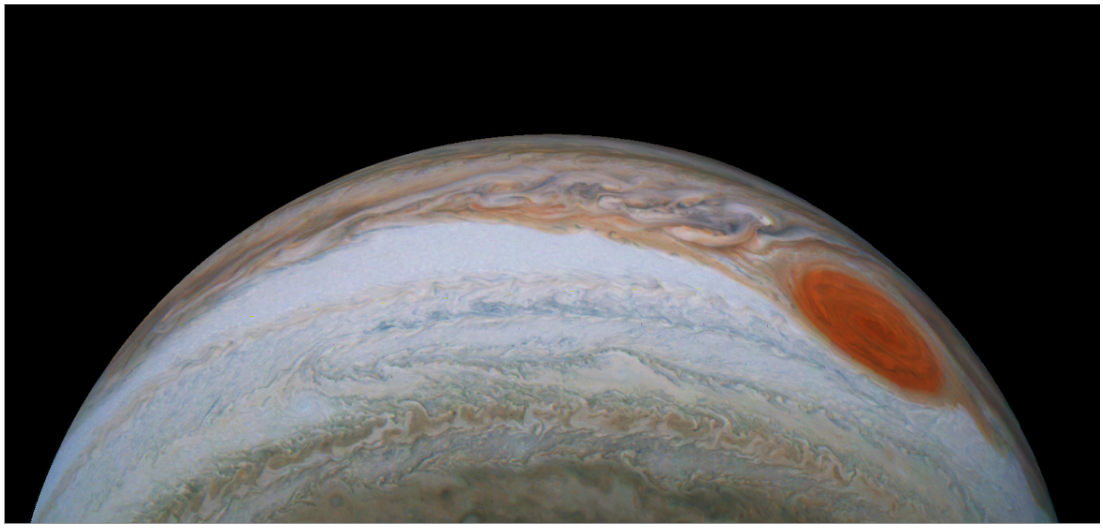


Figure 1.1.2: The Great Red Spot captured by JunoCAM, during Perijove 21 of the Juno Mission in June 2019. The image uses the visible filters on JunoCam, with enhanced colour and incredible detail. NASA/SwRI/MSSS/Aran Anderson (2019)

Moving away from the equator, above $\sim 50^{\circ}$ latitude towards the polar regions, the banded structure ceases, as shown in Figure 1.1.1. At the poles, the familiar stripes are replaced by a complex interaction of cyclonic storms, nine at the north pole, six at the south, each producing a stable formation, with a polar cap of haze, discovered by the Jovian Infrared Auroral Mapper (JIRAM) instrument on Juno in the infrared (Adriani et al., 2017b). Figure 1.1.3 shows this arrangement at the north pole as seen by the instrument. However, it is the sub-polar banded regions which will be of main focus for this work. Their changing nature makes them a challenge to understand as their appearance can change dramatically over a short period of time. For example, the Equatorial Zone cycles between a range of white to red colouring (which will be expanded upon in Section 1.3.1), Figure 1.1.1 shows how these changes can come and go over time. All of the bands of Jupiter's atmosphere undergo these changes, ranging in the scale of their disruption, duration, colour and speed of their alterations.

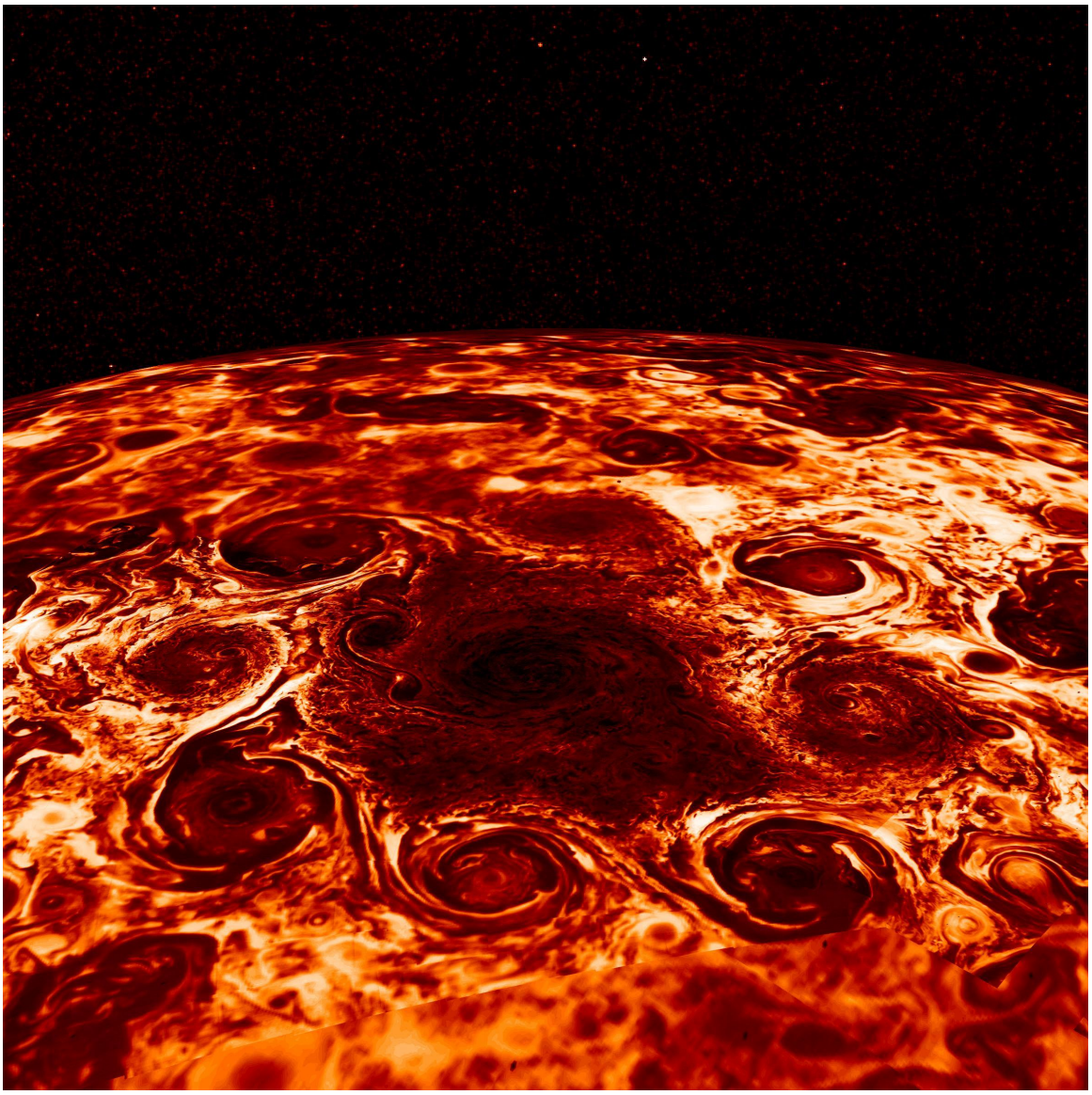


Figure 1.1.3: Composite image from JIRAM instrument (infrared around $5\mu m$) on Juno showing the North Polar region with its central polar cycle with eight surrounding cyclones. The image was taken in February 2017 during the third Perijove. Image Credit: NASA/JPL-Caltech/SwRI/ASI/INAF/JIRAM

1.1.2 Missions

Attempts to better characterise Jupiter's atmosphere have been a scientific focus for a long time, for as long as we have been able to distinguish features on its surface (17^{th} century). The first

fly-by mission of Jupiter occurred in 1973 with the Pioneer mission, providing close-up images of Jupiter with detail greater than anything taken from Earth at that time. The missions have expanded our wealth of observational data from Jupiter. Shortly after the Voyager missions reached Jupiter in 1979, these missions provided a wealth of data, with visible, infrared and UV instruments (alongside several others) which were able to further probe Jupiter as they orbited the planet. The Galileo Mission is notable due to its launch of a descent probe, see Section 1.1.2, which provides the only in-situ observations of Jupiter's atmosphere. Characterisation of the clouds through direct measurement should provide more affirmative evidence about the cloud structure, however, due to the highly varied nature of the atmosphere these measurements have often provoked more questions than answered. Despite only being a fly-by, the Cassini mission captured excellent data of Jupiter, as it was used for calibration of the instruments before reaching Saturn. The large optical remote sensing instrument payload led to a wealth of observations with a wider wavelength range than before. We are currently in an exceptional time for observing Jupiter due to the wealth of ground and space-based telescopes which can observe the planet in addition to the Juno mission which is currently orbiting Jupiter on its second extension to the mission. The future also looks bright with the Juice mission launched last year by ESA, continuing the wealth of measurements coming from the Jovian system.

Currently orbiting Jupiter is the Juno Mission. Now on its 9^{th} year taking observations, due to multiple extensions to its original observational lifetime. This craft provides regular observations of the planet during its orbit towards and after each Perijove (point of closest approach), however, the orbits are highly elliptical and can benefit from ground-based support to provide spatial context to its observations. The mission was designed to undertake elliptical orbits to ensure that the Perijoves passed close enough to the planet to be able to infer the internal structure from gravity perturbations, whilst not spending too long in the highly damaging radiation belts which lie in Jupiter's equatorial plane. Additionally, whilst being placed into orbit the boosters on Juno did not act as planned leading to a more elliptical orbit than planned to ensure craft safety, this has led to several extensions to the mission schedule, due to longer spacing between Perijoves meaning Juno spent less time in the damaging radiation belts than planned. Section 2.1.2 details the work

done as part of the global collective to support Juno from the ground. The spatial detail that the Juno mission has been able to provide from its instruments is unprecedented. Figure 1.1.2 shows the Great Red Spot (GRS) from the JunoCAM displaying the high resolution brought by the Juno mission. Unfortunately for observations in the visible, the spectral resolution of the observations is limited due to the use of wide filters, due to the outreach purpose of the JunoCAM. However, research using the visible spectrum can still be undertaken due to the high calibre of ground-based telescopes which are able to observe Jupiter. For this thesis, we predominantly use VLT/MUSE observations for our analysis, as are detailed in Section 2.

1.2 Atmospheric Composition

1.2.1 Major constituents

Despite its main constituents, hydrogen and helium, being colourless, Jupiter displays a huge range of colour variation across its disc. Further still, the main species expected to form cloud decks, (ammonia ice, ammonium hydrosulphide and aqueous ammonia) are also all typically colourless. As such, a key question becomes what is giving Jupiter its colours, which can be seen in Figure 1.1.2. Determining the cloud colouring compound, given the name chromophore, is challenging, both chemically; by trying to find its composition and formation pathway, but also by how it is distributed through the atmosphere giving the observed variegated appearance. As a gas giant, it must be clarified that when talking about the atmosphere we are referring to the upper regions of Jupiter's structure, i.e., the observable atmosphere above approximately 10 bar. The region of focus for this thesis is the troposphere and lower stratosphere, where we use a model with a pressure range of 10 bar – 0.01 bar. The temperature profile for this region can be seen in Figure 1.2.1.

Species	Volume Mixing Ratio	Error
Hydrogen, H_2	0.86	0.030
Helium, He	0.136	0.003
Methane, CH_4	0.0018	0.15×10^{-3}
Ammonia, NH_3	0.0007	0.32×10^{-3}
Water, H_2O	>0.0005	0.02×10^{-3}

Table 1.2.1: Global mean values of volume mixing ratios in the troposphere (∼0.1 bar – 10 bar) for the main Jovian species (Taylor et al., 2004).

Although predominately consisting of hydrogen and helium, Jupiter's atmosphere contains a wealth of species, albeit often in minimal quantities. The five main components are given in Table 1.2.1. Further minor species are often sparsely distributed due to their production mechanisms, such as photochemical reactions, which constrain them to particular regions of the atmosphere. Such species include photochemically produced hydrocarbons such as ethane, acetylene, and further products of their reactions which typically reside in the stratosphere.

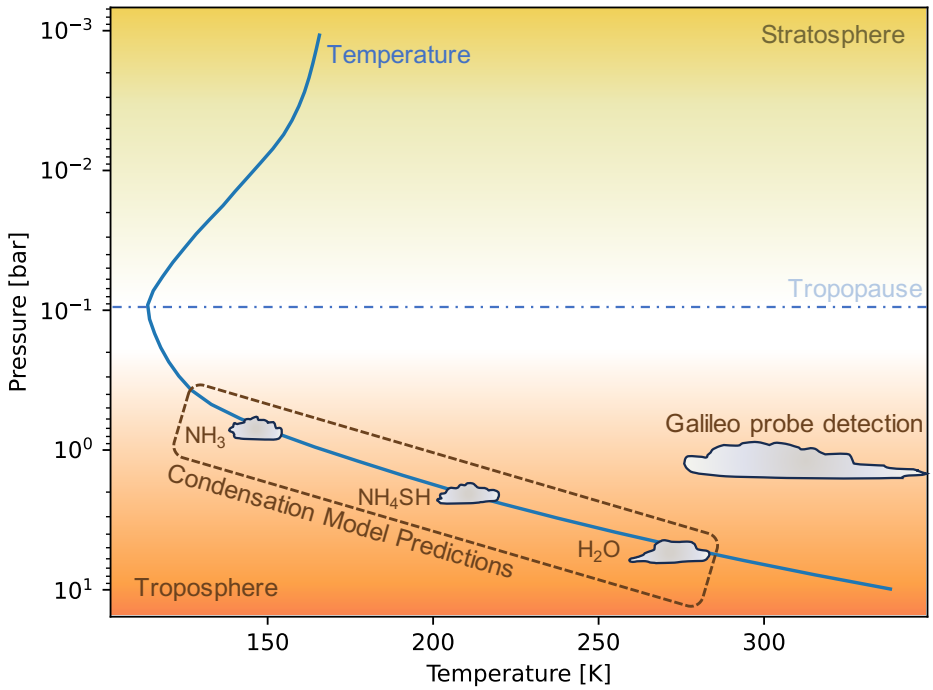


Figure 1.2.1: Temperature profile used for the NEMESIS runs, with the approximate locations for the predicted clouds from Cloud Condensation Models (Atreya et al., 1997), as well as the observed cloud from the Galileo probe (Ragent et al., 1998).

We are able to determine the species present, and their abundances, on Jupiter by finding absorption features in spectra. By identifying features we can confirm the presence of these minor species within the atmosphere. Helium is more difficult to conclude due to its monatomic structure which limits absorption features. Confirmation of the mixing ratio of helium (and additionally methane) came from the Galileo probe (Niemann et al., 1998), giving the value of 0.136 in Table 1.2.1. Other

species were detected by the probe but due to the inhomogeneous distribution of these species, these results cannot be assumed to be entirely representative of a global mixing ratio of the atmosphere due to species' ability to condense or inhomogeneous distribution due to limited production regions. Therefore, observations taken for the whole planet are more reliable for determining these mixing ratios.

1.2.2 Minor Species

Most minor species, such as the plethora of hydrocarbon species, are produced through high energy reactions, with the highest energy reactions mostly in the upper atmosphere (Moses et al., 2004). These reactions can occur due to photolysis from the absorption of incoming radiation, or when a high-energy electron collides with a species which predominantly occurs in auroral regions. The energy provided from the incoming photons and electrons overcomes the activation energy to start the reaction, leading to cascading pathways of species production. For example, methane reactions lead to a huge number of complex hydrocarbons to be present in the atmosphere (Moses et al., 2004). Photolysis of the numerous species within the atmosphere creates an even greater wealth of species in total. The pathways which lead to this plethora of hydrocarbon species could potentially also play a part in producing the chromophore material present across Jupiter. It is thought that this material likely has a similar photolytic origin (Carlson et al., 2016). Further information about the potential chromophore sources are given in Section 1.2.3.

Photolysis is important across much of Jupiter as it leads to the production of stratospheric and upper tropospheric hazes, which are widely distributed across the globe, though in variable amounts. Located above the main cloud layers predicted by thermochemical models, the hazes are likely predominantly formed of ammonia photochemical products, such as hydrazine (N_2H_4) (Atreya et al., 2005). Additionally, due to its depletion seen at higher altitudes, phosphine is likely to be an additional source of photochemical products. Other similar non-condensing species such as Germine and Arsine may also contribute to haze, but their depletion cannot be currently detected to confirm if this is the case (Irwin et al., 2004). The haze is split into two distinct layers. A minimal upper stratospheric layer is located above 100 mbar across the globe, increasing in altitude towards the

poles. The lower tropospheric haze is located just below the 0.1 bar level and is consistent in altitude below 50° latitude (Zhang et al., 2013). The lower tropospheric haze, which has an average location of 0.2 bar is key for reproducing the limb darkening (see Section 2.5.3) properties of observations (Zhang et al., 2013), which makes it a key component to characterise in the work outlined in this thesis.

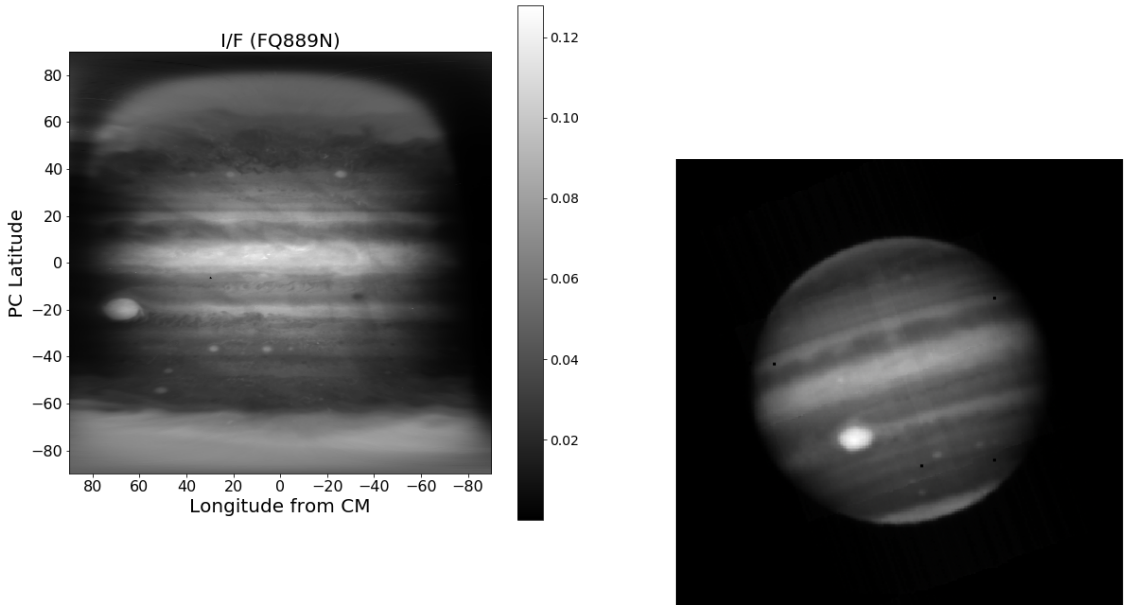


Figure 1.2.2: 889nm images of Jupiter. Left – HST/WFC3 FQ889 filter image of Jupiter from 2019 (OPAL team, Simon et al., 2015). Right – 889nm slice of 9th April 2018 VLT/MUSE cube (PI – A. Braude, Braude, 2019)

The zonal regions are associated with an elevated amount of haze, particularly the Equatorial Zone, as are features such as the Great Red Spot, plus the polar regions. Imaging the haze is possible and is most sensitive in bands which have strong methane absorption such as 889nm. From these observations we are able to clearly identify which regions have elevated haze levels due to the enhanced brightness in the associated regions, seen in Figure 1.2.2. The strong methane absorption of these bands means any bright regions must have particles which are located high in the atmosphere, above the methane which absorbs at these wavelengths and are seen as the dark regions in Figure 1.2.2. Other methane bands are able to help identify haze, but the 889nm absorption features is the

most prominent within the wavelength range of the observations used in this thesis.

Due to the additional electron bombardment from auroral sources, production of haze in the polar regions is far elevated when compared to the zones and belts, below $\sim 50^{\circ}$ latitude (Zhang et al., 2013). Along with the lack of visible cloud top zonal striping it is another way to differentiate these polar regions from the aerosol structure of the zones and belts which are the focus of this work. Once hazes have been produced there may be further processes which act upon them; transportation away from their production location, both vertically and horizontally, as well as further reactions. These changes can make it more difficult to characterise the haze on Jupiter and determine how its production links to its appearance.

Minor species mixing ratios are an important diagnostic due to the numerous factors that change their values. Reaction pathways of species lead to the depletion of reactants and an increase in their products. Further to this, vertical motion of the atmosphere leads to differing mixing ratios in regions associated with up-welling to down-welling. Air moving away from regions with a higher mixing ratio will bring species into a new region increasing their concentration, varying the mixing ratio expected at that altitude. Beyond just explaining compositional differences, mixing ratios can act as a tracer of circulation in the atmosphere.

Ammonia

Ammonia is one of the most important species at Jupiter. With its moderate volume mixing ratio, its presence in the atmosphere can be observed in a number of ways. It has key absorption features across much of the spectrum allowing it to be investigated through observations taken at most wavelengths. Many of the absorption features are in the visible and near infrared, wavelength regions of focus in this work (see Chapter 2). From these absorption features we are able to determine the ammonia distribution across the planet.

Due to the temperatures at which ammonia freezes and condenses, it is expected to contribute to the tropospheric clouds (Atreya et al., 1999), see Figure 1.2.1. Both aqueous ammonia and ammonia ice form at temperatures which lie within Jupiter's troposphere, leading to predictions that the clouds

may be comprised of these materials (Atreya et al., 1999). Additionally, a product of ammonia and hydrogen sulphide – ammonium hydrosulphide, also has its condensing point within the troposphere. (For more information about this please refer to Section 1.4). Therefore, ammonia is a significant species at Jupiter, due to its potential to form clouds at the temperatures being experienced. Hence, mapping the abundance of ammonia becomes more difficult than for non-condensing species. We can separate ammonia abundances into deep and tropospheric, with the deep values being below the condensation level and tropospheric ammonia incorporating the complexities brought about by condensation. However, due to the dynamic nature of clouds these values will be varying across the disc and will also being affected by the movement of air relating to cloud forming processes.

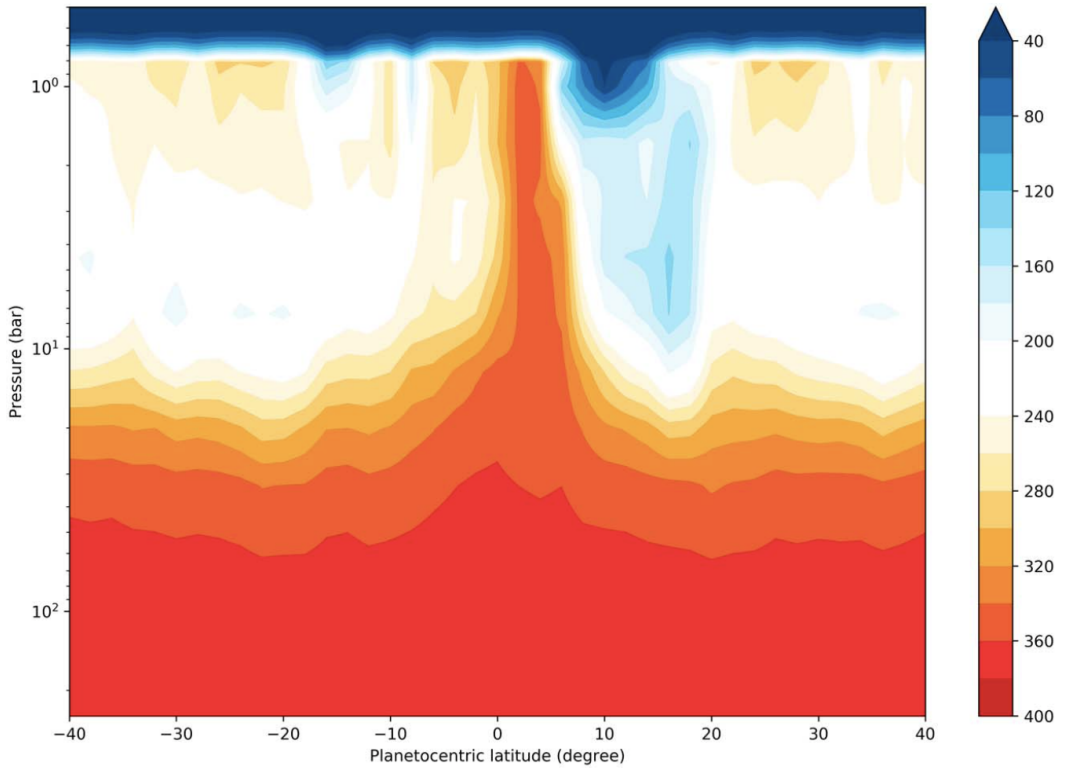


Figure 1.2.3: Ammonia concentration in parts per million from Li et al. (2017) during Perijove 1 of Juno flyby, inverted from nadir brightness temperature observations in several channels by MWR.

Ammonia is affected by more than its condensation and chemical reactions, dynamics of the atmosphere also shape how it is distributed throughout. Li et al. (2017) show that the mixing ratio of

ammonia is elevated just north of the equator ($\sim 5°$), above 10 bar, unlike other latitudes, leading to a tropospheric enhancement which is comparable to the deep level mixing ratio. It was then found to have a contrasting strong depletion north of this enhancement, as can be seen in Figure 1.2.3 (Li et al., 2017). Ammonia is expected to decrease with altitude due to the production of ammonia hydrosulphide and formation of ammonia ice clouds, as well as additional photolytic reactions (Fletcher et al., 2020). Therefore, this enhancement needs to be explained via dynamics of the atmosphere rather than through chemical pathways as this would only lead to depletion. The enhancement indicates a strong up-welling to bring ammonia up from depth (Fletcher et al., 2020). The movement of air is expected to be complemented by an associated down-welling region $\sim 8 - 20°$ (Fletcher et al., 2020), this can be seen in Figure 1.2.3, with a depletion of ammonia at these latitudes (Li et al., 2017). The Juno mission has revealed the ammonia distribution from deep in the atmosphere up to the troposphere, including the condensation level in its sensitivity range (Li et al., 2017).

More evidence for this circulation pattern is seen through phosphine mixing ratios, which follow the same pattern as ammonia with an elevated mixing ratio at the equator banded by lower amounts of phosphine (Irwin et al., 2004; Fletcher et al., 2009). It should be noted that these observations are probing higher in the atmosphere than Juno (upper troposphere, above the ammonia condensation level) using the CIRS/TEXES instrument. However, there are limitations to the amount of information which we can reveal through the use of tracers, detecting the finer dynamics of the atmosphere is something which is currently not possible, due to the observation resolution currently being attained (Fletcher et al., 2020). Therefore, it should be considered as tool for viewing the larger scale motions whilst acknowledging the effects of potentially masking or averaging the smaller scale motions which are occurring within the resolution currently attained. The large variation between the expected mixing ratio of ammonia and what is observed at some locations, despite being an easily observed species, exposes the complexity within the atmosphere.

Minor species and cloud composition

Beyond the species in Table 1.2.1, numerous further minor species are present in Jupiter's atmosphere which play major roles in the appearance we see. Through work with equilibrium cloud condensation models of Weidenschilling and Lewis (1973); Atreya et al. (1997) (see Section 1.4 for full details), three species have been expected to form as clouds in the troposphere; ammonia ice, ammonium hydrosulphide and aqueous ammonia. However, there has been far less spectroscopic evidence of the cloud material than would be expected if they are present across the planet as is normally assumed. Whilst ammonia spectral signatures from the atmosphere are clear, associated spectral features of ammonia ice, predicted through theoretical condensation models to the highest cloud layer, are harder to observe. There should be several features over the infrared range, such as a $9.4\mu m$ feature which should have a strong signature from the small particle size which is expected in this cloud layer from studies at shorter wavelengths (West et al., 1989). However, it is not seen. The spectral feature could be dampened by the presence of larger particle sizes than would be expected or non-spherical particle shapes could account for the lack of signal. For Galileo/NIMS observations, Baines et al. (2002) also did not find the expected strong absorption features across the globe of Jupiter. Instead, the signal was found across a very limited spatial extent, corresponding to less than 2% of global coverage, although more plentiful in some regions such as the Northern Equatorial Zone. The material that was found to have ammonia ice spectral features, was fresh material which was less than two days old (Baines et al., 2002). It is theorised then that older material could have its spectral feature masked due to other species coating the ammonia ice particles; this would also allow the particles to be smaller as is expected from shorter wavelength work. Further evidence of ammonia ice has been found spectrally by Wong et al. (2004), however this observation is again limited spatially. Therefore, there is little to no evidence to suggest the global layer of ammonia ice exists across the disc of Jupiter as is predicted by theoretical models.

Additionally, no direct evidence of ammonia hydrosulphide has been found spectrally either, although Sromovsky and Fry (2010, 2018) found that they were better able to fit to a $3\mu m$ feature when both NH_3 and NH_4SH particles were present. Spectral evidence has been found for water ice signatures by Simon-Miller et al. (2000), using spectra taken during the Voyager mission, however less than 1%

of spectral samples analysed displayed this signal, indicating minimal spatial extent to these clouds.

The lack of spectral identification of the predicted ammonia ice and ammonium hydrosulphide clouds is an oddity. A complete absence of these species is possible and would explain the lack of spectral features, but this seems improbable. Instead, the lack of distinct spectral signatures could be due masking of these spectral features, driven by the properties of the cloud material. It is unlikely that any ices present on Jupiter would be 100% pure, therefore, we need to account for how contaminants could affect the spectral signature of the pure ice. It is thought that ammonia ice could have material deposited onto its surface from above, such as from the photochemical haze present across the globe, leading to an impurity (Atreya et al., 2005). The signature of the ammonia ice could be obscured by the haze forming a coating on the ammonia ice, or the falling haze could act as a cloud condensation nuclei (CCN) (Atreya et al., 2005). The haze coating, if it exists, is thought to be shallow, less than $0.1\mu m$ forming quickly, in less than a week, which is estimated to be the longest lifetime of spectrally identifiable ammonia ice clouds (SIACs) (Baines et al., 2002). However, whether this would be thick enough to obscure the ammonia ice spectral features below is unclear (Atreya et al., 2005). This effect could also be achieved through a coating from a chromophore material (see Section 1.2.3 for more discussion). If instead the features are masked due to the presence of a CCN, it is not known whether a haze CCN could spectrally obscure the spectral signatures of ammonia ice (Atreya et al., 2005). However, Clark and Lucey (1984) shows for water ice that cloud condensation nuclei and other small sources of impurities can be successful in masking spectral features. Therefore, it would be unwise to rule out the same possibility occurring for ammonia ice clouds. To confirm whether both or one of the above processes are occurring for NH_3 and NH_4SH ices, masking their spectral features, laboratory experiments are needed to determine the spectral behaviour of these species when combined with possible coatings and/or cloud condensation nuclei.

1.2.3 Chromophores

From the species that have been introduced so far as predominantly present in Jupiter's atmosphere (see Table 1.2.1), there is nothing of note which can produce the range of shades which can be seen at Jupiter's clouds tops, such as in Figure 1.1.2. From white to brown to red, we acknowledge

that Jupiter's colours, albeit exaggerated by the processing of observations (Irwin et al., 2024), cause Jupiter to appear far more saturated in the red (due to an increase in absorption of blue wavelengths) than would be expected by the scattering of light from colourless gases and colourless aerosols. To explain this colouration, the idea of a chromophore material is introduced. When we see red, what we are witnessing is an absence of blue wavelength radiation compared to red wavelengths. It is this chromophore material which is responsible for the absorption in the blue wavelength range. Through this work we will focus on the wavelengths short-ward of approximately 600nm in our observations to characterise the chromophore; more information about the spectrum and what it shows is in Section 2.5.

Except for the Great Red Spot, which typically has the most intense red colouration on Jupiter, there is no steadfast rule to the colouration displayed by each region. Often belt regions have redder colouration, however as seen in Section 1.3.1, there is a huge amount of variation in their colour. Zones, which are typically whiter, also display a wide range of colours. Therefore we cannot constrain the chromophore material to a single region on the planet and must accept that it may be present in some form across the whole disc. Attempts to obtain further information about this colouring species are of high importance. However, it is very elusive due to a lack of knowledge about it. Its chemical form, components, production pathway, lifetime, mixing ratio and absorption properties are all unknown, instead, we can only compare laboratory samples to atmospheric spectra in the hope of uncovering information.

Proposed chromophore candidates

Multiple reviews have been conducted about chromophores, (West et al., 1986; Simon-Miller et al., 2001; West et al., 2004), which provide an extensive overview of the research which has been carried out to determine the species responsible for Jupiter's colour. To constrain what is needed from a chromophore's properties to produce the observed appearance at Jupiter, several things need to be considered. Such factors include the differences between regions of Jupiter that are coloured and how these differences materialise, as well as the intrinsic properties of the potential chromophore and how it is produced. Simon-Miller et al. (2001) use principal component analysis to determine what

is driving the visual changes on Jupiter by identifying which atmospheric characteristics produce the largest change within the spectra. A principal component is selected which accounts for the majority of the spectral responses, then additional components are chosen until the majority of the spectral response can be accounted for. Simon-Miller et al. (2001) show that ∼91% of all variation across Jupiter is due to differences in brightness not colour. Colour changes driven by chromophores are only responsible for 8% of image variance. There is then a further possible variation of colour through a third component present in the more unusual locations such as the GRS and anti-cyclonic features. From these results it can be expected that a single chromophore (with potentially altered properties to account for the final 1% of variation) is responsible for the colour variation seen at Jupiter (Simon-Miller et al., 2001). Therefore we can begin to focus on finding a singular chromophore candidate which alongside brightness changes can account for the majority of the observed spectral differences between regions.

West et al. (1986) focus on the importance of limb darkening and scattering models to determine which proposed species can best reproduce observations. Laboratory-based determination of species is difficult, often due to the challenge of reproducing the conditions experienced at the cloud levels on Jupiter. Again with principal component analysis, it becomes possible to differentiate the substances proposed and how successful they are at reproducing colours at Jupiter. West et al. (1986) conclude that a single species is more likely to be causing the colour differences with Jupiter but with a possible spectral alteration. When accounting for limb darkening, in addition to the brightness and colour variation, we could assume that the chromophore material is most likely to be located in the main ammonia clouds, rather than in the higher cloud or haze layers (West et al., 1986). It can then be concluded that the overlying white clouds, variable mixtures of ammonia combined with the chromophore and/or potential ice mantling of the chromophore could account for the variation seen across the disc of Jupiter (West et al., 1986). However, at this time the latter two statements had not undergone any quantitative analysis. Table 1.2.2 also demonstrates the wide range of species which can be considered viable chromophore candidates, broadly consisting of any minor species on Jupiter and its product. It is very difficult to eliminate any species as a chromophore candidate due to a lack of infallible evidence.

Species	Evidence For	Evidence Against
C_2H_2, CH_4 H_2C_6, HCN	Khare and Sagan (1975) Sagan and Salpeter (1976) Ferris and Ishikawa (1987)	Lewis (1976) Sill (1976) Rages (1977)
H_2S, H_xS_y, S_8	Khare and Sagan (1975) Lewis (1976)	Sagan and Salpeter (1976) Sill (1976) Rages (1977) Larson et al. (1984)
PH_3	Prinn and Lewis (1975) Lewis (1976) Larson et al. (1977) Guillemin et al. (2001)	Sill (1976) Ruiz and Rowland (1978) Lara et al. (1998)
Na	Wildt (1939)	Sill (1976)
NH_4SH, NH_3	Owen (1976) Sagan and Salpeter (1976) Ferris and Ishikawa (1987) Karkoschka (1998) Loeffler and Hudson (2018) Carlson et al. (2016)	Sill (1976) Lewis (1976) Sill (1976) Loeffler et al. (2016)

Table 1.2.2: Chromophore candidates for Jupiter. Updated table from Simon-Miller et al. (2001), to reflect new work.

Laboratory work on chromophores

In order to determine between the large number of chromophore candidates in Table 1.2.2, laboratory tests can provide some clarity. By testing the viability of producing the proposed candidate in Jupiter-like conditions, as well as examining the spectral properties, more likely candidates can be identified. Laboratory tests can reveal large amounts of information about candidate properties and plausibility, more so than chemical or radiative transfer models, but the research is costly, time-consuming and has few undertaking the work. Therefore, far more research in this area would be a huge benefit to the community, providing data to validate such theoretical models. Laboratory tests which have been undertaken attempt to produce material under the conditions expected at Jupiter. This then allows the spectral properties of the product to be analysed and to evaluate whether it is comparable to the spectral slope of Jupiter observations. Similar spectral slopes below 600nm indicate whether the product could be causing the broad absorption which we see in this wavelength range. The lack of strong absorption features of the chromophore should also be replicated; if the laboratory product produces a feature not seen in the spectra then it is unlikely to be present in the

atmosphere without modification. Another requirement is the chemical limitations of the reactions, which depend on the amount of reactants available and need to be similar to what is present at altitudes on Jupiter where these reactions are occurring. Finally, comparison of the colour of the material and Jupiter can help to theorise whether the material may be present, for example the Loeffler et al. (2016) product of photolysed ammonia, although matching the GRS spectrum in many ways, had a bright green colour which is not observed on Jupiter, weakening the plausibility for this chromophore alone to reproduce the colours seen in observations of Jupiter. However, further work in Loeffler and Hudson (2018), which incorporates work at lower temperatures is able to form a red compound, highlighting the delicate nature of laboratory conditions which affect the results found.

Previous experiments by Ferris and Ishikawa (1987) were have been built upon by Carlson et al. (2016), investigating reactions of ammonia and acetylene. The effect of methane on these reactions was also included in the original work. The gases were mixed and then exposed to ultraviolet light, simulating photolysis reactions that occur in Jupiter's atmosphere and measurements of the transmission properties of the product were then taken. The transmission can be used to derive the imaginary refractive index of the compound, which indicates the absorption properties for radiation at each wavelength. The produced solid matched well to GRS observations spectrally and also provided a visually similar colour comparison (Carlson et al., 2016). Additionally, the reaction would be viable at Jupiter due to sufficient amounts of the reactants (NH_3 and C_2H_2) being present at the reaction pressure in the atmosphere (Baines et al., 2019). However, the product did not provide characteristics which allow the exact chemical formula of the product to be identified (Carlson et al., 2016). Instead, only the atoms present (identified through mass spectrometry) and the functional groups (from infrared spectrometry) could be identified. The suggested formulae are $C_{2n}H_{4n}N_2$, $C_{2n}H_{4n+2}N_2$ or $C_{2n}H_{4n-2}N_2$, which indicate alkanes with azine (a functional group with double bonded nitrogen atoms) and/or diazo (two linked nitrogen atoms at the terminus) groups (Carlson et al., 2016). Routes to produce the source of products containing these functional groups are present in the detailed chemistry of Moses et al. (2010), making these products possible at Jupiter. Work is in progress to extract further information from the experiments carried out in Carlson et al. (2016)

as the chromophore presented consists of a sub-set of the sample when it had been irradiated for 70 hours. The full data set contained different irradiation times, as seen in Figure 1.2.4, which would lead to varying imaginary refractive indexes being extracted from the transmission data (Dahl et al., 2023). This provides multiple imaginary refractive index values extracted for a single chromophore material. Differing duration of exposure to the incoming sunlight is possible for chromophores as they may reside on cloud tops for longer in different locations. Hence, this could help explain some of the spectral differences between different red regions at Jupiter by having the chromophore change spectrally when having undertaken a longer exposure time (West et al., 1986).

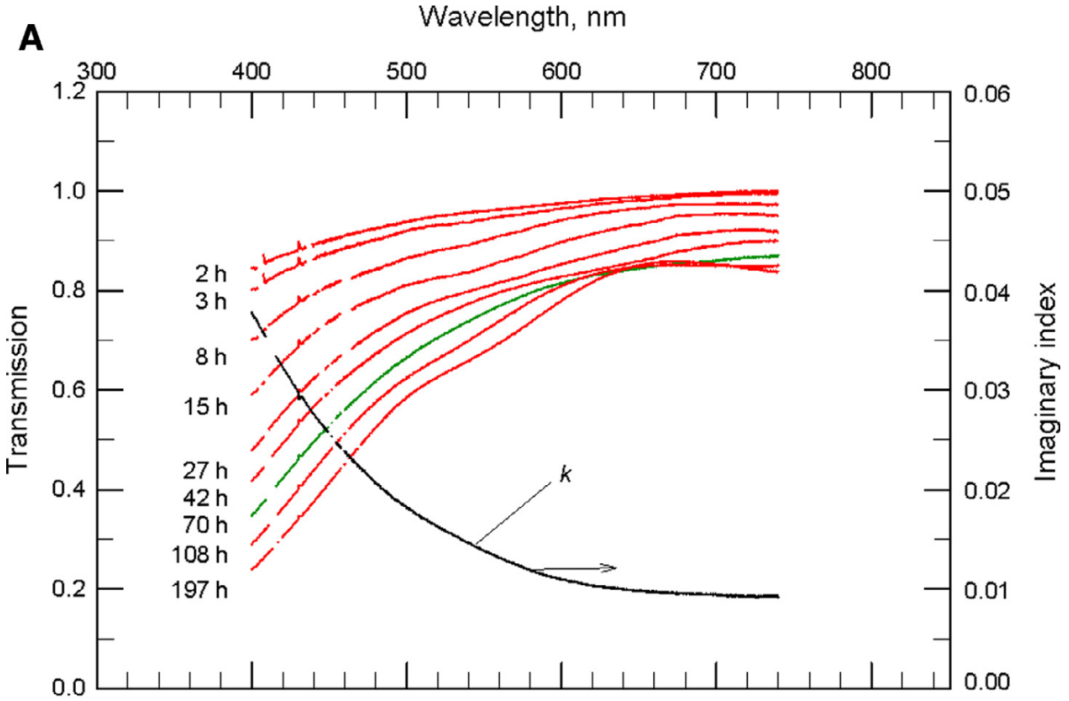


Figure 1.2.4: Transmission values for Carlson et al. (2016) chromophore material when exposed to radiation for differing amounts of time, the black refractive index line is taken for 70 hour radiation time (green), taken from Carlson et al. (2016).

The Carlson et al. (2016) chromophore was shown to be a good fit to spectra taken from Cassini/VIMS (2000/01) observations of the GRS. Baines et al. (2019) undertook radiative transfer modelling using the same observations of the GRS which were used for spectral analysis in Carlson et al. (2016). However, it was also shown that this chromophore can be used across the disc to explain other red

regions effectively using Cassini/VIMS observations by Sromovsky et al. (2017). More information about the models proposed in these works and others can be found in Section 1.4. Expansion of the location to which this material is applicable, allows this laboratory-based chromophore to be dubbed as universal due to its potential to reproduce observations across a range of features, through radiative transfer modelling.

1.3 Visible changes of Jupiter

1.3.1 Zone and Belt cyclic trends

Despite the huge scales of Jupiter's zones, belts and features exist on, (of the order of 100,000km), the timescales of the variations can be as short as hours (Fletcher, 2017). The most rapid events are convective storms which appear as a single up-welling region but then can trigger larger developments across an entire zone or belt. There are also other types of events which occur on longer timescales, as well as appearance changes which are not as widespread as some of the global zone/belt changes. However, the main types of disturbances are as follows (Fletcher, 2017):

- Gradual colouration events – due to changes in aerosol properties
- Gradual fades/revivals – caused by condensation/thickening and evaporation/thinning of aerosol respectively
- Sudden convective plumes – typically only in belts and jet streams

Additionally, discrete features, zones and belts undergo spatial changes, expanding and contracting, both with and without a related colour change. An overview of the changes which regions of Jupiter undergo is provided in Table 1.3.1. Underneath the cloud tops, which are being discussed here it should be noted that there are likely further linked processes occurring. The largest change, where an entire zone or belt changes colour rapidly sparked by a convective event, is known as an upheaval. These changes question how the cloud structure or properties of the aerosol profiles can vary to produce this dramatic appearance change over such a short period of time. Identifying the structural changes between such different appearances could help to better understand the causes of these major changes on Jupiter.

Upheavals, where the entire belt undergoes a colour change have been most extreme on cyclonic belts on Jupiter (Fletcher, 2017). The South Equatorial Belt (SEB) is one such example and has undergone dramatic changes; for example in Figure 1.3.1, in 2010 the SEB is very pale when compared to its neighbouring years (Fletcher et al., 2017). In this belt the fade to the paler colour in 2010 is more gradual whereas the revival event - to become red again - is a more rapid process (Fletcher et al., 2017). Characterisation of the cloud structure indicates , an increase in the cloud thickness as well as variation in the absorbing properties of the material was needed to reproduce the paler appearance in the visible (Pérez-Hoyos et al., 2012) and infrared (Fletcher et al., 2011).

Determining how the structure of belt regions changes in response to these visible cloud top changes is important, as identifying changes can help us understand and potentially link the processes which are driving these variations from below. The cyclic nature of the zone and belt variation has been well documented due to the regular observations of Jupiter. Shorter cycles can be characterised more easily, such as the NEB which undergoes a cycle every 3-5 years (Fletcher et al., 2017). Regular cycles allow us to prepare as a scientific community to gain observations of the planet to help characterise the phenomenon in multiple wavelengths. However, the cycles are not always predictable; for example, the NEB revival around 2016 did not fully progress to all longitudes as it had before (Fletcher et al., 2017). There is a lot which we do not know about the cyclic nature of Jupiter's appearance, its long years (12 Earth years) take time to observe repeatedly in order to better understand the vast number of changes which it undergoes, which can be seen in Figure 1.3.1. Continual observation is needed at Jupiter if we have any chance of beginning to fully understand these trends and how they occur.

Region and Latitude Range	***Event(s)***	***Description***
North Temperate Belt (NTB) 24–31°N	Jet outbreaks and revival	Outburst of convective plumes on southern jet; reddening of southern part of belt (last in 2020, and before in 2016) (Sánchez-Lavega et al., 2017)
North Equatorial Belt (NEB) 7–17°N	Expansion events	Narrowing and broadening into neighbouring zone with 3–5 year cycle (occurred in 2015–2016) (Rogers, 2019c; Fletcher et al., 2017)) Another began in 2020 but quickly subdued (Rogers and Adamoli, 2021)
Equatorial Zone (EZ) 7°N–7°S	Colouration episodes	Orange/yellow tint in EZ, occurred in 2012–2013, and again in 2019-2022 (Rogers, 2022)
South Equatorial Belt (SEB) 7–20°S	Fade and revival cycles	Whitening then convective revival (last in 2010–2011) (Fletcher et al., 2017). Smaller SEB outbreaks occur during "normal" state (Rogers, 2017).
South Temperate Belt (STB) 27–32°S	Fade and revival in discrete sectors	Outburst of spots on northern jet, but none as large as NTB outbreaks (Rogers, 1995, 2019b)
Oval BA ∼33°S	Colouration episodes	Formed in 2000, changes between red to white, with and without red external ring (Anguiano-Arteaga et al., 2023)
Great Red Spot (GRS) ∼22°S	Colour and size development	Changes in red colour and shrinking extent of storm in recent years (Simon et al., 2018) Also affects surrounding regions through 'flaking' of material, seen in 2019/2020 Rogers (2019a)

Table 1.3.1: Visual Cycles and trends on Jupiter, for both zones, belts and individual features. Updated table from Fletcher (2017), to include additional regions and newer observations using BAA reports (J. Rogers).

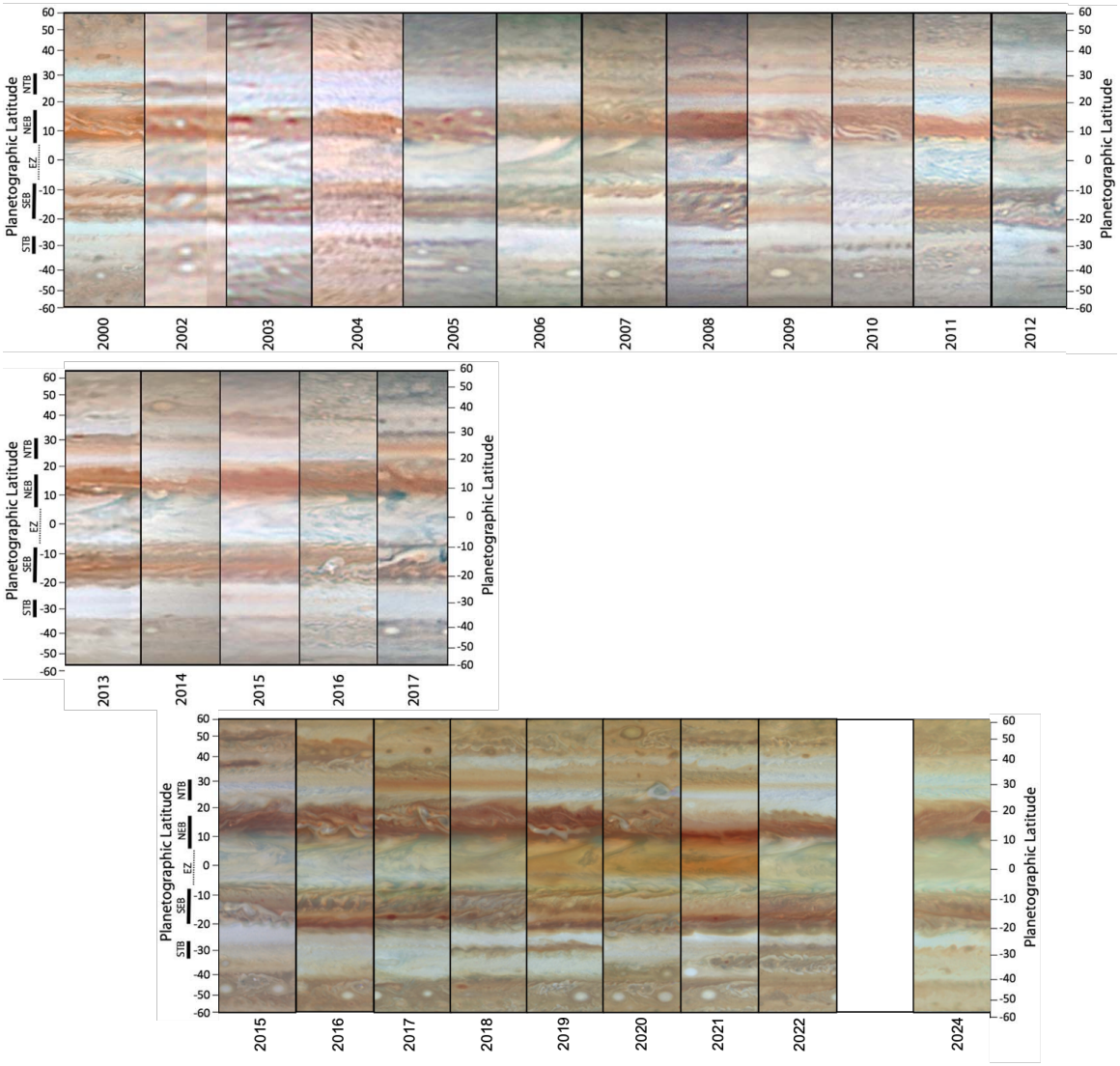


Figure 1.3.1: Cloud top variations of Jupiter observed through a combination of amateur observations 2000-2017, which is then extended to 2024 with HST/OPAL maps (Simon et al., 2015). Covering around 2 Jovian years (24 years) we can see the variation which occurs across the main belts and zones of the planet, each image covers approximately 15° longitude. The figure is adapted from Fletcher (2017).

1.4 Determining Vertical Cloud Structure

The visible changes observed at Jupiter's cloud tops are linked to the vertical distribution of aerosols in the atmosphere. Variation of the clouds forming is evident through visual changes at the cloud

tops, however we know that the clouds extend below this. However, determining the characteristics of the entire vertical cloud structure is difficult. Despite there being predicted locations for the clouds, which will be discussed further in this section, the evidence for them is not as strong as would be expected. The only in-situ observations are of an anomalous hot-spot region from the Galileo probe (Niemann et al., 1998), again not providing a clear foundation in which to base a global cloud structure upon. Therefore, attention has been shifted to work which uses radiative transfer modelling to attempt to uncover the structure of clouds in Jupiter's atmosphere.

Determining the vertical distribution of clouds in the atmosphere will always be a challenge: as a dynamical object they are ever-changing, plus the additional difficulties associated with remote observations makes modelling challenging. Relying on single snapshot observations to build up a model of dynamical features can mask some of the processes occurring by infrequent sampling. Establishing regular observations and attempting to determine the cloud parameters for each snapshot can reveal some of the workings of Jupiter's clouds, but can be time-consuming and competitive to gain frequent observing time. Gaining a full model and understanding of the intricacies on this gas giant is an aspirational challenge. Our current understanding of the clouds directly above our heads on Earth is incomplete, therefore the challenges faced when characterising clouds so far away is greater still.

The limitations which we have for modelling Jupiter's clouds, with unknown cloud compositions and locations, no regular in-situ observations, limited wavelength observations and variable observation frequency reveals the daunting task which is understanding the dynamic Jovian clouds. However, with more frequent observations - of a better quality - and with constantly evolving tools to analyse data with increasing computational power, we are constantly expanding what can be learnt about the Jovian atmosphere. In the sections below we will outline the different methods which can be used to determine more information about Jupiter's atmospheric profile. They include a variety of techniques, observations types and models but all aim to gain insights into the aerosol profiles on Jupiter.

1.4.1 Equilibrium Cloud Condensation Models (ECCM)

In order to predict the location of condensing clouds on Jupiter, models were developed which took into consideration the conditions on the planet and the properties of condensing species present on the planet. Such models are known as Equilibrium Cloud Condensation Models (ECCM), e.g., Weidenschilling and Lewis (1973). Using an atmospheric set-up, which includes certain species present at Jupiter, the theoretical location of where these species condense can then be calculated. Parcels of air are raised through pressure levels and the following calculations are undertaken, taken from Atreya and Romani (1985), to determine if condensation occurs.

The technique outlined in Figure 1.4.1 provides an estimate of the location of cloud formation for certain set-up parameters. The use of these models allows for an approximate cloud location and species to be determined for the pressure-temperature profiles which we see in Jupiter's troposphere. The expected cloud locations and densities from the Atreya et al. (1999) model are presented alongside other ECCM results in Figure 1.4.2. The 'classic' ECCM result, gives the expected cloud structure and species (for solar concentrations of condensable volatiles)

- Ammonia Ice Cloud ($NH_3[s]$) – 0.72 bar
- Ammonium Hydrosulphide (NH_4SH) – 2.21 bar
- Ammonia Water Cloud ($NH_3[aq]$) – 5.69 bar

However, these models have to apply simplifications to the atmospheric system, which reduce their ability to fully reproduce the intricacies of the atmosphere which affects their ability to model condensation. It is acknowledged that the steps outlined in Figure 1.4.1 estimate cloud densities to be much greater than what is expected in the atmosphere (Atreya et al., 1999), as displayed in Figure 1.4.2. It is estimated that those densities are 10^3 – 10^7 times higher than what is observed in situ (Wong et al., 2015). It was proposed this could be negated through precipitation by Atreya et al. (1999), however, the strong up-drafts also present in this model would make it unfeasible for precipitation to occur. In addition it was found that some models based on those by Weidenschilling and Lewis (1973) violate mass conservation laws (Wong et al., 2015). Even after a single step, results

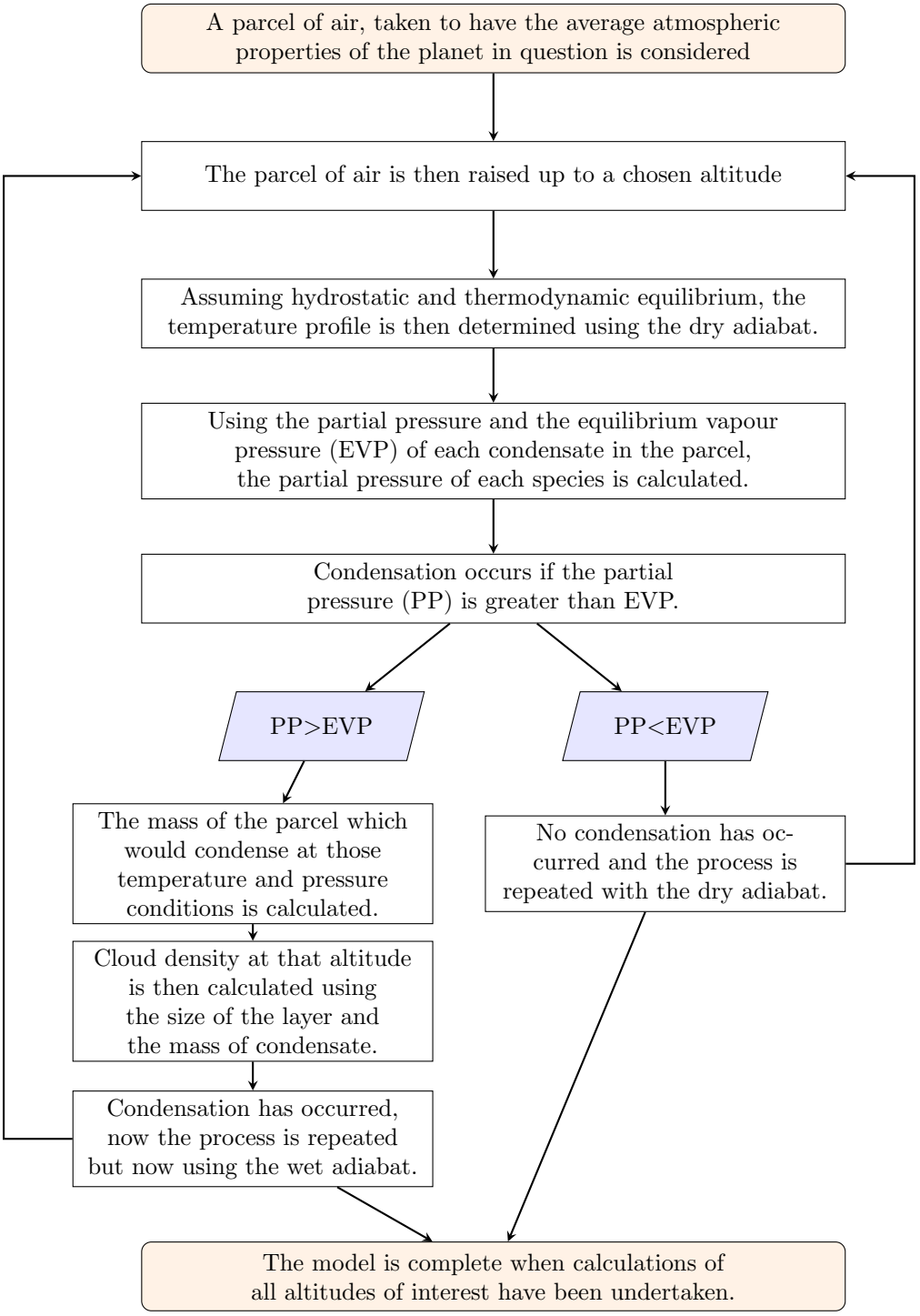


Figure 1.4.1: Flow chart depicting the steps of an ECCM model from Atreya et al. (1999).

produces four times the amount of condensate in the first model step than the mass of the vapour in the original cloud when at the base pressure of the model Wong et al. (2015). Therefore we must question the ability of these models to be able to predict condensation levels accurately, as the inability to accurately estimate cloud densities represents shortcomings in the physics within these models which may also impact other conclusions they draw. The lack of dynamics in the model, both downward vertical and horizontal mixing, again removes processes which are important in determining cloud location and density. As is the negation of micro-physical processes which impact cloud formation and depletion (Wong et al., 2015). The solely upward motions in the model is non-physical as it should be matched en-masse with downward motion, yet another limitation in the models ability to model realistic atmospheric conditions. Further to this, the original atmospheric conditions which initialise the model, such as the abundance of condensable volatiles, can produce a large variation in the model output, both for cloud location and density (Atreya et al., 1999). Therefore, we can accept that ECCMs provide a good first-order approximation of where clouds will form in the atmosphere. However, the limitations of the models have to be considered when discussing their results and there should be appreciable consideration that many major processes of cloud formation which are excluded from the models, impacting the conclusions which are being drawn and should not be treated as known values when initialising models.

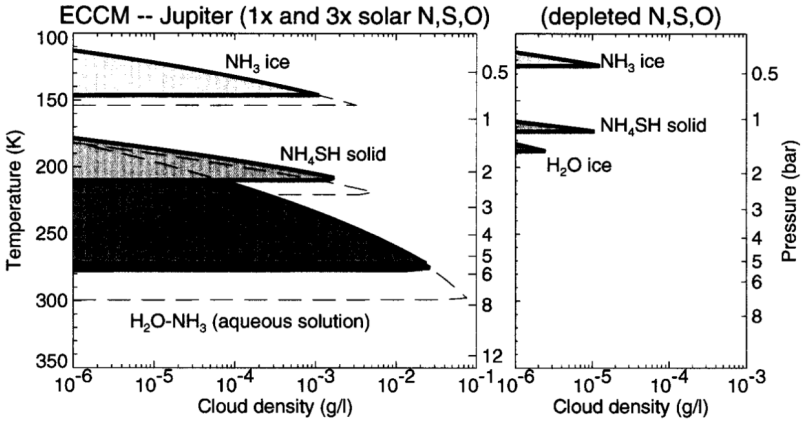


Figure 1.4.2: Results from ECCM models from Atreya et al. (1999), both for (Left) solar and 3x solar abundance of N, S, and O to give the expected cloud levels of the expected condensates. Right - ECCM results with highly depleted levels of N, S, and O attempting to reproduce the Galileo probe results.

1.4.2 Galileo Descent Probe

Designed to provide ground truth to the many models of Jupiter's atmosphere, the Galileo Descent Probe entered Jupiter's atmosphere in December 1995. The probe aimed to establish the vertical profile of clouds as well as their micro-physical properties (Ragent et al., 1998). This was achieved through the nephelometer (NEP) and net flux radiometer (NFR) instruments. The NEP measured laser light back-scattering from the atmosphere across 5 angles (Ragent et al., 1998). Whilst the NFR measured upward and downward flux to create a vertical profile over five wavelength bands (Sromovsky et al., 1998). These back-scattering reflectivities can be inverted to infer information about cloud location, density and radii of the cloud particulates. The NFR confirmed such locations and was able to determine some cloud properties depending on the clouds' effect on the signal in thermal wavelengths (Sromovsky et al., 1998). Overall the mission was successful and a descent was carried out transmitting information about the atmosphere from ∼0.4 bar down to ∼22 bar until the probe succumbed to the extreme conditions (Ragent et al., 1998). From this, the locations of the cloud are presented in Figure 1.4.3.

From the probe data it is not possible to determine the composition of the cloud material, but we are able to get a clear indication of the levels which the probe is sensitive to material. There are some readings which are less definitive than others on the descent profile due to some peaks only being recorded during a single observation point. However, it can be seen from Figure 1.4.3, that there is a modest signal for a cloud peaking at 1.34 bar (Ragent et al., 1998). There are other peaks in the signals at ∼1.65 bar as well as an increase in count between 2–4.5 bar indicating another structure (Ragent et al., 1998). The initial count recordings around 0.4 bar indicate a decrease in counts as the NEP began to transmit results, which is assumed to be the probe leaving a cloud layer but this cannot be confirmed. However, it can be seen that the results from the NEP disagree with what was expected for the cloud locations shown by ECCMs.

The results from the probe, which were hoped to be ground truth, are very different to those expected for Jupiter's cloud structure derived from ECCMs. With the main cloud reported at 1.34 bar (Ragent et al., 1998), this cloud lies between two ECCM predicted clouds, at 0.7 bar and 2.2 bar.

Questions of the cloud's composition begin to be raised as no pure species considered in ECCMs are meant to condense at these pressure levels. Despite the probe being the only in-situ observation of Jupiter's atmosphere, its anomalous descent location, means we cannot be sure of its application to the whole planet. With a confidence of more than 98%, it is believed that the probe entered a $5\mu m$ hotspot (Orton et al., 1998), a region which is non-analogous with over 99% of the planet (Orton et al., 1996).

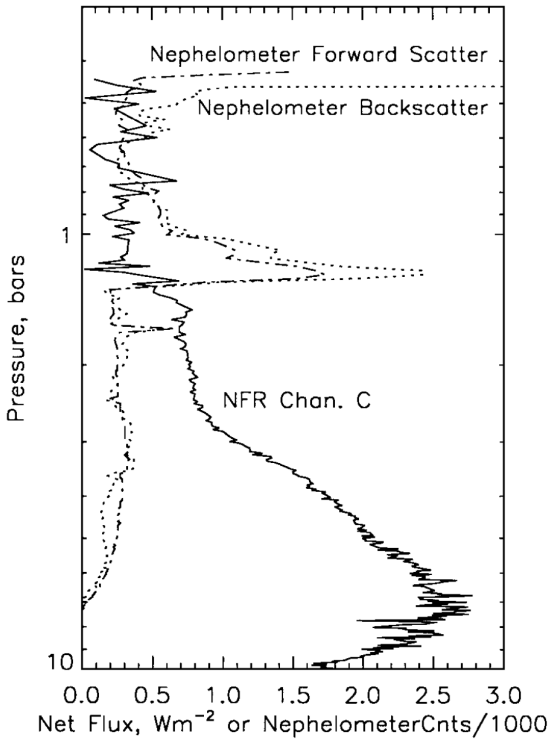


Figure 1.4.3: Results from the Galileo probe Nephelometer Ragent et al. (1998) taken from Sromovsky and Fry (2002), displays the evidence for cloud in the Jovian atmosphere from in-situ observations, net flux radiometer (channel C (3.5–5.8μm)) and the Nephelometer forward-scatter (dot-dash) and back-scatter (dotted) counts.

The spatial coverage of $5\mu m$ hotspots over Jupiter is low, with them only accounting for 1% of the global area. It was thought that the chances of hitting an anomalous hotspot region were low and so no further constraints were placed on the probe entry location. However, it was found after the descent that the $5\mu m$ hotspot spatial extent increased to 15% of the latitude band ($\pm 5^\circ$ of

the equator (Oneil and Mitchell, 1983)) the location of the entry site, once constrained by orbital dynamics (Orton et al., 1996). $5\mu m$ hotspots appear thermally warm in the $5\mu m$ window, and dark in the visual (Orton et al., 1996), their brightness at $5\mu m$ is due to radiation from deeper in the atmosphere being able to permeate upwards, as for these wavelengths the gases of Jupiter's atmosphere are highly transparent. This lack of absorption at these wavelengths allow us to see emission emanating from around the 10-bar level. What we can then see of the $5\mu m$ radiation is dependent on the opacity of the overlying clouds. Leading to anti-correlation between $5\mu m$ brightness and visible reflectance. Hence these $5\mu m$ hotspots tend to be associated with being relatively dry regions, with less cloud than the majority of the planet (Orton et al., 1996). Their low cloud density is thought to be due to predominantly down-welling air occurring at these locations (Orton et al., 1996). Therefore, the probe entered a region which has different properties to the majority of the planet, with low cloud cover causing a reduction in radiation absorbing species and increased thermal radiation due to deep emission (Ragent et al., 1998). It is these differences from the rest of the planet which mean the ground truths which were hoped for the probe to discover have not become the infallible results which were expected. The outcome of the probes location was unfortunate, reducing the ability to characterise the general atmosphere, however, it still provided unprecedented information with in-situ measurements.

Due to the unusual characteristics of the hotspot region, explanations for the difference between the ECCM results and the probe data have been attempted. It has been possible to reproduce the probe observations using extreme conditions in the ECCM models (Atreya et al., 1999). The results can be seen in Figure 1.4.2. However, to achieve this depleted abundances of the condensing species are needed, with H_2O depleted to 0.01%; NH_3 1%, H_2S (precursor to NH_4SH) 0.5% of solar abundance (Atreya et al., 1999).

Additionally, an updated ECCM of Wong et al. (2015), which includes a dependence on up-draft speeds to instead calculate a cloud density rate (which creates more realistic cloud densities), finds that strong up-drafts are needed to produce the clouds at the probe altitudes, despite the area typically thought to be associated with down-welling air. These contradicting ideas make it difficult

to determine whether these results can be relied upon to determine the general vertical structure of Jupiter. Clouds are typically associated with up-welling air as this provides the rapid cooling which is needed to condense the species (Wong et al., 2015), therefore indicating the down-welling nature of hotspots is not conducive to cloud formation. It is theorised the clouds observed by the probe could be due to horizontal motion of air, moving tendrils of cloud from the neighbouring equatorial zone which the 5.9°N hotspot laid within, into the fringes of the hotspot where the probe descended, explaining the low number density and presence in a potentially non cloud forming region (Ragent et al., 1998). However, the exact dynamics of the probe's location cannot be confirmed.

It should also be considered whether ECCMs are comparable to the modelling which will be undertaken in this thesis. These models are resolving on small scales, considering a single parcel of air which is moving, a single convection cell. Whereas the resolution in our observations is averaged over regions of both up-welling and down-welling in the atmosphere. Comparison between these very different length scales is not ideal, and it would be more suitable to choose models which also capture the bulk eddy mixing which our observations are averaging over.

The NEP also had the capabilities to identify other properties of the aerosol material which it descended through. Using the distribution of scattered light measured by its 5 detectors it can characterise particles up to a maximum radii of $10\mu m$ (Ragent et al., 1998). There are limitations to the results due to the assumption of solid spherical particles, as this negates the effect which particle properties such as shape, inhomogeneity, absorption, coatings and other properties have on the scattering properties of the particles (Ragent et al., 1998). Further to this there is also degeneracy between the cloud radii and the refractive index of the particles which are both being retrieved. A wider range of the solution space is provided in Ragent et al. (1998), and the results are ill-constrained due to differences which each channel and methods of inverting provided. However, one of two best fit solution sets for the 1.34 bar cloud is provided here. It is estimated that $1\mu m$ particles are present with a real refractive index of 1.7-1.8 at $0.9\mu m$ and an imaginary refractive index of $\sim$0.05 (Ragent et al., 1998).

Thus there are anomalies between ECCM models and the nephelometer data, likely due to processes

which are not understood fully or are not included in the model set up, as well as the unusual location of the probes entry. Though they agree in the first order there are significant differences which now need to be investigated to conclude what state the vertical profile is actually in. We should consider all conclusions drawn from both sources with care, as often the set-ups do not match large parts of the atmosphere, consider the wrong scale, or neglect processes which alter the final results. Neither of these results provide *a priori* estimates which we can confidently base any atmospheric models upon. In order to determine the vertical cloud structure without additional probes, we introduce what can be achieved through the use of remote sensing and radiative transfer models to infer the structure from afar.

1.5 Radiative Transfer Derived Models

1.5.1 Overview of previous models

The use of radiative transfer models has been adopted widely by the community due to the large amount of information which can be extracted for the majority of the atmosphere with a wide range of observations. These models work by attempting to match to an observed spectrum by taking an atmospheric profile and calculating what its spectrum would look like, and minimising the difference. Chapter 3 provides an overview of the radiative transfer model used in this work NEMESIS (Irwin et al., 2008), as well as some of the references discussed in this section, and may provide a greater insight into the working of radiative transfer models in general as well. The works which are presented here use a variety of observations and are focused on a range of atmospheric locations but they demonstrate the ability of radiative transfer models to determine information about Jupiter's atmospheric aerosol profile.

In this section we will discuss multiple atmospheric profiles which are also outlined in Table 1.5.1, then more comparable studies to the work in this thesis (visible and near IR radiative transfer models) will be discussed in more detail.

Literature	*Wavelength*	*Atmospheric Profile*	*Comments*
- Bézard et al. (1983)	5 – 45μm Voyager/IRIS data	Absorbing cloud between 1.2 bar-4 bar	Weak ammonia ice signal, most likely to be NH_4SH with possible deeper H_2O cloud
- Conrath and Gierasch (1986), Gierasch et al. (1986)	5 – 45μm Voyager/IRIS data	Cloud base 680 mbar	Mapping ammonia abundance and cloud opacities
- Banfield et al. (1998)	Galileo SSI Imager (889nm, 727nm, 756nm)	Optically thick cloud ($\sim$0.7 bar) Tropospheric haze ($\sim$0.7–$\sim$0.2 bar) Stratospheric haze up to 0.01 bar	Models differ opacity and pressure values for regions (EZ, South Eq. Jet, SEB, NEZ, Hot Spot, GRS
- Irwin et al. (1998)	0.7 – 5.2μm Galileo/NIMS	0.2 bar tholin haze, 0.7 bar NH_3, 1.4 – 5 bar NH_4SH	Edge of warm spot
- Irwin et al. (2001)	0.7 – 5.2μm Galileo/NIMS	1.2 – 2 bar	Opacity peaks at 1.4 bar, potential to be NH_4SH, H_2O, NH_3 or other species
- Irwin and Dyudina (2002)	5μm Galileo/NIMS	1 – 2 bar dominant opacity, haze $\sim$0.2 bar	Principal component analysis
- Matcheva et al. (2005)	7.18μm CIRS	1.1 bar possibly NH_4SH 0.9 bar possibly NH_3 ice	Peak of cloud absorption coefficient for a thin and thick cloud

- Roos-Serote and Irwin (2006)	0.7 – 5.2μm Galileo/NIMS	5μm Absorbing cloud must reside at p<2 bar	Limb darkening considered
- Sromovsky and Fry (2010)	0.7 – 5.2μm Galileo/NIMS	0.79 – 1.27 bar 0.5 bar	Deepest cloud had highest opacity Comprised of NH_3 and NH_4SH
- Perez-Hoyos et al. (2012)	200 – 950nm HST/WFC3	0.7 bar main cloud	Modelling profile during 2009 impact
- Giles et al. (2015)	4.5 – 5.1μm Cassini/VIMS	1.2 bar or lower pressure	Differing opacity models led to spectral variations
- Sromovsky et al. (2017), Baines et al. (2019)	0.3 – 1.05μm Cassini/VIMS spectrum	NH_3 Cloud ∼2.5 – 0.2 bar Directly overlying thin chromophore layer Haze ∼0.04 bar	Crème Brûlée model, Variable parameters for each location (GRS, SEB, EZ, NEB), Carlson et al. (2016) chromophore
- Bjoraker et al. (2018)	4.6 – 5.4μm iSHELL spectrum and 7.8μm Cassini/CIRS	Opaque cloud 5±1 bar Cloud 1.3 – 2.3 bar 570±30 mbar reflecting layer	Assuming NH_3 ice, NH_4SH and H_2O layers, also retrieving gas composition
- Baines et al. (2019)	0.3 – 1.05μm Cassini/VIMS spectrum	NH_3 Cloud ∼2.5- 0.2 bar Directly overlying thin chromophore layer Haze ∼0.04 bar Stratospheric chromophore haze ∼0.15 bar Main cloud 0.27 – 2.99 bar	Crème Brûlée model for GRS, Carlson et al. (2016) chromophore Poorer fit than CB

		Chromophore coated cloud model 0.1–7 bar	Poorer fit than both
- Braude et al. (2020)	$0.48 - 0.935\mu m$ VLT/MUSE spectrum	Cloud/haze profile peaking at ∼1.4 bar, chromophore layer above 0.6±0.1 bar	Continuous profile made of three components (haze <0.15 bar, cloud >0.15 bar and chromophore)
- Pérez-Hoyos et al. (2020)	HST/WFC3 9 filters 275nm – 889nm	Stratospheric haze 0.01-0.1 bar Tropospheric haze bottom 0.2±0.1 bar Bottom cloud 0.7 – 0.9 bar Haze 40±40 mbar Chromophore 200±200 mbar Cloud 1.0±0.5 bar	Chromophore mixed into tropospheric haze Crème Brûlée model with Carlson et al. (2016) chromophore
- Dahl et al. (2021)	$0.47 - 0.945\mu m$ NAIC spectrum	Crème Brûlée model NH_3 Cloud ∼2.5- 0.2 bar. Directly overlying thin chromophore layer, Haze ∼0.04 bar	Tested both Carlson et al. (2016) and Braude et al. (2020) chromophores and varying particle sizes
- Anguiano-Arteaga et al. (2021)	HST/WFC3 9 filters 275nm – 889nm	Stratospheric haze <0.1 bar, tropospheric haze based at 0.5 bar, deeper cloud deck	Requires two chromophore materials to fit to GRS

Table 1.5.1: Overview of work using radiative transfer models to reproduce observations through cloud models of the Jovian atmosphere. In the table, works that focus on the tropospheric region have been included but for a variety of wavelength ranges and instruments.

Table 1.5.1 provides an overview of the huge amount of variability that is present within radiative transfer modelling of Jupiter's atmosphere. Due to the significant amount of degeneracy which is present in the Jovian parameter space there are a huge number of parameter combinations which can produce an incredibly similar observational fit. Differentiating between which of these combinations

is the most realistic representation of the atmosphere is practically impossible due to the degeneracy. When comparing different works, the additional variation caused by different observation dates, wavelength ranges and instruments demonstrates how difficult it is to consistently model Jupiter's aerosol structure, and leads to the huge variety displayed in Table 1.5.1. We only include pressure levels of clouds and hazes to indicate how these models vary. Free parameters within each model, such as radii, refractive index values and opacity mean even more differences are present within the literature. However, there tends to be main trends appearing for the pressure levels of these models; those agreeing with the condensation models with a main cloud around 0.7 bar and those with a deeper cloud around 1.4 bar similar to the Galileo probe results. Attempting to determine which of these collections of models is correct remains a key question of modelling of Jupiter's atmosphere, and a clear example of the huge amount of degeneracy which is present in the system as both are able to match observations.

1.5.2 Post Carlson et al. (2016) chromophore models

Following the work of Carlson et al. (2016) producing a viable chromophore candidate, (Section 1.2.3), there have been several works published about the viability of this chromophore when combined into cloud models of Jupiter, seen in G onwards in Figure 1.5.1. As can be seen in Figure 1.5.1 there is a huge amount of variation in the retrieved parameters needed to model the same location.

These differing results are likely due to the degenerate pairs of parameters in the models, and it is hard to determine which profiles are most likely to represent the atmosphere most closely. The following pieces of work are most relevant to that of this thesis as they are investigating the tropospheric structure of Jupiter in the visible/near IR wavelength range. Using radiative transfer models, several works wanted to demonstrate the Carlson et al. (2016) chromophore's ability to model spectra universally across Jupiter. One such work is Baines et al. (2019) which introduces a 'Crème Brûlée' model for the GRS using the Carlson et al. (2016) chromophore (K in Figure 1.5.1). It is then extended across the other regions of the planet to look at the GRS, SEB and NEB by Sromovsky et al. (2017) (G – J in Figure 1.5.1).

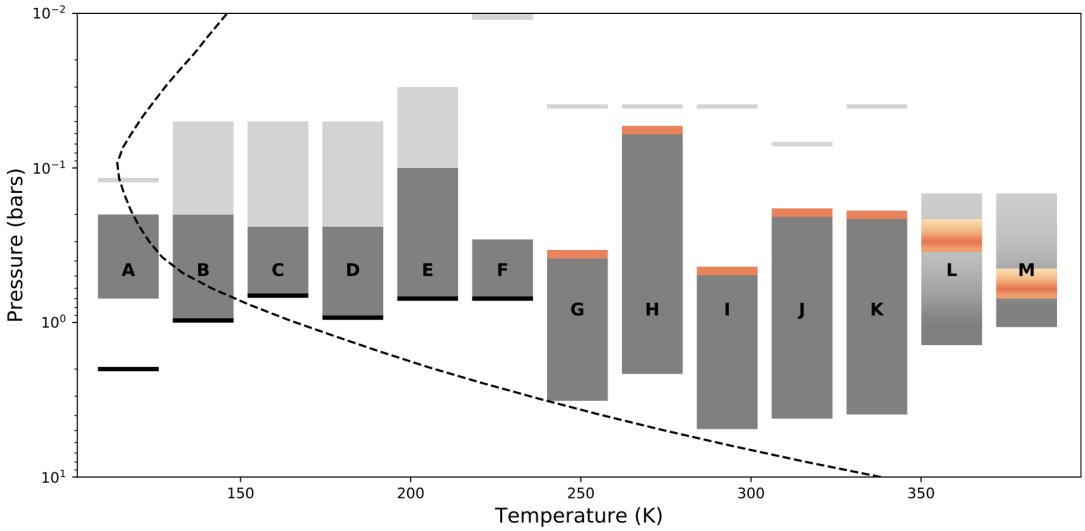


Figure 1.5.1: Figure taken from Dahl et al. (2021) shows a range of retrieved aerosol profiles which have been developed to reproduce spectra from different regions of Jupiter. Black lines are opaque tropospheric sheet clouds, dark grey is tropospheric hazes or clouds, and light grey indicates stratospheric hazes and can be represented by a line or block. Orange blocks and lines represent chromophore layers. Any colour gradients represent more complex models with clouds/hazes that vary more with altitude. *Model A* - Smith (1986) SEB, *Model B-D* - Simon-Miller et al. (2001) NEB, EZ, SEB, *Model E* - Strycker et al. (2011) EZ, *Model F* - Pérez-Hoyos et al. (2012) SEB (fade), *Model G-J* - Sromovsky et al. (2017) NEB, EZ, SEB, GRS, *Model K* - Baines et al. (2019) GRS, *Model L-M* - Braude et al. (2020) EZ, NEB.

The work of Baines et al. (2019) through modelling of the GRS spectrum attempts different ways of parameterisation of the Carlson et al. (2016) chromophore in the atmosphere. As a starting point, the refractive index of the chromophore material was fixed (to Carlson et al. (2016)) but the vertical profile of the cloud and distribution of the chromophore was unknown, so a range were tested. The GRS provided a prime location to attempt this study due to its red appearance which is indicative of enhanced abundance of chromophore material. Cassini/VIMS observations are used in this work, which observed the GRS both near the central meridian (17.8°W of the central meridian) and also at a higher viewing angle (55.8°W of the central meridian) for 0.35-1.05μm. For this work, a single pixel was taken to extract the spectrum from, the reddest in the GRS on each occasion. This work aimed to determine where in the profile the chromophore material was located, and what condition it existed in e.g, pure chromophore or coating on another material. Baines et al. (2019) used a value of 1.4 for the real refractive index, and a linear extrapolation of the Carlson et al. (2016) imaginary

refractive index for all wavelengths in the VIMS data. Three chromophore distributions were tested: A) chromophore material as a coating on the main cloud layer; B) chromophore stratospheric haze; C) thin layer of chromophore directly above the main cloud layer with an additional stratospheric haze, i.e., Crème Brûlée model. In all of these models the main cloud material is assumed to be a conservative scatterer, and the results are said to be invariable with regards to its base pressure but typically have values of $\sim$7 bar, but had a top pressure of $\sim$0.2 bar. Baines et al. (2019) found model C (Crème Brûlée) to have the best fit to the data, closely followed by model B. Chromophores as a coating on the main cloud (model A) were found to be unable to reproduce the blue slope part of the data, unlike models B and C (Baines et al., 2019). The observation towards the limb also displays the same results, albeit with poorer fits for all models, both viewing angles were not fitted simultaneously. The stratospheric haze model creates a blue slope which is too steep, leading Baines et al. (2019) to conclude that the chromophore is likely to remain in a thin layer just above the main cloud but not detached as this would affect the blue slope. The authors also stated that the chromophore would not be distributed within the cloud but this has only been tested for a coating scenario in this work, not as separate well mixed particles (or any other scenario) when located within the main cloud.

Differentiation between the likelihood of model B or C was done through the plausibility that the atmospheric properties could produce the chromophore in the correct location and amount in each scenario. The chromophore's main constituents are C_2H_2 and NH_3 (Carlson et al., 2016), and the stratospheric model would require far more of these species at a higher altitude than are, with current evidence, expected to be there (Baines et al., 2019). Further to this, ammonia would be expected to dissociate in the UV light which penetrate to these altitudes before being able to form the chromophore material (Baines et al., 2019). This would increase the timescales needed to produce a stratospheric layer of chromophore (decades or longer), which is far beyond what is seen through the rapid alterations of atmospheric appearance (revivals over months) hence making the stratospheric haze parameterisation less viable. Therefore, only scenarios in the troposphere allow for conditions where the correct abundances of parent species are available to produce the required amounts of chromophore. However, when considering diffusion mechanisms alone to replenish the

species in situ, both the stratospheric and tropospheric locations of the chromophore would lead to timescales in the order of centuries and above. This issue with dynamics can be solved by considering convective lightning, which is expected to be included in the GRS, which would reduce the time needed for a chromophore layer to be formed down to 1.5 months for the Crème Brûlée model, but this requires the GRS chromophore amounts to be elevated compared to other regions due to the enhanced convection within the storm (Baines et al., 2019). Additionally, the viability of chromophore forming lower down in the atmosphere was not discussed due to the poorer fit of that scenario. Hence, spectral fits combined with discussion of dynamics has led Baines et al. (2019) to conclude the Crème Brûlée model with Carlson et al. (2016) chromophore to be the best fit to their VIMS data for the Great Red Spot.

The Crème Brûlée of Baines et al. (2019) would then go on to be used by several works, testing its potential in other regions of Jupiter and also for different observations. One of these such works is Sromovsky et al. (2017), where the Carlson et al. (2016) chromophore is tested across the disc of Jupiter to test its viability as a global chromophore. Again using a similar model to Baines et al. (2019) this work is able to reproduce spectra for the EZ, GRS, NEB and SEB with both the Crème Brûlée model (main cloud, over-lying chromophore layer and stratospheric haze) and stratospheric haze model (main cloud layer with stratospheric chromophore layer), by varying each of the model parameters between each location to fit each observation. By doing this whilst maintaining the Carlson et al. (2016) chromophore, they were able to fit each spectrum with the most significant changes coming from a variation of particle size and optical depth, as well as cloud top and base pressure changes. It was found that the SEB and NEB did not have fits as good as the EZ and GRS at higher viewing observations taken nearer the limb, and therefore may not be best represented by the Crème Brûlée model. However, the fit retrieved to all four regions provides a good fit and the χ^2/n (used as a measure of goodness of fit, squared difference between observed and fitted spectrum divided by the number of points) value is minimised when the Crème Brûlée model is used. The four models for each region from Sromovsky et al. (2017) are shown in Figure 1.5.1 (G-J), here the variations in the vertical structure which are needed to match the observations can be seen. There are also significant variations of parameters, such as particle size of the main cloud layer which varies

by 169% between the GRS and NEB, which are done to fit the observations. However, the ability to match a range of observations across the disc is noted.

The work of Carlson et al. (2016); Baines et al. (2019); Sromovsky et al. (2017) invigorated the community as it provided new insight into how the colouring of Jupiter's atmosphere could be occurring. This then led to multiple further works, including this thesis, which wanted to test the viability of this work to slightly different atmospheric conditions and observations. The previous works had used data from the Cassini flybys, but since 2000/2001 Jupiter has undergone a wealth of changes. Now, with the observational data to document these changes we can test these observational set-ups to a plethora of different locations, observation dates, and instrument specifications.

One of these works is Braude et al. (2020), where an investigation into the ability of developed models to reproduce observations from the VLT/MUSE instrument was tested. The use of VLT/MUSE data continues the investigation with visible and near IR data, (MUSE is described in Section 2.1). Braude et al. (2020) use observations of the GRS taken between 2014-2018, and for other locations in 2018. Braude et al. (2020) begin to analyse the ability of the Sromovsky et al. (2017); Baines et al. (2019) Crème Brûlée model to reproduce subsequent observations. Braude et al. (2020) compares three main model types: a Crème Brûlée like model, then an variable three layer (haze, chromophore, cloud) model both with the Carlson et al. (2016) chromophore, and finally another where the refractive indices are allowed to vary. Braude et al. (2020) find that the Crème Brûlée model is unable to reproduce subsequent observations of the GRS, NEB, EZ or SEB for VLT/MUSE observations in 2018, including for the blue slope region. It is to be noted at this point that some other works such as Dahl et al. (2021) do not have this issue for the 2018 observations as modelled here, however these use a different instrument. Braude et al. (2020) find improved fits with the three layer model with the Carlson et al. (2016) chromophore fixed, but this model is superseded still by a chromophore with indices which are derived using their own observations, described below. Braude et al. (2020) theorise that the Crème Brûlée model is unable to reproduce more recent observations due to a potential steepening of the blue slope of the GRS over time, both with and without associated reddening of the cloud tops. As they model the GRS with observations taken more recently, the

goodness of fits decreases over time away from the VIMS data taken in 2000. Braude et al. (2020) suggest further issues with the VIMS calibration, with methane absorption peaks being nonphysical, which creates further differences when fitting to MUSE spectra, rather than VIMS.

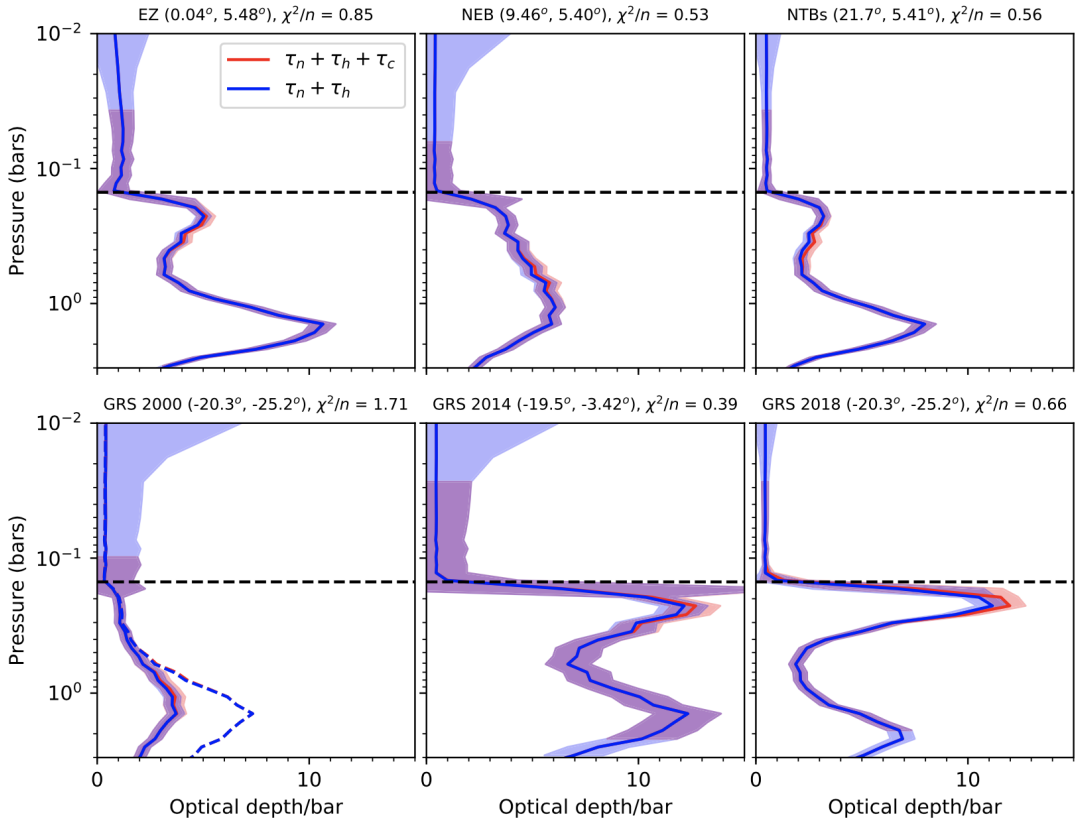


Figure 1.5.2: Figure taken from Braude et al. (2020) showing the retrieved cloud profiles for the EZ, NEB, SEB and GRS for the combined cloud (τ_n), chromophore (τ_c) and haze (τ_h) contribution to the aerosol optical depth in each region. The dashed line is at 0.15 bar and shows the cut-off point between haze above and the cloud below.

Due to this inability to fit observations using the Crème Brûlée model with the Carlson et al. (2016) chromophore, Braude et al. (2020) developed a chromophore which was more adept to fitting the observations of the VLT/MUSE, and Cassini/VIMS data set, through the analysis of the NEB. Spectra were taken for 5 viewing angles (-60°, -30°, 0°, 30°, 60°), with the NEB chosen for the region's homogeneity, red colour and lack of haze. Cloud models were then fitted to a smoothed spectrum of these regions whilst allowing the refractive indices to vary. The retrieved chromophore

was able to better fit to their observations (Braude et al., 2020). Now with the chromophore fixed, Braude et al. (2020) were able to derive the aerosol profile, Figure 1.5.2, ammonia profile (with both VMR and scale height varying) Figure 1.5.3, as well as other varying parameters such as particle size, to create a model which was best suited to each region across the disc. These observations were taken for a single viewing angle and for the rest of the disc, using a favourable observation, with excellent seeing conditions, taken on 9th April 2018 was used (Braude et al., 2020). Due to a lack of sensitivity to the stratosphere Braude et al. (2020) were only able to estimate a peak chromophore location of 0.6 bar, but this is not above all of the cloud, as it is for the Crème Brûlée model, and found the main cloud layer to peak around 1.4 bar consistently across the disc. However, the total opacity and vertical extent of the aerosol profiles vary between each region.

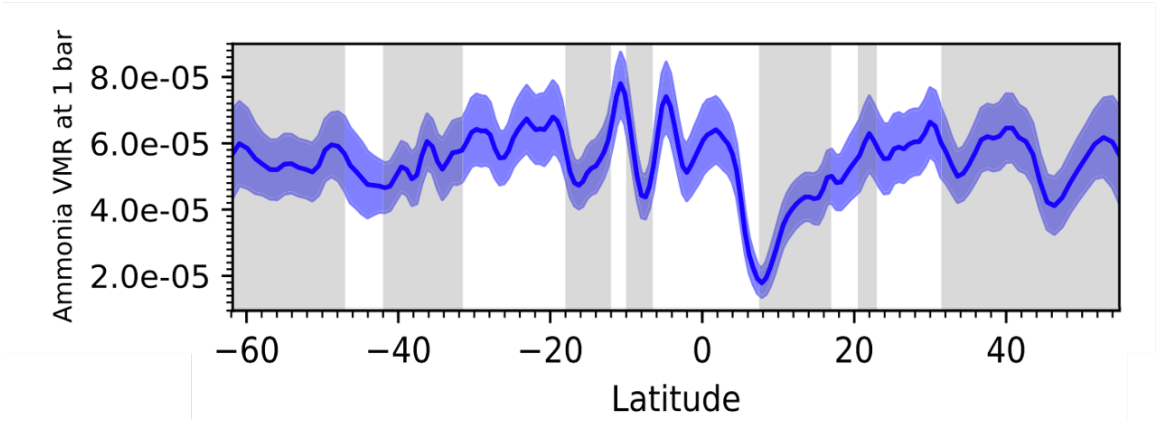


Figure 1.5.3: Figure taken from Braude et al. (2020) to show their retrieved ammonia profile across the disc for 9th April 2018 MUSE observations.

Dahl et al. (2021) also set out to discuss the applicability of the Crème Brûlée model to subsequent observations and were also able to prove that this model is able to reproduce observations albeit with some adaptations. This work again used visible/near IR data, this time from the New Mexico State University Acousto-optic Imaging Camera (NAIC) at Apache Point Observatory in Sunspot, NM, USA. This instrument produces spectral cubes, containing the whole disc of Jupiter, like VLT/MUSE observations but using an acousto-optic tunable filter, this is a crystal which can be tuned by radio waves to produces a filter centred on the wavelength of choice. Dahl et al. (2021) were able to tune the crystal filter to provide sampling every 2nm to produce a complete spectrum from 470 to 950nm.

The exposure time of each filter is short (around one second), however for the combined wavelength range the total exposure time is large enough to require calibration to account for the rotation of Jupiter across the wavelength range, unlike for VLT/MUSE observations. As with Braude et al. (2020), Dahl et al. (2021) use the NEMESIS retrieval model (Irwin et al., 2008), to fit the observed spectrum with a parameterised vertical cloud profile. Dahl et al. (2021) find that the Baines et al. (2019); Sromovsky et al. (2017) Crème Brûlée model is able to reproduce more recent observations of Jupiter from 2017, for the EZ, NEB and SEB unlike Braude et al. (2020). This may be due to the differences which are present between the spectra of Dahl et al. (2021) and Braude et al. (2020). It is thought that photometric calibration, instrument and filter shape, and even physical changes in the NEB could be the reason behind these differences, as both spectra have a similar wavelength range and errors of $\sim$5%. The Braude et al. (2020) spectra is brighter (by $\sim$0.06 I/F at 680nm) for the majority of the spectral range, except for methane absorption features where the I/F is smaller in these troughs than the NAIC spectra (I/F of 0.12 for NAIC compared to 0.04 for MUSE at 890nm) (Dahl et al., 2021). The disc averaged spectra of Dahl et al. (2021) also displayed shallower absorption features than the Karkoschka (1998) disc averaged spectra. The differences in the spectral fit of the Crème Brûlée model to fit to the spectra used in Dahl et al. (2021) and Braude et al. (2020) may be down to these absorption feature differences.

However, to produce the best fit to the data, Dahl et al. (2021) required some alterations to the parameters of the model. In particular, Dahl et al. (2021) fixed the base, pressure and the particle sizes for each layer ($1.0\mu m$ cloud, $0.15\mu m$ chromophore, $0.1\mu m$ haze) found through a grid search for each parameter for the three regions being fit. By doing this some of the degeneracy is removed by fixing the values. To fit each region, Dahl et al. (2021) finds that the chromophore imaginary indices need to vary away from the Carlson et al. (2016) values. However, it is noted that the variances retrieved in each region could relate to the differences in exposure time of the chromophore in the atmosphere, as younger chromophores have a brighter, less absorbing appearance, theorising that it could be the same chromophore compound across the disc but with differing exposure times causing an alteration in the chromophore indices. This could be occurring in the EZ and SEB regions, which retrieved smaller values for the imaginary refractive index of the chromophore. These differences

could be accounted for by overturning at the cloud tops which would reduce irradiation time for the chromophore and hence not be able to reproduce the Carlson et al. (2016) indices which require longer exposure times of 70 hours. Such variations with shorter irradiation times would result in a lower value for the imaginary refractive blue slope for each region, unlike Braude et al. (2020) which finds the blue slope indices to be more steeply varying. These differences could be due to physical differences in appearance as time passes between observations, differences in the model set up, such as particle size, or an observational difference which has led to differences in the retrieved result. Dahl et al. (2021) also conclude that the fit to the SEB is unsatisfactory compared to other regions leading to a conclusion that the Crème Brûlée model may be unsuitable for events such as the SEB outbreak which was occurring in 2016-7 (Dahl et al., 2021).

The differing results of Braude et al. (2020) and Dahl et al. (2021) for the same year indicate the complexities that are being captured through these vertical cloud models. Using observations taken within 13 months of each other it would be expected that solutions would be similar between the two works. However, the variation in particle size, cloud top and base pressures, and chromophore refractive index values elude to the huge number of solutions that are able to reproduce each observation within their errors. Some difference could be explained by physical changes within the atmosphere between the observations, but the differences between parameter values are often significant, and with minimal visual changes unlikely to be enough to drive the changes between the models. Hence, we have multiple solutions to these observations and are unable to differentiate which are most likely to be representative of the real atmospheric state. When deriving the atmospheric profiles neither of these works fit to multiple viewing angles simultaneously, although Braude et al. (2020) use different viewing angles when deriving the chromophore refractive indices. The introduction of limb-darkening information could help to break some of the degeneracy. By introducing more constraints on the data when we undertake retrievals we can hope to refine the retrieved atmospheric conditions to reproduce observations using a profile which is closer to real-life conditions.

The work of Pérez-Hoyos et al. (2020) focus on the NTB disturbance as a way to determine how the atmosphere responds to large visual changes; in this event the pale quiet belt transformed,

after interactions with storms, into a bright red belt (Sánchez-Lavega et al., 2017). This work used the Hubble Space Telescope (HST) Wide Field Camera 3 (WFC3), spanning wavelengths from 250nm to 890nm. However, these are filter images of Jupiter, so have far less spectral resolution of the works above (though far higher spatial resolution). Pérez-Hoyos et al. (2020) model two scenarios, the Crème Brûlée model as in Sromovsky et al. (2017); Baines et al. (2019) and also a well mixed chromophore within the tropospheric haze, below a stratospheric haze and above an assumed ammonia ice cloud. Due to the low spectral resolution of the filters it can be harder to resolve a solution due to less spectral information, as it provides less constraint to help break degeneracies. For the model runs with the mixed tropospheric haze, where the chromophore and fresh material (possible ammonia ice) share single retrieved refractive indices, these values are allowed to vary along with the base pressure, scale height and maximum peak abundance. All parameters of the extended stratospheric haze are fixed except the for optical thickness, as with the main cloud layer. For the main cloud layer, deeper in the atmosphere at a level where it is optically thick to observations, minimal information can be extracted about the cloud properties, such as base pressure, therefore all but the optical thickness is fixed for this layer.

Pérez-Hoyos et al. (2020) use the Minnaert Equation (Minnaert, 1941) to extract information about limb darkening (see Section 4 for more information) from the observations, and can then simulate the observations at any desired viewing angle. Through this any location on the disc can be approximated with synthetic filter averaged images with the desired viewing angle. For this work Pérez-Hoyos et al. (2020) use 7 viewing angles to ensure the models can incorporate the limb darkening as well as original nadir observations. This provides a higher level of constraint to the models as it ensures that the retrieved profiles are able to fit the observations well from a multitude of viewing angles, producing a result which should represent the real life scenario better.

It was found that although the Crème Brûlée model was able to fit the data well, it was instead the extended mixed chromophore layer which was able to better reproduce the data (Pérez-Hoyos et al., 2020). Both models were able to adapt to the visual changes of the NTB through an alteration of their parameters and both models require an increase in the amount of chromophore to reproduce the

reddening NTB. The extended chromophore layer requires a mix of twice as much chromophore in the layer, with a steeper blue absorption slope as can be seen in Figure 1.5.4, to match observations. The Crème Brûlée model requires a 100% increase in the density of the thin chromophore layer with a decrease in the lower cloud layer (Pérez-Hoyos et al., 2020). The variation of densities here are significant and may begin to contradict chemical models if the production rates necessary to produce such vast changes are non physical.

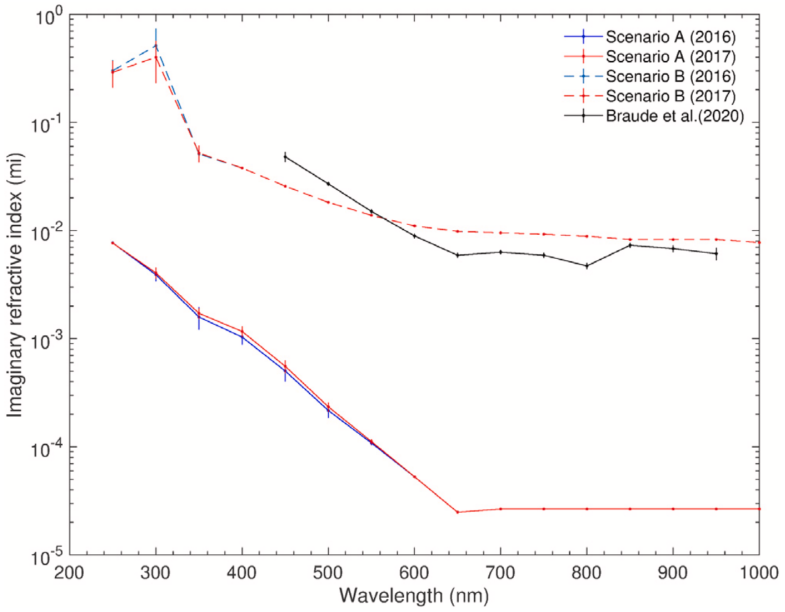


Figure 1.5.4: Averaged imaginary refractive indices retrieved by Pérez-Hoyos et al. (2020), model A is a mixed extended chromophore haze, model B is based off Sromovsky et al. (2017); Baines et al. (2019) Crème Brûlée model. 2016 observations are prior to the North Temperate Belt Disturbance, whereas 2017 observations are post-disturbance. Model A uses the (Carlson et al., 2016) chromophore as the *a priori* input. For Model B the (Carlson et al., 2016) is also used but is fixed for the wavelength range in their work (400-750nm) outside of this range the values are allowed to vary. They have been compared to Braude et al. (2020) (observations 2018) due to the steepened blue absorption compared to the Carlson et al. (2016) chromophore.

Both models required a chromophore with a steeper blue slope than Carlson et al. (2016), in order to capture the effect of limb darkening, see Figure 1.5.4. Due to the mixing of chromophore for the extended chromophore layer with a conservative scatterer, the refractive indices are much smaller than other retrieved pure chromophore values (Pérez-Hoyos et al., 2020). However, the blue absorption can be seen through the retrieved values, and is similar to the slope of the Crème Brûlée model

chromophore. Regarding the retrieved chromophore for the Crème Brûlée model it produced a imaginary refractive index which was similar to the Braude et al. (2020) value, which also included limb darkening effects when retrieved. Both of these effects can be seen in Figure 1.5.4, where the two model's (for 2016 before the NTB disturbance and 2017 after) retrieved imaginary refractive indices are compared to the Braude et al. (2020) values. Therefore incorporating limb darkening effects into retrieval work begins to cast doubts on the validity of the Carlson et al. (2016) chromophore, due to the current inability to reproduce observations taken at multiple viewing angles.

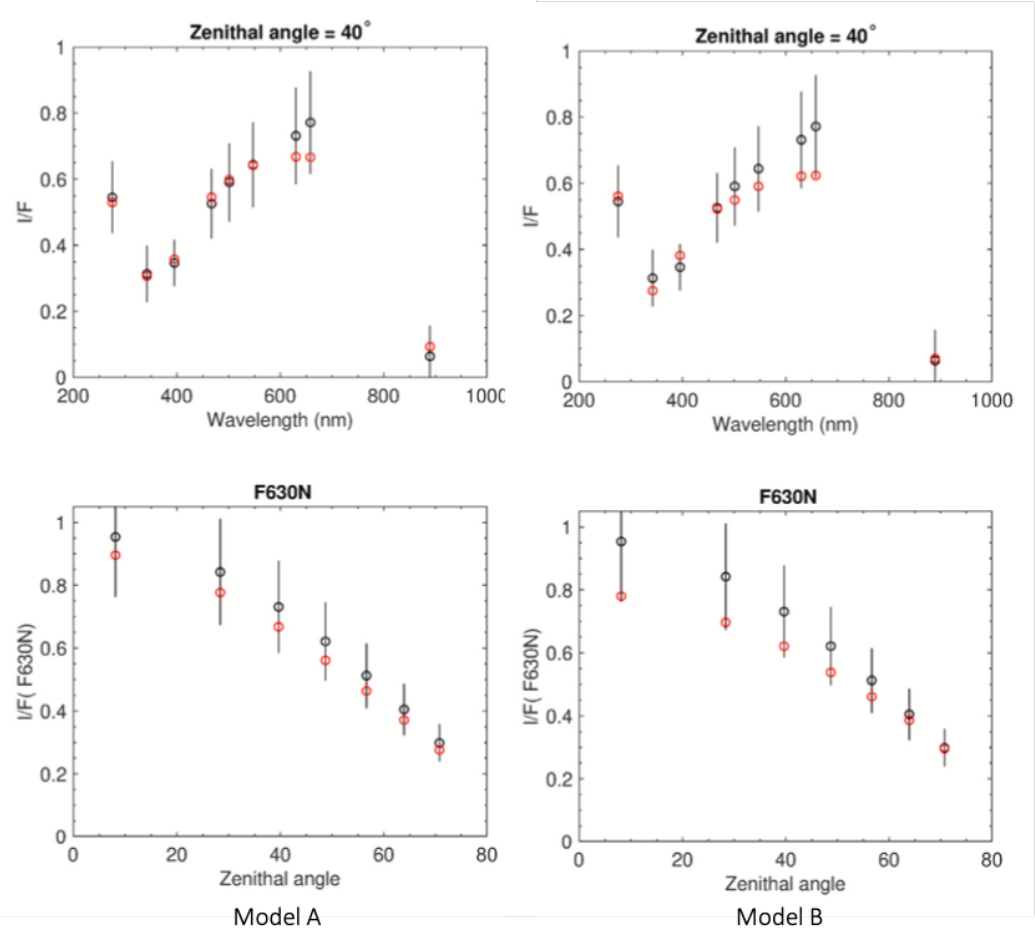


Figure 1.5.5: Selected results from Pérez-Hoyos et al. (2020). The left-hand side is for Model A (mixed chromophore), and the right-hand side is for Model B (Crème Brûlée model). In each panel, the black circles are observations from 22°N in 2017, and the red circles are the model fits. The top panels show the fits to each filter for a 40° zenith angle. The bottom panel is the 630N filter for each modelled zenith angle.

The use of multiple viewing angles, to incorporate limb darkening effects, provides a differential between the models, which can be seen in Figure 1.5.5. Through the results of Pérez-Hoyos et al. (2020) it can be seen that the Crème Brûlée model is unable to reproduce most filters effectively across all the viewing angles, demonstrated for 630N (a filter with a large limb darkening effect) in Figure 1.5.5. Pérez-Hoyos et al. (2020) conclude that the extended chromophore mixed cloud being able to best reproduce observations of Jupiter at multiple viewing angles. Indicating that the Crème Brûlée model may not best represent the atmosphere once limb darkening information is included through the observations.

1.6 Research goals

As can be seen through the discussion of various atmospheric models there is a large number of regions where these models find common ground, such as the need for a chromophore to match their observations. However, there is also a large amount of deviation between results such as the structure involved for the main cloud layers. With solutions grouping into those that find a main cloud at 1.4 bar (Irwin et al., 1998; Braude et al., 2020) like the Galileo probe results, and those who favour a higher main cloud such as the Crème Brûlée model (Sromovsky et al., 2017; Baines et al., 2019), as well as additional works who find solutions elsewhere in the parameter space such as (Giles et al., 2015; Pérez-Hoyos et al., 2020). As these models deviate on what they agree upon, what we can see is that there is a huge amount of uncertainty with these results and that we are unable to conclude what the exact profile of Jupiter's tropospheric aerosols should be. Therefore, further studies are needed with higher amounts of constraint through spectral information, and the incorporation of limb darkening constraint by using multiple viewing angle spectra, to determine which models are best able to reproduce observations. In addition to this, it is clear that the degeneracy within the parameter space is troublesome and can lead to models with large differences being able to match observations equally well. Hence, work to reduce the number of degenerate parameters which are being retrieved could help to minimise some of the issues that a huge number of variable parameters can bring. Finally, increased constraint to the models could be introduced through a greater use of the information which limb darkening can bring to a solution set.

Having outlined some of the limitations which can come with modelling Jupiter's atmosphere, we have also outlined the goals of this thesis.

- **Create an atmospheric model of Jupiter**
  - with high spectral constraint
  - utilising limb darkening constraint through multiple viewing angles
  - reducing degeneracy through the predetermination of parameters
- **Extend across the disc of Jupiter**
  - regular sampling beyond single samples in zones/belts
- **Expand across observation years**
  - see how parameters change year on year
- **Apply to the Great Red Spot**

If we are able to achieve the points above we will have an atmospheric model which is more simplistic but still able to reproduce multiple locations for several observations. Using more constraint through the application of dual viewing angle spectra will help to further differentiate between models allowing us to find the models which best represent atmospheric conditions. Awareness of degeneracy in the parameter space with attempts to minimise its affect through fixed parameters will also help to retrieve the best model possible. Deducing a model which can adapt to a wide range of regions will provide flexibility for its uses and allow more of Jupiter's atmosphere to be determined. We also hope to be able to identify what changes in the parameter space are occurring to produce visual changes between observations. Through all stages we will ensure that the model is realistic using all observational evidence possible to ensure that degeneracy does not affect the retrieved values, allowing us to produce a model which is as close as possible to true conditions.

Throughout the rest of this thesis we will outline the steps and methods used in order to achieve these goals. First we will outline the observations which have been used to investigate Jupiter in

Chapter 2. We will then introduce NEMESIS, the radiative transfer model used for all retrievals in this work in Chapter 3. In order to better constrain our retrievals we will present in Chapter 4 used to produce dual viewing angle spectra. The steps taken to find and fix parameter values for our parameterisation scheme are shown in Chapter 5. We will then present our results of the application of this parameters scheme to our observations from 2018 – 2023 in Chapter 6, and discuss what these results mean for the atmosphere of Jupiter.

Throughout this thesis the use of 'we' is used to discuss the work undertaken, all work was carried out by myself (Charlotte Alexander) but some tools used were developed by others which I will clarify here. In Chapter 2 observations were planned by a range of PIs (including myself) stated in Table 2.6.1, these observations were in Service Mode and were executed and provided with processed calibrations courtesy of the ESO VLT/MUSE operation team. These were then further calibrated by me, utilising scripts that had been designed by Patrick Irwin. Spectra were then extracted and processed by scripts written myself, following the Minnaert process outlined by Irwin et al. (2021). The NEMESIS retrieval algorithm was written and developed by Irwin et al. (2008). I created all inputs and processed all outputs from retrievals in NEMESIS and analysis using scripts written myself for the work presented in Chapters 4, 5, 6, 7.

Chapter 2

Observations

The large size of Jupiter combined with its brightness means it can be observed easily by a range of telescopes. Visible even with the naked eye, we are able to gain significant amounts of information about the planet as we upgrade observational equipment over time. Vast quantities of observations are taken of the planet by the amateur community, providing large time series of data, which have been supplemented with observations from the best telescopes we have. Working together allows us to continue documenting the ever-changing nature of Jupiter and help to determine as much as we can about the gas giant.

This Chapter will detail the observations from the VLT/MUSE instrument used in this thesis; and detail how they have been calibrated and reduced to produce usable spectra for retrieval work. This is then followed by an overview of observations of Jupiter, including the three observation blocks for which I was the principal investigator (PI), responsible for the motivation to observe, providing the telescope set-up, plus the schedule of potential observing opportunities to gain the targets of interest. We will then detail how our VLT observations have provided ground-based support for the Juno mission whilst meeting our aims and others. Then we shall present an example spectrum from our observations and detail the features of interest, including absorption features in the spectrum, including both sources from Jupiter and interference from telluric sources while identifying the advantages of our VLT/MUSE data and its use with Jupiter's atmosphere.

2.1 VLT/MUSE

2.1.1 Telescope Overview

Located in Chile, at the Very Large Telescope, the MUSE (Multi-Unit Spectroscopic Explorer) instrument is a visible and near infrared (IR) integral field spectrograph (Bacon et al., 2010). MUSE is able to take an image of Jupiter over hundreds of wavelengths 480-933nm simultaneously, creating a datacube where each pixel of the image is also a spectrum. 'First light' on the instrument was in 2014 and since then it has provided a great resource for the planetary science and further scientific communities. An overview of the instrument, and the progression of incoming light through the various components is shown in Figure 2.1.1. The main units include the Calibration Unit which produces the images needed for calibration of observations. The Fore-optics unit reshapes the image so that it can be fed into the slitting and relay optics. Here the observation is divided into 24 pieces so that each one can be fed to an Integral Field Unit (IFU) so that the observation can be recorded (Richard and Bacon, 2025). The instrument has a large field size of 60" x 60" in its wide field mode, which fits the entire disc of Jupiter (maximum apparent size of 50.1"). This removes the need for the tiling of multiple observations to produce a full disc observation, removing calibration errors resulting from varying observation conditions as well as rotational effects caused by Jupiter's rapid rotation time of 9.93 hours. The rotation leads to smudging of the observation for instruments with long integration times, reducing the quality and spatial resolution of the observations. However, the MUSE instrument is designed for deep field galactic surveys which are magnitudes fainter than Jupiter, therefore our observations require an incredibly short integration time of only 0.1 seconds to capture a full spectrum, which reduces common errors associated with observations of Jupiter. MUSE is also able to provide high spectral resolution of 0.125nm, alongside high spatial sampling of 0.2" x 0.2" (Bacon et al., 2010), although the spatial resolution (FWHM) is typically 0.3 – 0.4" due to the limitations which are brought by seeing conditions in the atmosphere. Combined, these qualities of MUSE make it a very powerful instrument for investigatory work of Jupiter.

Despite the MUSE wavelength range encompassing most of the visible and some of the near IR wavelength range, it unfortunately does not extend to the shortest visible wavelengths. For our

work with chromophores there is still absorption down to this blue limit and laboratory work such as Carlson et al. (2016) includes information wavelengths which we do not capture. However, work such as Dahl et al. (2021) which does include this lower limit, do not note any significant absorption features which the MUSE instrument would miss. Therefore, we are able to still characterise the properties of the chromophore to a similar extent with the MUSE wavelength range. Despite this disadvantage, a huge amount of information is contained in the wavelength range of the spectrum captured by MUSE, as described below in Section 2.5.

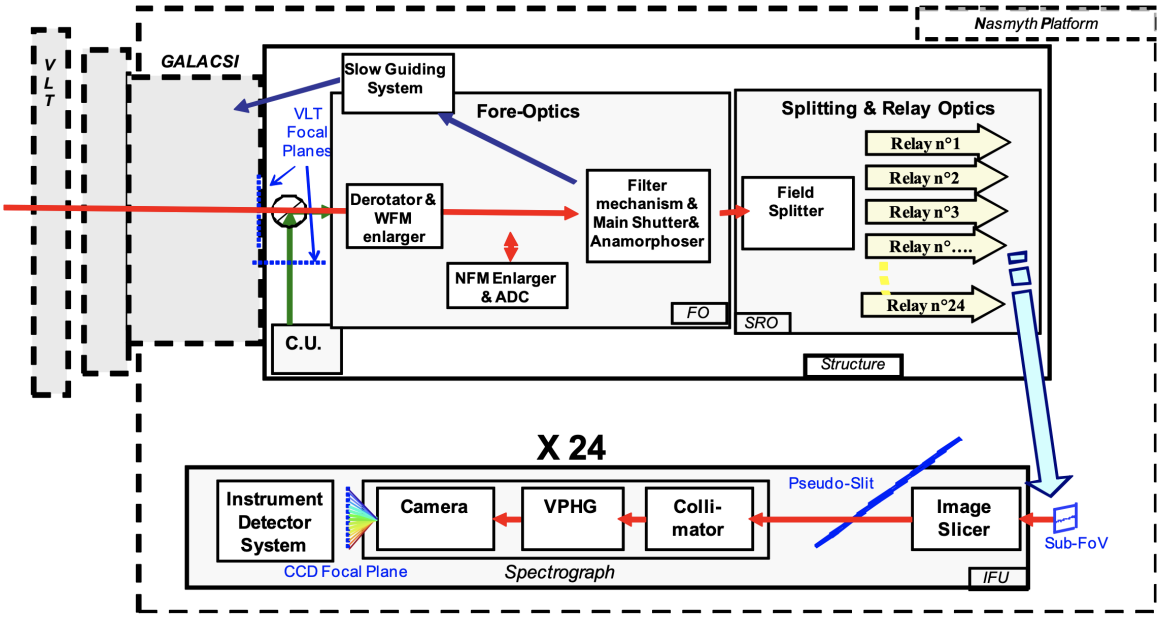


Figure 2.1.1: Block diagram of the VLT/MUSE instrument detailing how light is processed through the instrument, taken from Richard and Bacon (2025). Showing the Calibration Unit (CU), the Fore Optics (FO), the Splitting and Relay Optics (SRO) then the Integral Field Unit.

Adaptive optics (AO) (Ströbele et al., 2012; Arsenault et al., 2008) are available when using the MUSE instrument, several of our recent observations, see Table 2.6.1, use this feature to improve the spatial resolution. With the AO mode active, an observation's spatial resolution is constrained by the instrument's diffraction limited resolution rather than the atmospheric conditions, even when the atmospheric turbulence (seeing) is larger, as the system can use a laser guide star to correct for the atmospheric turbulence improving the spatial resolution. We can then reduce the tight constraints for the atmospheric conditions which limits the nights where observations are feasible,

as spatial resolution is not lost when using AO increasing the number of nights we are able to undertake observations. However, if the turbulence is too large the AO may not be able to lock onto the guide star. This increases the likelihood of our observations being completed in the tight time windows which we have to impose to get the desired observational properties (i.e., central longitude). Wavelengths are lost when we use AO, due to the laser guide star (LGS). Although the sodium laser itself is constrained to 588.9950nm and 589.5924nm, we lose 579 – 599nm from our observations due to the brightness of the laser affecting a wider wavelength range due to the spectrometer response function causing a signal tailing away from the LGS wavelengths. However, these wavelengths do not contain any overly important absorption bands for Jupiter's atmosphere.

One major downside to the adaptive optics mode is the additional overhead time required for these observations. This increases the observing block time (for 7 science exposures, 5 of Jupiter plus 2 space views, as well as the needed calibrations and read out time of the instrument) from 21 minutes for non-AO to 29 minutes for AO observations. Although small, this time can make the difference for the ever-growing competitive nature of gaining telescope time. In the past, we have decided that the improvement in the spatial resolution is worthwhile so we have requested AO in our recent proposals. This has led to a mixture of AO and non-AO observations in our recent blocks, (see Table 2.6.1). This is due to some atmospheric and geometric conditions, such as high wind speeds, or Jupiter being close to the horizon or unfavourable viewing conditions, which lead to non-AO blocks being acquired instead. On some nights the failure of the adaptive optics system due to the brightness of Jupiter also affected the tracking system meaning non-AO observations had to be taken alongside AO observations on the same night to meet our science goals. Additionally, the quality of many observations without AO is comparable to those with, due to the often minimal value of seeing which is possible at the VLT. Therefore, the use of AO for Jupiter may not be necessary for future observation blocks. During AO observations there are often more failures during exposures due to issues with the system, such as the guide star system failing, which can cause issues with the timings of observations when repeats are taken. Some of these issues can be seen in Table 2.6.1, where single targets have multiple sets of observations attempted. Combined with the more appealing shorter execution time of non-AO for proposals, the minimal improvements of AO for images taken

of Jupiter (due to the incredible quality of non-AO observations).

The wealth of information which can be extracted from the high spatial and spectral resolution of the VLT/MUSE spectrum provide a rich data set to analyse. With its sensitivity to the vertical structure of clouds and hazes within the troposphere, including the elusive chromophore, we successfully use the MUSE observations to test atmospheric models of Jupiter's troposphere and lower stratosphere.

2.1.2 Juno Support

In addition to the modelling work we undertake with our MUSE observations, it is also beneficial to ensure the continued observations of Jupiter. Our MUSE observations are part of a global effort to provide ground-based support to the NASA Juno mission.

2.2 Juno Mission

The Jupiter Near-polar Orbiter (Juno) (Bolton et al., 2017) arrived at Jupiter in 2016, and it has a highly elliptical orbit, with most of its coverage centred over the poles with a narrow swath of observations being taken across the rest of the disc, see Figure 2.2.1. Due to a fault in the propulsion system the time between Perijoves (point of closest approach) never decreased and stayed at around 53 days. This has allowed the mission to be far extended past its original end date of February 2018, with Perijoves now planned until October 2025. Extension of the mission was possible as Juno, on its new trajectories, spends less time in the destructive radiation belts preserving its instruments for much longer.

The mission objectives include discovering more about the polar regions of Jupiter, which are not observable from the Earth due to Jupiter's low obliquity. Juno was the first opportunity to observe the poles in their entirety. The other aim was to determine more about the internal structure of the planet; both the gaseous structure and its dynamics, right to the deepest extent down to the planet's centre.

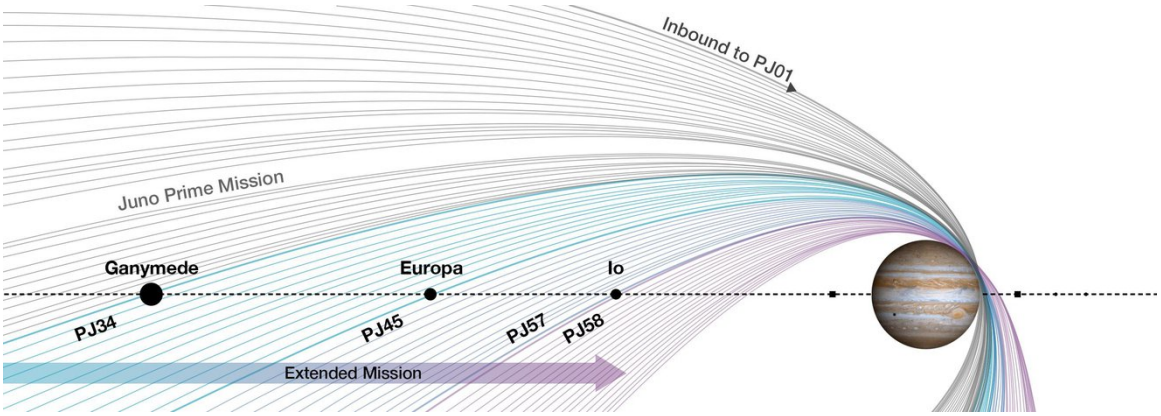


Figure 2.2.1: Juno orbit diagram, including the current planned extended mission Perijoves, which are moving further north as the mission progresses. Credit: NASA/JPL-Caltech/SwRI

2.2.1 Instruments onboard of Juno

The use of instruments such as JIRAM (Jovian Infrared Auroral Mapper) (2–5μm) (Adriani et al., 2017a) and MWR (Microwave Radiometer) (1.37–50 cm)(Janssen et al., 2017), which can observe Jupiter at wavelengths inaccessible to ground-based observations is beneficial, for example, JIRAM's wavelength range overlaps with many of Earth's telluric lines. The use of JIRAM as an imager and spectrograph in the infrared is key for unlocking information about auroral activity as this can be traced by the distribution of the H_3^+ ion which has strong emission lines in the JIRAM wavelength range (Dinelli et al., 2017; Adriani et al., 2017b; Mura et al., 2017), aiming to create a record of the aurora with each Perijove. Further to tracing aurora at the poles, limb observations can show the movement of electrons along magnetic field lines in the thermosphere, which can translate to energy transfer through the upper atmosphere, potentially answering questions about the 'energy crisis' in Jupiter's thermosphere, as it is far hotter than expected from typical heat sources, and theorised instead to be driven by auroral heating (O'Donoghue et al., 2021). Additionally JIRAM can sense down to 5-7 bar, extending its seeing power into the troposphere and helping to map vertical cloud and haze structure, as well as ammonia distribution. The work of Grassi et al. (2021) shows the potential for JIRAM to model cloud altitudes, opacities and optical thickness of clouds and haze, and the distribution of ammonia through relative humidity, although they state that fits there are not yet fully satisfactory due to the difficulties of fitting this wavelength range.

The Microwave Radiometer (MWR) (Janssen et al., 2017) onboard Juno is sensitive to the ammonia distribution from the cloud tops down to deep levels, with results from the first Perijove presented in Li et al. (2017). This has provided an initial benchmark for model results which deal with ammonia distributions. MWR covers wavelengths from 600MHz – 22GHz which enables it to probe a wide range of the atmosphere, from around 1 bar down to 1000 bar (Janssen et al., 2017); this allows both the tropospheric cloud level distribution of ammonia to be retrieved, as well as the deeper concentrations of ammonia, plus water deep beneath their cloud levels. Through detection of these species the dynamics of the deeper levels of Jupiter's atmosphere can be traced to see how the circulation is related throughout the atmosphere and if it is representative of the cloud top zone/belt patterns which we see. MWR can additionally map the synchrotron radiation from the radiation belts which occurs when the most energetic electrons rotate around the magnetic field lines (Janssen et al., 2017).

Finally, Juno also has a public outreach camera, JunoCam, which has four filters (RGB and methane filter). Despite the excellent spatial resolution of these images the lack of fine filters means that scientific extraction remains limited due to the very limited spectral resolution of these visible filters. However, remarkable scientific output is possible from JunoCam due to the extreme clarity that the images provide. It allows us to track individual features with care and see how they change with time. The access to the polar regions is unprecedented providing superior insight into these regions, more than anything which could be achieved by ground-based observations, due to Jupiter's slight obliquity. Further to this the observations have allowed us to monitor lightning flashes and get a better understanding on their frequency (Becker et al., 2020). This has led to consideration of how convective storms could look for a planet such as Jupiter and what it would mean for condensable species such as ammonia e.g., mushballs from Guillot et al. (2020). Further to this work, estimation on the height of storm clouds as they rise above the main cloud deck can be done using the shadows that are captured through the JunoCam images (Guillot et al., 2023). Reaching 20-30km above the main cloud deck and often in stark white, it is thought that these images are capturing plumes of fresh ammonia ice above the coloured clouds lying below forming the main cloud deck of Jupiter (Guillot et al., 2023).

The observations taken of Jupiter from Juno are diverse. However, there are limitations to these observations particularly when it comes to retrieving tropospheric cloud structure beyond the cloud tops and across the whole disc simultaneously. The broad filters used by JunoCAM were not developed to be used for retrievals, their resolution does not allow much information about the cloud structure to be retrieved as we have limited vertical sensitivity. Further to this, the spatial coverage of Juno's observations are often very limited due to the rapid orbit around the planet, restricted to mainly polar coverage with minor connecting bands across the main disc which vary with each Perijove. Hence, to supplement the Juno observations, the ground-based push to organise simultaneous observations of Jupiter, whilst Juno is performing a Perijove pass, has allowed for far more information to be uncovered. Our observations from MUSE provide fantastic context to the Juno mission as we have detailed spatial coverage of one half of the globe at once. Combined with the high spectral resolution of MUSE, these observations provide the missing links to globally base these Juno observations. For VLT/MUSE proposals we have aligned our observations with the longitude of focus for the Juno perijoves, and attempted to keep the observations close in time to each Perijove. Some Perijoves are not possible due to the observability of Jupiter throughout the year, additionally not all of our proposals have been accepted but the coverage which we have managed to achieve is listed in Table 2.6.1.

2.3 HST Observations

The Hubble Space Telescope (HST) provides a wealth of observations of the giant planets. The creation of the OPAL programme (Simon et al., 2015), ensures regular mapping (approximately yearly) of the entire globe of each giant planet, providing an invaluable time series. HST provides fantastic spatial resolution of the whole planetary disc. These include single observations taken as filter images of Jupiter's disc, which can also be combined to produce a map of Jupiter for all longitudes. HST Wide Field Camera 3 (WFC3) uses filters across the UV, visible and near IR wavelengths to record observations of Jupiter. As will be described in Chapter 4, HST/WFC3 data from the OPAL programme was used to calibrate the radiance of the observations taken by MUSE/VLT, ensuring that the observations are comparable across the years, reducing any potential instrumentation effects

that occur over time by taking the HST data as a baseline. This is possible due to the highest level of calibration undertaken for OPAL programme observations (more information on the process is given in Section 4.2) (Simon et al., 2015).

2.4 Calibration and Data Processing

Our MUSE observations are carried out in service mode (SM) and once the potential observation opportunities have been outlined, we have no control over the timings or execution of our observations, which instead are controlled by the astronomers locally. Due to the short exposure time of our observation and their spread through the observation period, SM allows us the most flexibility for straightforward observations, granting us the most opportunity to monitor Jupiter through VLT observations. Once an observation has been executed we are able to download the observations plus the processed calibrations. From this we are then able to fully calibrate our data to get it in a usable form to then extract spectra.

2.4.1 Image processing

From the ESO common pipeline library we use the ESO Recipe Execution Tool (EsoRex) to process the science cubes with the associated calibrations (ESO CPL Development Team, 2015; Ballester et al., 2006). Due to the huge amount of information collected for each MUSE observation the full field of of MUSE has to be split up to be read out. 24 integral field units (IFUs) are needed for this data to reduce the readout time. From which charge-coupled devices (CCD) can extract the signal from the IFUs to produce the data cube by tiling the information together. In order for the different IFU readouts to be tiled together to produce a cohesive data cube the process needs to be calibrated ensuring the mapping process is done successfully. The current form of the data is 2D, in a pixel table, so the data is both spatially and spectrally spread out and will be mapped to its 3D datacube form after calibration. This is done using a geometry table which is able to translate the pixel tables into a 3D datacube, ensuring the correct spatial location for each spectral point. Each output from the CCD uses the same geometry table and these are provided by the ESO team and then can be used for the calibration observations as well. Therefore we can undertake all of

the subsequent calibration steps before the datacube is stitched together. Once the steps detailed below have been completed, we have a fully processed science pixel table which can be formed into a 3D datacube, which contains an image of Jupiter taken for each of the 3600 wavelengths. More details on the instrument specifications and how the calibration is undertaken can be found in the MUSE Pipeline User Manual, but here we present a brief description of how the calibration process is undertaken to transform the raw observations into the final product using the processed calibrations produced by the ESO team.

Once we have the science cube correctly mapped we need to undergo several calibration steps to correct for observational effects, both spatial and spectral (Weilbacher et al., 2020). This uses a variety of observations which are taken before and during the observation run. The additional observations required to transform the raw science pixel tables into their final product are listed below. Some need to be taken at the time of the observation (or close by), while others can be taken months from the observation date due to minimal or no variation with time.

- **Bias Frame** – Determines the noise of the detector, they are zero-second exposures taken with the telescope dome shut.
- **Dark Frame** – Determines the 'dark current' of the detector produced from thermal excitation of the CCD, they are long exposures taken with the shutter closed.
- **Flat Frame** – Determines the sensitivity across the field to light and also identifies bad pixels, providing the illumination correction. These are recorded both when a bright light illuminates the telescope dome and when the dome is open at twilight.
- **Arc Lamps** – Determines the wavelength solution and spectral response and dispersion characteristics of the instrument across the wavelength range. Neon, Xenon and Mercury Cadmium lamps are used.
- **Standard Star** – Determines the telluric absorption and the response across the wavelengths. Observations of a spectrally known star are taken.

The bias frame is subtracted from the science pixel table removing any read out which is caused

by impurities in the CCD, this can be taken at any time as it is not dependent on temperature or observing conditions. Whereas, the dark frame is dependent on temperature which will change with each observation, and is also subtracted from the science pixel table. The observation is divided by the flat frame, removing the differing response to light which is recorded by each pixel of the CCD. The line spread function of each CCD is calculated using three arc lamp exposures, each lamp should induce a narrow spectral response and these observations determine how exactly the CCD responds. This is done through the recording of spectral wings tailing from the narrow spike of the response signal. The standard star observation allows the flux response for each night to be recorded and corrects the observation from a known response. It also allows the absorption from the Earth's atmosphere (such as oxygen and nitrogen absorption lines) to be corrected for in the spectral response. Once all calibrations have been applied to the science pixel table it is possible to use the geometry tables to map the observation into a 3D datacube. Further corrections can be done at this point using standard profiles to account for the detector response across the spectrum, velocity offsets across the field of view, reflectivity correction for horizon distance and final telluric effects (Weilbacher et al., 2020).

The output from the EsoRex pipeline produces the datacube which has both spatial and spectral extent. The pixels have a recorded radiance as well as an error value for each wavelength. These errors are derived by the pipeline from a range of sources including from the detector read out, flux calibration and deriving wavelength solutions (Weilbacher et al., 2020). Once we have the calibrated final datacube extracted from the EsoRex pipelines we are then able to apply more processing to the datacube to get it in a form which enables us to begin extracting spectra from the cube.

2.4.2 Formatting MUSE observations for NEMESIS retrievals

In order to get the observations in a format suitable for extracting spectra we have to align the cube, projecting coordinates (e.g., latitude, longitude, zenith angle, solar zenith angle, azimuth angle) onto each pixel. At this stage the MUSE observation has very fine spectral resolution of 0.125nm, which is very computationally expensive for a radiative transfer model. Additionally, as will be described in more detail in Chapter 3, NEMESIS uses absorption coefficients (e.g., methane) and solar spectrum

data which are not known with the same high spectral resolution. Hence, we are not currently able to model the native high-resolution MUSE data, which can be seen in Figure 2.4.1. Furthermore, smoothing the data also improves the signal to noise ratio of the observations. Reducing the resolution from 0.125nm, a spectrum with over 3600 wavelengths, down to 1nm resolution, it gives approximately 450 wavelengths in a single spectrum. Once these data has been smoothed using a HWHM of 1nm triangular function, there are some spectral features which will have been smoothed over, however, it is assumed that minimal information could be extracted from any of these features and the benefits are far greater. To do this we use IDL scripts developed by Patrick Irwin. These scripts have been refined to be applicable for all planets which have had MUSE observations taken of them.

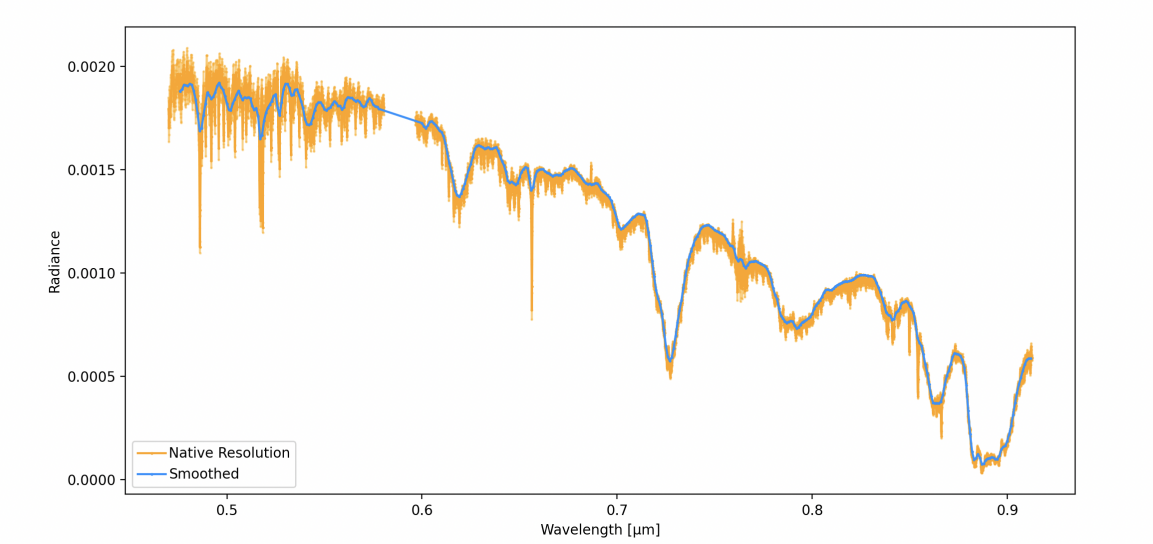


Figure 2.4.1: Comparison of Equatorial Zone spectra taken from 2023-09-23 observation, with both the native, 0.125m, and smoothed resolution, 1nm, shown.

To project information onto the observed disc of Jupiter we have to know about the geometry of the sun, observer and planet at the time of observation. We need to know the equatorial diameter, sub-Earth latitude, north polar angle, sub-Sun latitude and the difference in the sub-Sun and sub-Earth longitudes; all of these alter steadily and each observation requires individual input files to ensure the projection is accurate. Through MUSE instrument specification, we know both the x-pixel and y-pixel scales of MUSE are equal to 0.2”, allowing us to create a fitting ellipsoid to align

with the observation of the planet. An assumed oblateness for Jupiter of 0.062 is presumed to produce the ellipsoid, allowing the observation disc to fit inside the ring created by the routine. The fit is done through manual trial and error adjustment. Figure 2.4.2 shows how we align to the observation. Errors are introduced in this stage due to inaccuracies introduced by the user when trying to determine exactly where to set the boundary of the observation when matching to the ellipsoid. This is due to the background sky and the outer limb of the planet beginning to appear mixed right at the edge. However, a successful alignment is possible, allowing us to project values of the latitude, longitude, azimuth angle, viewing angle and solar viewing angle onto the observation datacube pixels. Once each pixel has had coordinates assigned individual regions can be selected and their information extracted.

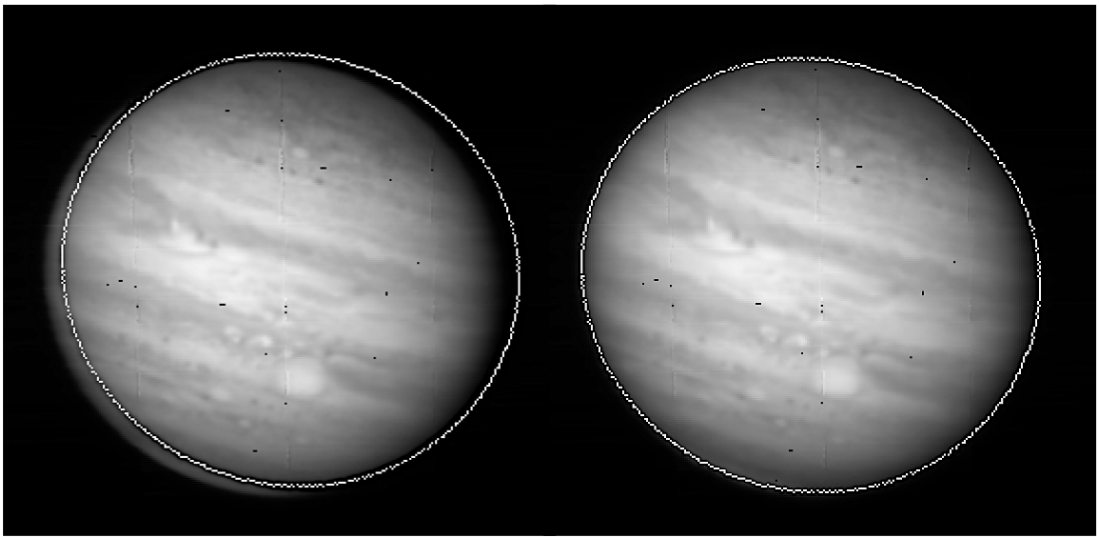


Figure 2.4.2: Comparison of a poorly aligned ellipsoid fitting on the LHS, where the edge of the disc can be seen to protrude outside of the white ellipsoid being fitted, compared to a properly aligned ellipsoid on the RHS.

2.5 Spectra

As we observe Jupiter we are able to collect the incoming light from the source and record information about the radiance of the light we receive. How that is processed by the detector, be it by eye, a filter based instrument or a spectrograph, determines what we can extract from the radiance collected

and what we can learn about the planet. In this thesis we work predominantly with spectra, these display the amount of incoming radiation for each wavelength of light. The source of the radiation is a combination of both the initial source, as well as emitted and reflected contributions. However, several factors ensure decrease the amount of radiation recorded by detectors for atmospheres these include; attenuation of the source can be caused by aerosols through absorption, reflection and scattering, and also absorption by gaseous species in the atmosphere. It is this variation of the signal which allows information to be inferred from the spectra about the state of the atmosphere. How the spectrum looks depends strongly on what wavelength regime we are working in.

2.5.1 Observing Jupiter from Ultraviolet to Radio wavelengths

A wide range of wavelengths have been used to study Jupiter due to the availability of instruments over time. Due to the sensitivity of different wavelengths to different regions of the extensive atmosphere, a huge amount of information can be extracted over the full spectrum of radiation. An overview of what information we are able to extract from each wavelength range is given below, adapted from Irwin et al. (2008). Figure 2.5.1 shows the spectral response across the wavelength range.

- **Ultraviolet 0.1–0.4μm**

  In this wavelength range the spectrum is dominated by Rayleigh scattering of incoming radiation from the sun, which can be modified via scattering by the highest altitude hazes. As this high-energy wavelength radiation interacts with the atmosphere it drives photolysis reactions, which leads to absorption features within the spectra. These reactions prevent these wavelengths from probing deep into the atmosphere. Towards the poles, there is also significant auroral glow due to the high energy bombardment along magnetic field lines.
  Instruments: *HST/WFC3, HST/STIS, Juno/UVS*

- **Visible 0.4–0.7μm**

  The domination from Rayleigh scattering rapidly diminishes as wavelengths become longer and lower rates of absorption mean these wavelengths can begin to probe deeper in the atmosphere (several bars) before they are reflected, scattered, or absorbed. Some weak absorption bands

(ammonia and methane) are present towards longer wavelengths. Information about colour, useful for chromophores, is available in this region.

Instruments: *VLT/MUSE, NAIC, HST/WFC3, JunoCam, Cassini/VIMS*

– **Near Infrared 0.7–5μm**

Stronger ammonia and methane absorption bands begin to dominate at these wavelengths. The stronger an absorption band is, the higher in the atmosphere we are sensitive to. Through these varying strengths, we are able to probe different levels in the atmosphere gaining information about the vertical profile, mainly for the upper clouds and hazes. Away from the absorption bands the atmosphere is optically thin meaning we can probe to deeper levels in the atmosphere. The $5\mu m$ window, a region with no absorption bands, allows us to observe thermal emission from deep in the atmosphere (around 10 bar) which provides information about the overlying clouds as the signal is modulated by the profile above. Sensitivity to H_3^+ occurs at these wavelengths, allowing auroral emission to be monitored additionally.

Instruments: *VLT/MUSE, NAIC, HST/WFC3, IRTF/SpeX, JunoCam, JWST/NIRCam, Juno/JIRAM, Cassini/VIMS, Galileo/NIMS*

– **Mid Infrared 5–20μm**

Towards longer wavelengths we are sensitive to vibrational/rotational absorption bands, the response from the solar spectrum diminishes and becomes secondary to the thermal emission emanating from the atmosphere itself. These wavelengths are sensitive to temperature and composition through the deeper atmosphere. At longer wavelengths there is some sensitivity to upper tropospheric aerosols.

Instruments: *VLT/VISIR, JWST/MIRI, IRTF/TEXES, VLT/CRIRES*

– **Far IR, Microwave, Radio >20μm**

At these longer wavelengths there is little to no sensitivity to cloud, instead, the spectrum is characterised by absorption features only. This allows species composition to be mapped without the degeneracy with aerosol structure in other wavelength regimes.

Instruments: *Juno/MWR, VLA*

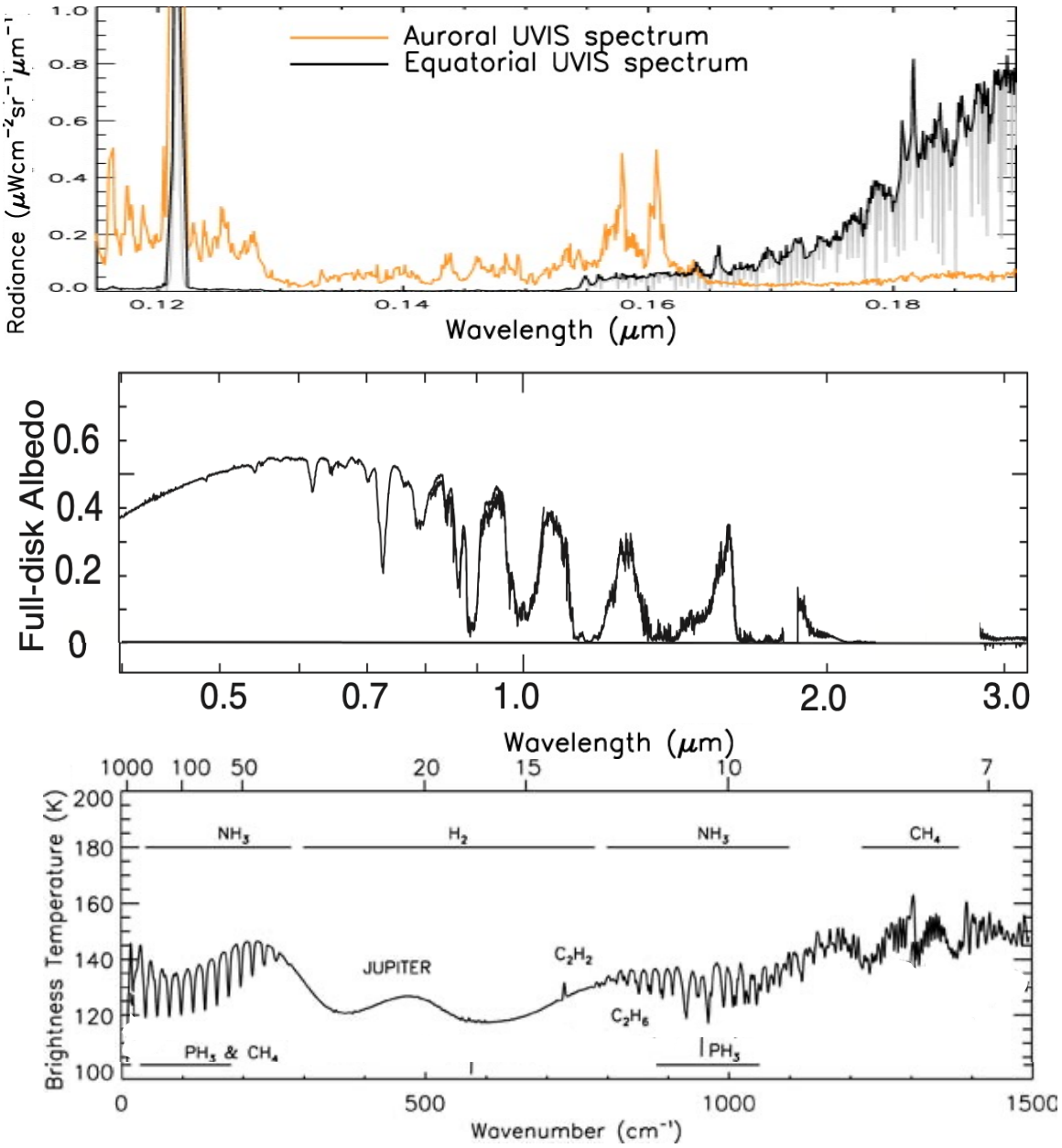


Figure 2.5.1: Spectrum of Jupiter across 0.1 – 1000μm, the top panel in the UV is in units of radiance observed by Cassini UVIS taken from Melin et al. (2020). The middle panel shows visible and near IR spectrum in units of reflectance, taken from De Pater and Lissauer (2015), with the data coming from 1.5-m ESO observatory at 0.4–1.05μm by Karkoschka (1994) and with the 3m IRTF telescope at 0.8–3μm by Rayner et al. (2009). The bottom panel shows the infrared spectrum of Jupiter, in units of brightness temperature observed by Cassini CIRS, taken from De Pater and Lissauer (2015) (Conor Nixon and NASA/GSFC/UMCP).

Although, in this thesis we will not use observations which cover the entirety of the wavelength ranges which are discussed above, we will be comparing and constraining our work with results from across the wider spectrum. Therefore, it is important to ensure we know how the entire radiation spectrum can affect our results, ensuring that we are not making conclusions which have been disproved elsewhere in the Jovian spectrum. Our work will focus mainly on the visible and near IR wavelengths as they provide us with the most sensitivity to the aerosol structure which we are attempting to understand better.

As we view Jupiter with the naked eye we see a pale appearance, often lacking in the contrast and saturation of colour which we have come to expect from images of Jupiter. A generally muted colour palette, with predominately shades of white, cream and brown still enables us see features from the disc, such as zone/belt contrasts and storms such as the GRS, but some of the more subtle variances can be lost. The differences between the response of instruments compared to our eyes is due to the way each processor configures the photons collected. However, it is possible to process observations in a way to make them appear as they would to our eyes, as done in Irwin et al. (2024). Digital images are gamma scaled before being digitised in order to look better in darker regions when displayed. The eye has a logarithmic response to light, this increases the contrast for images displayed this way. The application of a gamma correction term accounts for this and displays the images as they would appear with the eye. Further processing of observations with additional steps to incorporate both the eye's response, as well as correcting for differences incorporated through computer displays creates 'true colour' image of Jupiter in Figure 2.5.2 which appears much paler than most other images which have been included in this thesis. The lower contrast planet which we can see in Figure 2.5.2 provides grounding to the work which we are undertaking here, the changes are distinct but more subtle than we are often used to seeing with processed observations. Indicating that the visible changes which the parameter schemes are adapting to are more subtle than the images may imply.

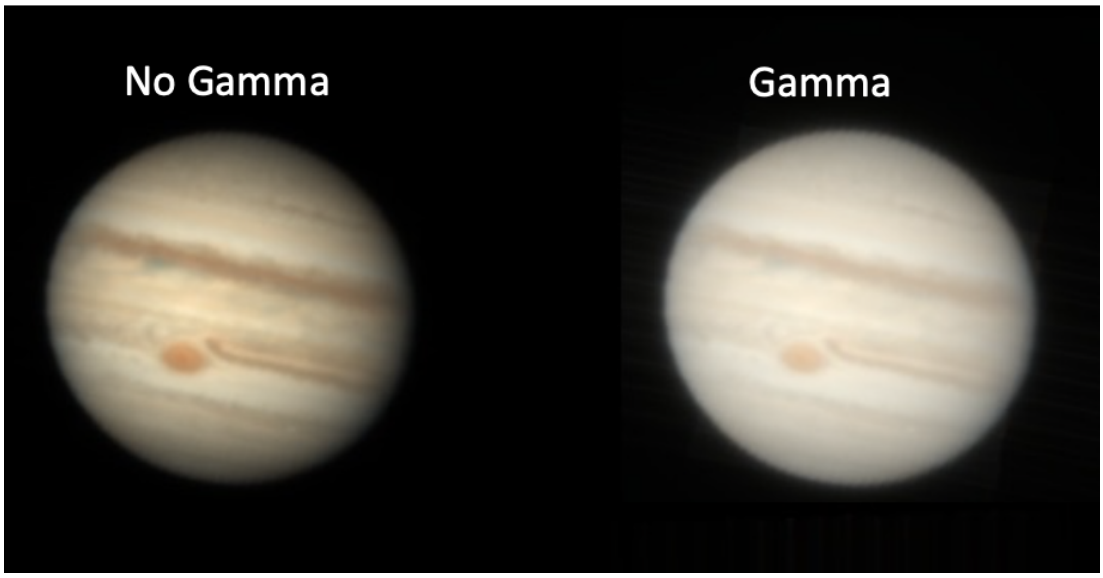


Figure 2.5.2: Observation from VLT/MUSE displayed with and without gamma correction (Irwin et al., 2024), also available online), which enables the image to be displayed as with the naked eye.

Using filters allows us to record information about different wavelength regions, this has been done successfully for many telescopes, ranging from amateur up to world class devices such as WFC3 on HST. The use of filters allows us to record the strength of signal from the source for the certain range of wavelengths. From this we are able gain some idea to how it responds in different regimes. To gain the most information possible we are able to adjust which filters are used for observations. For example we can select the FQ889N filter on HST, which is a narrow band filter centred over the 889nm methane absorption band, which makes us more sensitive to upper atmospheric hazes in Jupiter's atmosphere. The amateur community creates a highly valuable resource as the large number of observers leads to a huge number of observations, achieving global coverage of Jupiter on a regular basis allowing the appearance of Jupiter to be tracked far better than with professional observations alone. In addition to routine observations of the giant planets through the OPAL programme (Simon et al., 2015), these observations allow for temporal changes to be recorded in high spatial detail, through a range of filters from UV to near IR. The use of filters on instruments such as HST allows for high spatial resolution, high sensitivity and a larger wavelength range to be covered, as although still complex, the use of filters is more simple than a spectrograph and can be used in a wider range of instruments.

The development of spectrographs allows for far more information to be extracted from an observation due to the ability to examine individual wavelength measurements, creating much higher spectral resolution than filter measurements. It enables trends over wavelength ranges, such as the blue absorption slope, to be identified in more detail. Plus it allows more individual features to be analysed simultaneously providing far more sensitivity to atmospheric parameters. As spectrographs are observing far more wavelengths simultaneously the incoming radiance is split more for each detector and therefore the detector must be far more sensitive.

The development of new spectrographs provides advancements in the astronomical field. Their advantages make them preferable for many fields of research, such as exoplanets and high redshift galaxies, and so were considered during the development of the James Webb Space Telescope (JWST). The use of JWST for incredibly faint objects means it must have incredibly high sensitivity of its spectrographs, through large apertures and low noise detectors. This means that Jupiter, even with the lowest exposure time, saturates the detectors at some wavelengths. Therefore, observations of Jupiter have limiting factors on even the best detectors. Very few spectrographs exist with both the spectral range of interest for the Jovian clouds whilst also providing the field of view to encompass the whole planet, this makes the MUSE instrument almost unique in its capabilities. Alongside MUSE, NAIC observatory, as detailed in Dahl et al. (2021) (see Section 1.5 for more information), is the other capable visible/near IR spectrograph currently active. However, MUSE is the only instrument which can capture the whole disc without the need for de-rotation effects, due to its incredibly short exposure time (MUSE's 0.1s compared to NAIC's several minutes), plus better spectral and spatial resolution than NAIC. Therefore, MUSE is a world-leading telescope for investigations into Jupiter's atmosphere.

2.5.2 Extracting Spectra from VLT/MUSE Observations

Once we have the fully calibrated and processed MUSE cube, we can then extract spectra from locations on the disc to be fitted using the NEMESIS retrieval algorithm, detailed in Chapter 3. When producing each spectrum we can specify a location to extract a radiance for. Now that we have smoothed to a resolution of 1nm, each spectrum has approximately 450 wavelengths. This

can vary slightly depending on whether the AO laser guide star wavelengths need to be excluded. Trimming of the wavelength range may additionally be required due to noise that can occur for the peripheral wavelengths due to the instrument.

How we extract spectra depends on what we wish to achieve when using NEMESIS and what part of the planet we are interested in. Previous works would use disc averaged spectrum due to a lack of spatial resolution, not an issue we have with MUSE observations. Therefore, we can extract a spectrum from a more localised region, such as a single belt, a storm or even a single pixel of interest ($\sim$700km$x$700km). Each pixel as well as containing the radiance for all wavelengths, also contains spatial information such as the longitude, latitude, zenith angle and solar zenith angle, all assigned during the projection stage of calibration. Choosing a larger region, containing multiple pixels, and hence spectra, would mean co-adding the values, including the spatial information, to produce an average spectrum for that region.

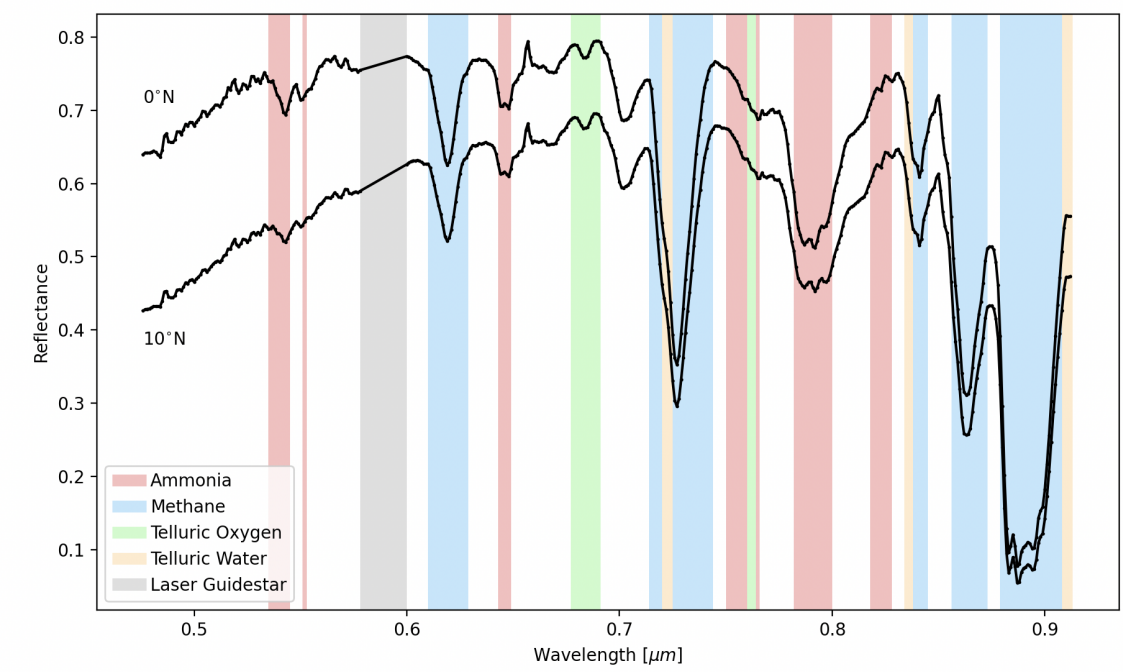


Figure 2.5.3: Two spectra from VLT/MUSE cube from 01/07/2022 extracted from 0°N and 10°N latitude bands, marked with the key absorption features of ammonia and methane in the wavelength range as well as telluric absorption, which is corrected for during the calibration with the standard star, some small residuals may remain. The VLT laser guide star wavelengths are also marked.

In the visible and near IR wavelengths the observed spectrum is dominated by reflected sunlight from the clouds which is scattered by aerosols in the atmosphere. This spectrum is then characterised by absorption from species in the atmosphere. The dominant absorption signatures come from ammonia and methane and are marked in Figure 2.5.3. The sweeping broad slope at wavelengths less than 600nm is due to the characteristics of the chromophore material which is present; it is presumed that the chromophore does not have any more spectrally distinct signatures, as these have not presented themselves in laboratory work nor as a distinctive shape in the spectra. Corrections for telluric absorption are applied by the EsoRex pipeline, but some residuals may be left due to differences between individual observations and the air mass of the corrective observation. However, these effects are negligible and are known so care can be taken during analysis to ensure they are noted.

For this spectrum we are sensitive to the reflected light, but across the wavelength range responses are different. Whilst each wavelength is sensitive to various altitudes in the troposphere, the exact pressure varies depending on wavelength. We can determine the level to which each wavelength is sensitive by finding the two-way opacity across the spectrum. We can then see where in the atmosphere the incoming radiation can reach, as shown in Figure 2.5.4. The increasing opacity at shorter wavelengths is due to the inclusion of the extinction opacity for Rayleigh scattering in the calculation. Where the opacity reaches one is where we are able to sound down to, below this we are not sensitive to what is happening as no incoming radiation can reach those levels. This is due to absorption by species in the atmosphere. In regions with strong absorption, such as the 889nm methane absorption band, allow only penetration down to the uppermost highest clouds. Incidentally, wavelengths around this range are excellent probes of the tropospheric haze. Hence using a wavelength range with transmission depth variety is useful as it allows us to gain information about all regions of the cloud vertical structure.

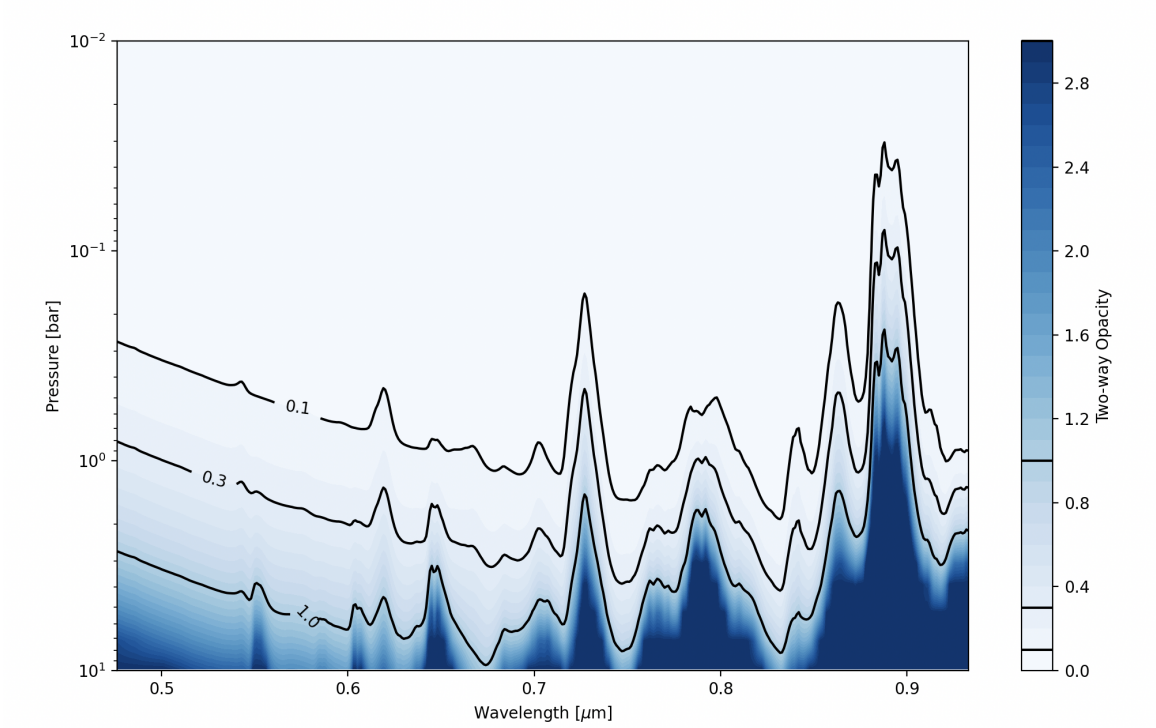


Figure 2.5.4: Two-way opacity showing for wavelengths within the VLT/MUSE range, the contour line at 1.0 indicates where we are able to probe down to. These values are calculated with the inclusion of the extinction opacity of Rayleigh-scattering, without any absorbing or scattering aerosols, only the background species.

2.5.3 Limb Darkening

Limb darkening is the effect seen when observing a planet or star where towards the edge of the disc the appearance begins to darken, becoming darker and darker as you move towards the extremity of the disc. It can be seen on Jupiter in Figure 2.5.5, with the brightest parts of the observation being nearer the centre of the disc and dimming as you move outwards. Due to the inhomogeneity of Jupiter, the effect is less visually pronounced than for stars, as differences due to cloud top appearances and storms visually detract from the limb darkening effect, however, it is still present. For the thermal infrared, the case is more similar to stellar limb darkening, where the temperature affects the observed radiance, and towards the limb, the radiance is coming from the outer parts of the atmosphere which are cooler providing a weaker source of radiation to be observed. Whereas in

the centre of the disc, the radiation is coming from deeper in the atmosphere as well and provides a greater temperature hence source of radiation. In the visible, we are dealing with scattered and reflected light in the atmosphere, so we are also dependent on the phase function of both the solar and viewing angle. Towards the limb the incoming sunlight has a path through less dense atmosphere, as it is passing through only the upper layers, hence there is less scattering of the light back towards the observer due to less material in the path, causing a darker appearance towards the edge of the disc.

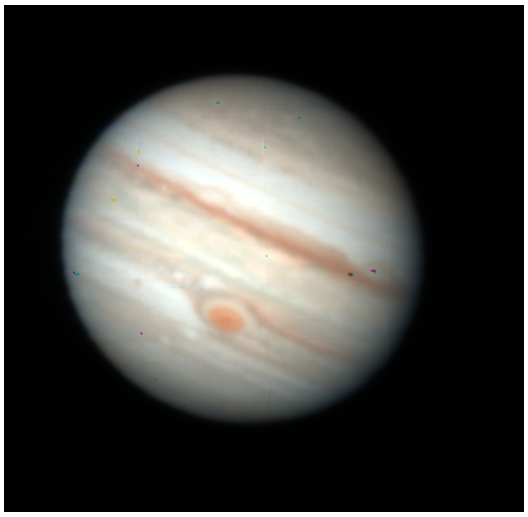


Figure 2.5.5: RGB composite image from VLT/MUSE observations from July 2023, the darkening towards the edge of the disc can be seen demonstrating the limb darkening experienced when observing the planet.

Observations at higher viewing angles have more sensitivity to the cloud and haze layers which we are attempting to study. This is because the light emitted towards the limb has a greater path length, meaning the radiation has passed through a greater amount of upper atmospheric aerosols when compared to those from a zero zenith viewing angle, as can be seen in Figure 2.5.6. Hence, by including spectra from higher viewing angles we are able to incorporate this additional information into our retrievals, which provides a better constraint on our models. As the optical thickness of the atmosphere is dependent on wavelength, the limb darkening effect is also due to the variation in the atmospheric path of the radiance for each wavelength.

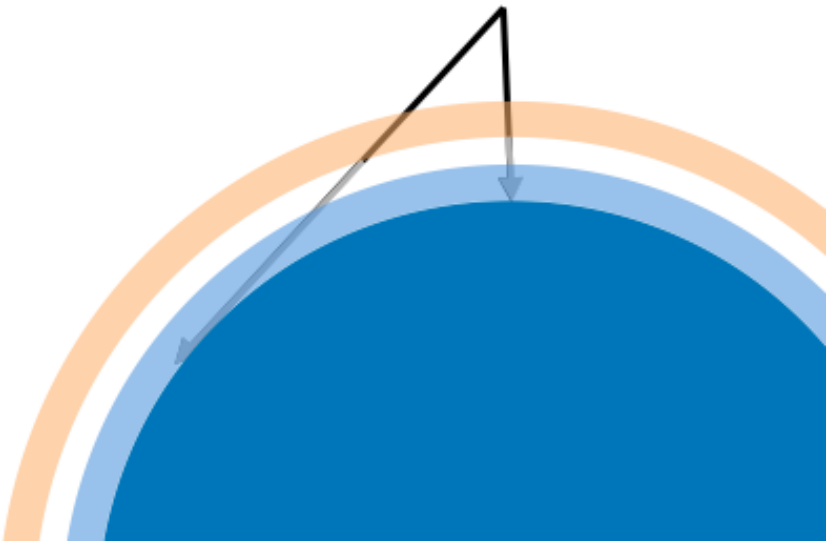


Figure 2.5.6: Examples of the path that two viewing angles take through the atmosphere of Jupiter when based on a two-cloud model. The left side arrow is at a higher viewing angle and thus has a longer path length within the haze than the nadir path.

2.6 List of Observations

Date	Juno Perijove period	GRS present	Notes	
04-02-2014	-	Y	-	MUSE calibration
17-02-2014	-	N	-	observations
08-03-2016	-	Y	-	Observations used in Irwin et al. (2018a)
31-03-2016	-	Y	-	
02-04-2016	-	Y	-	
10-01-2017	3	N	-	
15-05-2017	5	N	-	
28-05-2017	6	N	-	Observations used in Irwin et al. (2018a)
20-07-2017	7	N	-	
26-07-2017	7	N	-	
15-08-2017	7	Y	-	
09-04-2018	12	Y	noAO	Observation used in Braude et al. (2020)
14-04-2018	12	N	''	
18-05-2018	12	N	''	
25-05-2018	13	Y	''	Contemporaneous VISIR observation

28-05-2018	13	N	''	
12-07-2018	13	N	''	
11-09-2018	15	N	''	
11-07-2019	21	Y	AO	PI F.Clarke (ID – 0103.C-0769(A))
23-03-2020	26	Y	noAO	
16-04-2021	33	N	Y	
10-05-2021	33	N	Y	
08-11-2021	38	N	AO	PI C. Alexander onwards
15-12-2021	38	N	AO	
29-06-2022	43	Y	AO	
01-07-2022	43	Y	noAO	
27-07-2022	43	N	noAO	
29-07-2022	44	Y	AO	Contemporaneous JWST observations
30-07-2022	44	Y	AO	
06-09-2022	45	N	AO	
19-09-2022	45	Y	AO	
15-07-2023	53	N	AO	
19-07-2023	53	Y	AO	
20-07-2023	53	N	AO	
22-07-2023	53	Y	AO	
12-08-2023	53	Y	AO	
15-08-2023	53	Y	AO	Issues with AO system leading
16-08-2023	53	N	AO	to repeated observation blocks
22-08-2023	54	Y	AO	
15-09-2023	54	Y	AO	
23-09-2023	54	Y	AO	

Table 2.6.1: MUSE observations of Jupiter, the Perijove period of Juno that the observation falls into is also marked, as is the visibility of the Great Red Spot. Those in bold have been used in this thesis. Observations taken after May 2021 were PI C. Alexander, those in 2018 were PI A. Braude, 2019 was PI F. Clarke, all other observations were PI P. Irwin. Exposure time for all observations is 0.1 seconds, with 1 second integration time, with spectral resolution of 0.125nm.

Chapter 3

NEMESIS Retrieval Algorithm

The collection of all of the remote sensing data, from the VLT/MUSE observations detailed in this thesis, as well as hundreds of other observers based across the globe and data collected in orbit around Jupiter, serve a purpose. At face value the cumulation of images and spectral information can be used to determine changes and differences of the planet as it is imaged through time. However, we are able to achieve far more if we can use this data beyond its initial appearance. Using a more quantitative approach, through radiative transfer and retrieval algorithms, we can determine what atmospheric conditions are able to reproduce the observations, thus determining far more about the atmosphere. In this thesis we extensively use the **N**on-linear **E**stimator for **M**ultivariat**E** spectral analy**SIS** code (NEMESIS) (Irwin et al., 2008) to undertake retrievals using spectra extracted from the VLT/MUSE observations.

NEMESIS is a highly versatile code for modelling planetary atmospheres, and is able to accommodate both solar system bodies and exo-planets, across a huge swath of the spectral range and for a huge number of parameterisations of the atmospheric composition and structure. Originally derived to model the data returned from the Cassini mission to Saturn, it was then extended to accommodate a wider range of planets and observations (Irwin et al., 2008). Through its wide range of parameterisation schemes to model atmospheric properties such as cloud structures or species distribution, it can represent many atmospheric types. Further flexibility comes from the ability

of NEMESIS to handle observations using both filter-averaged and spectral data from UV to microwave wavelengths. This flexibility means it has now been used on virtually every major body and moon (with an atmosphere) in the solar system, as well as beyond our immediate system. Within this thesis we have used NEMESIS to model spectra of Jupiter to determine information about the structure of Jupiter's clouds and the distribution of ammonia within its troposphere across the disc of Jupiter over time.

NEMESIS uses non-linear optimal estimation to minimise the difference between an observed spectrum and a simulated spectrum calculated from the atmospheric parameters specified in the set-up. Through the adjustment of these parameters from the *a priori* values that are specified by the user, the model is able to reduce the difference between the observed and simulated spectra. From this process NEMESIS we can determine what atmospheric profiles are able to simulate observed spectra, giving us an insight into the properties of the atmospheric environment.

3.1 Radiative Transfer

The interaction of radiation with the atmosphere must be understood in order to model the spectrum of an atmosphere. How incoming radiation interacts with the molecules within the atmosphere, being reflected and transmitted in differing amounts with species and conditions, determines what can be seen in observations. By being able to represent these interactions through equations, we form the basis of the NEMESIS code, and we can then calculate what is happening in each atmospheric layer in the model. Radiation is affected by matter in the atmosphere through absorption, emission and scattering. This can be represented through aerosol layers in the atmosphere as well as non-condensing species in the atmospheric composition. As the vertical region of the atmosphere being studied is represented by a number of layers, through calculating the state of the permeating radiation at each level it can then be combined with layers either side to provide an overall picture of atmosphere in the model.

In order to do this, it must be understood what is happening to the radiation impinging on the layer as it moves through the molecules within that section of atmosphere. As there are further sources

from the thermal emissions deeper in the atmosphere these can also contribute to the radiation in each layer. Within the wavelength range of MUSE observations scattering from solar radiation are of most importance to the produced spectra, however, the deep emissions should be noted due to the information we can infer from them from certain features, such as $5\mu m$ hotspots from previous literature. The scattering of incoming solar radiation is most indicative of the aerosols present through clouds; both liquid droplets and solids such as ice, they can cause huge scattering effects on the incoming light. How the light is scattered is dependent on the implicit scattering mechanism invoked by the size of the aerosols. For smaller aerosols, where their size is far smaller than the wavelength of the light, Rayleigh scattering is invoked. Larger particles which are comparable in size and greater lead to Mie scattering. When considering the larger particles such as cloud droplets there are also additional geometric effects which need to be considered, such as rainbows and glory. How these effects are dealt with by NEMESIS are detailed further down in this section.

Here we will introduce some of the basic radiative transfer equations which explain some of the processes which are going on in the atmosphere as light passes through. We start with the radiative transfer equation, which describes the effects of the intensity of light as it passes through an absorbing and emitting medium.

$$\mu \frac{dI(\lambda)}{dz} = \kappa(\lambda)\rho_a(S(\lambda) - I(\lambda)) \tag{3.1.1}$$

Where I(λ) is the intensity of the incoming radiation, S(λ) is the source function, z is the distance travelled through the medium, μ is the dependence on the zenith angle of the incoming radiation as $\mu = \cos\theta$, κ_λ is the extinction coefficient, which is composed of the sum of the absorption and scattering coefficients for the medium. ρ_a is the density of the material in the layer which affects incoming radiation.

Optical depth, $\tau(\lambda)$, is a measure of how deep into the atmosphere light can penetrate. It is wavelength and material dependent. All of the light entering the layer passes through when the optical depth is zero, meaning the atmosphere is clear and fully transmitting. Instead, when the optical depth is equal to infinity it represents all of the radiation having been absorbed and/or

scattered. As the optical depth reaches one it represents the medium as an opaque layer to the incoming radiation. This allows us to estimate how deep in the atmosphere the light can penetrate to.

$$\tau(\lambda) = \int_{z_0}^{z} \kappa(\lambda)\rho_a dz \tag{3.1.2}$$

As z is the height at the top of the layer, dz is the specific height of a certain layer, κ_λ is the extinction coefficient and ρ_a is density of the species which affects radiation, integrated over the width of the layer, where z_0 is the bottom of the layer.

Combining Equations 3.1.1 and Equation 3.1.2 we have the equation of radiative transfer in terms of the optical depth:

$$\mu \frac{dI(\lambda)}{d\tau(\lambda)} = S(\lambda) - I(\lambda) \tag{3.1.3}$$

As we have a large amount of scattering occurring within the atmosphere of Jupiter we must consider the likelihood of an aerosol particle to scatter the radiation it interacts with instead of absorbing. To do this we need to consider the single scattering albedo (ω_0), which provides a measure of the ratio of radiation which is scattered compared to being absorbed by the material. It is a ratio of the scattering optical depth (σ_s) to the total optical depth (scattering and absorption (σ_a)) and is dependent on the wavelength of the incoming radiation.

$$\omega_0(\lambda) = \frac{\sigma_s(\lambda)}{\sigma_s(\lambda) + \sigma_a(\lambda)} = \frac{\sigma_s(\lambda)}{\sigma_{ex}(\lambda)} \tag{3.1.4}$$

The source term, $S(\lambda)$ is affected by the single scattering albedo as it determines how much radiation is not absorbed by the material and present to continue propagation through the atmosphere once scattered.

$$S(\lambda, \tau'_\lambda) = \frac{\omega_0 J(\lambda, \tau_\lambda)}{4\pi} + (1 - \omega_0) B(\lambda, \tau_\lambda) \tag{3.1.5}$$

where $J(\lambda, \tau_\lambda)$ is the mean overall intensity at a certain location and $B(\lambda, \tau_\lambda)$ is the blackbody

function. This can now be combined into Equation 3.1.3 where the RHS has been integrated to give the radiative transfer equation

$$I(\lambda,\tau_\lambda) = I(\lambda)_{deep}\exp\Big(\frac{-\tau(\lambda)_{deep}}{\mu}\Big)\int_0^{\tau(\lambda)_{deep}} S(\lambda,\tau_\lambda)\exp\Big(\frac{-\tau(\lambda)}{\mu}\Big)d\tau(\lambda,z) \tag{3.1.6}$$

With the radiative transfer equation (3.1.6), which is dependent on the wavelength of the radiation and the optical path through the atmosphere, we have the basis of the calculations which must be considered by the NEMESIS code. The atmosphere is split into 39 layers and at each of those the radiative transfer occurring through this layer needs to be calculated. This then leads onto the neighbouring layer until the overall transfer of radiation through the atmosphere has been calculated.

Up to this point we have considered single scattering within the atmosphere, but the true picture is more complicated as the radiation continues to scatter as it interacts with material in each layer as long as it is not absorbed. Therefore we must calculate multiple-scattering throughout the atmosphere. NEMESIS uses the doubling and adding matrix operator detailed in Plass et al. (1973) to calculate multiple-scattering. To further complicate the situation we are also able to consider the angle dependence of these calculations to add further constraint to the solution we are retrieving. When we extract a spectrum from an observation we have to include the intrinsic properties of the observation such as the viewing angle (angle between the observer's line of sight and the line perpendicular to the surface being viewed (nadir)) as well as the solar zenith angle (angle between the line from the sun to the nadir), as the radiation observed is dependent on these properties. We are also able to use these differences in radiation propagation to our favour by using the effects of limb darkening (Section 2.5.3) and by making approximations (Chapter 4) in order to produce observations which have the idealised viewing angles to create a more constrained retrieval due to the enhanced sensitivity we can gain through angle dependency. To use the radiative transfer model we must be able to calculate the absorption coefficients of the gases in the atmosphere. Several methods can be used to do this, such as line-by-line (LBL) model and correlated-k approximation, which will both be detailed below.

3.1.1 Line-by-line Model

The most accurate method of calculating the gas absorption in the atmosphere is through a line-by-line (LBL) model. For this technique every spectral line is calculated for every pressure and temperature within the atmosphere. The line data is taken from huge databases such as HITRAN (high-resolution transmission molecular absorption) database (Gordon et al., 2022) which contain thousands of line transition data from experimental measurements. To resolve every absorption line the wavelength sampling rate must be finer than the width of each line in order to fully capture each feature to ensure all the absorption in the atmosphere is calculated. This leads to a huge number of calculations due to the fine sampling rate, masses of absorption lines and the range of pressures and temperatures each line must be calculated for. Therefore to produce a single spectrum it is a hugely computationally expensive and time consuming. This makes the method incompatible for retrieval algorithms as perpetual calculations of spectra, with the resolution used in this work, would lead to incredibly slow retrievals.

Despite their unmatched accuracy LBL calculations should be reserved for retrievals of very small spectral regions or those with minimal absorption lines. In addition, the resolving power of many instruments does not produce a spectrum as fine as those calculated through LBL needed to capture each line. This leads to a huge amount of computational time being wasted as smoothing of the high resolution LBL spectrum would have to be done to be comparable to that observed by our instrument. A compromise between accuracy and computational speed needs to be taken in order to create medium resolution forward model spectra in a timely manner. The best compromise was found through the correlated-k method due to its ability to be used for multiple-scattering atmospheres, unlike band models, whilst being favourable for both resolution and computational speed (Irwin et al., 2008).

3.1.2 Correlated-k Method

The correlated-k method provides a method which is able to calculate a spectrum with sufficient resolution, efficiently enough to be used by a retrieval algorithm. It is able to reduce the number of calculations required to calculate gas absorption by introducing an intermediate step of pre-

calculating k-tables. These can then be used by NEMESIS as look-up tables when calculating each individual spectrum during retrievals, allowing us to include gas absorption information without explicit LBL calculations. The way in which k-tables can be used for by NEMESIS can be seen in the following equations which have been taken from Irwin et al. (2008).

The mean transmission $\bar{\tau}$, for a path through the atmosphere for a particular frequency interval ν_0 to $\nu_0 + \Delta\nu$ is given by

$$\bar{\tau}(m) = \frac{1}{\Delta\nu} \int_{\nu_0}^{\nu_0+\Delta\nu} \exp\Big(- m \sum_j k_j(\nu) \Big) d\nu \tag{3.1.7}$$

Where m is the total absorber amount (molecules cm^{-2}) in the column of atmosphere being considered. $k_j(\nu)$ (cm^2 molecule^{-1}) is the absorption spectrum of the j^{th} line (taking into account the gas volume mixing ratios), where the sum includes all of the gases which cause absorption in the atmosphere in this frequency interval. To preserve the accuracy of the spectrum, we need to ensure that the frequency interval is smaller than the individual line shapes, to ensure that they are each resolved. However, this would lead to thousands of calculations still, as with a line-by-line approach, and not reduce the computational intensity.

When calculating the mean transmission, there is no dependence of where in the interval an absorption coefficient occurs. Therefore only the fraction of the frequency range, $f(k)dk$, occupied by absorption coefficients between k to $k + dk$, needs to be known. This allows us to convert the mean transmission function into

$$\bar{\tau}(m) = \int_0^\infty f(k) \exp(-km) dk \tag{3.1.8}$$

where $g(k)$ is a cumulative function

$$g(k) = \int_0^k f(k) dk \tag{3.1.9}$$

As $g(k)$ is a smooth single-valued, monotonically increasing function, it is possible to calculate its inverse the k-distribution function, $k(g)$, which is also a smoothly varying function. Therefore we

can now write the mean transmission as

$$\bar{\tau}(m) = \int_0^1 \exp(-k(g)m)dg \tag{3.1.10}$$

However, unlike $k(v)$ in Equation 3.1.7 which is rapidly varying, $k(g)$ requires far less sampling to reproduce the function when integrating numerically, and so we can approximate the integral as

$$\bar{\tau}(m) = \sum_{i=1}^{N} \exp(-k_i m)\Delta g_i \tag{3.1.11}$$

where k_i is the value of the k-distribution for an atmospheric path at the i^{th} quadrature point and Δg_i is the corresponding weight. NEMESIS uses a Gaussian quadrature for its sampling. The number of ordinates dictates both the accuracy of reproducing the function but also the computational intensity of the calculations and overall speed. Typically a value of N=10-20 is used to ensure that the k-distribution is properly sampled without slowing down the calculation overly.

In order to use this k-distribution method NEMESIS requires the k-distribution function to be pre-calculated for each gas which is spectrally active for the planet which is being modelled. This has to be done over a range of temperatures and pressures which would be found in the modelled region of the atmosphere and for the resolution of the spectrum being modelled. Once the function has been calculated over the grid of pressure temperature values at the correct resolution, for all gases active in the wavelength range we have the k-distribution tables required to run NEMESIS. To produce a spectrum for an atmospheric path, NEMESIS interpolates the k-tables of each gas to the specific temperature and pressure of that path. As the absorption for each path is dependent on multiple gases, the k-tables of each gas have to be combined using the overlapping line approximation. To do this, the k-tables are weighted with volume mixing ratios of the associated gas and it is assumed that the absorption lines of each gas are not correlated with each other (which introduces some error through this assumption). From this we can calculate the absorption, scattering and emission which is occurring to the radiation caused by the species in the atmosphere. Adding in the effects of the atmospheric profiles, such as absorption caused by the clouds and aerosol opacities specified, as well as collision induced absorption (where forbidden electric transitions are induced through collision of

two particles, leading to the absorption of photons) such as H_2-H_2 and H_2-He, creates a full range of the atmospheric processes acting upon impinging radiation at Jupiter.

The real path considered through the atmosphere will not have a single pressure and temperature along its length, therefore the use of the correlated-k approximation is required when using k-distribution tables for an inhomogeneous atmosphere. We split the atmosphere into a suitable number of layers (M) where we can assume each layer to be homogeneous (again introducing error into the approximation). Then we can calculate the k-distribution for each layer as if it were homogeneous. Through this method, we find regions of high absorption are consistent through all the other layers, as with middle and weak absorption. After calculating the k-distributions for each layer (out of the total M), the mean properties of the entire atmosphere can be represented as

$$\bar{\tau} = \sum_{i=1}^{N} \exp\Big(- \sum_{j=1}^{M} k_{ij} m_j \Big) \Delta g_i \tag{3.1.12}$$

where k_{ij} is the k-distribution of the j^{th} layer at the i^{th} quadrature point.

Using the correlated-k method we are able to produce accurate spectra which are far less computationally expensive than the line-by-line method, without significantly compromising on accuracy. Comparison of accuracy of the correlated-k to LBL models depends on the number of quadrature and the exact atmospheric properties. For certain cases with 10-20 quadrature points, Irwin et al. (2008) find the correlated-k approximation accurate to $\sim$ 5%. This can only be assessed through comparison with LBL results. For the calculations done in this work with MUSE, it is hard to compare as the line data of methane only goes down to $\sim$800nm (more information about line data in Section 3.4). Therefore alongside the uncertainties from observations, the level of error introduced from the correlated-k method will not be detrimental to the overall results.

Using the correlated-k method we are able to produce synthetic spectra to compare to our observations. The exact atmospheric set-up we want to compare can be altered through the parameterisation schemes of NEMESIS (see Section 3.3) to give a different output of the spectrum. In the likely case

that the initial *a priori* values for parameters which we specify do not create a spectrum which closely resembles our observed one, adjustments to the inputs must be made. However, these parameters are linked and affect the output spectrum in related ways and it is hard to identify which exact parameter needs to be changed to fit the spectrum better. Hence, NEMESIS has the ability to undergo a retrieval mode where it is able to adjust multiple parameters on every iteration to minimise the difference between the input observed spectrum and the modelled output spectrum.

3.2 Retrieval of a Spectra

Producing a modelled spectrum using NEMESIS, which matches closely to our observed spectrum, allows us to consider the set-up used to be representative of the conditions of the atmosphere. Ensuring a good fit to observations is challenging due to the large number of parameters required to fully describe the conditions. In addition, each parameter is able to affect the spectrum in similar ways and combine to produce effects which make it difficult to manually determine necessary changes. However, NEMESIS can use non-linear optimal estimation to more easily find the best fit to the observed data, through the calculation of synthetic spectra alongside the functional derivatives, which detail the rate of change radiance with respect to atmospheric variables, to minimise the difference between the calculated and observed spectra (Irwin et al., 2008).

Here we outline the processes, as described in Irwin et al. (2008), when NEMESIS undertakes a retrieval. To reproduce an observed spectrum we must create an atmospheric model which represents the true atmosphere, we can use multiple vertical profiles which combine to create a synthetic spectrum which closely resembles observations of the planet. The number of profiles used is $NPARAM$, these profiles have $NPRO$ vertical levels (enough to represent vertical variation). Each profile is initially set with *a priori* values as a starting point for the retrieval. We can fix profiles to these *a priori* values if desired, leading to $NVAR$ profiles being retrieved, where $NVAR \leq NPARAM$. The state vector X contains a value at each $NPRO$ pressure level for each profile retrieved, giving $NX{=}NVAR{\times}\ NPRO$ when every profile being retrieved is continuous. As we use parameterisations of atmospheric profiles for NEMESIS, this results in a far smaller value of NX than for continuous

profiles. Therefore, for each iteration we have fewer values of the state vector to update. During each iteration NEMESIS also calculates the rate of change of each variable atmospheric profile property, creating a property gradient matrix, M, with size (NX, $NPARAM$, $NVAR$), this contains a value for each element of the state vector, x.

For the retrieval, NEMESIS splits the atmosphere into different vertical layers to retrieve the profiles, $NLAYER$. These layers are assumed to be homogeneous, but must still be of a small enough width to be able to resolve the transmission weighting functions $w(z) = d\bar{\tau_{\nu_0}}(z)/dz$, where $\bar{\tau_{\nu_0}}(z)$ is the mean transmission to space from a certain altitude, z. Typically $NLAYER$ is less than $NPRO$. Through several steps which are outlined in more detail in Irwin et al. (2008), NEMESIS is able to represent how each of these parameters, in each layer, affects all other parameters in the model. This is done through a variety of matrices which contain both the explicit values for properties such as optical depth, transmission and radiance of the atmospheric layers as well as the rate of change of these properties with respect to other atmospheric profiles. These are then combined in ways to output a synthetic spectrum which can be compared to the output, as well as a final functional derivative matrix called a Jacobian matrix K, which can also allow us to infer additional information about the atmosphere as it is a matrix which contains elements which describe the rate of change of radiance with respect to each element in the state vector for each wavelength of interest.

Attempting to reproduce an atmospheric profile from an observation is an ill-posed problem due to the data set being finite, through a number of recorded spectral points, yet the atmospheric profile we are attempting to reproduce is continuous. In order to solve this ill-posed problem the number of degrees of freedom of the atmospheric parameterisation needs to be constrained in a way so that there are fewer points than the number of measurements. This can be achieved in several ways using NEMESIS. However, a more significant issue, which is far less easily avoided is the noise and error contained in every observation measurement, which increases the number of atmospheric profiles which are able to fit one set of observations to be practically infinite. This is harder to solve and has to be considered when we are looking at retrieved profiles to ensure that they are realistic with the information that we are aware of for the planet. Further to this when retrieving the vertical

profile we have to ensure that we do not create an unrealistic profile which may occur if we attempt to extract too much vertical information, in an effect called ill-conditioning. Although it seems ideal to extract the most vertical information as possible, the ill-conditioning effect can lead to a highly varying profile which is not realistic. Hence, we have to find a balance between vertical resolution and retrieval error and not attempt to gain a level of vertical resolution which is not possible. Now we are aware of the limitations that we have when attempting to retrieve a solution to our atmospheric profile we can begin to outline how we get to a result.

Starting with a priori estimates of the profile and covariance matrix we can estimate a spectrum and compare it to the observed spectrum. How the modelled and observed spectra differ can be defined by the cost function, which we aim to minimise to produce the best fit we can from the estimated profile. The cost function is given by

$$\phi = (y_m - y_n)^T S_\epsilon^{-1}(y_m - y_n) + (x_n - x_0)^T S_x^{-1}(x_n - x_0) \tag{3.2.1}$$

Where y_m is the measured spectrum, y_n is the calculated spectrum to the specified atmosphere, represented by a model state vector x_n, the measurement covariance matrix (S_ϵ) contains errors from the measurements and estimated forward modelling errors, x_0 is the a priori state vector and S_x is the a priori covariance matrix. NEMESIS aims to reduce the cost function when it is fitting modelled spectrum to that observed. As the retrieval proceeds changes in the cost function between each model iteration is reduces and NEMESIS converges when the difference between subsequent cost functions is less than 0.1% (or the maximum number of iterations has been reached).

The optimal estimation approach of NEMESIS was derived for interpreting Earth observations, for which the a priori state vector and covariance matrix are relatively well constrained from climatology. However, for Jupiter, there is far less prior constraint. Therefore the a priori covariance matrix, S_x has to be formulated, with the diagonal components being set to the square of the a priori errors and the off-diagonal elements being set to

$$S_{ij} = (S_{ii}S_{jj})^{1/2} \exp\Big(- \frac{|\ln p_i/p_j|}{c} \Big) \tag{3.2.2}$$

where p_i and p_j are the i^{th} and j^{th} pressure levels and c is a correlation length which determines the number of scale heights over which we assume the values of the profile to be correlated. Without this information, the issue of ill-conditioning can become more pronounced for continuous profiles, however, in this work we predominantly use parameterisations for the vertical profiles. These parameterisations prevent ill-conditioning as there is vertical smoothing incorporated into the parameterisation.

Using the cost function, Equation 3.2.1, we can calculate the difference between the observed spectra and the one produced through the current atmospheric set-up of measurement vector x_n. Through this, we can estimate a new trial vector x_{n+1}

$$x_{n+1} = x_0 + S_x K_n^T (K_n S_x K_n^T + S_\epsilon)^{-1} (y_m - y_n - K_n(x_0 - x_n)) \tag{3.2.3}$$

where K_n is the functional derivative matrix (Jacobian) for the n^{th} iteration. To keep the retrieval stable, without K_n varying too greatly, the new state vector, x'_{n+1}, is modified from x_{n+1} using a Marquardt-Levenberg formulation.

$$x'_{n+1} = x_n + \frac{x_{n+1} - x_n}{1 + \lambda} \tag{3.2.4}$$

where λ is set to one in the first attempt. If the calculated value of x'_{n+1} when used in the cost function, reduces it, then the new state vector is accepted, the λ is multiplied by a factor of 0.3 and the next iteration is started. However, if the calculated value of x'_{n+1} increases the values of the cost function then λ is increased by a factor of 10 and x'_{n+1} is calculated again from Equation 3.2.4 until the cost function is minimised. As the cost function is minimised and the value of each x'_{n+1} improves the fit, the value of λ begins to tend to 0 as the model converges.

Reaching the best estimate for atmospheres, where the a priori values are not as well known or as constrained, can often take 10-20 iterations to reach a minimum in the function. Additionally, at times the model can get stuck in a minimum where the cost function has been locally minimised but is not the global minimum of the parameter space. To avoid settling for a lesser solution the run can

be trialled using a multitude of starting a priori values. Introducing the concept of multiple starting points raises the question of why other methods are not used, such as nested sampling which is often more favoured to ill-constrained parameter spaces, hence their frequent usage for exoplanetary studies (Feroz and Hobson, 2008). However, this method which fits a huge number of combinations in a parameter space to find the best fit by removing the poorer fitting combinations until a final solution has been sought, is very time consuming for the high spectral resolution, multiple-scattered spectrum of Jupiter recorded by the VLT/MUSE instrument. Hence, utsing nested sampling is not possible for the retrievals we are undertaking for Jupiter due to their long running times.

The handling of errors with optimal estimation is very important. We have two types of error, those introduced through the errors in the measured spectrum, which determines how closely we try to match the observations and the errors of the *a priori* state vector elements, which dictate how much these elements can differ from their starting values. As the algorithm seeks to minimise differences between the observation and modelled spectrum, the errors described determine whether a better fit is required and how much we can alter the input values to accomplish this. If the errors given to the *a priori* values are too small then when calculating the next state vector x'_{n+1} the values will not perturb greatly and the final retrieved value will remain close to the initial input values. This reduces the chances of NEMESIS finding the true best fit to the profile if the *a priori* estimates are inaccurate. Conversely, setting the *a priori* errors too large means that NEMESIS attempts to overly reduce the difference between the modelled and observed spectra, and can lead to unrealistic values retrieved. If continuous profiles are being retrieved this can also lead to highly varying, non-realistic vertical profiles as it seeks to minimise the difference between the two spectra, producing very small retrieval errors. Therefore, when setting the *a priori* error it must be done in consideration of these effects occurring at each extremity.

In conclusion, NEMESIS is a highly efficient tool which enables us to reproduce high resolution spectral observations of Jupiter whilst minimising the computational demand of such calculations, through the use of k-distribution and correlated-k methods. We use parameterisation schemes to further reduce computational time whilst still capturing the observed spectrum through the

improvement of the atmospheric representation through updates to parameters through the retrieval model.

3.3 Parameterisation of atmospheric profiles with NEMESIS

As NEMESIS is a multi-functional code which has been designed to be able to be used for a multitude of tasks for all planetary set-ups there are a variety of ways in which it is possible to define the atmospheric structure which you are looking to retrieve. Once the basic atmospheric set-up is selected, the user can then define what exactly they want to retrieve for the vertical profile. In some cases this could be a temperature profile, but for this work we look to retrieve the aerosol profile, as well as the ammonia abundance. It would be possible to attempt to retrieve all of these parameters in a single run, but the lack of prior knowledge might easily lead to a highly unconstrained and unreliable retrieval. By reducing the number of parameters being retrieved we can have more confidence in the atmospheric profile that has been retrieved as there are fewer parameters to play off each other when matching the observed spectra. However, as mentioned earlier due to the error that is present in the observed data there are a huge amount of solutions to the vertical profile that match the observations. Therefore, even an almost perfect fit produced by NEMESIS may not be the exact representation of what is happening in the atmosphere. Further to this uncertainty about retrieved profiles matching the real atmospheric conditions, we are further plagued by parameters in the atmosphere which have significant degeneracy. This introduces another way in which retrieved parameters may not represent the actual atmosphere being observed.

3.3.1 Degeneracy of atmospheric retrievals

In this work we define degeneracy as the ability for different parameter changes to produce almost identical changes in the spectra. There are several degenerate pairs within the Jovian atmosphere where the same spectral response can be elicited from different parameter combinations, such as increasing the optical depth of a cloud layer, which can have the same spectral alteration as an increase in layer's particle size. Both these parameters also have further degeneracies with other parameters such as aerosol density, cloud location (top, bottom and peak pressures), particle size and distribu-

tion of size, refractive indexes (both real and imaginary parts) as well as the ammonia profile in the troposphere which we are sensitive to in the MUSE/VLT spectral range for the atmosphere. This leads to masses of degeneracy, and it becomes very difficult to disentangle which property is causing the atmospheric effect at each wavelength. Increasing the constraint on the observations, such as through increased spectral resolution but also with multiple viewing angles and fixing parameters can help to break this degeneracy in retrievals.

Dahl et al. (2021) investigated the degenerate nature of the parameter space for the visible/near IR wavelengths by recording the spectral response of atmospheric models when a single parameter was changed by 50%, whilst all other parameters were fixed. This gives an estimation of which wavelengths are more sensitive to changes in each parameter. Through this we can see degenerate parameter pairings, where similar spectral responses are elicited from different parameter changes. When trying to fit to a spectra, determining which parameter change best reproduces the spectrum is difficult when the spectral response of multiple parameters is very similar. One such example in Dahl et al. (2021) is an increase of the main cloud particle size from $1.71\mu m$ to $2.56\mu m$ which causes an increase of I/F of $\sim$25% at 890nm. An increase in the optical depth of the haze from 0.98 to 1.48 also invokes the same spectral response. Therefore determining which parameter change is needed to improve the fit at this wavelength becomes incredibly difficult due to the very similar responses. However, the spectral responses are often different across the entire wavelength range, for example increasing the optical depth of the haze also causes an 8% increase in I/F over the whole spectral range unlike the change in cloud radius (Dahl et al., 2021). This provides some ability for us to differentiate between parameters and break the degeneracy. However, as we have many degenerate pairs in our parameter space, and combinations of multiple changes can combine to again produce very similar responses over the whole spectrum, it can still be very difficult to differentiate. Therefore, attempting to retrieve large numbers of free parameters can lead to result being significantly affected by degeneracy despite NEMESIS being able to differentiate between (as the parameter pairs are not truly degenerate). If we can find ways to reduce free parameters, as will be discussed in Chapter 5, then we will have more awareness of our parameter space and avoid overwhelming degeneracies as they are confined to fewer variable parameters, allowing us to retrieve

a more realistic atmospheric model.

We will be detailing in the following chapters some of the ways we attempt to reduce the problem of degeneracy within our retrievals. One of the main ways in which this can be done is by reducing the number of parameters which are being retrieved each time, a focus of the work which will follow in Chapter 5. Another way to reduce the number of variable parameters at work is to use the parameterisation schemes which are built into NEMESIS. Even for a 'free' profile the layering scheme used for NEMESIS limits the number of values retrieved, however, in this work we mainly use parameterised aerosol layers to further reduce the number of parameter values which we are retrieving. In addition to minimising some of the degeneracy issues, these parameterisations are far faster to retrieve due to there being fewer values for each profile which need to be found by NEMESIS.

In this work we use only a few of the tens of profiles which are available to represent the atmospheric profiles. These are explained in Section 3.3, and the full steps taken to create a parameterisation scheme are then discussed in Chapter 5. Further information about all of the parameterisations can be found in the NEMESIS manual which can be found in the repository.

3.4 Set-ups of NEMESIS specific to this work

3.4.1 Layering Scheme

We use a layering scheme which spans from 10 bar (∼87 km below the 1 bar level) up to 0.001 bar (∼145 km above the 1 bar level), this includes both above and below the likely locations of atmospheric profiles of interest to ensure the entire picture is captured. We use 39 layers, which have varied spacing to capture the regions of interest with more vertical resolution, which can be seen in Figure 3.4.1.

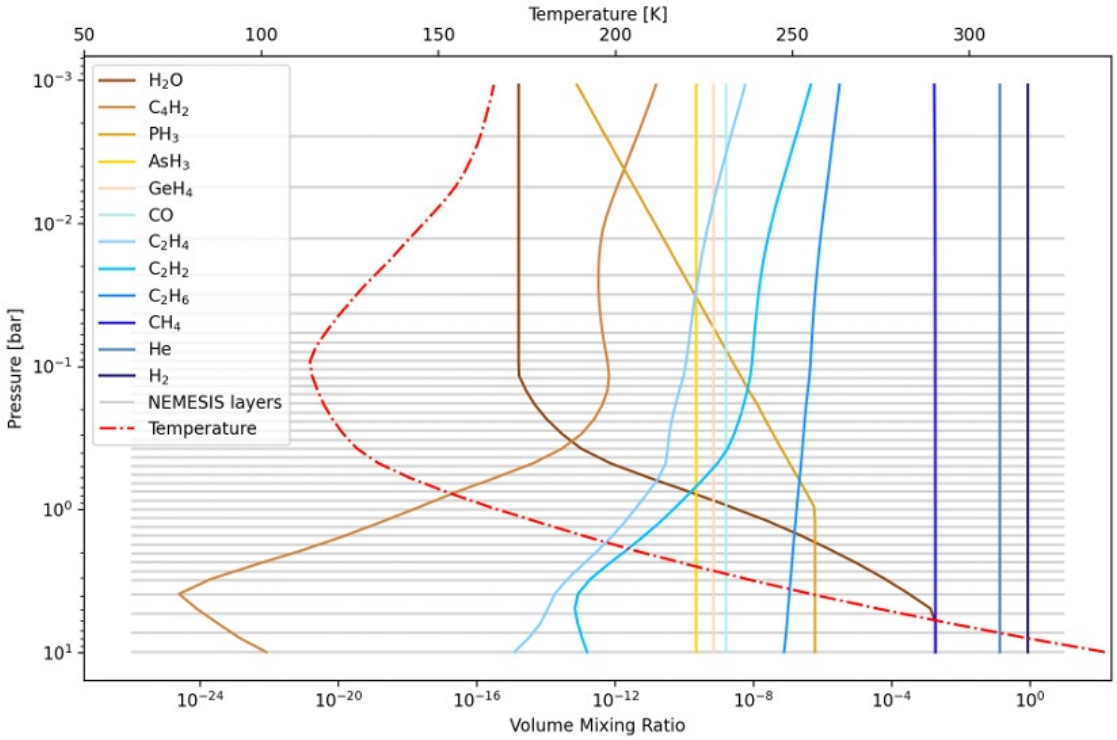


Figure 3.4.1: Grey lines – Layering scheme used in NEMESIS, with 39 layers. The spacing is smaller in regions of more variability of the aerosol profile. Coloured lines – Reference atmosphere volume mixing ratio of species used in NEMESIS setup. We are only sensitive to NH_3 and CH_4 (and He and H collision-induced absorption) spectral signatures in the MUSE wavelength range. Red line – Temperature profile used in NEMESIS setup.

3.4.2 Reference Atmosphere

For several species in the atmosphere we set the mixing ratio values of our reference atmosphere to be those derived from the Galileo probe entry, as in Table 1.2.1. We use a deep volume mixing ratio of 0.86 hydrogen, 0.134 helium and for methane we set the mixing ratio to be 1.8×10^{-4} (Niemann et al., 1998), with all three gases assumed to be well mixed across the globe and atmospheric column. Additional minor species are included in the reference atmosphere, as shown in Figure 3.4.1, have fixed profiles, we are only sensitive to absorption from NH_3 and CH_4 and CIA absorption in the MUSE range. The additional species profiles are included for completeness. For ammonia, we are retrieving its abundance, as it is not expected to be well mixed due to condensation and

has been documented to vary across Jupiter (e.g., Li et al. (2017)). We retrieve the deep mixing ratio of ammonia at each location, assuming a knee pressure of 0.7 atm (approximate ammonia condensation level) and a fractional scale height of 1 for the decrease above this point until it reaches the condensation point in the model, more information in Section 5.3.4. The condensation level is dependent on the temperature profile and above this point in the model, the volume mixing ratio of ammonia will decrease far quicker than the profile dictates. We are also limited to 100% relative humidity for ammonia. From the retrieved deep mixing ratio we will be able to determine the global distribution of ammonia for our observations and discover how our retrievals of the atmospheric profile depend on ammonia. We use a simplified step profile for our ammonia retrievals despite each cloud layer affecting the mixing ratio of ammonia according to ECCM, however, we want to keep the parameterisation simplistic especially when we are not confident the ECCM model is a true representation of the belts or even the zones.

3.4.3 Temperature Profile

The temperaure profile used for the NEMESIS runs is shown in Figure 3.4.1. For the upper parts of our atmosphere, those with pressures less than 0.8 bar, we use the temperature profile which was derived from the Cassini/CIRS mission (Fletcher et al., 2009). Below this point, the temperature profile has to be extrapolated using a dry adiabat to cover the model pressure range as done in previous work (e.g., Irwin et al., 2018a; Braude et al., 2020). Despite our retrievals spanning across the disc we still use the same temperature profile for all locations. Although the temperature profile varies across the disc, it is often by small amounts $\leq$5K between zones and belts and typically limited to pressures less than 1 bar (Fletcher et al., 2009). We expect the deep atmosphere to be barotropic, and therefore the temperature on a single pressure level will be constant. As our cloud parameterisations are only dependent on pressure, a single temperature profile will not be a significant source of error.

3.4.4 Absorption Line Data

To represent the gas absorption using the correlated k method we have to produce k-tables. For Jupiter, we need k-tables for ammonia, methane, and Collision Induced Absorption (CIA) of helium and hydrogen (and weak quadrupole H_2 absorption). NEMESIS also includes additional CIA calculations, which include the pairings of H_2-N_2, H_2-CH_4, N_2-N_2, CH_4-CH_4 and H_2-CH_4, these have negligible effect on the absorption but are included for completion. The majority of the absorption of incoming radiation in the visible and near IR wavelengths of our observations is due to the absorption from ammonia and methane, despite their relatively low abundance. These species create strong spectral features in the spectrum as they readily absorb at several wavelengths in our data (Figure 2.5.3). Therefore it is important to ensure that the line data which is used to create the k-tables has high enough accuracy to recreate these absorption features properly. We then assume that all other gases within the atmosphere are either non-absorbing within our wavelength range or are in negligible quantities above the cloud tops and thus minimally affect the spectra.

For ammonia we use k-tables which have been generated using line data from the ExoMol–C2018 NH3 database from Coles et al. (2018). Irwin et al. (2019) found that this data set best reproduced the smoothed MUSE observations of Jupiter, for its wavelength range and its medium resolution. This line set contains new absorption features compared to previous works over the visible and near IR range which had previously only had coarse information in this range (Irwin et al., 2019).

To produce the methane k-tables, the line data of Karkoschka and Tomasko (2010) was used as there is limited line data for the MUSE wavelength range below 800nm. This data set is not solely laboratory observed line data, it is instead produced from methane band absorption data which is extrapolated using observed planetary spectra of Jupiter and Titan alongside laboratory transmission data. These coefficients introduce some error into our simulations however they are the only data set which covers the entirety of the MUSE wavelength range.

We also include hydrogen absorption data for its molecular form, H_2 as there are weak quadrupole line transitions which are included due to the high abundance of H_2 in the atmosphere. This is

taken from the HITRAN 2012 database (Rothman et al., 2013). The amount of absorption from hydrogen is far less significant than from methane and ammonia, but due to its prevalence in the atmosphere, it improves the retrieved spectrum with its inclusion. Additionally, hydrogen and helium also provide collision-induced absorption within the atmosphere via H_2-H_2 and H_2-He interactions. As with previous works which have used MUSE data for Jupiter, such as Braude et al. (2020) this is modelled as in Borysow and Frommhold (1989); Borysow et al. (2000). For shorter wavelengths within the MUSE range, we have to consider opacity from Rayleigh-scattering for H_2, He, CH_4 and NH_3, this was modelled via standard theory (e.g., Goody et al., 1989) as done in previous works (e.g., Braude et al., 2020; Irwin et al., 2018a)

3.4.5 Scattering Phase Functions

Scattering is a dominant process in the Jovian atmosphere, we are unable to reproduce spectra without a good representation of the process in NEMESIS. Due to a range of particle sizes, how we can approximate these processes depends on how the light interacts with particles of their size. For the smaller particles which are present within Jupiter's atmosphere, such as gas molecules, we can use the Rayleigh approximation to calculate the scattering phase function, $P(\theta)$ due to their size being much smaller than MUSE wavelengths. At these sizes, the particles are purely scattering and have zero absorption cross-sections (Irwin, 2009).

$$p(\theta) = \frac{3}{4}(1 + \cos^2\theta) \tag{3.4.1}$$

where $p(\theta)$ is the scattering phase function and θ is the scattering angle, given by Goody et al. (1989).

However, this approximation is not appropriate for every particle in the atmosphere due to the larger sizes which occur for some particulate matter. As we are dealing with condensed droplets and ices their particle size begins to become comparable and larger than the MUSE wavelengths, and here the Mie scattering approximation takes over. Mie scattering assumes perfectly spherical particles, which holds for a liquid droplet, however, we are also likely working with ices in the troposphere of Jupiter. It is possible to include analytical methods to account for these non-spherical crystals, but to a

first approximation, it is possible to model non-spherical ice particles using Mie theory (Mishchenko et al., 1997). We are able to do this as long as the Mie calculated phase functions are approximated with combined Henyey-Greenstein functions (Equation 3.4.2) (Henyey and Greenstein, 1941), (Irwin et al., 2018b). This smooths over features in the Mie scattering which only occur with spherical particles, such as 'glory' (increase in scattering 180° opposite to incidence ((anti-solar point)) and the appearance of 'rainbow' (coloured apparition 40 – 50° from anti-solar point) (Irwin et al., 2023). The use of the Henyey-Greenstein functions also has the additional benefit of speeding up the scattering code (Irwin, 2009).

The double Henyey-Greenstein approximation (Henyey and Greenstein, 1941) is given as

$$p(\theta) = f\frac{1-g_1^2}{(1+g_1^2-2g_1\cos\theta)^{\frac{3}{2}}} + (1-f)\frac{1-g_1^2}{(1+g_2^2-2g_2\cos\theta)^{\frac{3}{2}}} \tag{3.4.2}$$

where g_1 is the asymmetry of the forward-scattering lobe between 0 – 1, g_2 is the asymmetry of the back-scattering lobe between 0 – -1 and f is the fractional contribution between 0–1 of the forward-scattering part.

Due to the smoothing by the Henyey-Greenstein approximation, we are able to use Mie theory (Goody et al., 1989) as an approximation for non-spherical particles. Allowing us to compute the extinction cross-sections, single scattering albedos and phase functions as a function of wavelength from the complex refractive index spectra ($m_r + im_i$) of the particles and size distribution. Mie theory shows us that the particles are most efficient at scattering light which has a comparable wavelength to its radius, and as the particles become larger they become more forward scattering (Irwin, 2009). As particles become smaller compared to the wavelength, the extinction cross-sections tend to $1/\lambda^4$, and the phase function tends back to Rayleigh scattering (Irwin, 2009).

3.4.6 Parameterisation profiles in NEMESIS

Here we will overview some of the parameterisation schemes which have been used in this work in more detail to provide more clarity in further sections. As NEMESIS only has a finite number of atmospheric layers there needs to be a way to represent the aerosol profile over the limited number

of points. The further parameterisations reduce the number of parameters being retrieved, both speeding up the retrieval time and reducing some of the degeneracy present in the parameter space. In the text below several parameterisation schemes of the aerosol profile, are given alongside the number of the profile in the NEMESIS manual, for ease of reproduction. Within NEMESIS the standard units of aerosol densities are particles/gram (rather than particles/cm^3).

Continuous 0 – profile is treated as continuous over the pressure range with the same number of points as atmospheric layers. Each pressure point has an *a priori* input and associated error, with a correlation length for the profile (pressure range over which points assume correlation to help reduce ill-conditioning). This profile was used for the Bracket and Snippet analysis, detailed in Chapter 5.

Reduced Continuous 25 – similar to continuous profile 0, but it is represented through a smaller number of pressure points (to reduce computational time) than the main layering scheme, the retrieved layers are interpolated to the main layering scheme using a cubic spline, developed for Braude et al. (2020).

Gaussian 47 – profile which uses the shape of a Gaussian line to create the specific density profile [particles/g] (ratio between the mass of a volume of gas compared to corresponding volume of dry air). Input parameters are the centre pressure of the cloud, fractional width defining the extent of the cloud and the defined total opacity and their associated errors. Similar profiles exist with different units (12, 14) such as altitude or peak specific density. This profile has been used for the main cloud and haze layer in this work, discussed in Chapter 5.

Knee Pressure 1 – profile has a constant deep value (and error) up to a certain 'knee' pressure, from this point it then declines with a specified fractional scale height and error. The Volume mixing ratio (VMR) retrieved is limited by 100% relative humidity and above the condensation level will experience depletion due to condensation. This profile has been used for the representation of ammonia in this work and will again be detailed in Chapter 5.

As well as a profile number, as detailed above, NEMESIS also has an additional input parameter

which identifies the type of profile being retrieved. For gases, such as ammonia, there is a corresponding ID based on HITRAN, which gives the species properties for that profile. For aerosol profiles, such as our retrieved haze and cloud profiles, we do not assign the profile to a known species. Instead, we can use codes to decide what we want to retrieve about these profiles, for our retrievals this has been set to be the refractive imaginary index of the profile constituents. The complex refractive index is needed when dealing with absorbing materials, the real part of the index deals with refraction (the ratio of the speed of the radiation inside the material, to the free speed outside of the material). The imaginary part of the index describes the attenuation of light through the material, considered a measure of absorption.

Imaginary Refractive Index 444 – retrieves the imaginary part of the cloud's complex refractive index (RI), but also sets the cloud's particle mean radius, size distribution and error of both. The number of wavelengths for which the imaginary RI is retrieved is defined, plus the correlation length between each value (to control ill-conditioning). The reference wavelength for which the real refractive index is defined and its value is stated, as well as the wavelength at which the extinction cross-section spectrum is normalised to. Then a value of the imaginary refractive index for each wavelength, and its error is stated.

After we have retrieved an imaginary RI spectrum, and have defined a value for the real RI at a certain wavelength, we can use the Kramers-Kronig analysis to reconstruct the entire real RI spectrum (Irwin et al., 2015). Now with the full refractive index spectrum (both real and imaginary) we can use Mie theory to compute all the other values needed (extinction cross-sections, single scattering albedos and phase functions). A standard Gamma distribution is used with the mean radius and variance specified in the parameterisation.

Using a combination of the above profile parameterisations we can create a good representation of the atmosphere. From this we will be able to reproduce our observations using NEMESIS, determining the atmospheric conditions. The inherent flexibility built into NEMESIS means the parameterisation scheme is extensive, requiring trial and error to gain familiarity with the profiles in order to gain the desired results with the best representation of the atmosphere. Through the

parameter scheme, a balance can be struck between the most realistic retrievals, such as a continuous profile, and the speed and simplicity of highly parameterised models, which may lack some of the intricacies of the system. However, this is the dilemma when modelling atmospheres in general, not just the parameterisation schemes of NEMESIS. Now as we present the steps which were undertaken to produce our parameterisation scheme, we hope to present a model which can straddle both of these camps, providing a model which captures most of the complexities of the Jovian system, whilst being simplistic enough to provide computationally moderate usage and the ability to apply to new observations with ease.

Chapter 4

Minnaert Approximation

In this Chapter we will fully introduce the Minnaert approximation which is used to take advantage of the information that limb darkening can provide. Through the application of this technique, we can generate idealised synthetic spectra which enable us to extract the most information from each location, through optimal conditions. This allows us to more rigorously test our observations and resolve some of the issues that linger between comparative works due to degeneracy.

4.1 Introducing the parameterisation

Across the disc of the planet, the radiance is not consistent, and varies according to the location, and properties of the viewing and solar zenith angles. μ_0 is the cosine of the solar zenith angle, which is the angle which the sun makes with a line straight up from the spot which we are looking at, μ_0 is equal to one when the sun is directly above the point on the planet (solar zenith angle is $0°$). The viewing angle is the angle which a line from the observer makes with a line straight up from the spot which we are looking at, μ is the cosine of the viewing angle.

If the clouds can be approximated as Lambertian, where the reflectance was independent of the viewing angle, with light scattering equally in each direction, then we would not expect observations of Jupiter to be limb-darkened. Towards the limb, the solar zenith angle increases, θ, $\mu_0 = \cos(\theta)$.

These are related through the relationship given here,

$$I = \frac{R_L \mu_0 F_0}{\pi D^2} = I_0 \mu_0 \tag{4.1.1}$$

where I is the measured radiance, R_L is the Lambertian reflectivity, μ_0 is the cosine of solar zenith angle, D is the solar distance from the planet, I_0 is the radiance when the sun is directly overhead, and F_0 is the solar irradiance.

Jupiter typically displays a limb-darkened disc due to the cloud structure which means that it cannot be represented through the Lambertian approximation. This is because at some wavelengths the clouds do not appear optically thick, this allows light to penetrate further into the cloud deck and leads to multiple scattering. Due to this, the Lambertian approximation is not appropriate as the scattering is dependent on the viewing angle of the observer. Here we can introduce the Minnaert limb-darkening approximation (Minnaert, 1941).

$$\frac{I}{F} = \left(\frac{I}{F}\right)_0 \mu_0^k \mu^{k-1} \tag{4.1.2}$$

where I/F is reflectance, $(I/F)_0$ is the reflectance when the sun is directly overhead (nadir reflectivity), and k is the limb darkening parameter. A value of $k > 0.5$ represents limb-darkening, and a value of $k < 0.5$ shows limb-brightening. If $k = 1$, the model reverts to the simple Lambertian case. This relation is wavelength-dependent and must be calculated for every wavelength of interest.

Typically Equation 4.1.2 has been used to correct for limb darkening effects on observations in an attempt to remove the effect towards the edge of the disc. However, as introduced in Pérez-Hoyos et al. (2020), this relationship can instead be used to produce synthetic spectra of the desired viewing angles. With this, we can then produce spectra from across the whole disc that can be analysed in the same way, as the dependence on viewing geometries has been removed. Furthermore, extracting dual viewing angle spectra can be done with the same viewing geometries for every latitude which is not possible when a spectrum is directly extracted from an observation.

Extracting a spectrum from a certain region and wavelength, requires us to fit the Minnaert equation

to extract the limb darkening parameters. We first take logarithms of the Minnaert approximation (Equation 4.1.2) to give

$$\ln\left(\frac{I}{F}\right) = \ln\left(\frac{I}{F}\right)_0 + k\ln(\mu_0) + (k-1)\ln(\mu) \tag{4.1.3}$$

which can be rearranged to give

$$\ln\left(\mu\frac{I}{F}\right) = \ln\left(\frac{I}{F}\right)_0 + k\ln(\mu\mu_0) \tag{4.1.4}$$

As we now have a linear relation between $\ln(\mu\frac{I}{F})$ and $\ln(\mu\mu_0)$ we can perform a least-squares fit to extract the Minnaert parameters, which is demonstrated in Figure 4.1.1 for observations at 500nm in a latitude band centred at the equator with a width of 2°. Within this plot, k is the gradient of the slope and I/F_0 is the y-intercept. When we use this method we are assuming that the latitude band which is being plotted is homogeneous so that the radiance of each pixel is only dependent on the viewing angles. This approximation is appropriate when we use a narrow latitude swath on Jupiter to ensure only a single region is included in the analysis, so as to minimise the variation across the region. Jupiter contains small-scale features, such as storms, which are not homogeneous nor symmetrical about the 0° longitude meridian line. For many of these smaller features, they exist over very few pixels and will be negligible in the fitting process. However, for larger storms such as the Great Red Spot (GRS), which have much greater spatial extent, it is necessary to mask these features to ensure that the least-squares fit is not affected by having multiple pixels which differ greatly from their surrounding areas in regards to their radiance. Therefore, when an observation contains the GRS we want to mask it by imposing conditions at 889nm where the GRS is far brighter than its surroundings, as can be seen in Figure 1.2.2. Setting latitude constraints alongside a maximum radiance value creates a mask for the GRS in 889nm which we then use for all wavelengths in the observation datacube.

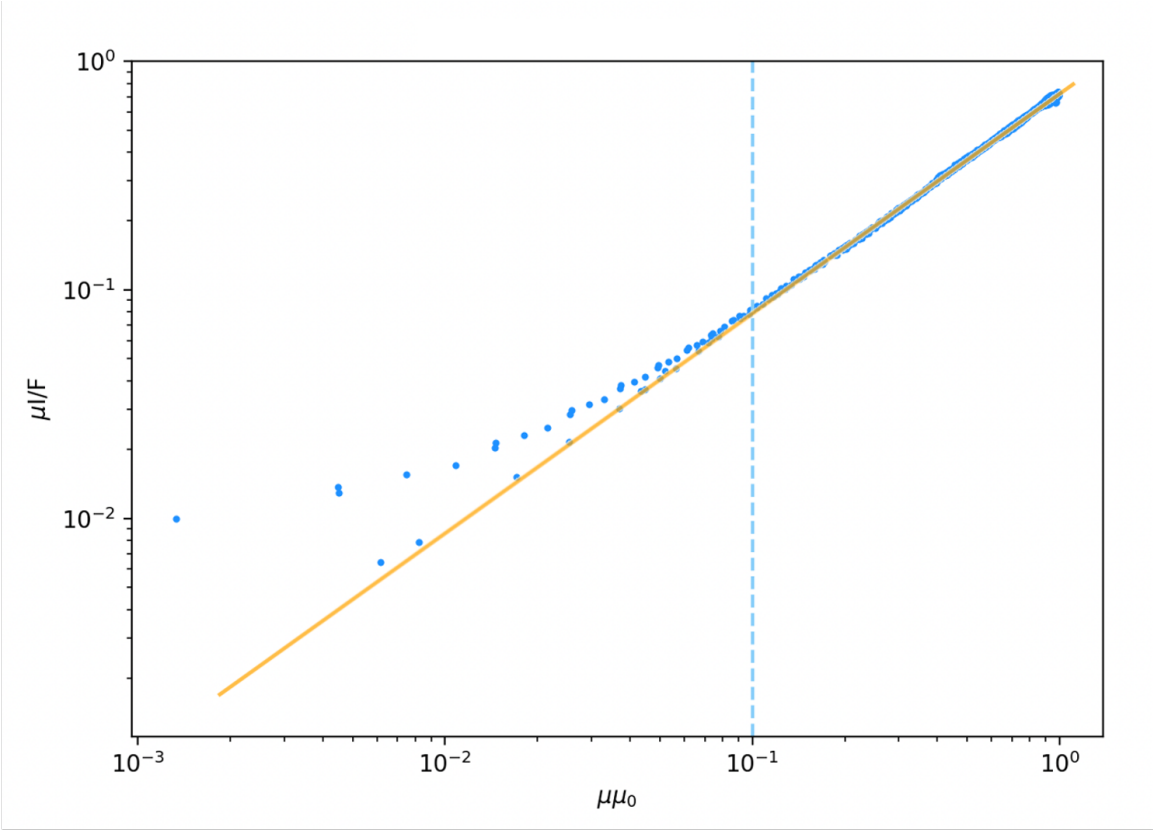


Figure 4.1.1: Observation taken from 0°N for 500nm 23rd September 2023 observation, with $\log(\mu\mu_0)$ plotted against $\log(\mu\frac{I}{F})$, the linear relation between these two values allows us to apply the Minnaert approximation and extract the Minnaert parameters (k=0.96, $(I/F)_0$)=0.889). The cut-off at $\mu\mu_0 <$ 0.1 is shown which removes the edge of the disc, where slight misalignment of the latitude and longitude grid becomes more pronounced at the edges leading to a bifurcation of the relation.

As we extract pixels towards the edge of the disc slight misalignment of the longitude and latitude projections become more pronounced. These extremity points then do not follow the approximation and lead to a bifurcation of the $\ln(\mu\frac{I}{F})$ and $\ln(\mu\mu_0)$ relation and need to be excluded when calculating the fits. In addition at the very edge of the disc, we have mixing with space due to the finite size of the instrument point spread function which also needs to be excluded. To do this only points with $\log(\mu\mu_0)$ greater than 0.1 are used to calculate the fit, ensuring that we do not include those measurements on the very edge of the disc, as can be seen in Figure 4.1.1. With the fit calculated, we can extract the Minnaert parameters, k and $(\frac{I}{F})_0$ for the particular region and wavelength. This is then repeated for every wavelength in the observation datacube, as well as for the latitudes required.

We can now recreate radiance values for any viewing geometries required by inserting the extracted Minnaert parameters into Equation 4.1.2 along with the desired viewing and solar zenith angles.

When extracting the spectra we have to set the error of the associated spectrum. We now have a combination of the observational error and error associated with the fitting of the Minnaert approximation but we have reduced random error values due to the use of multiple pixels in the fitting, creating small error values. When fitting spectra with NEMESIS we want to retrieve a final χ^2/n values of approximately 1 for all retrievals. This ensures we set errors for the retrieved parameter values which are appropriate for the spectral fit. Setting the errors to be 1/50 of the maximum radiance value within a 50nm range, was found to create this balance in our retrievals (and in other works using the Minnaert approximation (Irwin et al., 2022, 2023; James et al., 2023).

4.1.1 Advantages to the Minnaert approximation

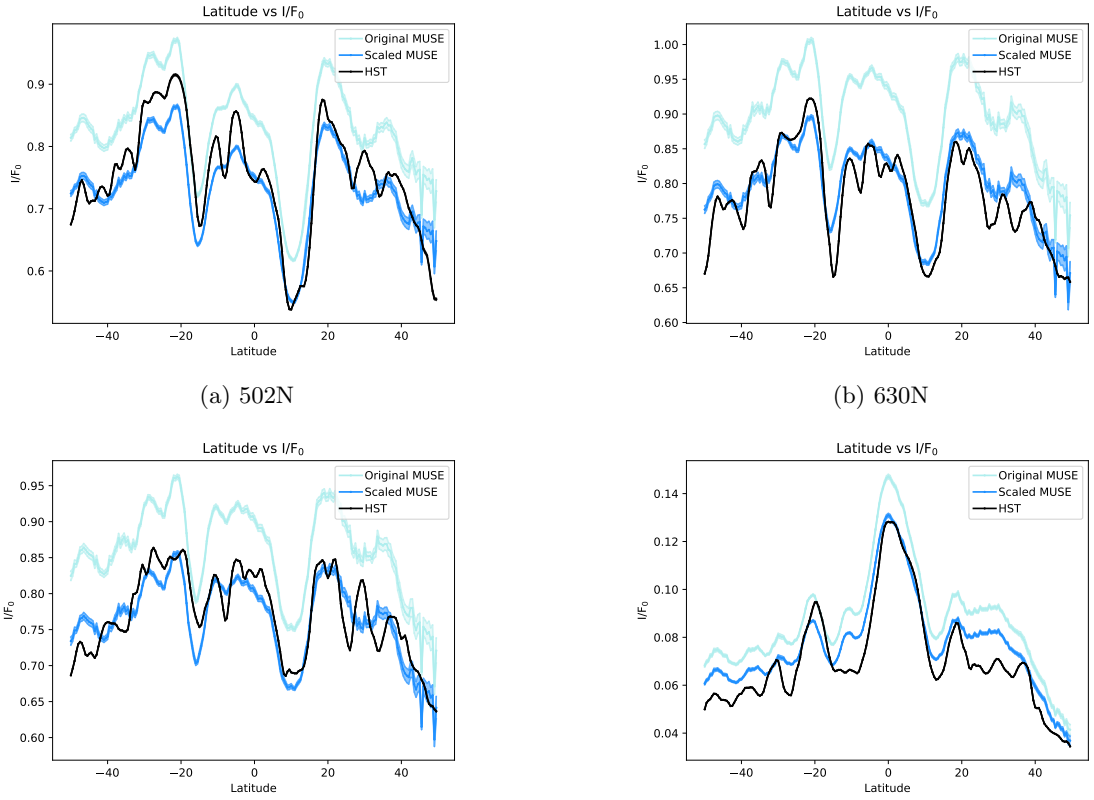
The ability to define the observer's viewing angle, μ, when producing synthetic spectra, is one of the key strengths of this technique as we can choose angles which are fulfil our goals whilst also being fast to compute. Once we have found the Minnaert parameters we can construct our spectrum for any solar and viewing angles which we desire by setting μ and μ_0. By doing this, we are able to customise the reconstructed spectrum so that it is most advantageous for our uses. In this thesis, we want to better constrain our atmospheric model by considering limb darkening effects. We are able to do this by simultaneously fitting to two viewing angles. We first choose the nadir angle ($0.0°$) as it is the fastest geometry to compute with the Matrix-Operator multiple-scattering code. To incorporate the limb darkening we have to compromise for speed, accuracy and extracted information. Angles closer to the nadir are quicker to compute but contain less limb darkening information. We can increase the accuracy by choosing an angle used in the Guass-Lobatto zenith angle quadrature scheme of the Matrix-Operator model, to avoid any errors arising from interpolating between calculation zenith angles (Irwin et al., 2021). The other main advantage is the reduced random error in the observation when using the synthetic spectra, as it is produced from multiple pixels across each latitude band and then reconstructed through a fit. Therefore, the random error present through our observations is reduced and we can expect more consistent errors across both wavelength and location.

The Gauss-Lobatto quadrature scheme uses five zenith angles; 0.0000, 21.1420, 42.3729, 61.4500, 80.4866, to then linearly interpolates the given zenith angle from the observation between the two closest angles in log(zenith angle) space (Irwin et al., 2021). Unless the given zenith angle is too close to the edge of the disc, this method can reproduce any angle on the disc, however, there are some disadvantages to the method. As the angle has to be interpolated, two sets of calculations have to be done from the two closest zenith angles. The interpolation between these points can lead to errors, especially at larger zenith angles. The azimuth integration is done with Fourier decomposition. At points towards the disc edge, a larger number of Fourier components are needed to calculate these larger viewing angles, slowing down the retrieval. By creating synthetic spectra we can ensure that the viewing geometry aligns with the schemes within NEMESIS, removing the need to interpolate between points. Now each spectrum will align exactly with the Guass-Lobatto scheme used by NEMESIS and will remove errors associated with these approximations. Therefore, when producing the two spectra for each latitude used in this work we use the same viewing and solar zenith angles for each spectrum, one extracted for 0.00° and another for 61.45°, both spectra have an azimuth angle of 180°. We have decided on the use of 61.45° as it incorporates characteristics of limb darkening into the retrievals by being towards the limb, without slowing down computational time overly. The use of an additional viewing angle (42.37°) was considered. Additional constraint of a third angle is provided by the fitting of another set of spectral points in the retrievals but this was not found to be beneficial enough compared to the longer computing time (∼50% longer) required for three angle retrievals. As it did not provide further limb darkening information than the 61.45° viewing angle alone, it was decided that the additional time was not worth this minimal additional constraint. Alone the 42.37° could not capture as much limb darkening information as the 61.45° spectrum if used for two angle retrievals. Therefore, just the 0.00° and 61.45° angles were used for retrievals.

4.2 Calibration with HST data

When we are fitting to spectra extracted from our observations from VLT/MUSE we want to ensure that the radiance differences are due to atmospheric changes of Jupiter rather than observational

differences such as instrument calibration and observation processing. Therefore, we must calibrate our observations against observations which have been extremely well-calibrated themselves. For this purpose, we use HST/WFC3 observations.



(a) 502N

(b) 630N

(c) 658N

(d) FQ889N

Figure 4.2.1: Calibration of a MUSE observation taken on 9$^{\text{th}}$ April 2018, compared against HST observations from 17$^{\text{th}}$ April 2018. This figure shows a comparison of filter averaged data for the F502N, F630N, F658N and FQ889N filters from HST with the MUSE data averaged using the filter profile, both with (dark blue) and without (light blue) the calibration factor of 0.89 used for this observation.

The OPAL programme (Simon et al., 2015), regularly records global maps of Jupiter for the purpose of creating a time series of observations which can be used to document how Jupiter changes year on year. This comparative goal of the OPAL data means that it must be well photometrically calibrated to ensure changes observed are due to physical changes in Jupiter and not observational differences. Simon et al. (2015) go beyond the standard Hubble processing, to ensure that introduced photometric

error, due to fringing from detector effects, is corrected for. Filters which include wavelengths affected by methane absorption, such as FQ889N, require additional correction beyond the standard flat fields corrections for other filters, instead requiring flat fields generated from the Karkoschka (1998) disc-averaged reflectance spectrum. Due to this additional photometric calibration of the OPAL programme we can assume that it can be used as a comparative source in which to check the calibration of our own observations. The yearly observations allows us to calibrate our observations against theirs to normalise the observed radiances minimising any differences in radiance due to observational effects rather than physical changes in Jupiter.

Observation	Scaling Term
9^{th} April 2018	0.89
14^{th} April 2018 *	0.89
11^{th} July 2019	0.89
10^{th} April 2020	1.0
8^{th} November 2021	0.84
29^{th} June 2022 *	0.84
1^{st} July 2022	0.84
30^{th} July 2022 *	0.84
19^{th} September 2022 *	0.84
23^{rd} November 2023	0.82

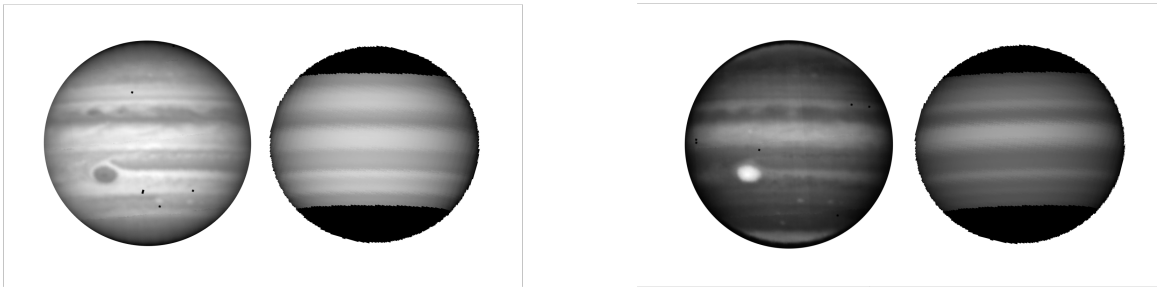
Table 4.2.1: Observation dates with the calibration scale factor required to match HST observations taken at a similar time to counteract observation variability and ensure that I/F_0 values are realistic. * observations used for the GRS Minnaert approximations.

HST/WFC3 uses filters for its observations, and so to compare observations we must filter average the spectrally resolved observations from VLT/MUSE with the filter responses which match those of HST. For each filter we can then extract the radiance for each latitude for both observations to compare the radiances from each observation. We compare $(\frac{I}{F})_0$ for both to negate any angle dependence of the radiance introduced by observational geometries. As found by Braude (2019) some observations taken using VLT/MUSE have greater radiances which can lead to values of $(\frac{I}{F})_0$ greater than one (a physical impossibility). Figure 4.2.1 shows the differing $(\frac{I}{F})_0$ between 9^{th} April 2018 MUSE observations and 17^{th} April 2018 HST observations. Therefore, a scale factor term is calculated for the VLT/MUSE observations to ensure that the values are physically realistic, and close to the well calibrated HST/OPAL observations. We compare for all HST filters which reside in the MUSE spectral range, and ensure that a similar correction value is needed for all filters. The

calculated scale factors are listed in Table 4.2.1 for all observations used in this work. For Figure 4.2.1, a scale factor of 0.89 was used for the 2018 datacube.

4.3 Extracting spectra

Once the MUSE observations have been scaled to align with the HST OPAL observations we are able to proceed with extracting spectra for the regions of interest on the disc. As we are interested in sampling across the disc to discern how the retrieved values vary latitudinally we want to use Nyquist sampling (having overlapping samples by sampling twice over the sample length, e.g., sampling every 1° with a 2° latitude band) to ensure that the trends retrieved are continuous across the disc. Therefore we use spacing which is smaller than the width of the latitude band which is being selected for the Minnaert analysis. When extracting spectra our latitude spacing varies depending on how many points we wish to investigate across the disc, the smallest latitude resolution used in this work was 2° latitude bands spaced every 1° for the final results presented in Chapter 6. Wider bands of width 10°, spaced every 5° were used for initial investigatory work (e.g., Section 5.2.1) to reduce the computational load whilst still sampling the entire disc.



(a) 620nm (b) 889nm

Figure 4.3.1: Reconstructed images of Jupiter made using the calculated $(\frac{I}{F})_0$ and k parameter values extracted from the Minnaert approximation, shown for an observation taken on 9$^{\text{th}}$ April 2018 at 620nm and 889nm.

With all Minnaert coefficients for a particular wavelength at each latitude band calculated we are able to produce a reconstructed image of Jupiter. By using the measured values of μ and μ_0 from the real observation, the modelled values of $(\frac{I}{F})$ can be calculated across the disc for each wavelength. In Figure 4.3.1 this is done for 620nm and 889nm. As it can be seen the general zonally-averaged

reconstructed disc is able to reproduce the appearance of the observed disc well, reproducing the reflectivity dependence on viewing angle and latitude. Individual features have been lost due to either masking or the smoothing of the reproduced disc due to the approximation that each latitude band being reproduced is homogeneous. However, the similar radiances retrieved and limb darkening on the reconstructed disc display the ability of the Minnaert technique to successfully reproduce the Jovian disc.

4.3.1 Dual viewing angle GRS spectra

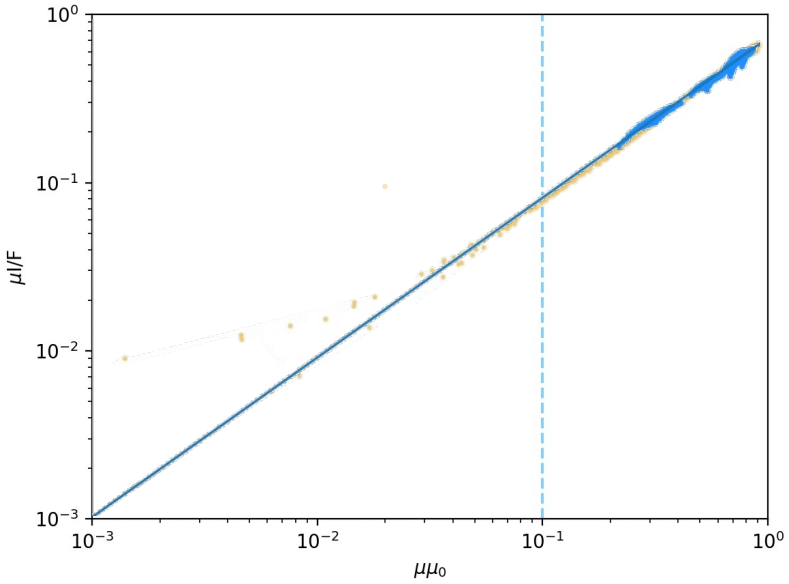
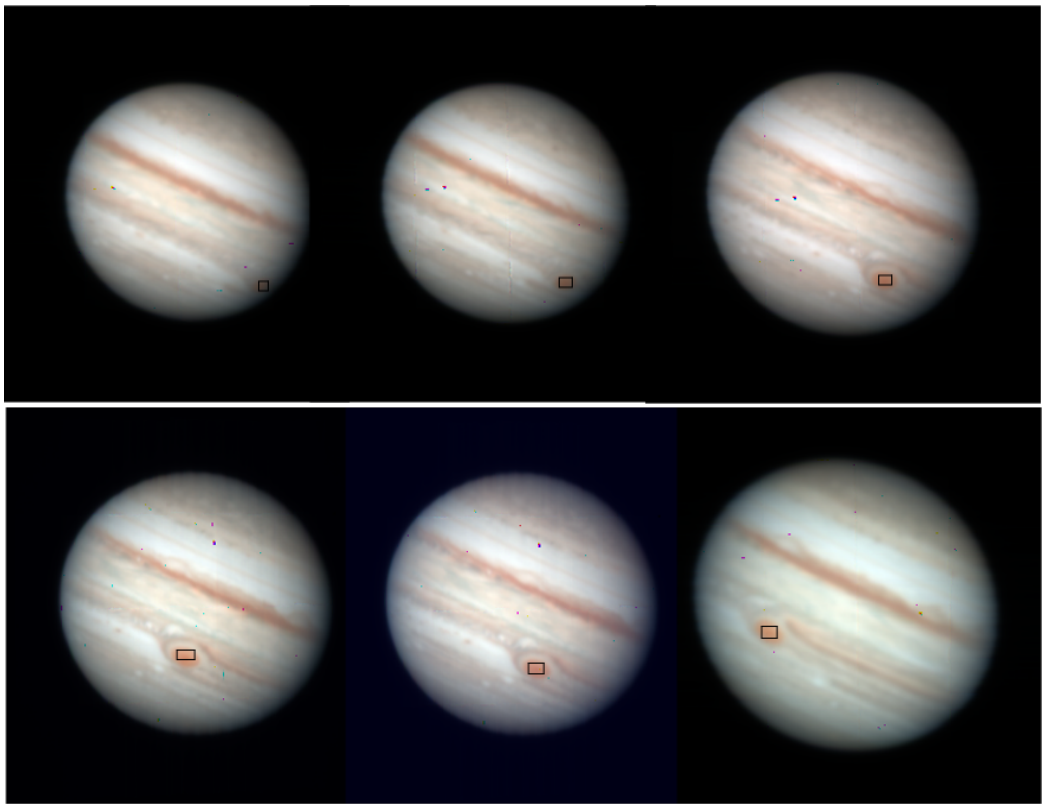


Figure 4.3.2: Minnaert fit applied (k=0.94, $(I/F)_0$=0.667) for six 2022 observations (29/06, 01/07, three on 30/07, 19/09 to span a wide range of GRS locations) where only a box around the GRS is extracted, these data points are shown in blue for 0.7μm, the yellow points are for the 0° latitude band for comparison.

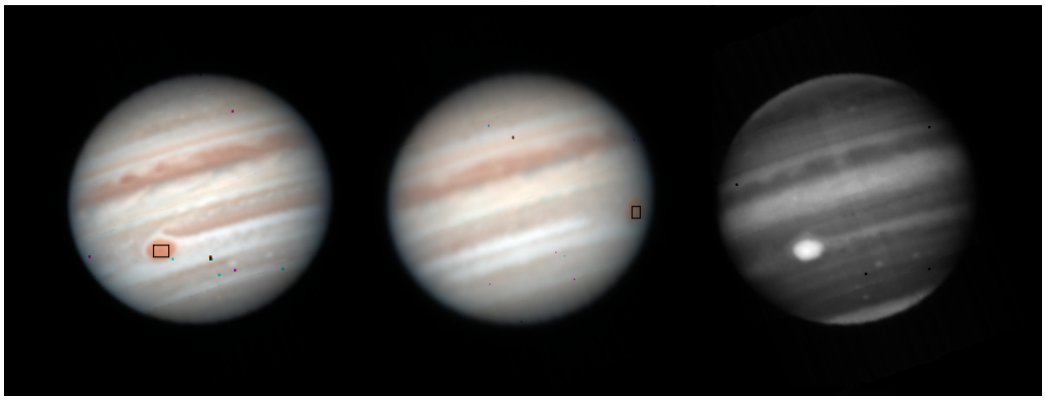
Due to the advantages that the Minnaert method brings it is beneficial to apply it also to the GRS to extract dual viewing angle spectra. The GRS has a limited spatial extent, only covering $\sim 15°$ longitude. A single observation cannot provide the range of values needed to fit to the Minnaert approximation, and would introduce a large amount of error through the fitting of the linear relation to extract the parameters. Instead if we are able to increase the range of viewing angles that are

being fitted, we can have more accuracy when calculating the Minnaert parameters, creating a more realistic spectrum for both viewing angles. This can be done by using multiple observations of the GRS where it is located at different positions across the disc. We select the central region of the GRS to minimise any radiance differences caused by different physical conditions. Due to the observations being separated in time we have to assume that over a short period that there has been no variation in the radiance of Jupiter due to physical changes. Through the use of multiple observations we have a greater range of points to fit, which can be seen in Figure 4.3.2, which is a combination of six observations from 2022, and so we can be more confident in the extracted Minnaert parameters.

Due to the short execution time of the observation blocks (approximately 30 minutes), the rotation of Jupiter during this time does not provide enough variation in the viewing angle between the first and last exposure to attempt this process for a single observation block. Instead we have to use observations taken within a few months of each other (typically same observation periods). For older observation blocks we had designed observations to complement the Juno Perijoves alone. This led to a range of target longitudes, both with and without the GRS. More recent observing blocks ensured that at least one set of observations were targeted on the GRS, which developed into multiple GRS observations to ensure a range of viewing angles to use the Minnaert method. From this we can often have at least two observations which are close in date, often less than one month apart, where the GRS is present on the disc at different viewing angles, as shown in Figure 4.3.3. The pixels extracted from within the central GRS are shown in Figure 4.3.2, and are used when fitting for the Minnaert parameters. We have to consider the structure of the GRS as the high spatial resolution of our observations allows us to differentiate between different parts of the GRS. Therefore, we need to ensure that we are extracting pixels which are more likely to consist of the same vertical structure of the GRS.



(a) 2022



(b) 2018

Figure 4.3.3: Observations which include the GRS across multiple viewing angles. Figure a) shows observations from 2022 (Left to Right, Top – 29/06, 01/07, 30/07, 30/07, 19/09) given as RGB images (R-675nm G-530nm B-480nm) and those from 2018 (left – 9th April RGB, centre – 14th April RGB, right — 9th April 2018, 889nm). The black box indicates the pixels extracted to create spectra using the Minnaert method giving reconstructed spectra of the GRS with two desired viewing angles.

4.4 Testing previous works with the Minnaert Fit

As discussed in Section 1.5, there are several previous works which creates good fits to the observations of Jupiter used in their work. However, attempts to apply certain models to new data sets have not always been as successful. Using the Minnaert method to extract dual viewing angle spectra allows us to test previous models with a more robust observational constraint. Now that we have extracted spectra, we wanted to test these previous models to determine whether they also provided a good fit when fitting two viewing angles simultaneously.

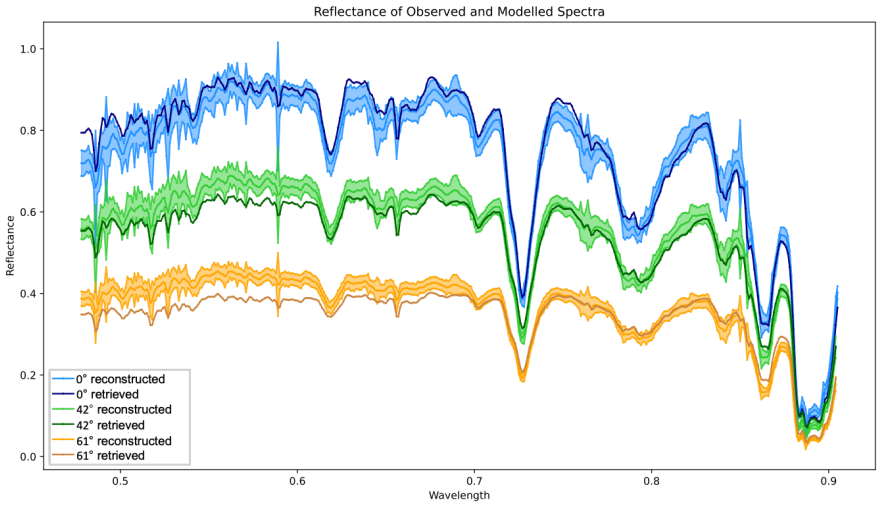


Figure 4.4.1: Braude et al. (2020) parameterisation scheme applied to three viewing angle spectra extracted from the same observation as the original work to the Minnaert-reconstructed MUSE spectra from 2018 at the equator.

Using the dual viewing angle spectra produced from the same 9th April 2018 datacube as used in Braude et al. (2020) we were unable to fit to both angles simultaneously using their model, even when allowing the aerosol profile to vary, as shown in Figure 4.4.1 and in Figure 4.4.2 for the varying profile. We found that the Braude model could successfully reproduce the 0.0° viewing angle spectrum, as found in Braude et al. (2020), but it provided a poorer fit to the 61.45° viewing angle. Even when the parameterisation scheme was allowed to vary, in an attempt to improve the fit, the model was unable to simultaneously fit to two viewing angles. The inability of the Braude model to reproduce the blue slope at higher viewing angles, plus the decrease in brightness across a wide swath of the wavelength

range displays its unsuitability to reproduce these observations and possible deviation from the true atmospheric profile on Jupiter. The inability to fit to the higher viewing angles suggests that the Braude model is unable to capture the limb darkening effects, which this viewing angle better captures, and highlights the weaknesses in the vertical cloud profile which the dual viewing angle method is more sensitive to. The work of Braude et al. (2020) only incorporated higher viewing angle spectra into their work when formulating the chromophore properties: elsewhere it extracted a spectrum from near the central meridian for each region. Therefore, we begin to question the similarities between the vertical cloud profile of the Braude model compared to true conditions.

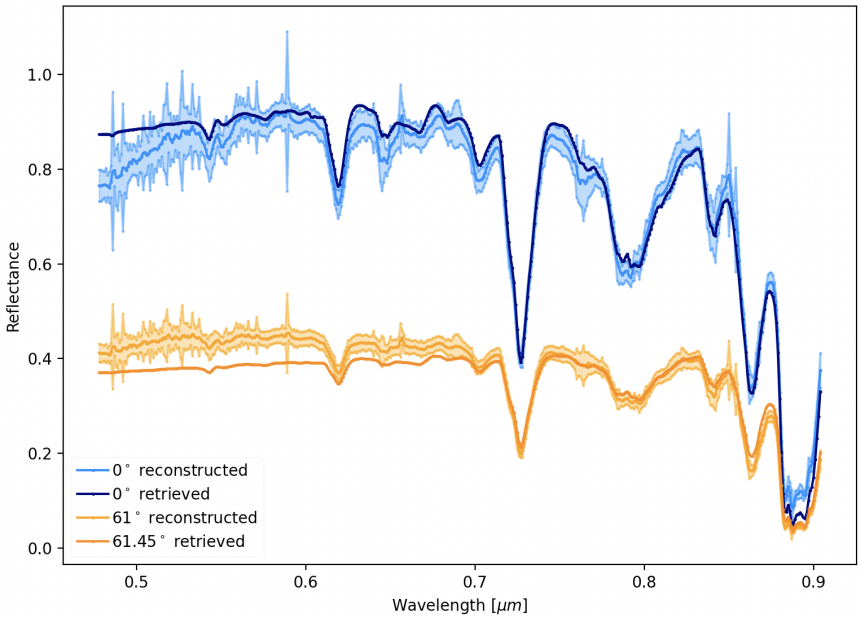
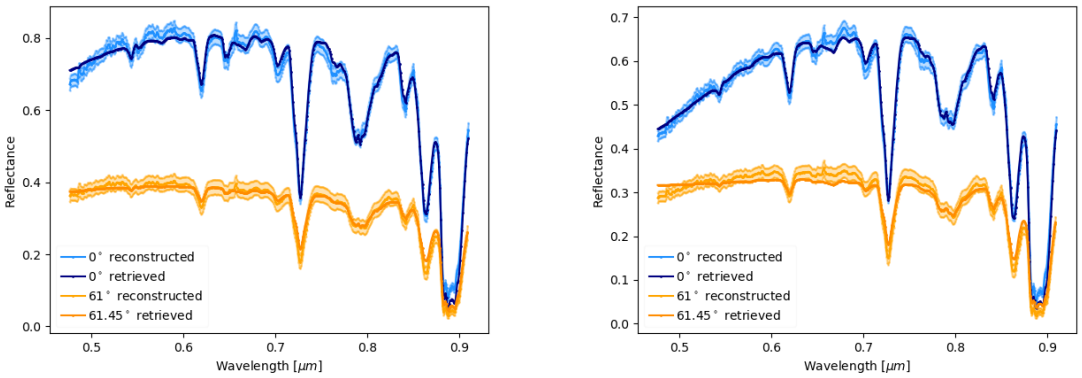


Figure 4.4.2: Braude et al. (2020) parameterisation scheme applied, with the aerosol profile allowed to vary to try and improve on the spectral fit in Figure 4.4.1. However, the model is still unable to simultaneously fit to both viewing angles.

We also tested the Crème Brûlée model of Sromovsky et al. (2017); Baines et al. (2019) to determine how capable it was of fitting dual viewing angle spectra. Although higher viewing angles were fitted in previous literature, it was not done simultaneously, nor were higher viewing angles used to produce the model. We found for the 0° viewing angle, that the Crème Brûlée model was unable to fit the blue slope effectively, whereas at 10°N it was the larger viewing angle of 61.45° the Crème Brûlée

model failed to reproduce our observations. The error and spectral resolution of our VLT/MUSE spectra is smaller than the VIMS spectra used by Baines et al. (2019); Sromovsky et al. (2017).



(a) 0°N (b) 10°N

Figure 4.4.3: Retrievals on the Minnaert-reconstructed MUSE spectra from 2018 using the Crème Brûlée parameterisation of Sromovsky et al. (2017), for both 0°N and 10°N.

The Crème Brûlée model was able to adapt to the dual viewing angle better than the Braude et al. (2020) model, however, neither results are able to simultaneously fit both viewing angles. The inability of both of these previous models to match the observed MUSE spectra whilst simultaneously fitting both viewing angles raises the question of whether these models are good representations of the vertical cloud profiles on Jupiter. The constraint provided by the additional viewing angle displays how we can begin to distinguish between different models. As we develop a model which combines dual viewing angle constraint throughout we can hope to produce a model which is able to adapt to different locations and observations more readily than previous models discussed here.

Chapter 5

Parameterising Jupiter's clouds

In this Chapter we will detail the steps which were taken to create an atmospheric model that was able to reproduce our dual viewing angle observations. Due to the degenerate nature of the parameter space, we wanted to pre-determine parameters before undertaking a full atmospheric retrieval using NEMESIS. To do this, we have to introduce new methods to extract information from the spectrum to determine values to fix our parameters to, before undertaking a full retrieval. The additional constraint of the dual viewing angle, extracted using the Minnaert method, allows us to have more vertical information contained in our results.

As introduced in Section 1.5 there is a huge amount of variety within current models of Jupiter's troposphere/lower stratosphere. These models have a huge range of parameters which are able to vary, allowing them to match observations. However, they are then very complex to adapt to new regions and/or new observations. In this work we have set out to simplify the atmospheric model whilst maintaining the ability to reproduce observations with the additional dual angle constraint. By testing a simpler model we are able to more easily adapt to new observations, and more easily note how visible changes transfer to model variations. From this we can establish how tropospheric clouds vary across the observation range.

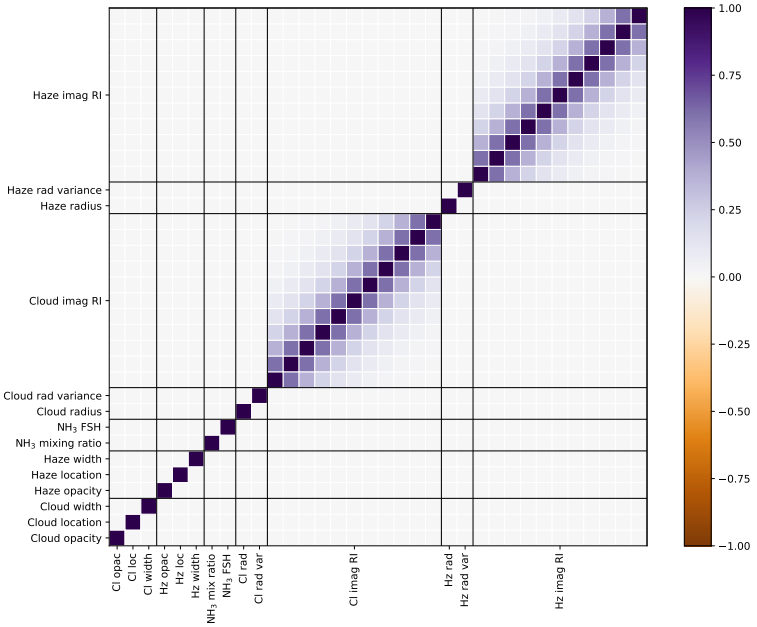
There is a limit to what parameters we can predetermine, and due to the variance between regions

of the atmosphere we still need some variable parameters to capture the characteristics of the atmosphere across the disc. We have minimal *a priori* values which are known in enough confidence to fix, so we instead need to infer them using methods detailed below. We can use radiative transfer models for this without running a retrieval to determine all parameters of the atmosphere. Instead we need to see what can be extracted from observations without strong dependence or degeneracy with other parameters. This then allows parameters to be fixed reducing the total degenerate pairs in the final retrievals, which makes the degeneracy easier to manage for the parameter space.

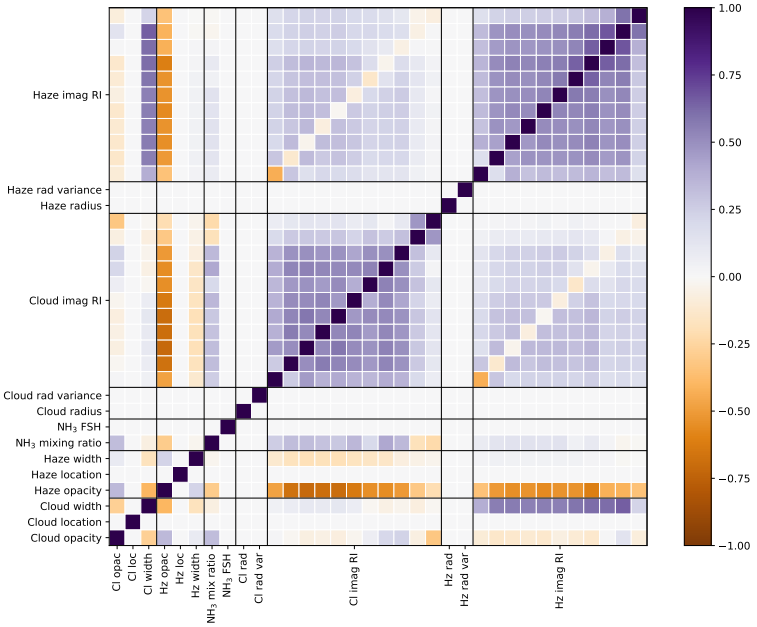
We are able to identify some of the degenerate pairs in the parameter space using the covariance matrices which are calculated for the *a priori* input and the calculated output. From these matrices we are able to see which parameters are linked and have the strongest correlation. Figure 5.1.1 show the covariance matrices for a retrieval where some parameters have been fixed (demonstrated through 0.0 values for all other parameters in the retrieved covariance matrix) such as cloud and haze radii and radii variance, but both imaginary refractive indices have been allowed to vary. From Figure 5.1.1b we can see from the variable parameters that these parameters have correlation with most other parameters and will impact their retrieved values. This huge amount of correlation which is shown between the parameters, is the degenerate nature which we are trying to remove from our parameter space.

5.1 Why is a simplified model needed?

We needed to identify a simpler model as initial work applying dual viewing angle spectra to the work of Braude et al. (2020) did not produce a satisfactory spectral fit. The inability to fit to the more constraining dual viewing angle spectra, extracted from the same observation in 2018, indicated that there was inaccuracy within the model when scrutinised more. Therefore, we began to explore the parameter space in the hope of being able to find a combination which was able to better represent the dual viewing angle spectra. As the Braude et al. (2020) profile had almost no parameters fixed apart from refractive indices it made it very difficult to determine values for the model which would improve the spectral fit.



(a) *A priori* covariance matrix



(b) Retrieved covariance matrix

Figure 5.1.1: Top panel is the *a priori* covariance matrix with the bottom panel being the retrieved covariance matrix. Both matrices are normalised so that the diagonal elements are 1.0. For this retrieval both the cloud and haze imaginary RI values are allowed to vary. For the *a priori* we see correlation away from the diagonal for the imaginary refractive index values for both the cloud and haze as we have specified a correlation length which correlates the parameters. Where tiles are non zero in Figure 5.1.1b it is demonstrating that there is a correlation between these parameters.

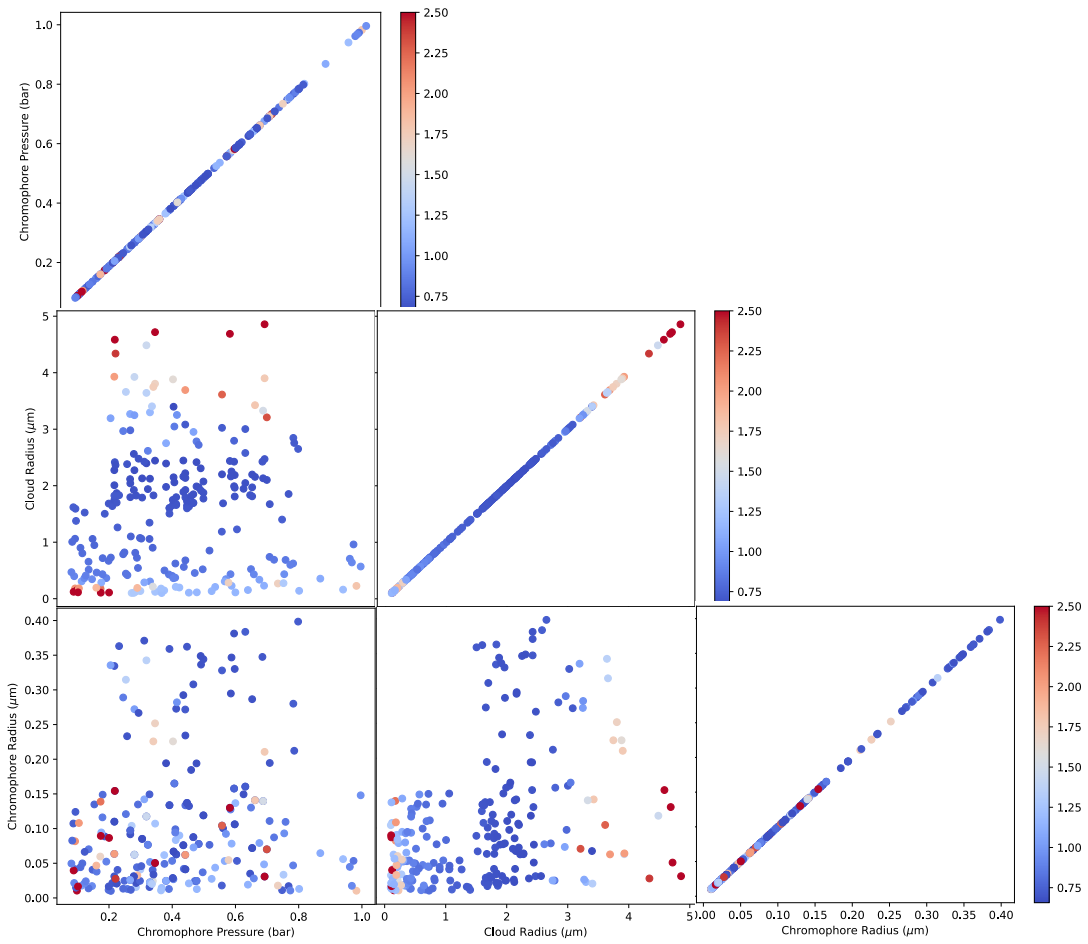


Figure 5.1.2: Parameter search for Braude et al. (2020) model, varying Chromophore and cloud radii, as well as Chromophore peak pressure, for dual viewing angle spectra at 0.0° and 61.45°.

We focused on adjusting values for the chromophore, through peak pressure of the Gaussian profile (residing within the main cloud layer), and the radii of both cloud and chromophore particles. We undertook a grid search for these parameters, assigning random values within a range for each parameter and compared how well each set was able to reproduce its observation, using χ^2/n_y as a measure of the goodness of fit. However, we found a large amount of degeneracy within this parameter space, which can be seen in Figure 5.1.2 as there is no clear relation between parameter values and a reduced χ^2/n_y value. The sampling of the parameter space is a combination of two parameter searches with different limits for the parameter searches, hence the lack of sampling in

some of the edges of the parameter spaces. Due to the lack of clear trend in each space it was decided unnecessary to expand the search to these areas.

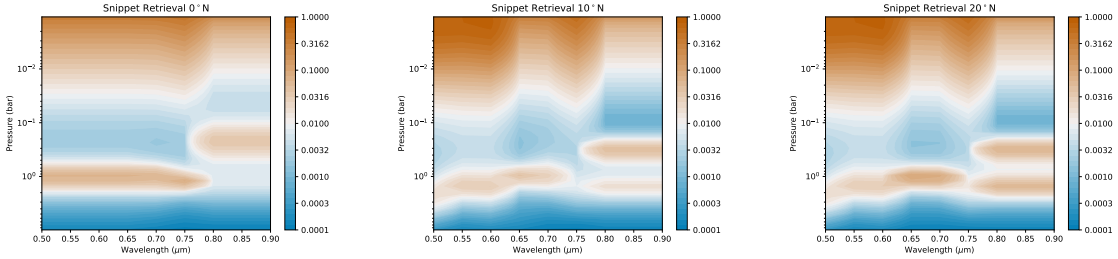
Due to the large number of variables within this model and the inability to begin to see a way to improve the model's fits for the dual viewing angles, it was concluded that simplified model which had fewer variable parameters was needed. The extra constraint which the dual viewing angle spectra provides will allow for this model to be developed with more rigour.

5.2 Determining the vertical location of clouds

We are able to determine information about the cloud profile by assessing where we are sensitive to aerosol in our vertical profile. This removes any assumptions introduced through *a priori* estimates. When we undertake this method we need to be aware which altitude in the atmosphere we are sensitive to at each wavelength, which is shown in Figure 2.5.4: we need to be most aware that above $0.8\mu m$ that we are highly sensitive higher in the atmosphere, responding mostly to haze rather than the main cloud layer. However, most other wavelengths are able to reach further down in the atmosphere, reaching the main cloud layer. Therefore, across our MUSE wavelengths we should be able to determine the vertical location in the atmosphere to which we are sensitive to cloud and where we should set the peak of our vertical cloud location to be.

5.2.1 Snippet and Bracket Methods

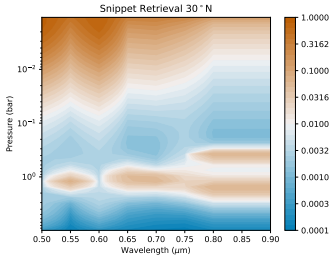
To determine the location of the cloud layers in our vertical profile we undertake 'Snippet' and 'Bracket' retrievals, as outlined in Irwin et al. (2022). In this method we identify regions of sensitivity through the Snippet retrievals and then consolidate the results with the assurance of the Bracket method.



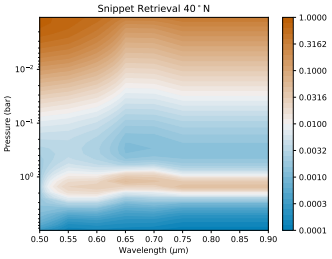
(a) 0°N

(b) 10°N

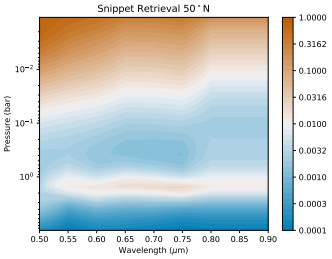
(c) 20°N



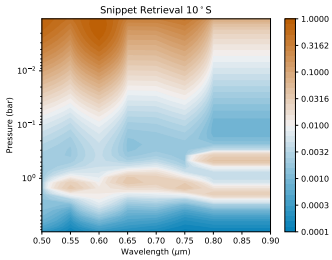
(d) 30°N



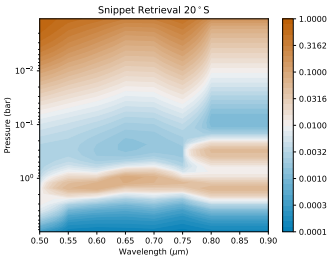
(e) 40°N



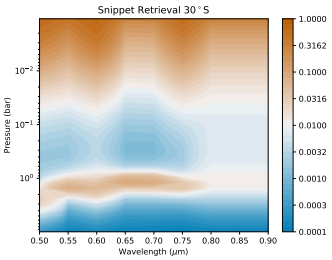
(f) 50°N



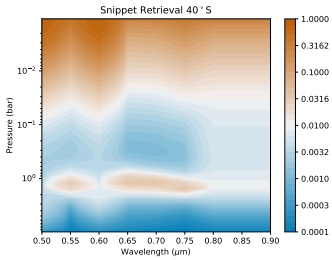
(g) 10°S



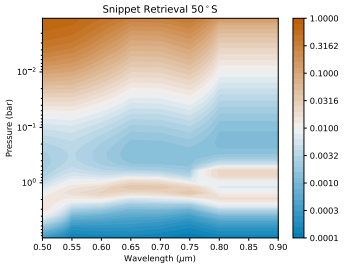
(h) 20°S



(i) 30°S



(j) 40°S



(k) 50°S

Figure 5.2.1: Snippet retrievals for 50°N - 50°S, regions where the aerosol profile has deviated away from the *a priori* values we can infer that we are sensitive to a cloud at this level. At longer wavelengths, where methane absorption becomes strong at 890nm, the Snippet retrievals indicate a second, detached layer of aerosol at lower pressures.

The Snippet technique allows us to remove any predetermined assumptions we have about the Jovian atmosphere to determine information about the aerosol profile. We do this analysis with short wavelength snippets, spanning 100nm at a time with Nyquist sampling every 50nm, covering 500-900nm (the majority of the MUSE wavelength range). We break the wavelength range into snippets as it allows NEMESIS to converge whilst having minimal free parameters. Each wavelength snippet is sensitive to a different pressure level (see Figure 2.5.4), but, most wavelengths are probing deep enough to be able to identify the main cloud layer with expected peak pressures somewhere below 0.5 bar but above 3 bar. This is not the case for wavelengths around 890nm due to the strong methane absorption. Hence the 800-900nm snippet will mostly be sensitive to the haze. We extracted Minnaert analysed spectra in bin widths of 10°, spaced by 10°, for this analysis.

We find the pressure levels of the aerosol by using a continuous profile of specific density (particles/cm^3) and a single particle type with variable imaginary RI (which is assumed to be constant over the wavelength range being considered) and fixed real RI. The aerosol profile has an *a priori* profile with constant number density per cm^{-3}. This leads to an input where the specific density (i.e., particles/gram) is greater at lower pressures than at higher pressures deeper in the atmosphere. A constant particle/gram approach was also trialled and was found to have similar results. For Figure 5.2.1 the scale bar is also the *a priori* profile. For all the wavelength ranges sensitive to the main cloud we converge to a cloud layer around 1.4 bar, as can be seen in Figure 5.2.1. At the longer wavelengths where we are sensitive to higher altitudes as well, two cloud layers are retrieved indicating a detached haze layer peaking around 0.2 – 0.3 bar. As we have no prior assumptions about the aerosol column, the consistent location retrieved for each latitude provides confidence for locations to be considered for aerosol layers.

Although the cloud layer is generally found to peak at around 1.4 bar at all latitudes, as seen in Figure 5.2.2 for the 0.75μm snippet, there is some variance in the width and exact peak pressure of the cloud. We are able to adapt to these variations by how we parametrise the cloud layers in our main retrieval model (which will be discussed later in the Chapter), allowing us to fix the peak of the main cloud layer at 1.4 bar and the haze at 0.2 bar and still be able to represent the whole disc

through variable cloud widths.

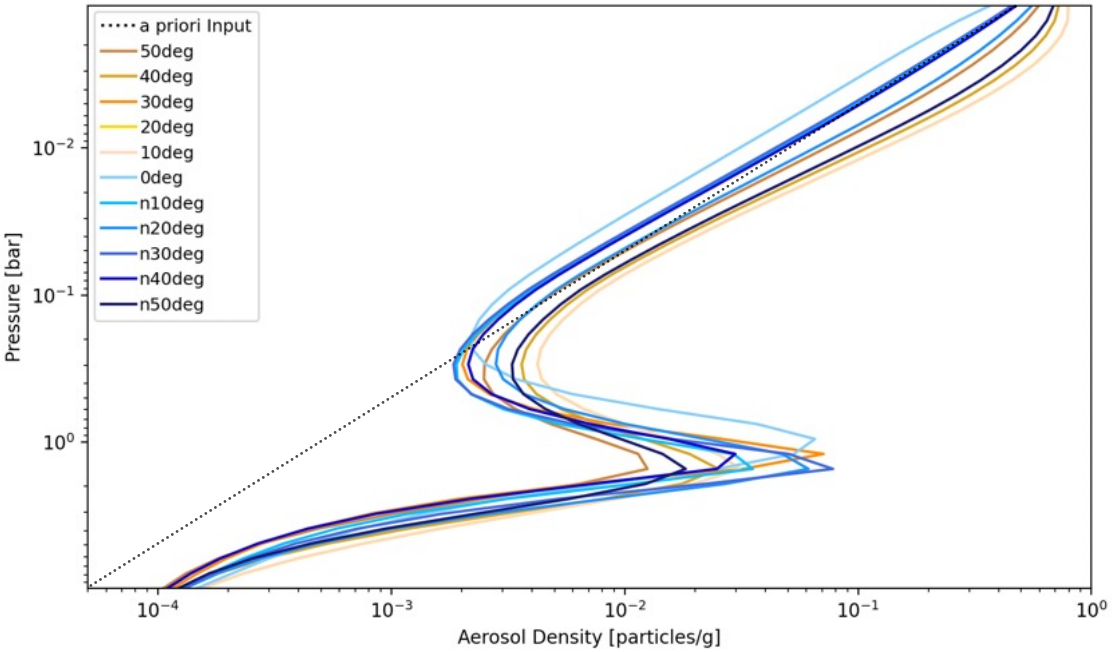


Figure 5.2.2: Snippet retrieval for $0.5 - 0.6\mu m$ at 10° latitude intervals from 50°N to 50°S, converging away from the *a priori* values (set to a constant specific density of 0.005g/cm^3 at 1 bar for the whole pressure column. The profiles are seen to diverge away from the *a priori* input where there is sensitivity to aerosol opacity.

Through the snippet method we have been able to determine the location of the cloud layer without the associated degeneracy which is often involved between this parameter and others within models. Therefore, we have been able to predetermine a parameter which will reduce the solution space and reduce degenerate pairings in the work, allowing to focus on remaining degenerate pairs. To confirm the results found through the Snippet method we also use the 'Bracket' analysis to ensure that this result is robust. The aim of this method is to check that the same result is retrieved with different starting *a priori* inputs to ensure that the retrieved result is not being affected by the starting values. A range of *a priori* specific densities were selected ranging from $0.125 - 5 \times 10^{-4} g/cm^3$. The panels in Figure 5.2.3 show the convergence of these results for different starting *a priori*, giving more confidence in the results derived by the Snippet method.

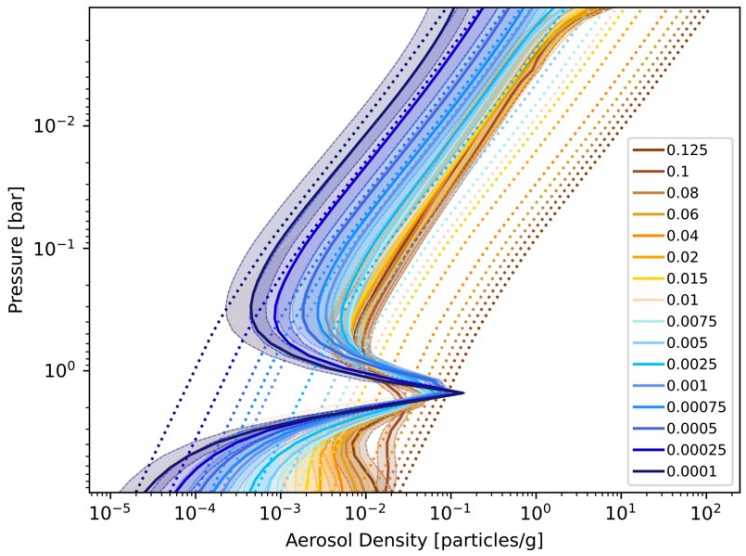


Figure 5.2.3: Bracket retrievals for the $0.5 - 0.6\mu m$ snippet, with a range of specific density [particles/cm^3] *a priori* profiles set at the 1 bar level for 0°N, each profile converges away from their *a priori* where they are sensitive to the aerosol profile.

5.3 Investigation of the further parameter space

We now need to explore the rest of the parameter space of the aerosol profile to create a full model for the Jovian tropospheric/stratospheric cloud model. Having identified the vertical location and number of the aerosol layers needed through 'Snippet' analysis, we then aim to reduce the number of free parameters in the final model to create a simplified parameterisation with less degenerate pairs remaining. To do this we have to gradually build up our knowledge by running a series of parameter searches to find the value which minimises the χ^2/n value and improves the spectral fit, whilst keeping other parameters fixed. As we fix one parameter we then move onto others which need to be determined. Due to the degenerate nature of the parameter space we then have to revisit previously fixed parameters to ensure that their values are still the best fit to the spectra. Due to the huge number of combinations this process could go on indefinitely, at a certain point we have to conclude that the parameter values chosen are a good representation of the parameter space and proceed to other aspects of the model.

5.3.1 Shape of aerosol layers

Whilst determining the cloud location from the Snippet retrievals is extremely helpful, it does not provide all the necessary information to conclude the shape and structure of both cloud layers confidently. Therefore, an investigation into the optimal shape of the vertical cloud profile needed to be done. We want to parametrise the clouds, rather than use continuous profiles as this reduces the number of retrieved values and reduces the complexity of the model making it easier to adapt to new observations. For the main cloud layer the profiles retrieved from the snippet retrievals were more indicative of a Gaussian shape cloud, with a peak opacity at the centre of the cloud which tails off above and below the peak pressure level, set to be 1.38 bar, as from the Snippet analysis. The haze was found to peak around 0.2 bar but the shape of the haze profile was not clear from the Snippet retrieval.

Determining the shape of the haze vertical profile was more challenging due to the more limited information which could be drawn from the Snippet analysis from just a single wavelength region near 890 nm sensitive to the higher altitude haze. A free profile was used to see if the retrievals tended to a certain shape which could be parameterised. Multiple profiles were retrieved using this method, unable to differentiate between a Gaussian profile or a increasing specific density profile controlled through a scale height. Measures of the goodness of fit, χ^2/n, had limited sensitivity between these different profiles.

Instead we were able to determine the profile of the haze layer by looking at the rate of change of reflectivity with height as this acts as a proxy for aerosol density. We use a narrow wavelength range of 820 – 910nm so that the haze properties are consistent across it, but we are also sensitive to both lower pressures around the haze layer as well as deeper pressure levels around the lower level cloud, to capture the full vertical structure. We calculate the two-way transmission spectra $T(\lambda)$, for all of the pressure levels. Each pressure level is then assessed, if $T(\lambda) > \exp(-1.0)$ (two-way opacity is less than 1) for all wavelengths then the vertically-integrated cloud reflectivity of this layer is zero. If $T(\lambda) < \exp(-1.0)$ (two-way opacity is greater than 1) we can average over the observed reflectivity spectrum for these wavelengths and set the vertically-integrated cloud reflectivity layer

$R(p)$ to this. We can now calculate the rate of change of reflectivity with height $R(p)/d\ln(p)$, which is our proxy for cloud density, as seen in Figure 5.3.1. By looking at the change in reflectance against the change in pressure between each layer we are able to reveal the structure of the aerosol profile through this opacity proxy. This shows that there are two clearly separated aerosol layers which can be represented through Gaussian parameterisation. Although this produces a very clear profile, we are not incorporating multiple scattering effects nor limb darkening with this method, nor are we sensitive to pressure levels at $p < 0.1$ bar, therefore we are not as sensitive to aerosol pressure levels as the 'Snippet' method but it provides clear indication of the separation between the aerosol layers.

We use a Gaussian profile parameterisation for both cloud layers identified in our model. We have three parameters for this profile, a peak pressure level which is set to the values found via the 'Snippet' analysis, where the maximum opacity resides. A fractional width value which controls the vertical extent of the profile, variable in our retrievals alongside the total opacity of the cloud layer. The total opacity for both the cloud and haze has been normalised at $0.825\mu m$.

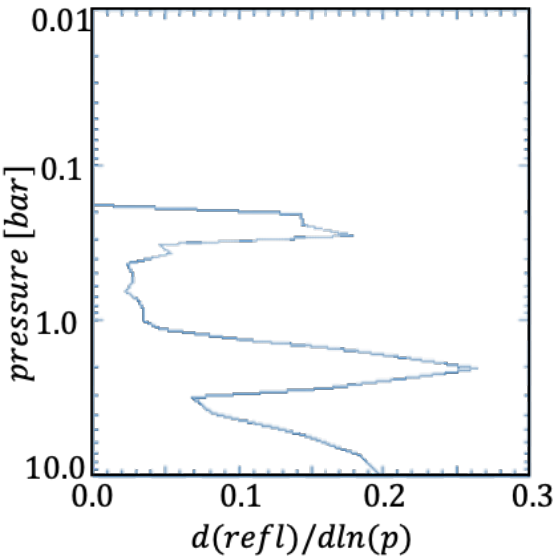


Figure 5.3.1: Change in reflectance against change in the log of the pressure (proxy for aerosol density) viewed for each layer in the atmospheric parameterisation used in the NEMESIS set-up, done for 820 – 910nm at the EZ, revealing the aerosol structure.

5.3.2 Isolating haze characteristics

We know from the spectrum that the 889nm methane absorption is a region in the wavelength range where we are only sensitive to the upper atmospheric haze. In other wavelength ranges the haze reflectivity is drowned out by stronger reflection from deeper in the atmosphere. It was hoped that through an attempt to fit just the wavelengths in this absorption feature we would be able to determine the properties of the haze alone. However, we find that this approach could not fully characterise the entire spectra, and had to be verified alongside full wavelength retrievals.

For the small wavelength retrievals we used a Gaussian distribution for the haze, centred at 0.2 bar, and attempted to retrieve the real imaginary refractive index, assumed to be constant across the wavelength range (real fixed at 1.42) and haze particle size (with a variance of 0.1). We use a small wavelength range, of 882–900nm corresponding to the methane absorption feature. It was hoped that the retrieved imaginary refractive index of the haze would be applicable across the entire wavelength range of the MUSE spectra. However, fixing the retrieved value for the whole wavelength range we were unable to match to observations. The final haze RI values, which were set using the whole wavelength range are discussed in Section 5.3.6.

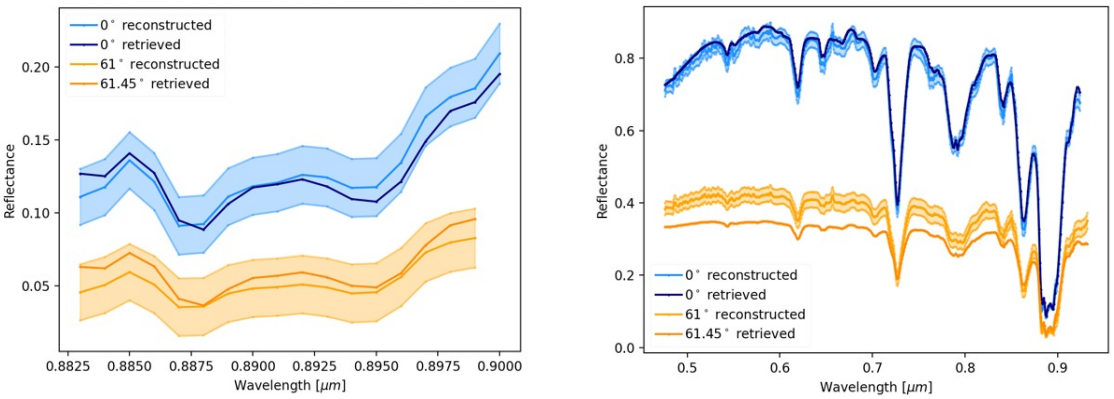


Figure 5.3.2: Left – Short wavelength retrieval focused on the 889nm methane absorption peak to try and identify an appropriate haze particle radius using a wavelength range sensitive only to haze. Right – Full wavelength retrieval using the 1.05μm haze radius, with 0.1 size distribution, as identified in the short wavelength retrieval shown, such a large radius haze is unable to reproduce the larger viewing angle observation outside of the methane absorption feature.

The information which was retrieved about the particle radius for the small wavelength ranges was of more use. The small wavelength range retrievals tended to require larger particle sizes of the haze to reproduce the methane trough, however, when applied to the rest of the wavelength range this did not provide a good fit to observations, Figure 5.3.2. Therefore, to reconcile these differences we were able to increase the variance of the haze radii. Previously, the variance of the haze particle sizes had been set to a value of 0.1. This created a small range of values in which the haze radii could be with the given size and variance. So that more of the haze population had larger radii, but a smaller particle size was still dominant, we are able to increase the variance of the particle size distribution (Hansen, 1971) which is given as

$$n(r) \propto r^{\frac{(1-3b)}{b}} \exp\left(\frac{-r}{ab}\right) \tag{5.3.1}$$

where $n(r)dr$ is the number of particles per unit volume with radius between r and $r + dr$, a is the effective mean radius and b is the effective variance.

Another grid search was then performed with a larger size variances, ranging up to 0.5. The best fit was found to be a variance of 0.31 with a radii, r, of $0.36\mu m$ which was able to reproduce both the methane absorption feature as well as the rest of the spectral range.

The distribution of haze across the globe is one of the few parameters which we are able to clearly see through our observations without any retrievals of values. The distribution can be seen in 889nm images on Jupiter, see Figure 1.2.2, where bright regions align with elevated levels of haze, such as in the EZ. If the retrievals across the disc do not reproduce the haze distribution seen at 889nm, then we must further investigate the parameter space as the current results are non-realistic. This allows us to break some of the degeneracy between parameters due to the haze distribution being known without any degeneracy.

5.3.3 Determining cloud radius

The radius of both the haze and cloud particles are parameters which had to be regularly assessed as we fixed other parameters for the model. These values have degenerate tendencies with several other

parameters, so we had to ensure that the optimal value was being used through regularly reassessment. Cloud radius values were assessed using a grid search trialling values from 0.5–7.5μm (done separately, with a different atmospheric set up, to that shown in Figure 5.1.2). For each retrieval the cloud radius was fixed with the same parameter combination for the rest of the atmospheric model. Within the parameter space we were searching we had to perform additional verifications as often the minimal χ^2/n values did not have a satisfactory spectral fit or reproduce haze distributions. For example, the minimum χ^2/n values favoured larger radii, but produced non-realistic values for the haze opacity, diverging from the expected distribution as seen at 889nm. We then focused on a cloud radius which was able to reproduce the haze distribution, performing a parameter search for cloud radius between 1.0–3.0μm. As the previous search favoured larger radii, the variance of cloud size distribution was increased (see distribution described in Equation 5.3.1) to see if this could minimise the χ^2/n values whilst fitting the spectra and reproducing the haze distribution. A grid search of variances 0.1 – 0.4 with the 1.0–3.0μm radius were conducted, the best fit was found for a radii of 1.62μm with 0.35 size variance.

5.3.4 Ammonia profile parameterisation

Ammonia is represented throughout using a knee profile (profile 1), where there is a deep mixing ratio up to a knee pressure, which then decreases by a given fractional scale height above this. The fractional scale height is the decrease in a parameter by $1/e$ (scale height) relative to the atmospheric scale height (27km at Jupiter). We also limit the ammonia profile so that it cannot exceed 100% relative humidity. The knee pressure is always fixed and to further reduce the number of free parameters we can then fix one of the other values whilst still allowing variation in the amount of ammonia across the disc. For the knee pressure we used the approximated ammonia condensation level of 0.7 atm, tests were done at 0.6 atm as well, due to its use in Braude et al. (2020). It was found that there was little difference between the values, but 0.7 atm had a slightly improved fit and has been used more widely in the literature, so was used in this work. We then decided to fix the fractional scale height factor to 1.0 above this level, this means we are equal to the scale height on Jupiter. We retrieve the deep mixing ratio to reproduce the variability of ammonia across the disc. Having only one free parameter reduces the degeneracy between these parameters and reduces the

complexity of the model.

Through our retrievals we wanted to ensure that the ammonia distribution across the disc was able to reproduce the observations taken by the Juno Mission (Li et al., 2017) and from ground based observations (Moeckel et al., 2023; Hill et al., 2024). Most notable is the large spike around 5°N of the equator and rapid decrease north to a minimum in the North Equatorial Belt, around 10°. Through our retrievals this had not always been achieved with certain set-ups, which allowed us to further verify the plausibility of each set-up beyond the spectral fit. We found that variations in the haze profile shape (opacity and width) displayed degeneracy with ammonia retrievals, often minimising the goodness of fit measured but not retrieving realistic atmospheric conditions, (as also found with the haze distribution for other parameters). By ensuring both of these distributions are as expected, we provide more confidence that our retrievals are matching real conditions on Jupiter.

5.3.5 Information about chromophore drawn from spectra

The more information about the aerosol profile which can be retrieved before undertaking final retrievals, the better. One such way to determine information is to assess the observed spectra. As we have extracted two viewing angles for each location we are able to compare how each of these spectra varies for the same location. Taking a region which is a deep shade of red, associated with an enhanced amount chromophore material, we can determine where in the atmosphere this material is located by viewing its spectra. By comparing the blue slopes of an observation we can see which observation has the steeper slope to determine where the chromophore is located. As discussed in Section 2.5.3, Figure 2.5.6 shows that the higher viewing angle has a longer path length through the haze material. Therefore, if the haze contained the chromophore material the higher viewing angle would have a steeper blue slope as more absorption would occur due to the longer path length through the absorbing material. Figure 5.3.3 displays spectra from 10°N (NEB) in 2018, it can be seen that the 0° viewing angle spectrum has a steeper blue slope compared to the 61.45° spectrum. We can therefore expect to find the chromophore material below the haze level and in the main cloud layer. This conclusion leads to a different approach to the imaginary refractive indices with the haze expected now to have a relatively flat imaginary refractive indices, and the cloud indices to

instead have higher absorption at shorter wavelengths associated with the chromophore material.

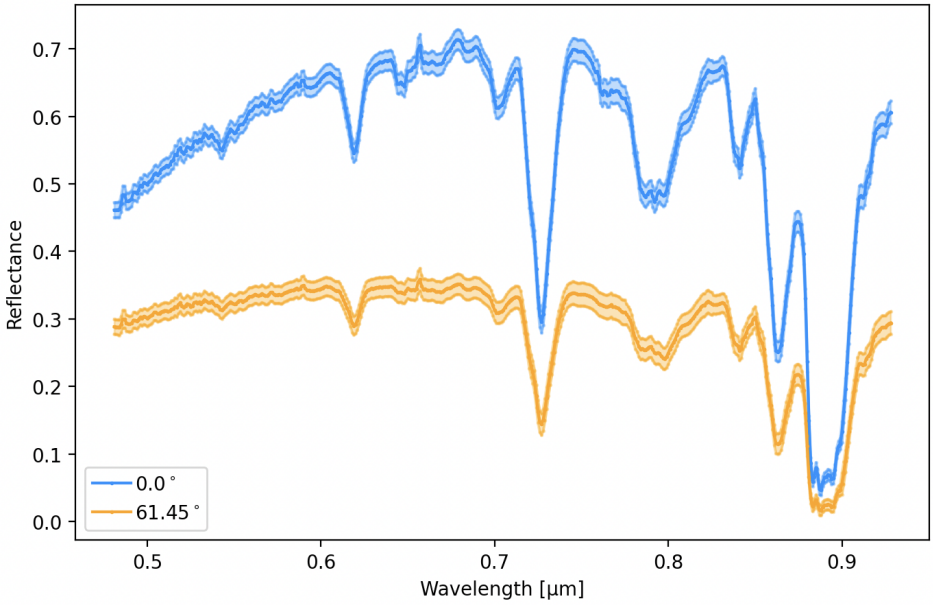


Figure 5.3.3: Spectra of the North Equatorial Belt which displays a red colour, reconstructed for both 0.0° and 61.45° viewing angle. The steeper slope of the spectrum of 0.0° viewing angle, compared to the higher spectrum indicates that the chromophore (material which causes the absorption at these wavelengths) is more likely to be located in the deeper cloud layer rather than the haze.

5.3.6 Refractive indices for cloud and haze

The refractive index of both aerosol layers needs to be assessed, both for the real and imaginary parts. As we are unsure of what the clouds are composed of, we do not have any predetermined values to be used. However, due to the location of the main cloud layer it is possible that it could be composed of NH_4SH ice, which has a real refractive index of around 1.75 (Ferraro et al., 1980). We undertook a parameter search around this real refractive index, ranging for values of 0.5 – 2.5. No clear improvement was seen through this range with limited sensitivity between values used and improvements in the spectral fit. Therefore a real refractive index for the cloud of 1.7 at 825nm was chosen due to its plausibility with potential cloud composition and its ability to fit to the spectra. A similar assessment was done for the haze real refractive index, similar results were acquired with minimal sensitivity between real refractive index values, and a value of 1.7 at 825nm was also chosen.

Assessing the imaginary refractive index (RI) for these models was far more challenging due to the large amount of change which differing the indices values can invoke on the fit to the observed spectrum. Both the haze and cloud have 11 imaginary RI values across the wavelength range of the spectra. These values also have a correlation length which can be adjusted to apply constraint on the retrieved values by altering how much each retrieved value depends on others around it. This helps to reduce spikes in the retrieved indices, as with a small correlation length NEMESIS introduces unrealistic variation between values to help improve the spectral fit, which creates an unrealistically variable refractive index profile. Instead increasing the correlation length will produce a more smoothly varying set of values.

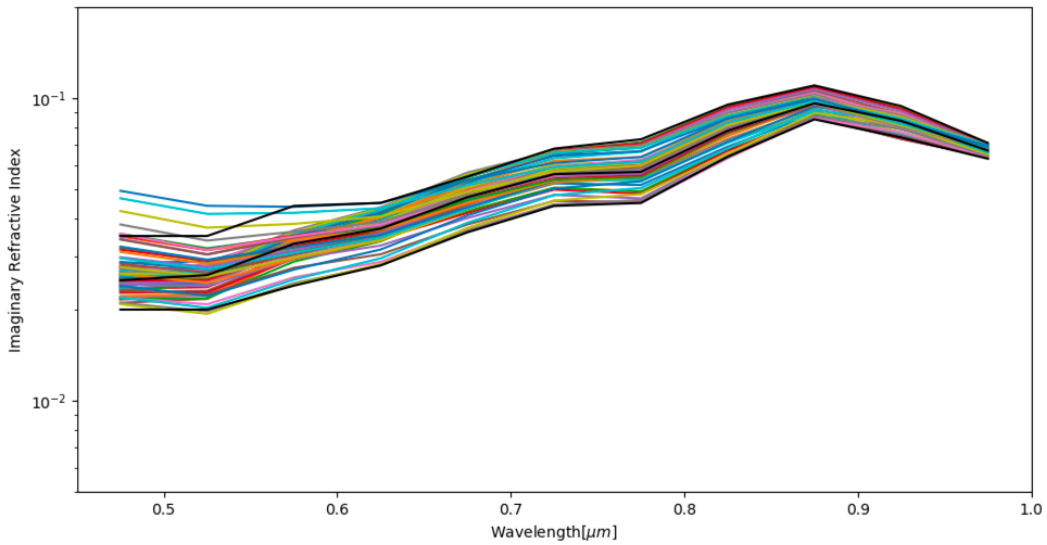


Figure 5.3.4: Imaginary refractive indices retrieved for the haze when it was allowed to freely vary. The black lines show the three sets of trial RI tested to produce the best fit for the whole latitude range with a single set of haze imaginary refractive indices.

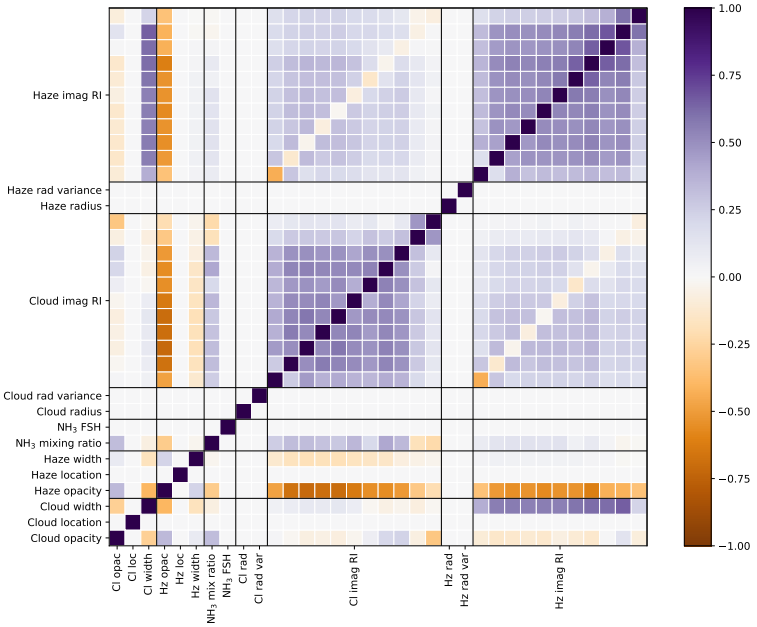
Throughout the attempt to fit the parameter space, the refractive indices for both aerosol profiles were left to freely vary, as without more confidence of the whole parameter space it could be possible that the refractive indices would compensate for a poor parameter choice. Once we had more parameters fixed (cloud and haze locations, ammonia profile, aerosol radii and variance) and were able to reproduce the spectra of Jupiter across a number of latitude bands we began to investigate fixing the imaginary refractive indices. For a set of retrievals with the same flat *a priori* values

(1×10^{-3}) across the disc, which were then allowed to freely vary, similar values for the haze imaginary RI were retrieved for 40°N–40°S, seen in Figure 5.3.4. Three sets of retrievals were then undertaken with fixed imaginary RI values taken from maximum, mean and minimum values from the spread of retrieved values in Figure 5.3.4. The maximum value for the imaginary RI was found to produce the best fit across the latitude range with only the cloud RI now varying. The final imaginary refractive index values used in retrievals, fixed for haze and allowed to vary for the cloud layer (given with errors) are presented in Table 5.3.1.

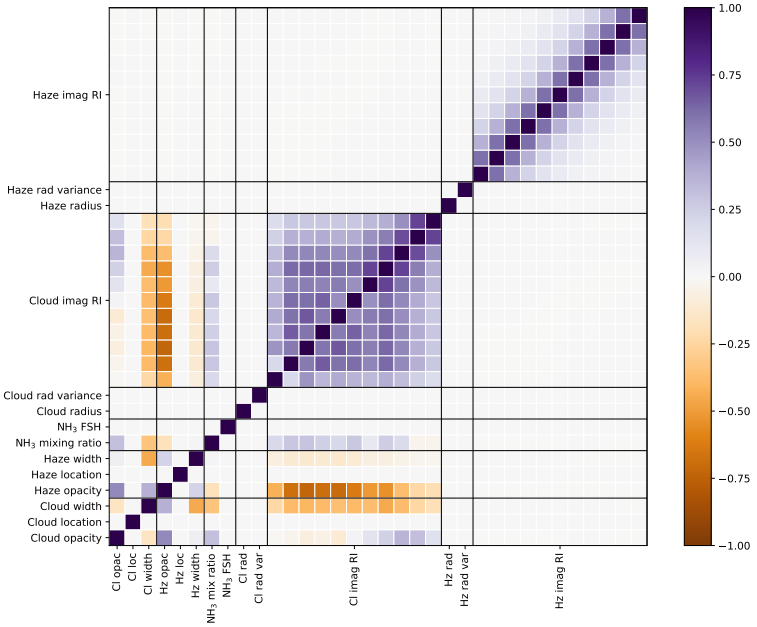
Wavelength [μm]	Haze Imaginary RI	Cloud Imaginary RI	Cloud Error
0.475	0.035	0.0030	5×10^{-4}
0.525	0.035	0.0024	5×10^{-4}
0.575	0.044	0.0018	5×10^{-4}
0.625	0.045	0.0015	5×10^{-4}
0.675	0.067	0.0013	5×10^{-4}
0.725	0.068	0.0012	5×10^{-4}
0.775	0.073	0.00074	5×10^{-5}
0.825	0.095	0.00054	5×10^{-5}
0.875	0.11	0.00021	5×10^{-5}
0.925	0.094	0.00018	5×10^{-5}
0.925	0.071	0.00018	5×10^{-5}

Table 5.3.1: Imaginary refractive indices for the haze (fixed for retrievals, with error of 1×10^{-7}) and the cloud layer (free to vary, presented with errors).

Through the fixing of the haze imaginary refractive indices we are able to significantly reduce the number of degenerate pairs within the parameter space. Figure 5.3.5 demonstrates the difference in correlation between the same parameter space, with and without the haze RI being fixed. The bottom panel, Figure 5.3.5b, shows correlation between the values of the haze RI despite them being fixed, this is due to stated correlation length in the *a priori* which is irrelevant due to the values not varying during the retrieval. However, in Figure 5.3.5b we can see the decrease of parameters which are shown to have a correlation, which has reduced the complexity of the parameter space, allowing us to have more confidence for the values for the retrieved parameters. We can still see that there is a significant amount of degeneracy remaining in the parameter space due to the parameters which are variable, such as haze opacity with cloud imaginary RI, and cloud and haze opacity and cloud width with the ammonia mixing ratio. By fixing the haze refractive indices we are removing a huge number of degenerate pairings.



(a) Varying haze imaginary RI



(b) Fixed haze imaginary RI

Figure 5.3.5: Retrieved covariance matrices with the same *a priori* set up (*a priori* covariance matrix can be seen in Figure 5.1.1a) except for the haze imaginary refractive index, variable top panel, fixed bottom panel.

The cloud refractive indices are left to vary as we expect variance in the chromophore properties across the disc to account for the variation in colour across the disc. We use an *a priori* taken from an average of runs from 40°N – 40°S where cloud RI is allowed to vary, with fixed haze imaginary RI. To retrieve cloud RI values that vary smoothly across the wavelength range we had to increase the correlation length. This is particularly an issue at longer wavelengths as retrievals often over-fit to the methane absorption trough as the errors are smaller there (due to the radiance being smaller and the 1/50 error subsequently being smaller). The correlation length has been extended to 0.25 for the cloud imaginary RI, shown in Table 5.3.2. The retrieved cloud imaginary RI values for each observation are presented in Chapter 6.

5.3.7 Final Parameterisation

Using the parameterisation scheme outlined in Table 5.3.2 (with Table 5.3.1) we have minimised the number of variable parameters, reducing the amount of degenerate pairs present in our retrievals. We are then able to conduct retrievals for multiple locations across the disc of Jupiter and for multiple observation dates. The results from these retrievals using this set-up will be discussed in Chapter 6. The number of parameters which have been allowed to vary has been minimised (5 profile parameters and the cloud imaginary RI values (11)) and those remaining are to ensure we are able to fully capture the expected variations in clouds and ammonia across the disc.

Cloud – *Gaussian Profile*

Parameter	*a priori*	Error	Fixed or Variable
Total Opacity (for 0.825μm)	10	10	**V**
Peak Pressure [bar]	1.38545		F
Fractional Width	1.0	0.25	**V**
Mean radius [μm]	1.62		F
Variance of radii	0.35		F
Real RI (at 825nm)	1.7		F
Imaginary RI Correlation Length [μm]	0.25		F
Imaginary RI	Please see Table 5.3.1	1×10^{-4}	**V**

Haze – *Gaussian Profile*

Parameter	*a priori*	Error	Fixed or Variable
Total Opacity (for 0.825μm)	0.4	0.4	**V**
Peak Pressure [bar]	0.2		F
Fractional Width	0.1	0.01	**V**
Mean radius [μm]	0.36		F
Variance of radii	0.31		F
Real RI (at 825nm)	1.7		F
Imaginary RI Correlation Length [μm]	0.1		F
Imaginary RI	Please see Table 5.3.1		F

Ammonia – *Knee Profile*

Parameter	*a priori*	Error	Fixed or Variable
Knee Pressure [atm]	0.7		F
Scale Height Factor	1.0		F
Deep Volume Mixing Ratio	1×10^{-4}	1×10^{-4}	**V**

Table 5.3.2: Parameterisation scheme used with each selected value or given *a priori* value.

Chapter 6

Application of the parameterised retrieval scheme to MUSE observations of Jupiter

In this Chapter we will apply our parameterised retrieval scheme, described in Chapter 5 and summarised in Table 5.3.2. First, we will discuss the observation on 9th April 2018, whose spectra were used to develop the parameterisation scheme, detailing how the scheme captures latitudinal variation of ammonia and aerosols in Jupiter's atmosphere. We will then introduce subsequent observations each year up to 2023, and compare the observed and retrieved spectra (see Table 4.2.1 for observation dates). Next, we will compare the retrieved parameters for all years, linking the cloud top appearance to a deeper cloud structure. Finally, we present a discussion of the results of the parameterisation scheme for the GRS spectra from 2018 and 2022.

For each observation we retrieve the latitudinal variation of the cloud profile from 40°N to 40°S, in bands of width 2 degrees, sampled every degree to achieve Nyquist sampling. From the fitted Minnaert parameters at each wavelength we extract spectra with two viewing angles of 0.0° and 61.45° for each latitude band. The GRS spectra are calculated using multiple observations where

the GRS is at a different position on the disc in order to fit the Minnaert limb-darkening parameters and extract spectra with two viewing angles of 0.0° and 61.45° for 2018 and 2022.

6.1 2018

6.1.1 Appearance and spectral fits

The 2018 observation used for this work is shown in Figure 6.1.1, and shows a pale EZ, tinged slightly red and a darker red coloured NEB. The SEB is a paler red than the NEB with the STZ south of the GRS being the palest region on the disc. Through the 889nm image we can see the haze is most enhanced at the equator, with increases at the NTZ and part of the STZ, however the brightness at this wavelength indicates that we do not have particularly high amounts of equatorial haze as the 889nm radiance is not significantly brighter at the EZ compared to other regions. We have the GRS on this image but it has been masked to create symmetry whilst using the Minnaert approximation, we will discuss results for the 2018 GRS in Section 6.8.

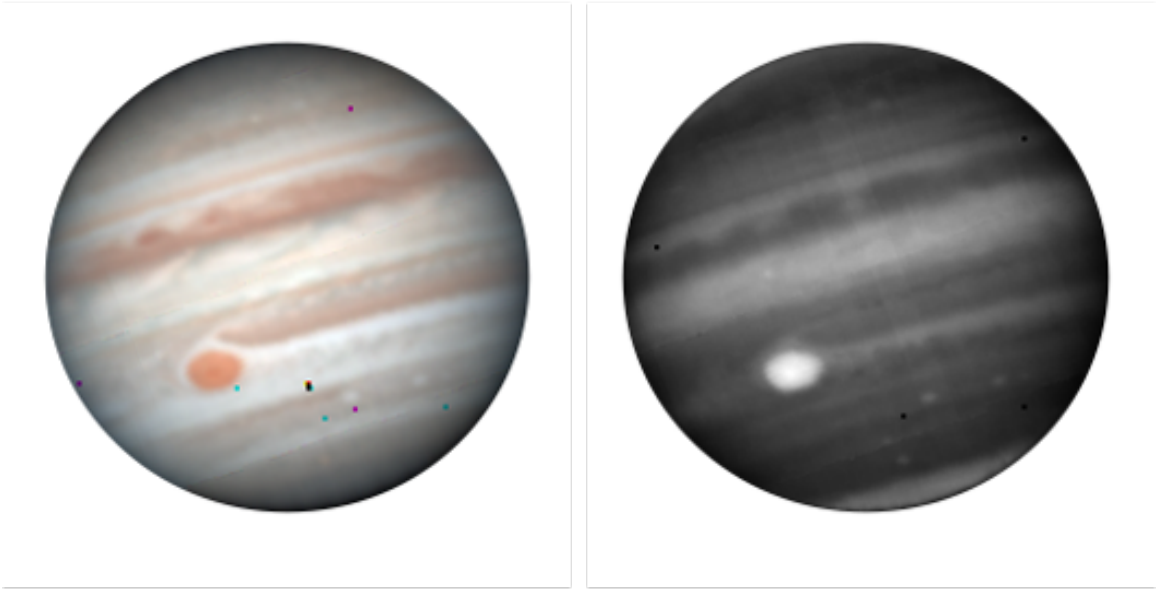
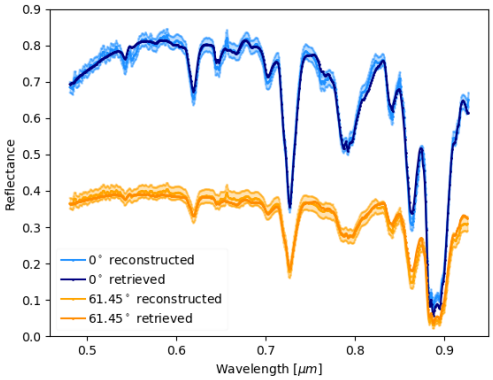


Figure 6.1.1: VLT/MUSE observation of Jupiter on 9th April 2018; left RGB (R–675nm, G–530nm, B–480nm) image, right 889nm observation.

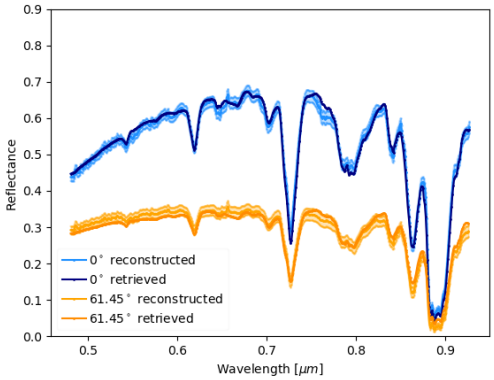
Using the parameter scheme given in Table 5.3.2, we will present the results of retrievals below for the 81 latitude bands. In Figure 6.1.2 we present a selection of the retrieved spectra spanning across the disc, spaced every 10° to represent the different zones and belts. The spectral fits need to match well to both viewing angles simultaneously whilst reproducing the blue slope absorption due to chromophore material, as well as the key absorption features such as the 889nm methane and the 647nm ammonia features. The χ^2/n goodness of fit factor gives a measure of how well we can reproduce observations for each latitude location (Figure 6.1.2j). For the majority of the latitudes, we have been able to minimise the χ^2/n factor; however, for the region around 5 – 15°N we have some higher values for our fit due to degeneracy between two parameters, the deep ammonia VMR and the distribution of the haze and cloud which can be seen in Figure 5.3.5, which we will discuss below.

For the majority of the observations, despite the wide range of cloud top appearances we have been able to fit to our observed spectra to a $\chi^2/n < 1$. These retrievals have been successful despite the more constraining dual viewing angle method, fitting two spectra simultaneously which has not been possible with previous models (Braude et al. (2020) model & Sromovsky et al. (2017); Baines et al. (2019) Crème Brûlée Model). This is due to us having developed the parameterisation scheme using two viewing angles throughout, capturing the limb darkening effects.

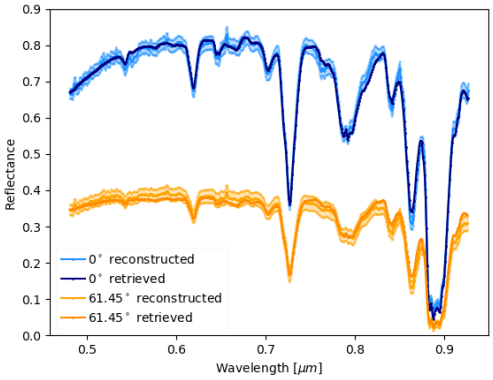
As can be seen in Figure 6.1.2, with the few variable parameters remaining (cloud width and total opacity and imaginary refractive index, plus haze total opacity and width) we are able to adapt to the different characteristics of the spectra in different regions. For example, the steeper blue slope at 10°N compared to 0°N, is able to be accounted for through the variances in the aerosol amounts as well as the refractive index properties.



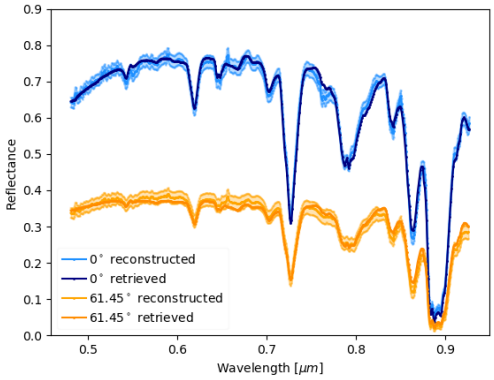
(a) 0°N



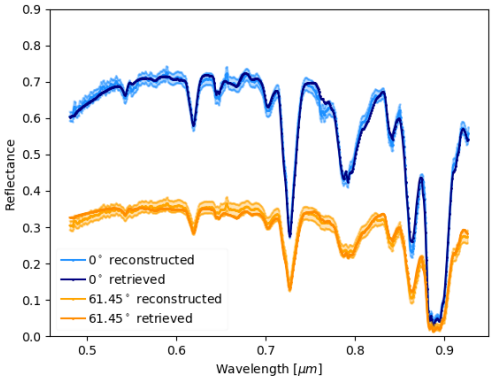
(b) 10°N



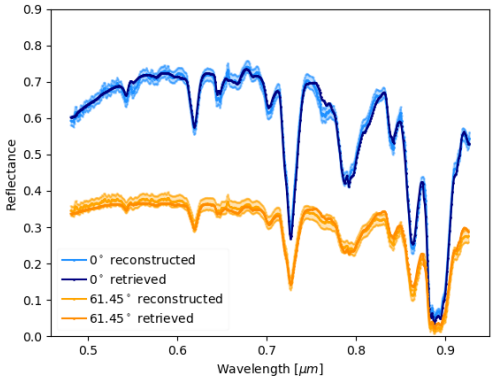
(c) 20°N



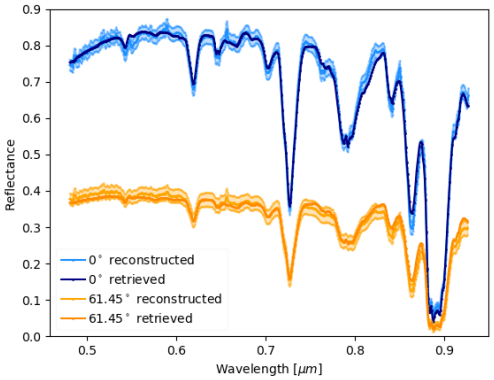
(d) 30°N



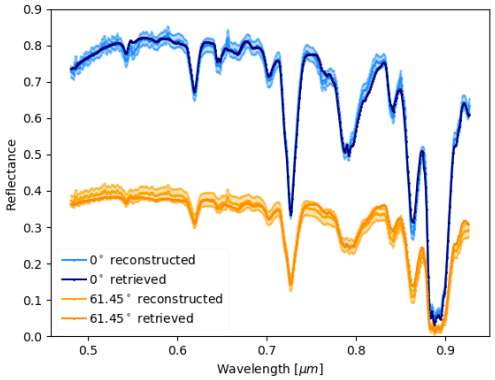
(e) 40°N



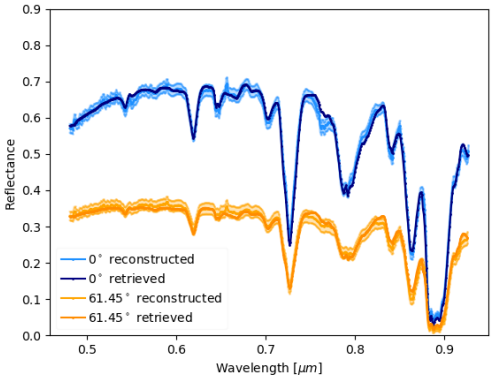
(f) 10°S



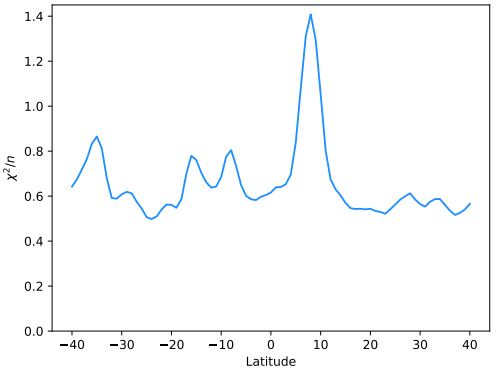
(g) 20°S



(h) 30°S



(i) 40°S



(j) χ^2/n

Figure 6.1.2: Retrieved spectra for dual viewing angle retrievals for 2018, Blue – 0.0° viewing angle Yellow – 61.45° viewing angle, with the paler of each colour being the observation and calculated error of 1/50 error. The darker line for each angle is the retrieved spectrum. 6.1.2j shows the χ^2/n for all retrievals.

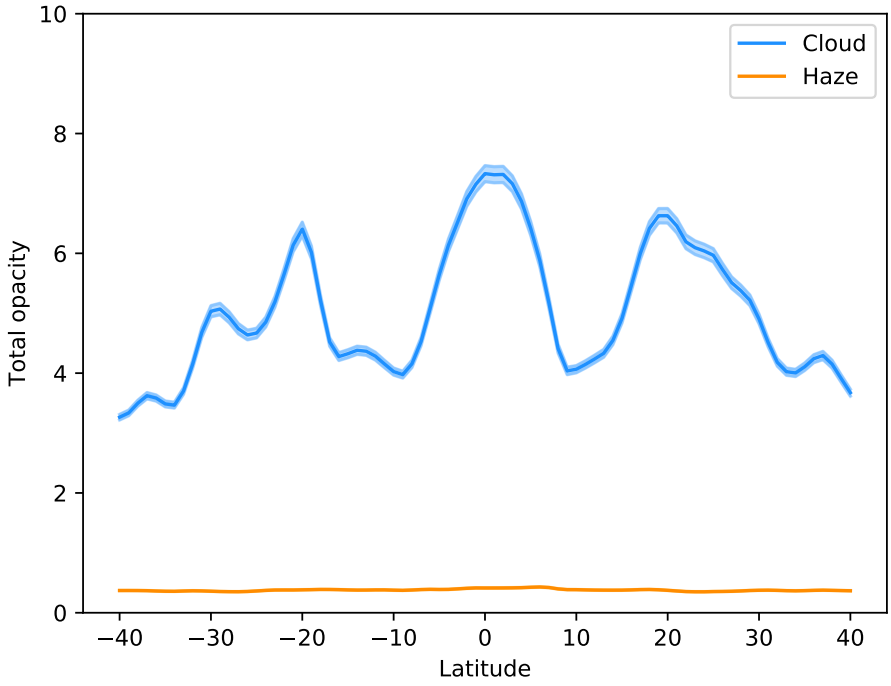
6.1.2 Cloud and haze opacity

The total opacity is one of the variables within the parameterisation for both the cloud and haze layers. Our total opacity is normalised at $0.825\mu m$ for both haze and cloud. We expect a large amount of variation in these values across the latitude range. For the cloud layer, we expect to capture the characteristics of the zone and belt regions across the disc. With thicker cloud layers typically associated with zonal regions, due to the up-welling air which is conducive to cloud formation. We see this in our retrievals (Figure 6.1.3) with the zonal regions having retrieved a far

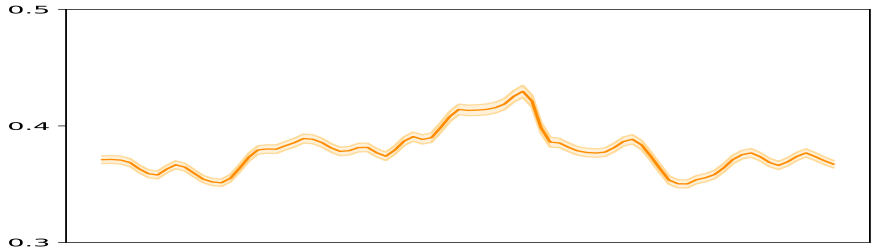
thicker total opacity for the cloud layer than belt regions. The equatorial region has the thickest retrieved opacity out of all regions, associated with the strongest up-welling. As the main cloud layer is mixed, containing chromophore material, the highest total opacities for the equatorial zone, despite its pale appearance, indicates that the refractive index changes have a greater influence on the variation in the cloud top colouration than the opacity of the cloud alone. The retrievals of haze can be checked against the 889nm observations to ensure that the highest opacities correspond to the brightest regions observed (Figure 6.1.1).

We are aware of degeneracy between parameters which reduces the quality of fit between 5 – 15°N, where χ^2/n values greater than 1 are retrieved for 8 – 11°N (Figure 6.1.2j). We can also see the very slight increase on haze opacity within this latitude region, causing the peak haze opacity to be at 5°N (Figure 6.1.3) which is not seen in 889nm (Figure 6.7.2a), although we still expected an elevated opacity at this latitude as part of the EZ enhancement of haze. For earlier retrievals, we often had non-physical haze retrievals at these latitudes, causing a significant peak at 5°N, and an increase in the haze opacity to the north of the EZ not seen in the 889 nm image. The minimised enhancement seen in the final retrievals is far more realistic than previous results where the *a priori* of the haze fractional width was greater. At this latitude (5 – 10°) there is a huge amount of change in the retrieved ammonia VMR as its abundance changes rapidly across these latitudes from an enhanced level down to depletion. With the depleted retrieved VMR we have less absorption higher in the atmosphere, and we believe that NEMESIS may be attempting to increase the haze to remedy the effect of this. The massive rate of change with latitude in this region mean that our averaged latitude bands of 2° width contain a large range of values of the ammonia VMR. The degeneracy with the haze parameterisation is causing an increased value in the χ^2/n for this small latitude region. As we have been able to retrieve both a realistic haze distribution, one of the few parameters we are able to confirm easily through observations, and an ammonia distribution similar to previous works (e.g., Li et al. (2017)), we are compromising with χ^2/n values between 1 and 1.4 for the 4° latitude region 8 –11°. The ability of this parameter scheme to provide both realistic retrieved values for all other parameters as well as χ^2/n values under 1.0 for all other latitudes (Figure 6.1.2j), leads us to believe that it is still a good representation of the aerosol profile on Jupiter. Despite our reduction

in the number of free parameters these variations have shown that error due to degeneracy is still present, as seen in Figure 5.3.5, within our model, however, ensured that it has minimal affect on our retrievals when possible and can be identified.



(a) Cloud and haze total opacity



(b) Haze total opacity

Figure 6.1.3: Retrieved total opacity of the cloud and haze layer, normalised at $0.825\mu m$, for both the cloud and haze layer across all latitudes (40°N – 40°S) for the 2018 observation. The bottom panel below shows the haze on a smaller scale.

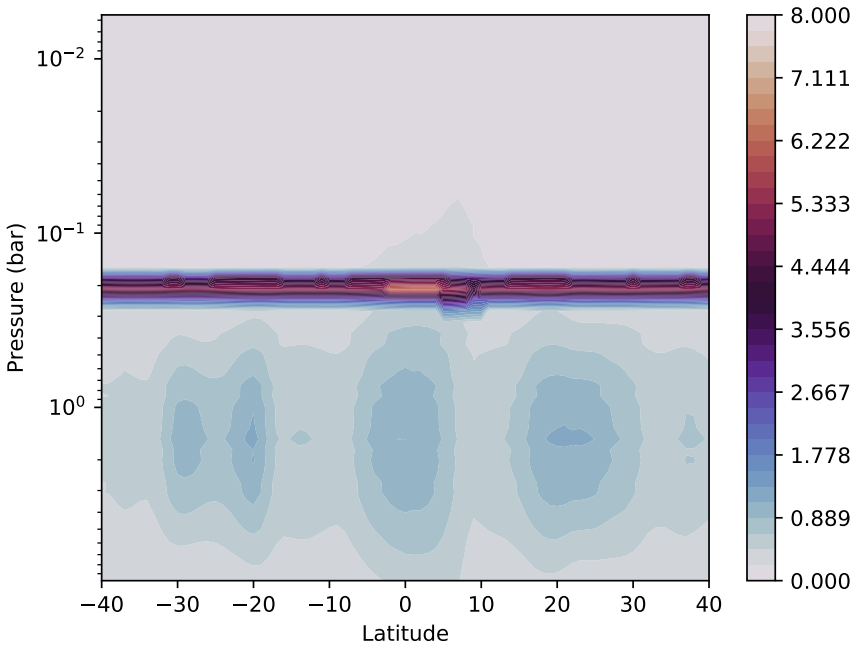


Figure 6.1.4: Retrieved opacity depth per bar of the cloud and haze layer across all latitudes for the 2018 observation, displaying the opacity across the vertical profile. The two aerosol layers can be seen peaking around 0.2 bar (haze) and 1.4 bar (cloud).

Figure 6.1.4 displays how the retrieved aerosol profile varies with altitude and latitude, plotting the aerosol profile in units of opacity/bar. As we parameterise the aerosol layers with a Gaussian profile we are both retrieving the total opacity of the cloud layer, and the width of the cloud through the fractional width parameter in the Gaussian profile, with the peak pressure level parameter fixed. The combination of these two free parameters means at each latitude the shape of the Gaussian parameterisation varies, to best represent the vertical distribution of the aerosol. We can see that the haze becomes a thin layer of very dense aerosol, typically spanning less than 0.1 bar width. However, over the EZ where we have the highest amount of haze, we have a small amount of opacity spanning higher in the atmosphere, above the majority of the haze. The main cloud layers are far wider than the haze, providing the greater total opacity through a less dense but more expansive layer. A zone belt pattern appears, with the zonal regions having larger opacities and generally broader cloud depths than the less cloudy belts.

6.1.3 Ammonia distribution

Figure 6.1.5 shows the ability of the parameterisation scheme to reproduce the ammonia distribution which has been found through retrievals from Juno as well as the VLA (see Figure 6.1.6), demonstrates that our parameterisation scheme is a realistic representation of the atmosphere. The retrieved volume mixing ratio (VMR) of ammonia at 1 bar is shown in Figure 6.1.5. In our model the VMR is constant below the condensation model and the values in Figure 6.1.5 are the same throughout the deep atmosphere. We are able to reproduce the main pattern across the disc, where we have elevated ammonia, VMR of 1.55×10^{-4} just north of the equator around 5°N, before a decrease in the VMR down to a minimum VMR around 10°N, to 4.9×10^{-5}. The VMR then recovers to a smaller value north of this decrease to a steadily varying VMR around 1.1×10^{-4} here and south of the equator. The smaller peaks retrieved either side of the main distribution generally respond to zonal regions on the disc, regions that are associated with up-welling air which would link to increased amount of ammonia being lifted up into these regions.

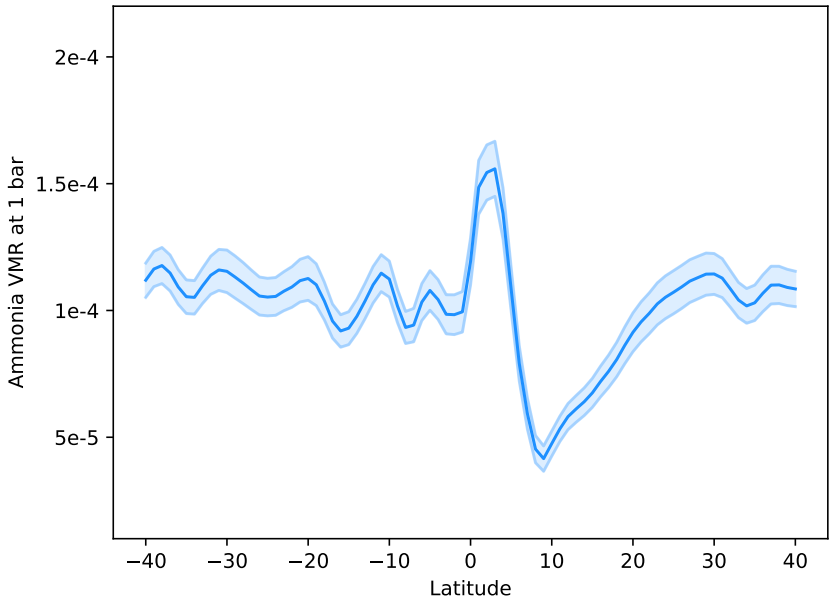
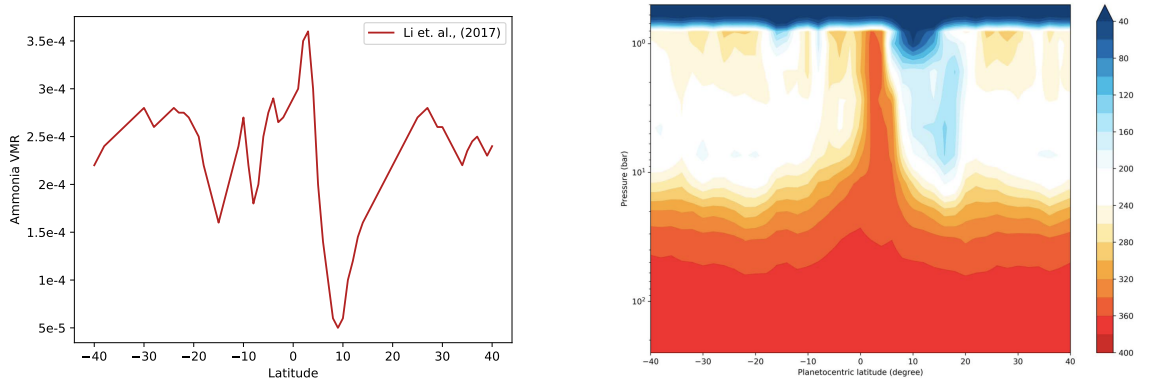


Figure 6.1.5: Ammonia distribution across all latitudes retrieved for the 2018 observation, presenting the deep volume mixing ratio of ammonia.



(a) 1 bar level

(b) MWR pressure range

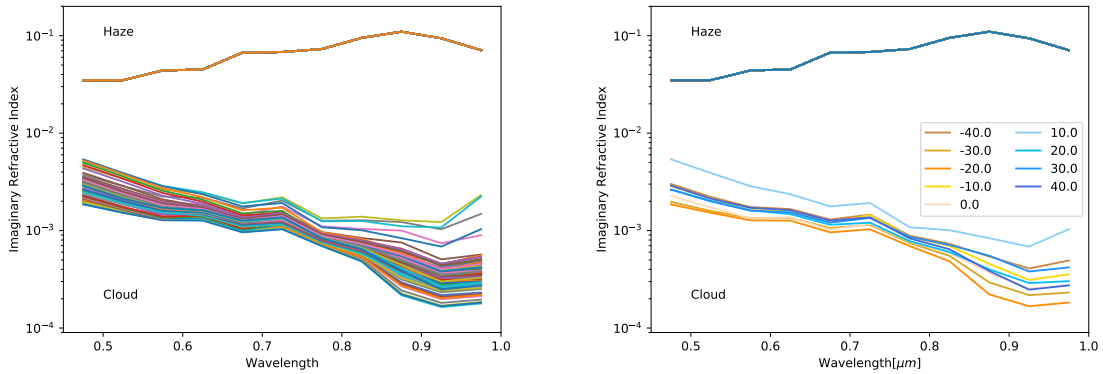
Figure 6.1.6: Retrieved ammonia from Li et al. (2017), shown on the left for the one bar level and for all pressure levels on the right. We can see a similar retrieved pattern in the ammonia retrieved by the model, however the VMR is higher for the results from Li et al. (2017) than those retrieved in this work.

6.1.4 Imaginary refractive index

We allow the imaginary refractive index of the cloud to vary during our retrievals. We expect these values to change across the disc, accounting for the visual changes which are likely linked to the varied dynamics of the atmosphere producing different conditions for different locations. These variations lead to different mixing ratios of material as well as exposing the chromophore material to different conditions, leading to different RI properties retrieved across the disc. All retrieved imaginary RI values are given in Figure 6.1.7a for the full wavelength range, and then RI spectra spaced every 10° are shown in Figure 6.1.7b. The retrieved RI values for 525nm across the disc are shown in Figure 6.1.8a, then the comparison between the retrieved values at 525nm and 625nm, a measure of the blue slope absorption, is given in Figure 6.1.8b.

The imaginary cloud RI values follow a similar trend across all latitude,s but there are differences in the slope and values for each region. Above $0.8\mu m$ there are a handful of latitudes which retrieved a shallower decrease. We can see that both the largest values for the 525nm RI as well as the slope measure correspond to the reddest latitudes on the disc, notably the NEB which can be seen in Figure 6.7.10a as the 10° has greater values at all wavelengths and a steeper blue slope. The

expected variation of the haze at longer wavelengths is not definitively known, but an increase in values after $0.8\mu m$ is seen for other retrievals of the NEB (e.g., Dahl et al. (2021)). Figure 6.1.8b shows the for paler regions we have flatter RI slopes, leading to less blue absorption, as would be expected for their visual appearance.

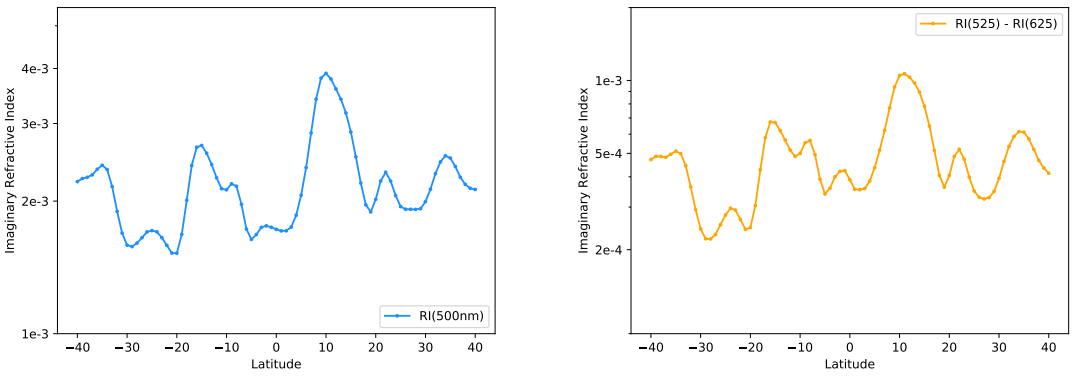


(a) All latitudes

(b) Every 10°

Figure 6.1.7: Latitudinal variation of the retrieved imaginary RI spectrum, Left – all latitudes, Right – every 10° between 40°N – 40°S. The assumed constant haze imaginary RI spectrum is also shown for reference retrieved imaginary RI values for the cloud with the fixed haze values.

The imaginary refractive spectrum of the cloud layer has significant degeneracy with practically every parameter within the atmospheric model, see Figure 5.3.5. The lack of free parameters in our model helps to reduce this degeneracy as it reduces the number of degenerate pairings making it easier to determine true values. In addition, the similarities between the retrieved values across a wide range of latitudes provides positive encouragement that the cloud parameterisation is able to reproduce the observations without the imaginary refractive indices undergoing huge variation to account for changes. However, there is still a significant range of values retrieved. We believe that variations in the mixing ratios of the chromophore as well as variations in its exposed properties can account for these changes, but the lack of information into exactly how these changes manifest themselves over the disc means we must be aware of the variability which the indices can account for.



(a) Retrieved imaginary refractive index for 525nm from 40°S to 40°N.

(b) Difference between the retrieved imaginary refractive index for 525nm and 625nm from 40°S to 40°N.

6.2 2019

6.2.1 Appearance and spectral fits

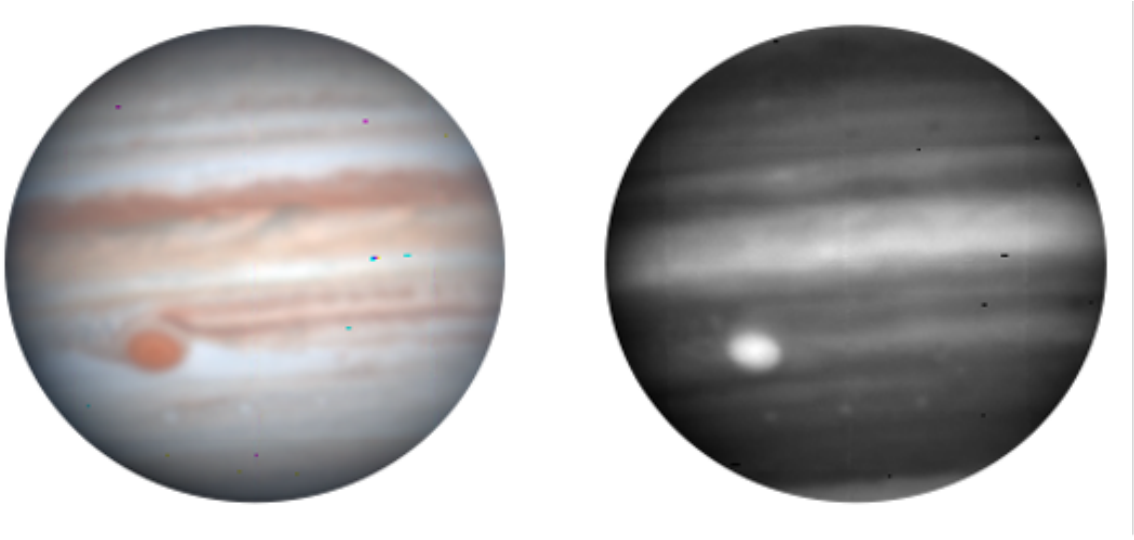
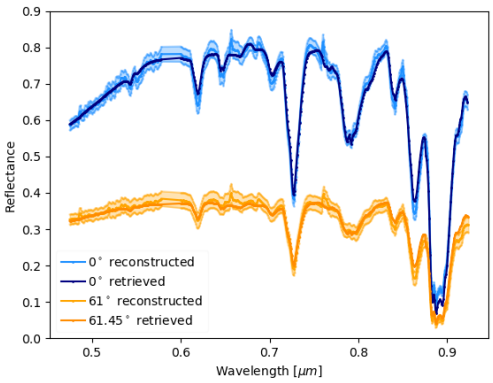


Figure 6.2.1: 11th July 2019 RGB (R–675nm, G–530nm, B–480nm) image and 889nm

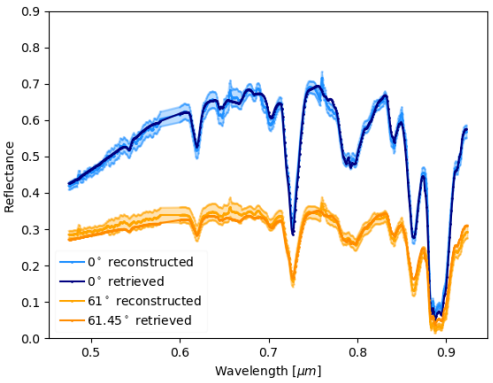
Just over a year after the previous observation in 2018, Jupiter has undergone a colouration event in the EZ, seen in Figure 6.2.1. The previously pale EZ, now displays a redder appearance with a pale red hue spanning the central region. It is still paler than the NEB, which has remained a similar

shape and shade as in 2018. However, many of the other belts and zones at higher latitudes have become paler, including the start of the fade of the NTB. The SEB, eastward of the GRS, now has two prongs of red colouration rather than a single region of eastward colouration.

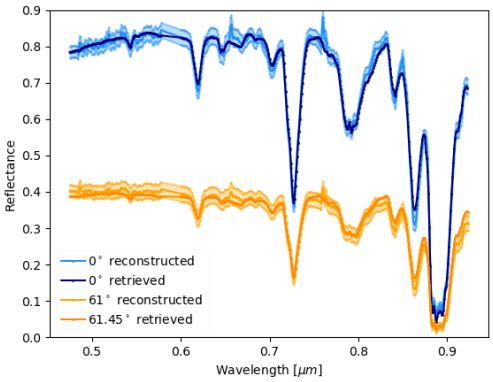
Figure 6.2.2 displays the ability of the parameterisation scheme to adapt to these changes and reproduce the observations across the disc. As the EZ has reddened, we now have a steeper blue slope for the 0°N observation, whereas some of the higher latitudes both south and north now have a flatter spectral slope due to the paler appearance of the disc. Despite these changes, we are able to retrieve χ^2/n values less than 1.0 for the majority of latitude regions.



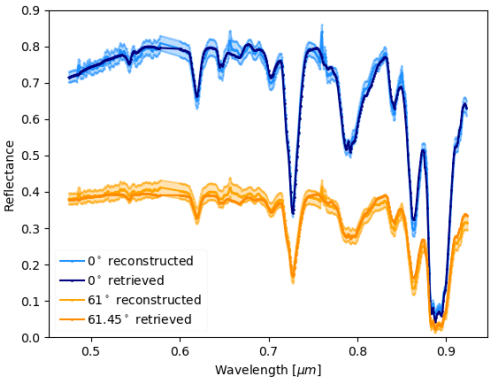
(a) 0°N



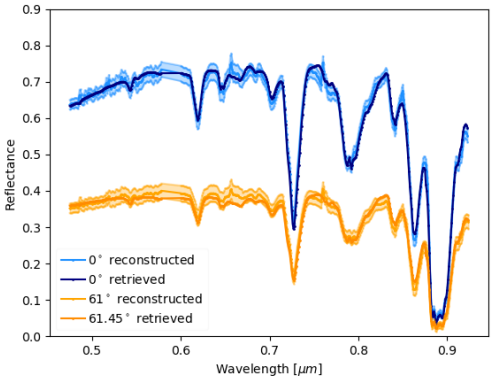
(b) 10°N



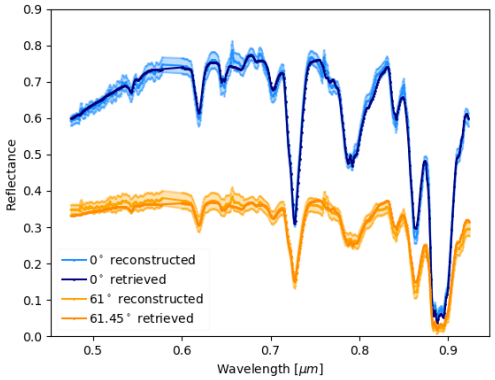
(c) 20°N



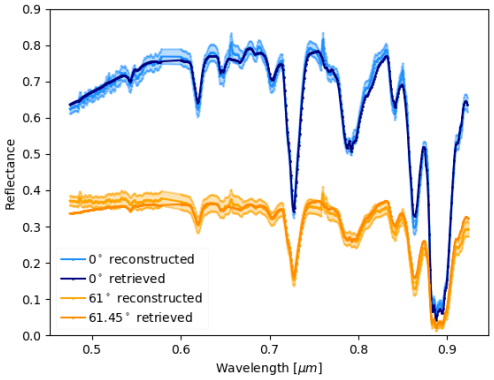
(d) 30°N



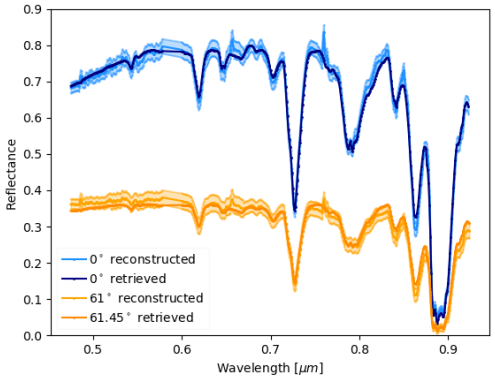
(e) 40°N



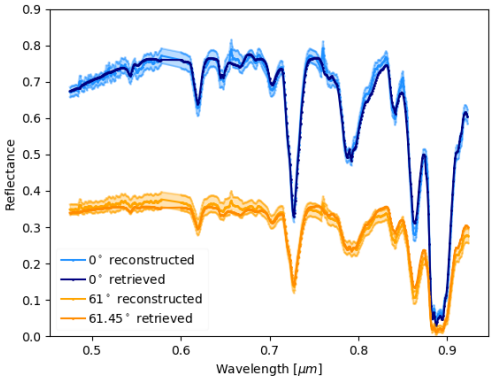
(f) 10°S



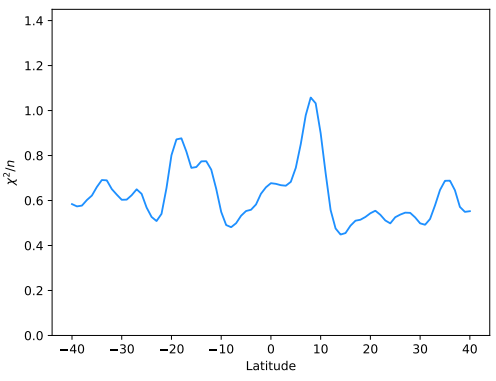
(g) 20°S



(h) 30°S



(i) 40°S



(j) χ^2/n

Figure 6.2.2: Retrieved spectra for dual viewing angle retrievals for 2019, Blue – 0.0° viewing angle Yellow – 61.45° viewing angle, with the paler of each colour being the observations and the darker line being the retrieved spectrum. 6.2.2j shows the χ^2/n for all retrievals.

6.3 2020

6.3.1 Appearance and spectral fits

In 2020 the revival of the EZ has finished and the zone is reverting back to its paler state, as can be seen in Figure 6.3.1. The NEB remains a vivid red region, with a similar extent to previous years. The southern regions have continued to pale, with both the SEB and STB paler than previous year. The bifurcation of red in the wake of the GRS to the east, in the SEB, continues as in 2019.

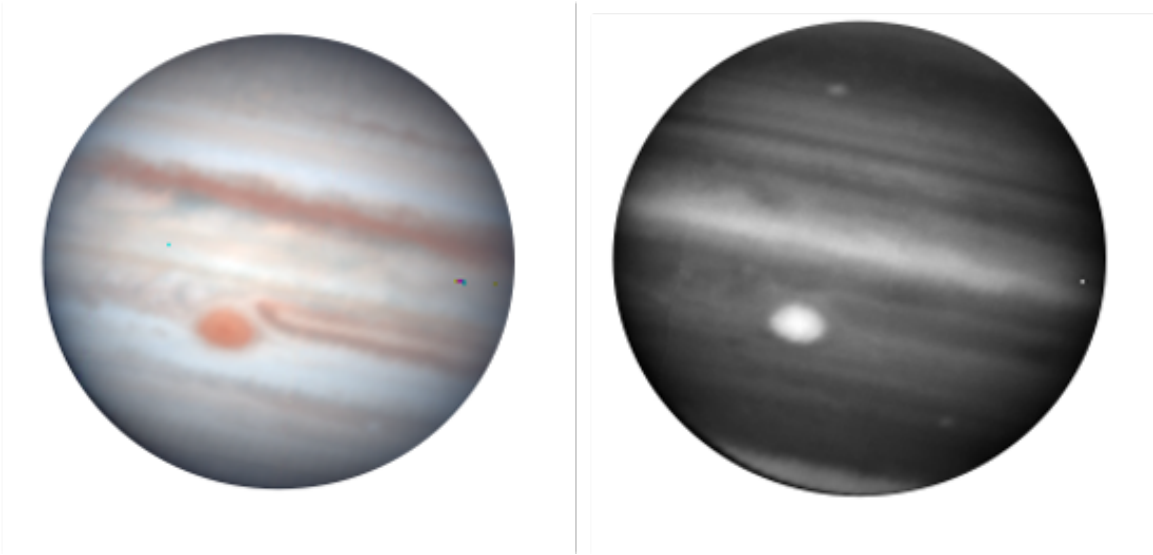
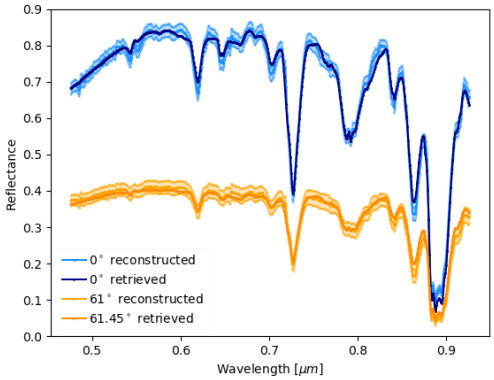
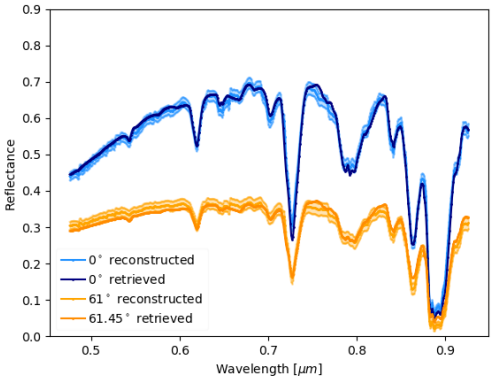


Figure 6.3.1: 23rd March 2020. RGB (R–675nm, G–530nm, B–480nm) image and 889nm

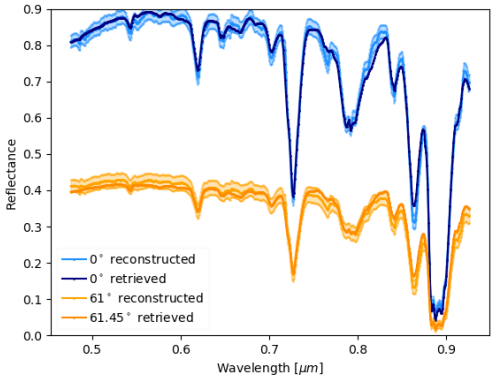
The paler colouration of both the North and South Tropical Zones has produced a brightened region with an increased I/F compared to previous years, but, the parameterisation scheme has been able to adapt to these regions as they change, as can be seen in Figure 6.3.2. There are some elevated values of χ^2/n between 18 – 30°S, but the spectral fits are still reasonable, although the model underestimates the higher viewing angle radiance for the blue slope for these regions. This may be due to the asymmetry of this region due to the bifurcation of red material in the wake to the east (see Figure 6.3.1) therefore, the decrease in the quality of fits could be due to a poorer fit during the Minnaert fitting in this region. Although there is asymmetry around the GRS for the 2018 observation, the variation east and west of the GRS is not as large as for 2019 or 2020.



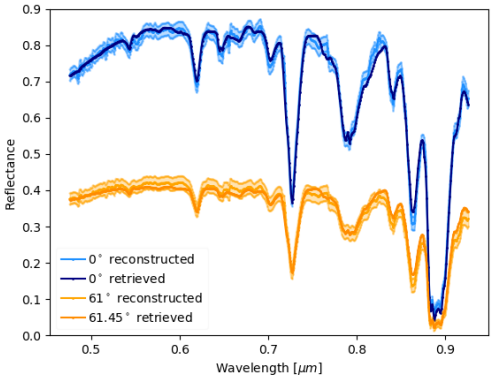
(a) 0°N



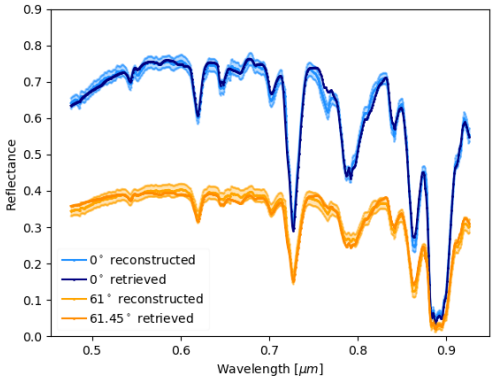
(b) 10°N



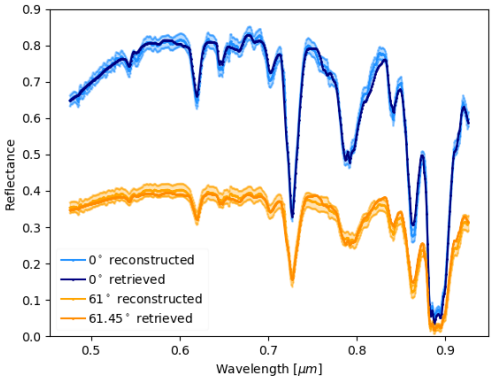
(c) 20°N



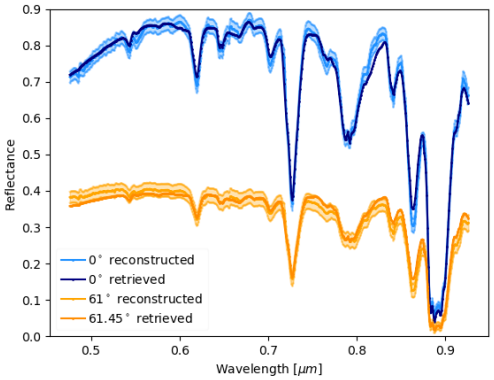
(d) 30°N



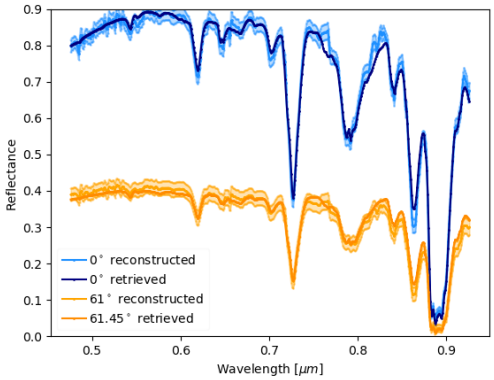
(e) 40°N



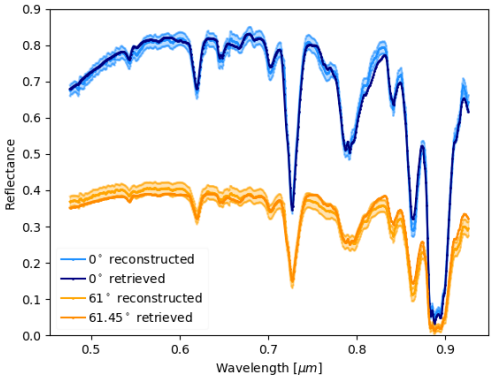
(f) 10°S



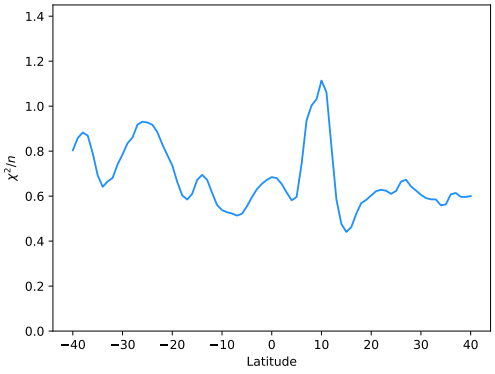
(g) 20°S



(h) 30°S



(i) 40°S



(j) χ^2/n

Figure 6.3.2: Retrieved spectra for dual viewing angle retrievals for 2020, Blue – 0.0° viewing angle Yellow –61.45° viewing angle, with the paler of each colour being the observations and the darker line being the retrieved spectrum. 6.3.2j shows the χ^2/n for all retrievals.

6.4 2021

6.4.1 Appearance and spectral fits

In Figure 6.4.1 we have the first observation without the GRS on the disc, which produces a more symmetrical appearance to the bands on the disc. Since the 2020 observation, the disc has undergone significant changes in the colouration and extent of several of its zones and belts. The EZ has again undergone a colouration event, as has the SEB and there is a small region of paler cloud tops between

these zones. The North Temperate Belt has darkened again creating a clearer separation between the two pale zones – North Tropical and North Temperate. The NEB has changed with a darker red colouration but with a lesser spatial extent than seen in previous years.

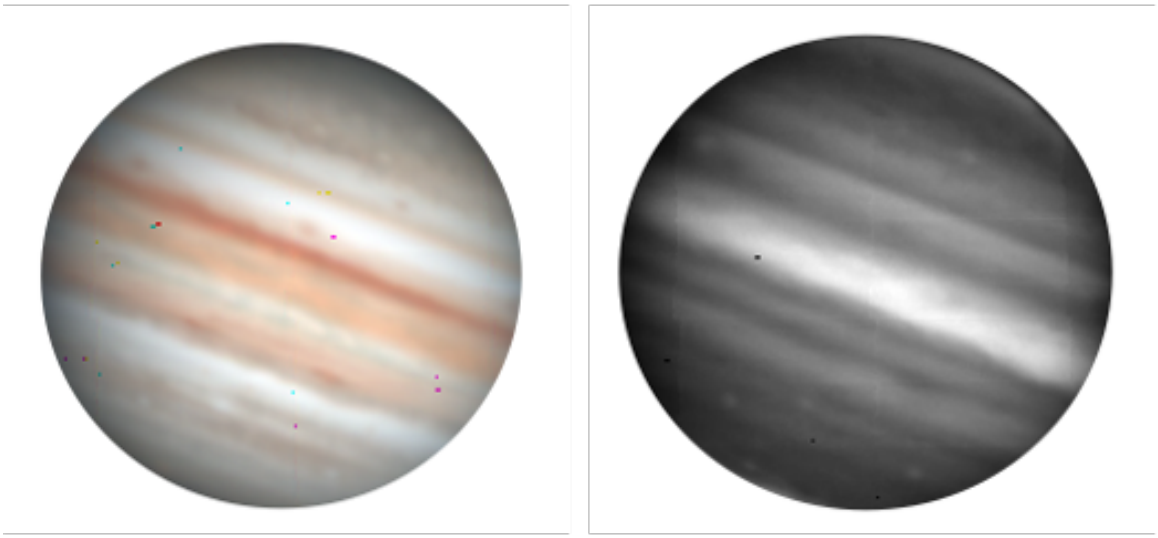
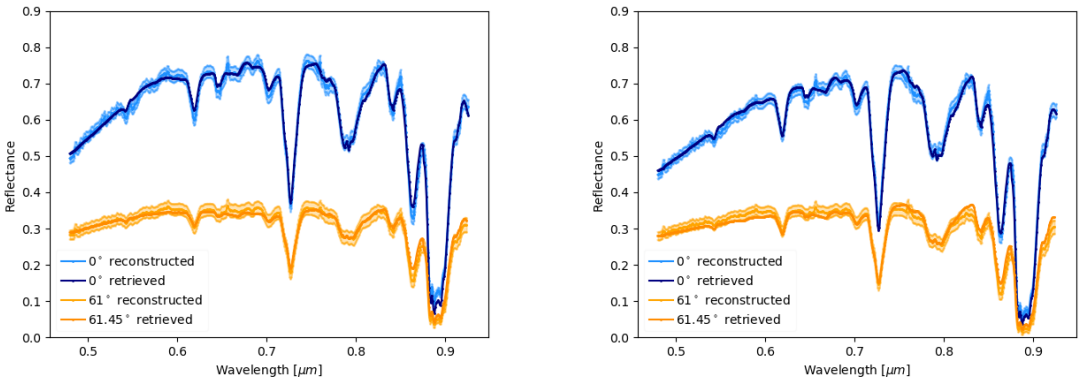
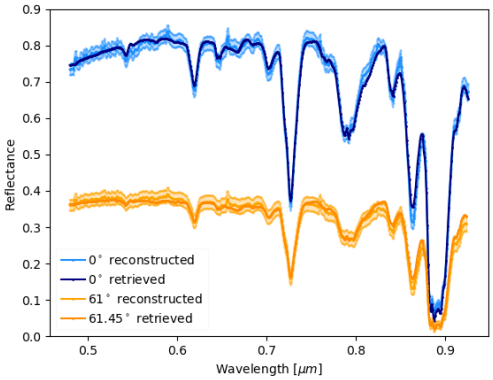


Figure 6.4.1: 8th November 2021 RGB (R–675nm, G–530nm, B–480nm) image and 889nm

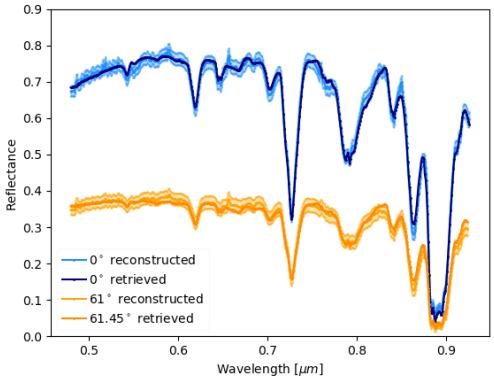
Despite the significant changes of many regions, the parameterisation is able to adjust to the conditions and produce retrieved spectra that match the observations across the disc, as can be seen in Figure 6.4.2.



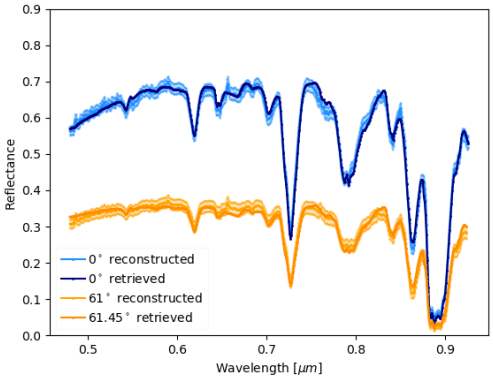
(a) 0°N (b) 10°N



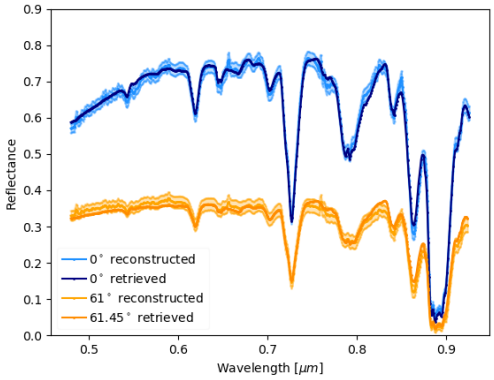
(c) 20°N



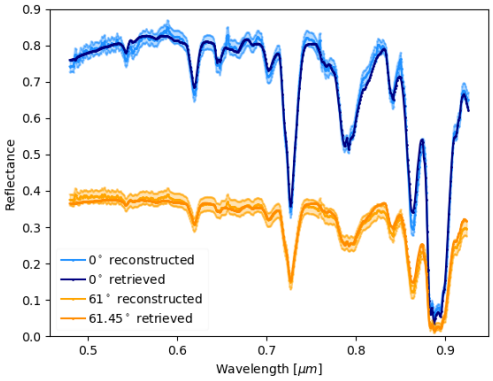
(d) 30°N



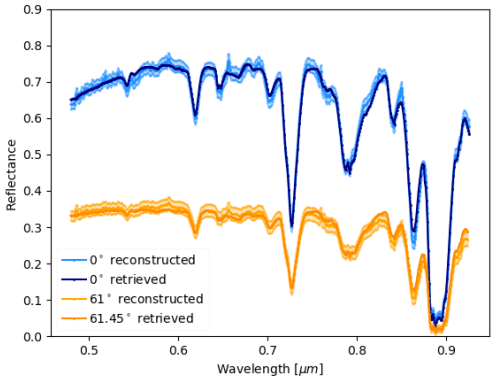
(e) 40°N



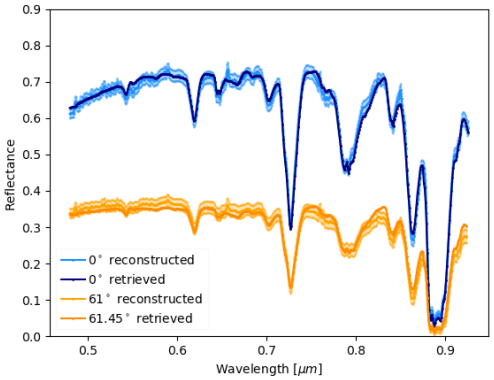
(f) 10°S



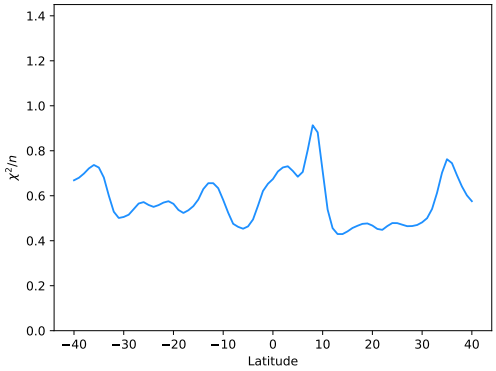
(g) 20°S



(h) 30°S



(i) 40°S



(j) χ^2/n

Figure 6.4.2: Retrieved spectra for dual viewing angle retrievals for 2021, Blue – 0.0° viewing angle Yellow –61.45° viewing angle, with the paler of each colour being the observations and the darker line being the retrieved spectrum.6.4.2j shows the χ^2/n for all retrievals.

6.5 2022

6.5.1 Appearance and spectral fits

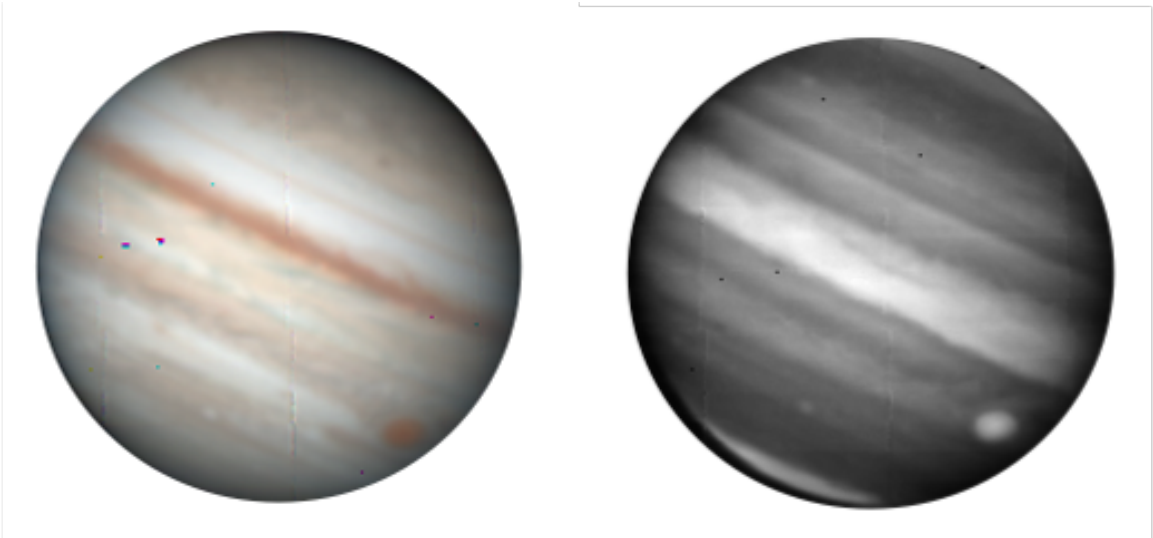
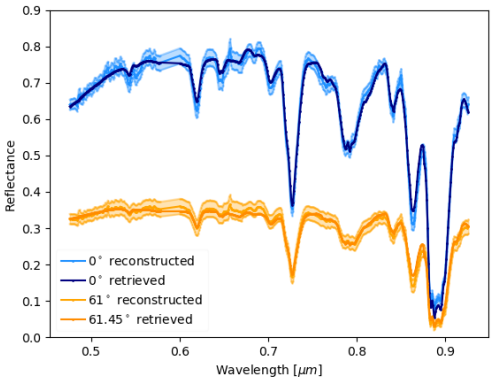


Figure 6.5.1: 1^{st} July 2022 RGB (R–675nm, G–530nm, B–480nm) image and 889nm

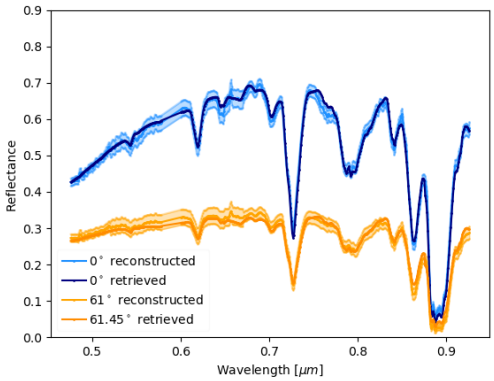
Much of the colouration which had occurred in the previous year has faded again by the 2022

observation, seen in Figure 6.5.1. The red enhancement south of the NEB has mainly faded and instead a much paler colour dominates. The diminished width of the NEB has begun to restore its thickness of previous years as it has now become wider and is also a darker shade of red than the previous year. As the GRS is towards the eastern limb we are not impacted by the wake to the east of the GRS in this observation.

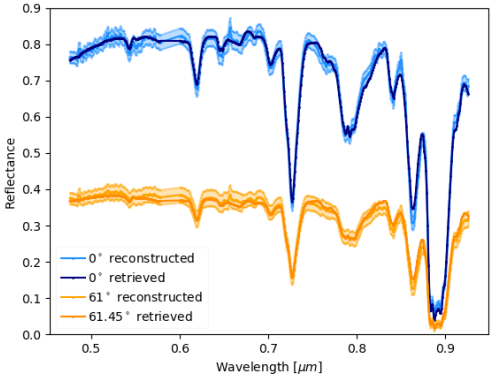
As with previous years, Figure 6.3.2 shows the ability of the parameterisation to reproduce the spectral variations observed across the disc.



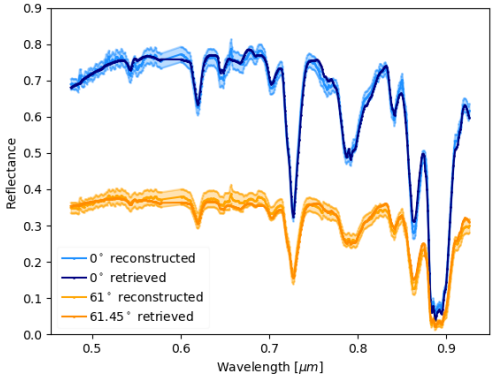
(a) 0°N



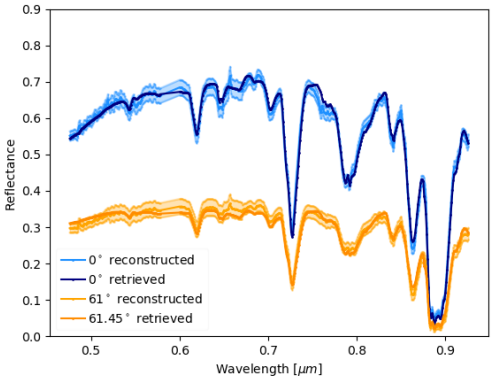
(b) 10°N



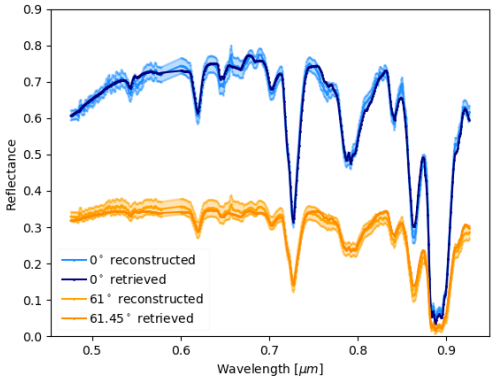
(c) 20°N



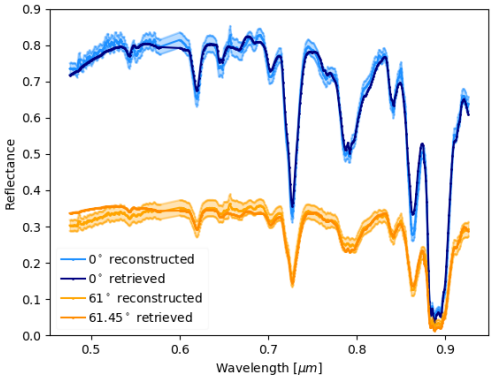
(d) 30°N



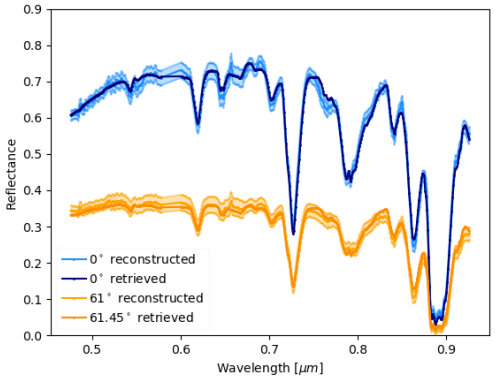
(e) 40°N



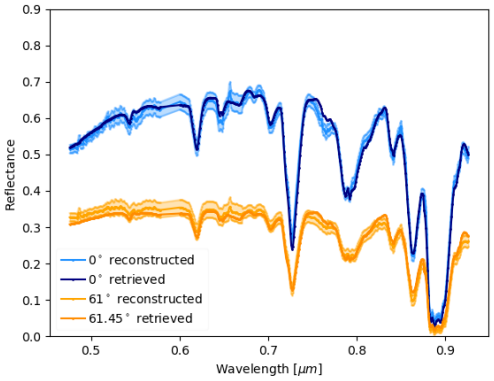
(f) 10°S



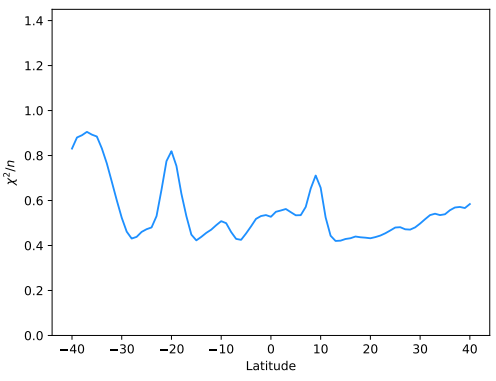
(g) 20°S



(h) 30°S



(i) 40°S



(j) χ^2/n

Figure 6.5.2: Retrieved spectra for dual viewing angle retrievals for 2022, Blue – 0.0° viewing angle Yellow –61.45° viewing angle, with the paler of each colour being the observations and the darker line being the retrieved spectrum. 6.5.2j shows the χ^2/n for all retrievals.

6.6 2023

6.6.1 Appearance and spectral fits

The final observation in our time series, taken in 2023 is shown in Figure 6.6.1. We now have a more 'typical' view of Jupiter with a pale EZ, NTZ and STZ alternated by a red NEB and SEB, similar to that seen in 2018. The NTB is in a pale state and is not contrasting against its neighbouring belts, which have a similar pale shade. The bifurcation of the wake of the GRS seen in 2019 and 2020 does not appear to be the case anymore and a single band of red is seen trailing to the east of the GRS. No region has a particularly extreme shade, be it red or white, and the disc remains coloured with the average shades expected at Jupiter. The contrast between the haze has reduced, with the equatorial enhancement looking less bright than for previous years.

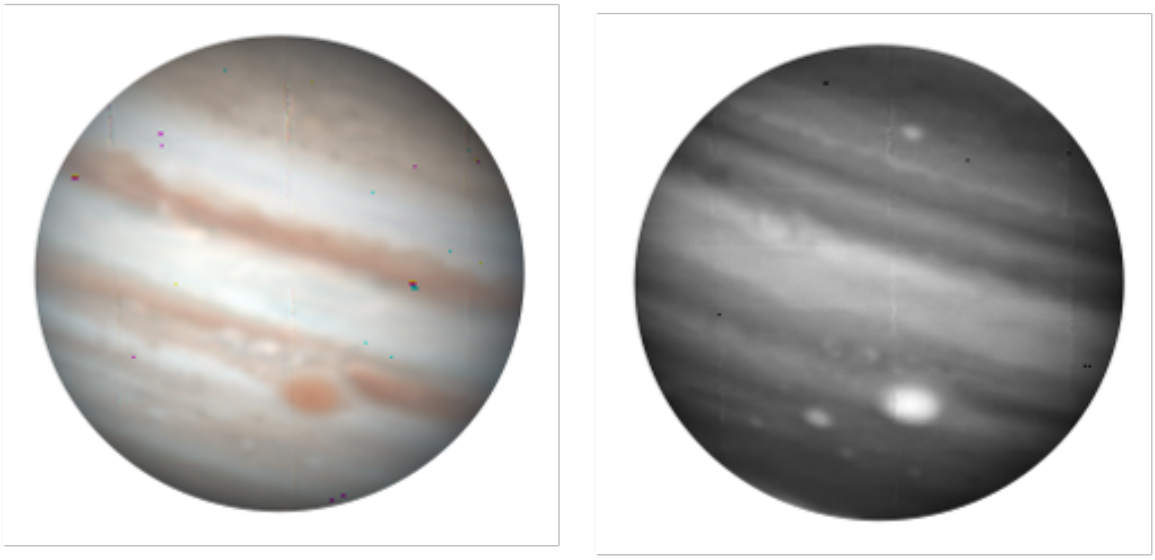
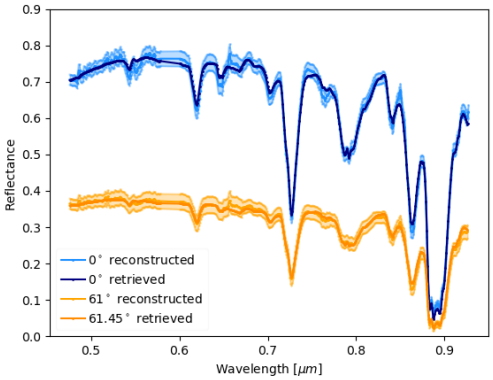
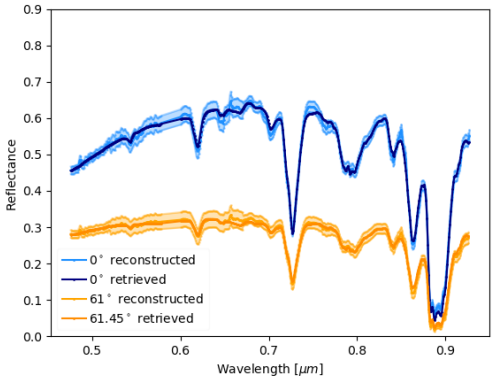


Figure 6.6.1: 23$^{\text{rd}}$ September 2023 RGB (R–675nm, G–530nm, B–480nm) image and 889nm

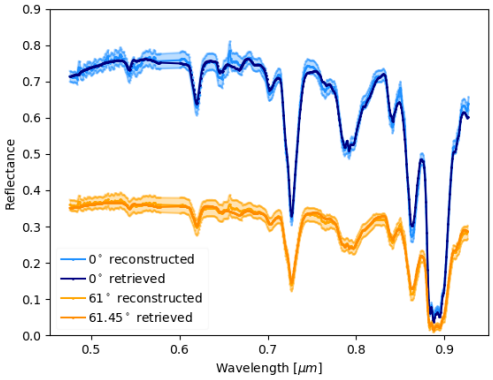
In Figure 6.6.2 we can see that we are able to reproduce the observations incredibly well, with the lowest χ^2/n values of any year.



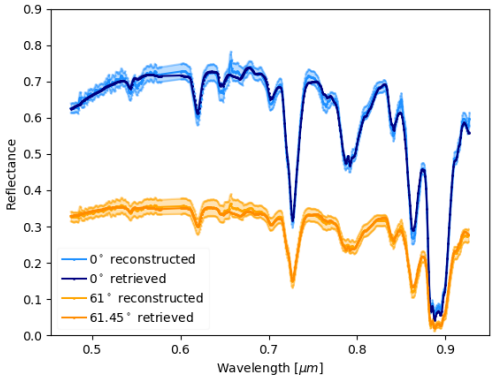
(a) 0°N



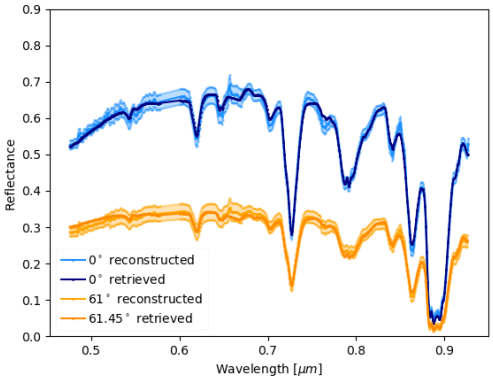
(b) 10°N



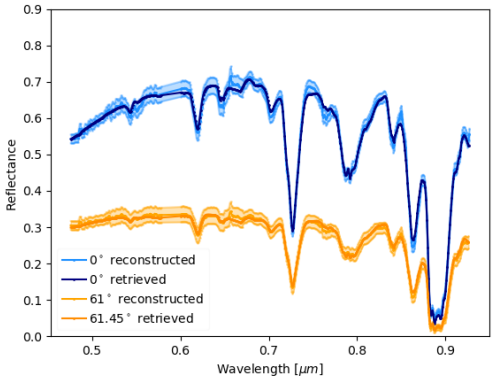
(c) 20°N



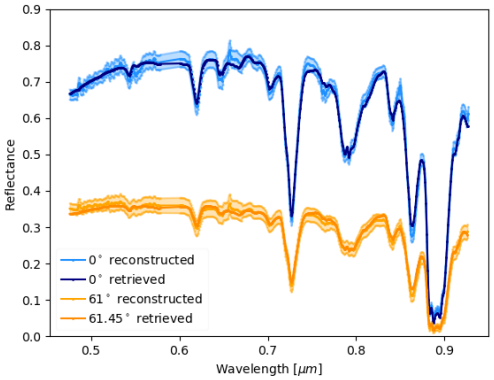
(d) 30°N



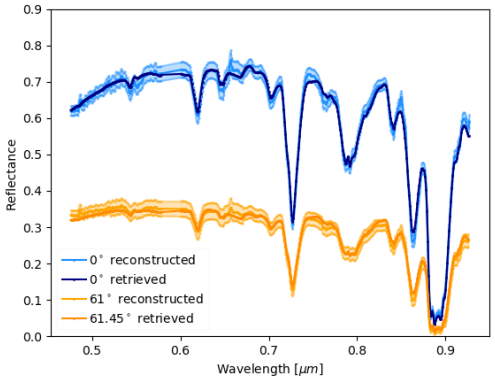
(e) 40°N



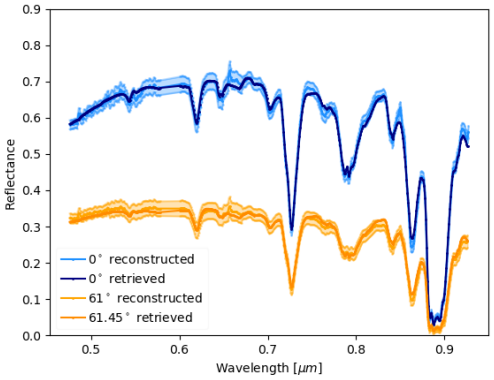
(f) 10°S



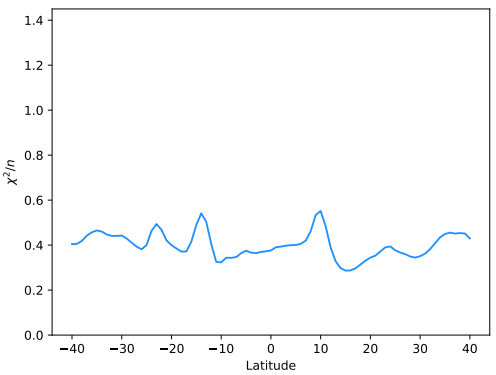
(g) 20°S



(h) 30°S



(i) 40°S



(j) χ^2/n

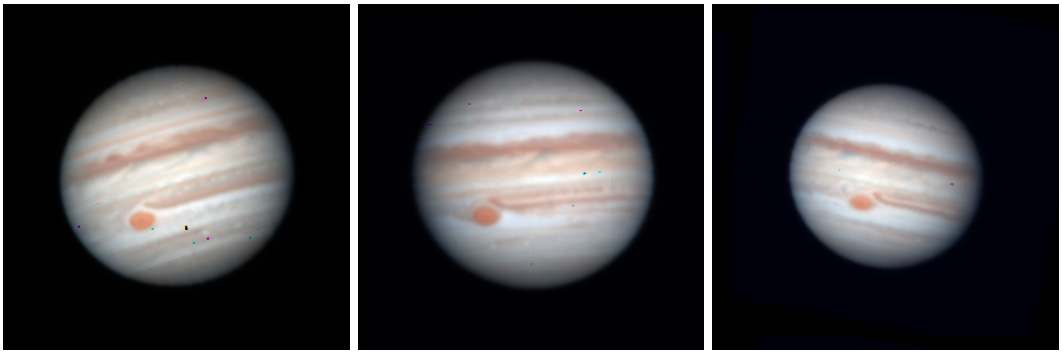
Figure 6.6.2: Retrieved spectra for dual viewing angle retrievals for 2023, Blue – 0.0° viewing angle Yellow –61.45° viewing angle, with the paler of each colour being the observations and the darker line being the retrieved spectrum. 6.6.2j shows the χ^2/n for all retrievals.

6.7 Inter-annual variability of parameters

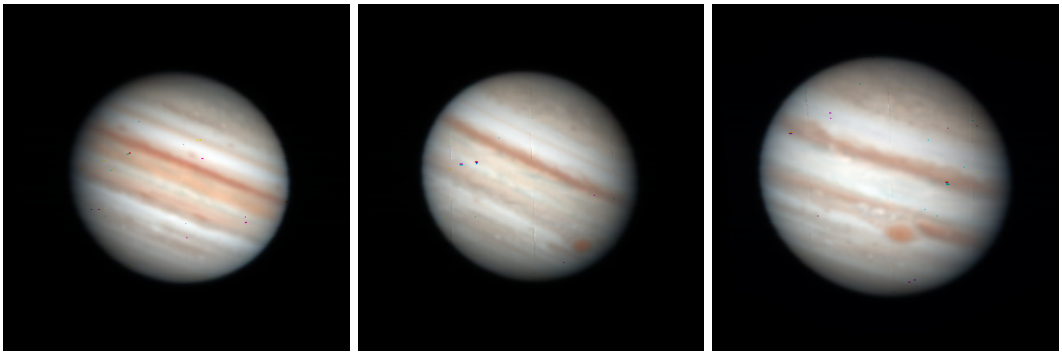
Having successfully reproduced observations for each year in our dataset, we now compare the retrieved parameter values to determine more about how the atmospheric conditions are linking to the cloud top appearance on Jupiter, (Section 6.7.1). Through the retrievals of the variable parameters, ammonia volume mixing ratio (Section 6.7.2), cloud and haze total opacity and width (Section 6.7.3), and cloud imaginary refractive indices (Section 6.7.4) we can compare between years to see how the planet changes year on year. Through these retrievals, fitting to medium-resolution

visible/near IR spectra with clear ammonia and methane absorption features, we are able to retrieve aerosol profiles as well as ammonia abundances, we can then link to cloud-top appearances through the changes in the retrieved imaginary refractive indices. Despite their simplicity and minimal variable parameters we will demonstrate below how this model is able to adapt to several regions across multiple observations over six years.

6.7.1 Appearance



(a) 2018 (b) 2019 (c) 2020

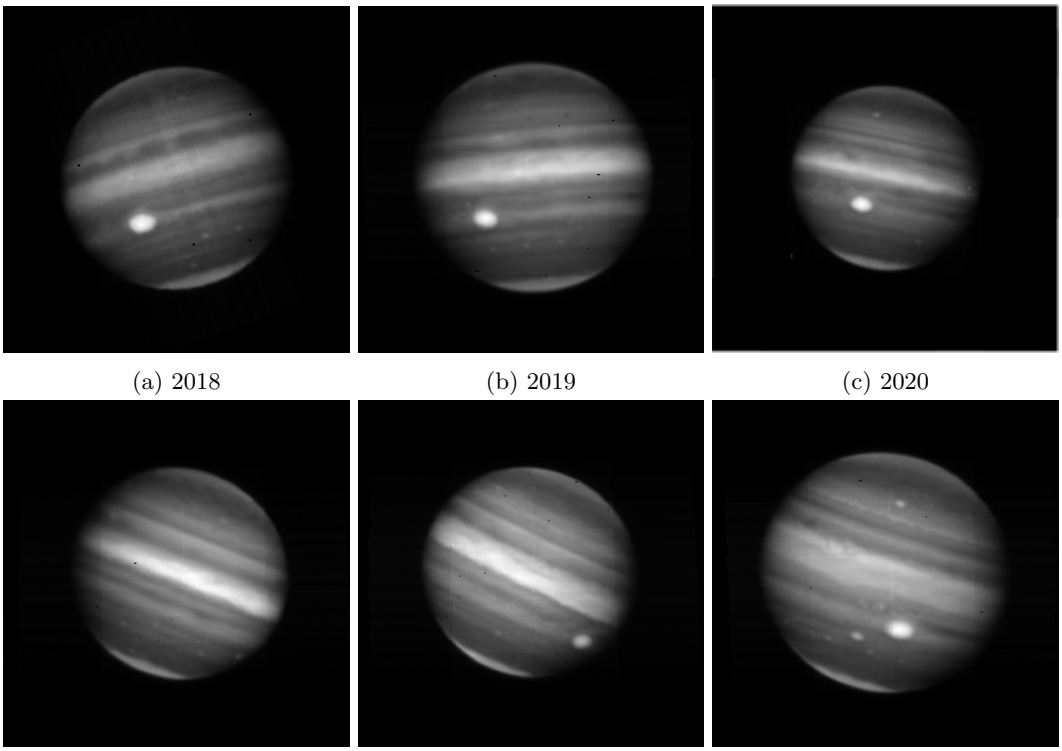


(d) 2021 (e) 2022 (f) 2023

Figure 6.7.1: RGB images (R–675nm, G–530nm, B–480nm) for each observation from 2018 to 2023, capturing the variation of the Jovian cloud top appearance over the span of 6 years.

Between each year there is a significant amount of variation to the visible appearance of Jupiter, shown with RGB images in Figure 6.7.1. The most significant retrieved changes in the parameterisation typically relate to colouration events as regions fluctuate between red hues and paler colours, such as the reddening of the EZ in 2019 and 2021. As we are extracting idealised spectra for this

work, the small scale changes due to individual features are not represented in the reproduced spectra as we are creating an average for each latitude band. This includes the GRS as it is masked when the limb-darkened latitudinally-averaged spectra are Minnaert-fitted. The results for the GRS are presented in Section 6.8. Instead in this section we focus on the broader changes which are happening across Jupiter's disc.



(a) 2018 (b) 2019 (c) 2020

(d) 2021 (e) 2022 (f) 2023

Figure 6.7.2: 889nm images for each observation used, showing the high level haze variance.

There are multiple changes to the appearance of the Equatorial Zone over the 6 years of observations, undergoing two major colouration events in 2019 and 2021, where both observations have a red/orange appearance compared to the typical pale white-ish colouration of this zone. For all years the NEB is our most prominent shade of red within the zones and belts, yet it still undergoes variation. The spatial extent of the dark red colour of the NEB varies, with it at its narrowest extent in 2021, and diminished in 2022 as well. The SEB, undergoes colouration variations of its own, with varying depths to its colouration, however it also has variation due to the distribution of

the dark red material to the east of the GRS. Whilst the GRS itself is masked for these retrievals the variation around it is not. Therefore we will have captured the variation in the red distribution to the east of the spot which has a single larger red area in 2018 and 2023, and a two pronged area for 2019 and 2020 (2021 and 2022 are unknown due to the longitudes in view).

Figure 6.7.2 shows each observation at 889nm, which captures information about the haze across the disc. For each year we see that the equatorial zone is brightest region, indicating the largest amount of haze across the disc, (except for the GRS which is masked for these retrievals). For the observations in 2019 – 2022, the equatorial region has a brighter signature indicating a more significant abundance of the haze in this region compared to the rest of the disc.

6.7.2 Ammonia distribution

Figure 6.7.3 displays the retrieved volume mixing ratio of ammonia for the deep atmosphere for the retrievals 40°N – 40°S, Figure 6.7.5 show each year plotted together. For each year we have been able to reproduce the ammonia distribution reported by previous studies (Li et al., 2017; Moeckel et al., 2023), with a peak ammonia amount around 5°N before a strong depletion around 10°N. The retrieved amounts are mostly consistent across the time period, typically peaking around 1.5×10^{-4}.

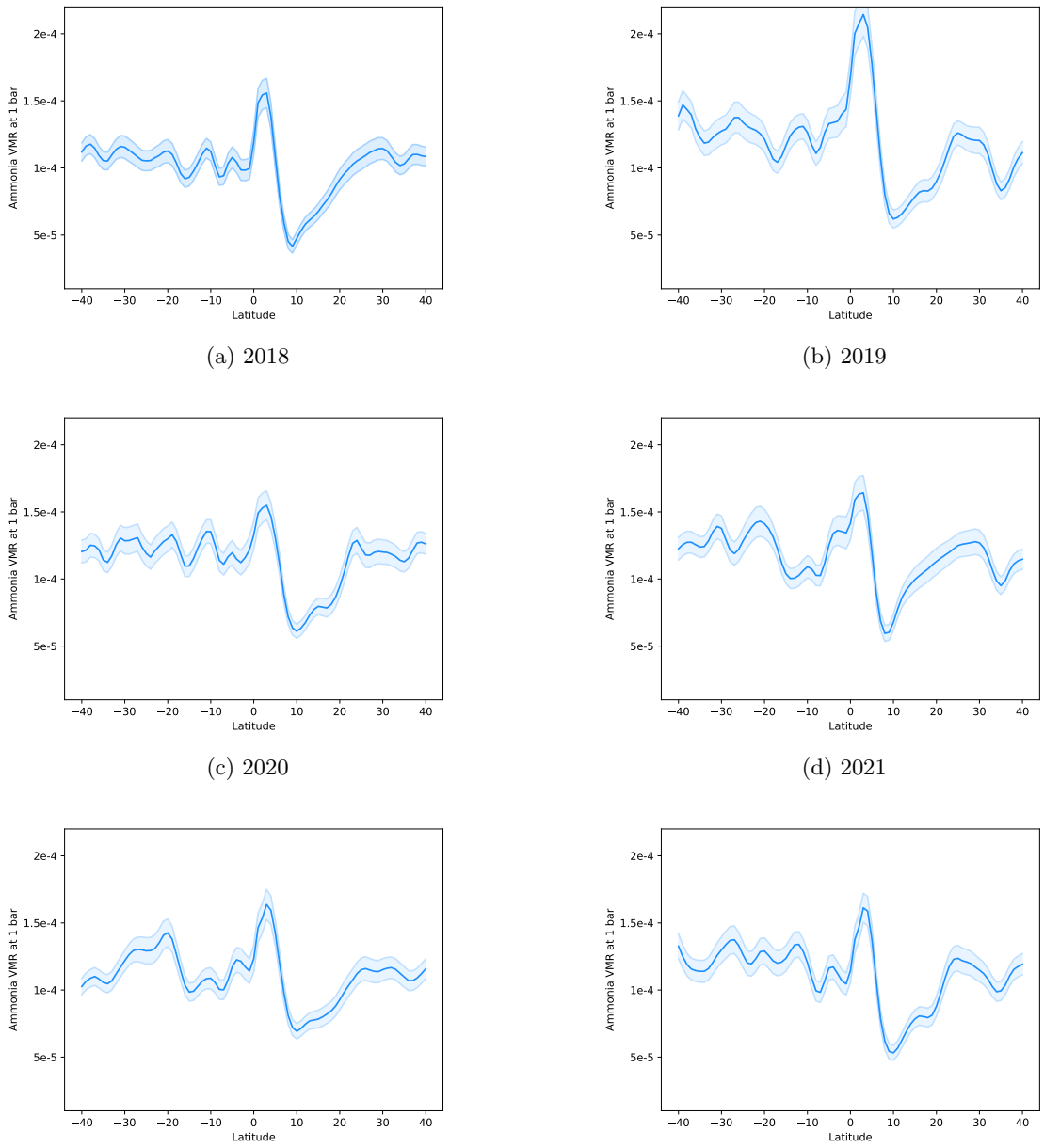
The 5°N peak for most observation years retrieved a VMR value of $\sim 1.5 \times 10^{-4}$, except in 2019 where we instead retrieved a peak VMR around 2.2×10^{-4} before returning to similar values for the following years (Figure 6.7.4). As we have previously identified degeneracy between ammonia and haze opacity, as well as cloud opacity and width (Figure 5.3.5), we cannot be sure of this result and it may not be reflecting true conditions in the atmosphere. We can theorise that the increased VMR could be associated with a temporarily strengthened circulation pattern leading to stronger uplift at the equator, bringing more ammonia from deeper levels enhancing the mixing ratio. As proposed by Guillot et al. (2020), small scale circulation patterns for the equatorial region would lead to enhanced ammonia concentrations over a small spatial ranges. The increased circulation strength would likely bring about an enhanced amount of haze, but this is not clearly seen for the 2019 observations (Figure 6.7.2) or the retrieved opacity (Figure 6.7.6) where no significant variations are

seen between the observations before or after. However, the lack of increased haze does not rule out enhanced uplifting during 2019, as the haze amounts are not solely controlled through dynamical motion of the atmosphere and are also associated with other factors such as temperature changes and abundance of cloud condensation nuclei (Fletcher et al., 2020). The haze also resides above the pressure where we see the ammonia enhancements, therefore if the increased circulation does not extend as high into the atmosphere it would not cause an enhancement in the haze.

It is also possible that this retrieved ammonia enhancement is a side effect from the degeneracy which we have between parameters within our model. For example, we have noted a degeneracy where the retrieved haze opacity and ammonia abundance are sometimes anti-correlated, but on inspection we do not see unusual retrieved haze parameters for this region. However, other degeneracies may exist that have not been identified, leading to the larger VMR to be retrieved for the 2019 observations. Further investigation to determine whether the enhancement retrieved here is real or an artefact of our degenerate parameter space should be undertaken before further conclusions are drawn about the ammonia variance. If it is determined to be a true feature, discovering the time scale of the enhancement could help to determine more about the dynamics of the atmosphere by using ammonia as a tracer species. However, this work is outside of the scope of this thesis.

The retrieved VMRs differ from radio retrievals of ammonia, Moeckel et al. (2023) find a value in excess of 3.5×10^{-4} for the peak VMR at 1 bar at the equator in 2013. However, the Moeckel et al. (2023) work is subject to different degeneracies than this work, instead affected by degeneracy with temperature profile rather than the aerosol profile. Undertaking our retrievals over a wider parameter space may be leading to degeneracies which result in smaller retrieved VMRs. The reduced VMRs could also be attested to the simplification of the vertical distribution of ammonia in the atmosphere due to the use of a parameterisation scheme, rather than a retrieval of a continual profile. Either of these shortcomings of the retrieval scheme could lead to the reduced deep volume mixing ratio being retrieved. However, the ability of a single *a priori* value for all latitudes being able to reproduce the expected ammonia distribution provides confidence that the parameterisation scheme is a good representation of Jupiter's atmosphere through its ability to reproduce the pattern

of ammonia distribution found in other works focused solely on this (Li et al., 2017; Moeckel et al., 2023).



(a) 2018

(b) 2019

(c) 2020

(d) 2021

(e) 2022

(f) 2023

Figure 6.7.3: Retrieved volume mixing ratio of deep ammonia (below 0.7 atm) for 40°N – 40°S for all observations. Retrieved errors are in pale blue.

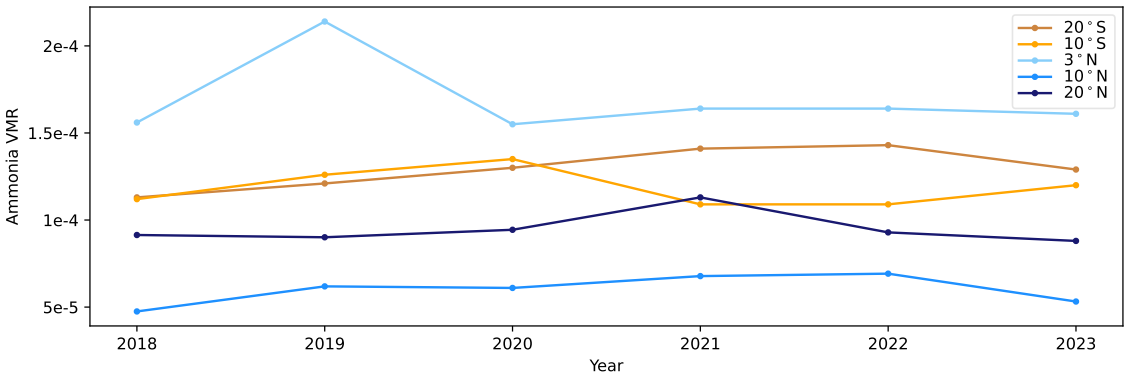


Figure 6.7.4: The deep VMR of ammonia (below 0.7 atm) for a selection of latitudes (20°S, 10°S, 3°N (peak VMR), 10°N, 20°N) plotted for all observation years.

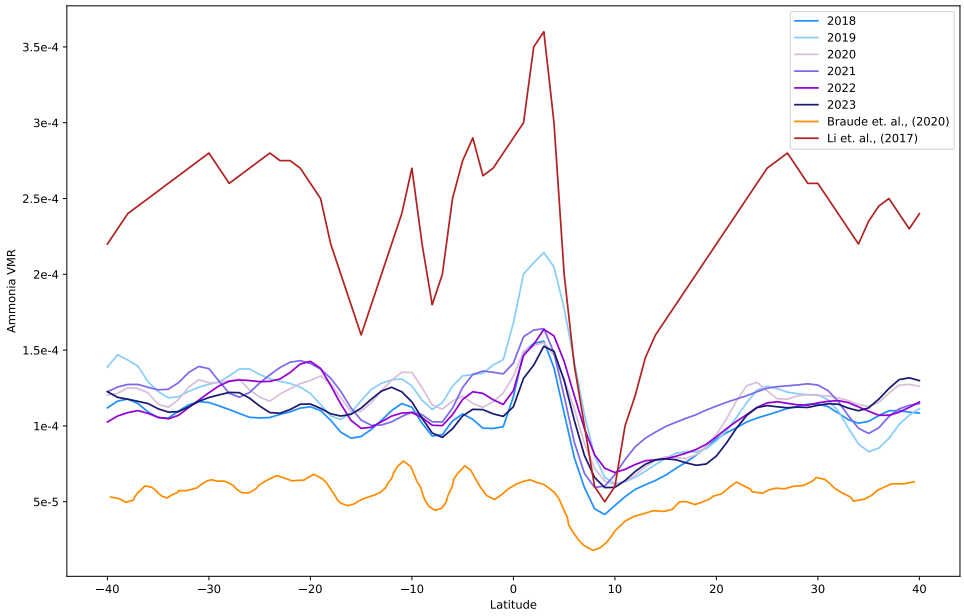


Figure 6.7.5: All deep VMR of ammonia for all observations plotted alongside Li et al. (2017) Juno VMR ammonia abundance at 1 bar as well as Braude et al. (2020) retrieval of ammonia VMR.

As our model is retrieving a wide range of other parameters for the atmosphere, comparison with like works allows us to understand how our retrieved ammonia values compare to other multiple

parameter retrievals. Braude et al. (2020) retrieved a single longitude swath fitting a single viewing angle, for the same observation as ours in 2018, allowing us to compare retrieved values across the disc (Figure 6.7.5). For their ammonia profile they were retrieving both the VMR as well as the fractional scale height. The minimum in the ammonia abundance was found at 10°N with a retrieved VMR of 2.0×10^{-5}. Although this decrease came from a local maximum, a clear enhancement at 5°N over all other regions was not retrieved. Instead there are larger VMRs retrieved at 5°S and 10°S, which were not seen in this work, nor that of radio retrievals (e.g., Li et al. (2017)). Braude et al. (2020) find a typical VMR of 6.0×10^{-5}, whereas the typical VMR for a radio observation is larger, around 2.5×10^{-4}. Dahl et al. (2021) also find inconsistencies with their retrieved ammonia distribution for their model set up which is most similar to that of Braude et al. (2020) (Model 2). However, for this work only comparisons between the scale factor of an ammonia profile between the EZ, SEB and NEB are possible. Model 2 in Dahl et al. (2021) (based on Braude et al. (2020)) retrieved a larger scale factor, thus VMR, for the NEB compared to the EZ, opposite to that expected. Dahl et al. (2021) Model 1, which was based on the Crème Brûlée model of Sromovsky et al. (2017), retrieved an enhancement of ammonia at the EZ and depletion at the NEB, resembling the expected ammonia distribution more closely than Model 2, using both fixed and retrieved RI parameters. The same enhancement for the EZ region and depletion at the NEB was also seen by Sromovsky et al. (2017) with the Crème Brûlée model results. However, with only three data points to compare for these retrieved ammonia distributions it is hard to fully characterise the ability of these models to retrieve ammonia across the disc at every latitude.

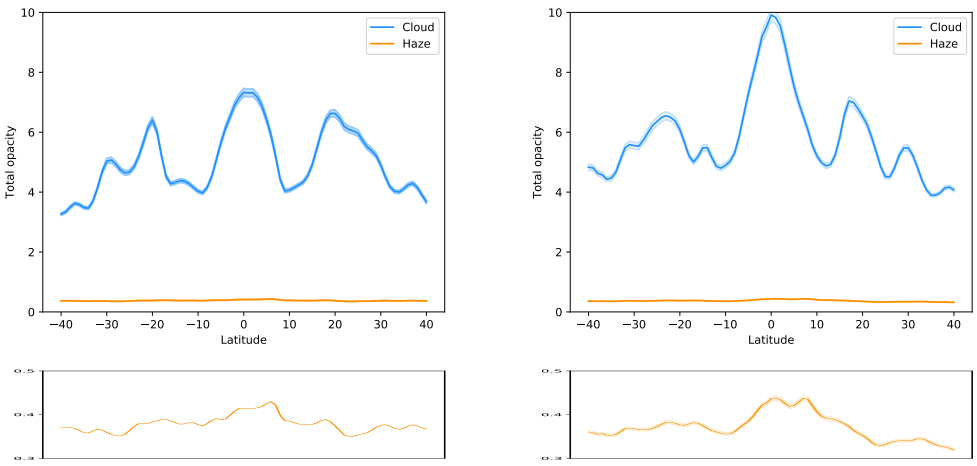
The ability of our parameterised scheme to retrieve a realistic ammonia distribution across Jupiter with a single variable parameter, whilst retrieving an aerosol profile simultaneously provides confidence in the ability of our parameterisation scheme to be a good representation of the atmosphere. Matching the spatial distribution of radio observations (e.g., Li et al. (2017) and Moeckel et al. (2023)) whilst retrieving other parameters may introduce some degeneracy within our parameter space, leading to smaller VMRs than those retrieved when studying ammonia alone. However, our ammonia distributions, with an enhancement at 5°N and depletion at 10°N, are more similar to the radio retrievals of ammonia than previous works, and have been retrieved with a smoothly varying

profile across the latitudes of interest for multiple observations.

6.7.3 Opacity

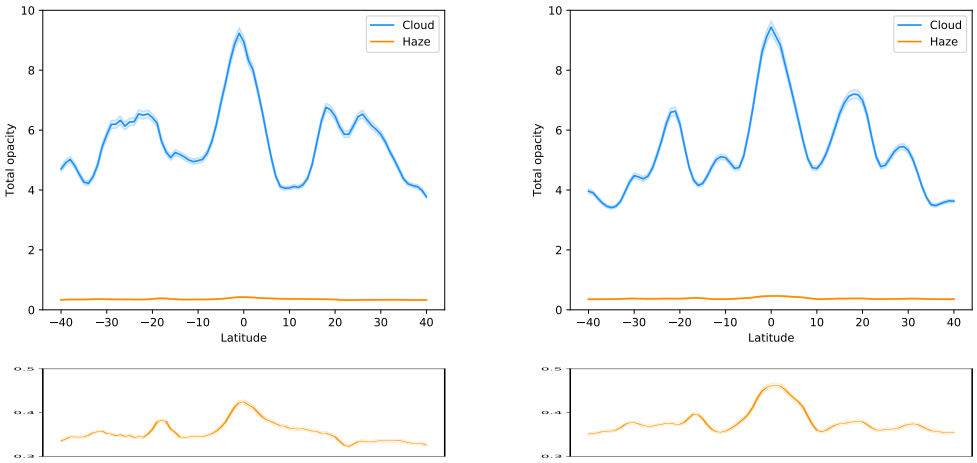
Within the parameter scheme the most variable part of the atmospheric model is the opacity of the haze and cloud layers. With both the fractional width of the Gaussian layer and the total opacity being variable parameters for both haze and cloud layers. Through their variation alongside the imaginary RI values, we are able to fit to observations across the disc. Figure 6.7.6 shows the retrieved total opacity (i.e., cloud and haze) for all observations and Figure 6.7.7 shows the opacity per bar across the disc for each observation. Every year we can see a pattern appearing for the retrieved cloud opacity which captures the variation of the zone and belt regions, with higher total opacities of cloud forming in zonal regions which are associated with up-welling air. For each year the equatorial zone has the largest opacity, linking to its strong up-welling circulation.

The variation in the cloud top appearance of the EZ, through the change in colour from a pale region in 2018 to a light red in 2019, then a pale year in 2020 before the strong colouration event in 2021, before fading through 2022 to the palest of our observations in 2023, is not strongly linked to variation in the retrieved total opacity, Figure 6.7.8a shows relatively flat retrieved opacity for latitude bands which undergo strong colour changes during the observation period. For some of these colour changes we are able to see variation through the retrieved cloud total opacity, with larger total opacities retrieved in 2019 and 2021 aligning with the years of the boldest colours. However, we also see an enhancement in 2020 where the EZ is more faded in its shade, and mainly an off white shade. Therefore, we are not expecting a greater opacity of the cloud layer, which contains the chromophore, to explain the red appearance alone. The colour of each region will also be affected strongly by the retrieved imaginary refractive index (Section 6.7.4), therefore through a combination of both the cloud opacity and imaginary refractive indices we are able to reproduce observations.



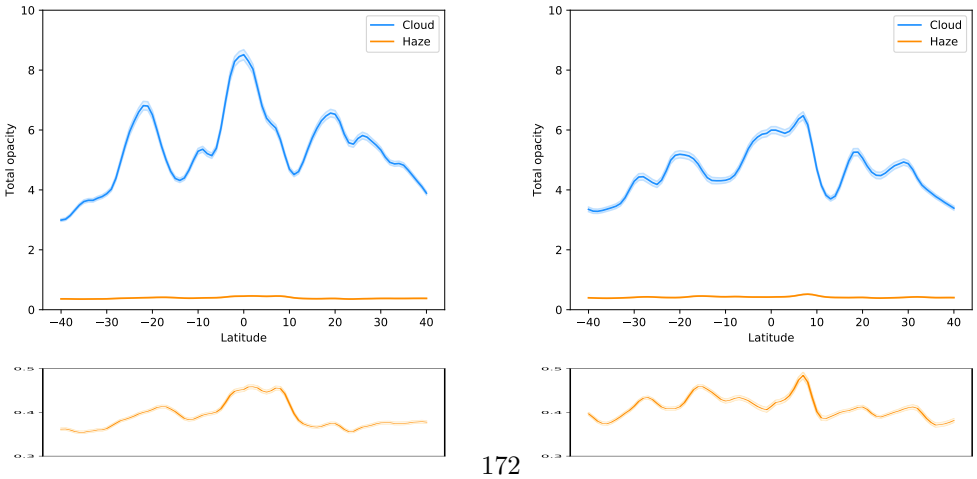
(a) 2018

(b) 2019



(c) 2020

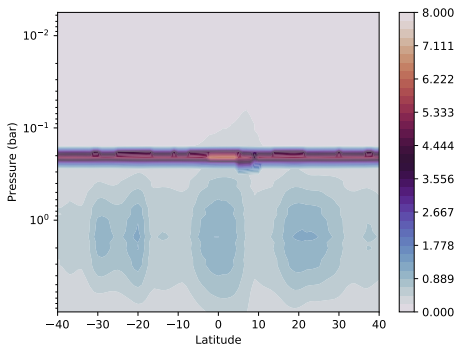
(d) 2021



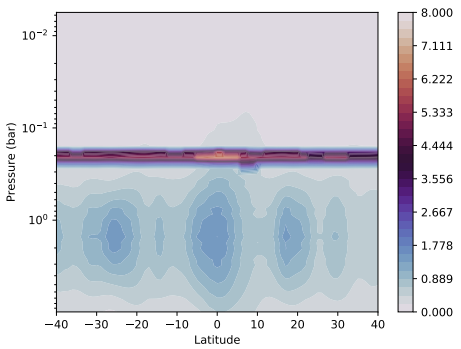
(e) 2022

(f) 2023

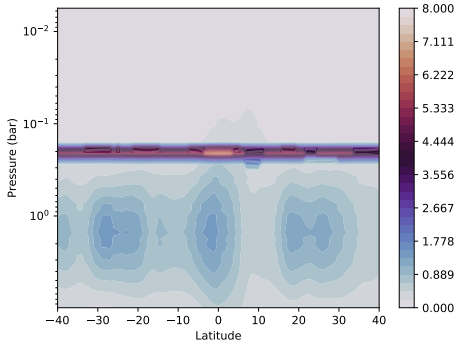
Figure 6.7.6: Retrieved total opacity for all observations, with the cloud layer in blue, with pale blue retrieved error, and the haze in orange, with pale orange retrieved error, the bottom panels show the haze opacities on a different scale to better show how they vary across latitudes and time.



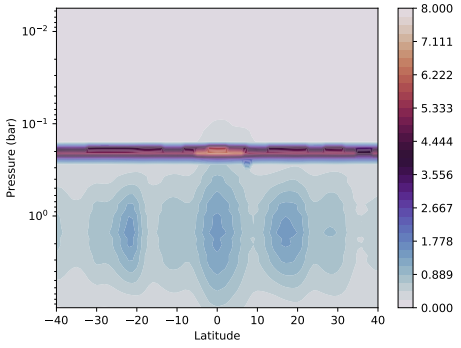
(a) 2018



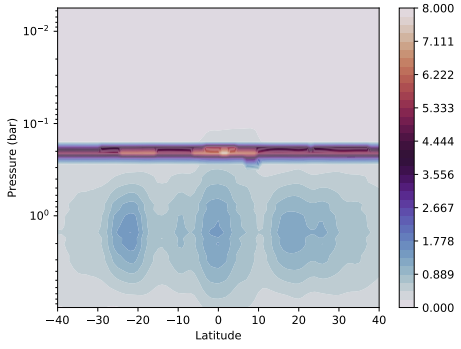
(b) 2019



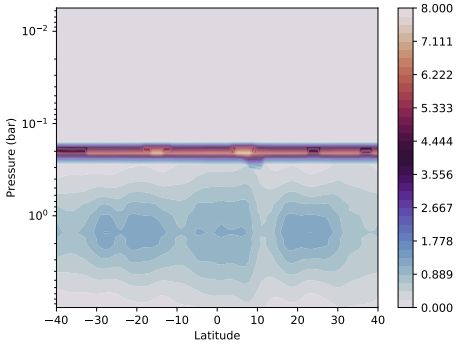
(c) 2020



(d) 2021



(e) 2022



(f) 2023

Figure 6.7.7: Opacity of the vertical profile for all observations 2018-2023, for latitudes 40°N – 40°S, displayed in opacity/bar units.

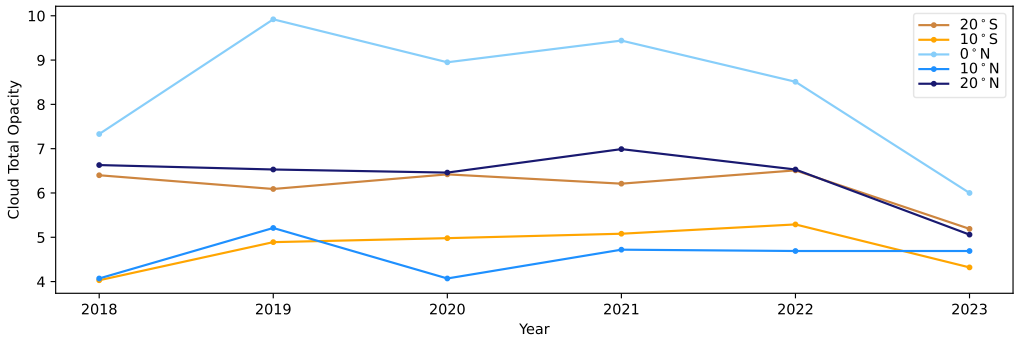
The retrieved haze distribution also matches the observations with the peak in the haze being around the equatorial regions. The location of the peak haze amount varies between years, seen both in

Figure 6.7.2 and Figure 6.7.6. For example, in 2020 and 2021 the brightest part of the equatorial haze in 889nm is seen to the south of the equator, as is retrieved in the total opacity of the haze peaking more towards 5°S. During this time we have a large change in the visible appearance of the equatorial zone as it turns red, so it's possible an alteration in the haze could indicate changes to the uplift and circulation patterns of the EZ. For more absorbing chromophores to be produced they likely require a longer time to be irradiated indicating a reduction in the rate of overturning. This could lead to more haze accumulating if the removal mechanisms have slowed down. Pérez-Hoyos et al. (2020) found an increase in the tropospheric haze based at 0.2 bar during a NTB colouration event. The opposite is seen for the two observations in 2018 and 2023, where the haze has the least enhancement at the equatorial zone compared to other regions, and where both have similar pale appearances. This would indicate a potentially more rapid circulation, leading to less haze accumulation and paler chromophore RI values due to less irradiation time to match the observations. Over the observation period, we also see a gradual enhancement in several locations away from the Equatorial Zone, seen in Figure 6.7.8b. This could indicate a variation in the distribution of the haze, where the enhancement becomes less apparent over the EZ alone and an enhanced background level is retrieved, which is seen in Figure 6.7.7 additionally.

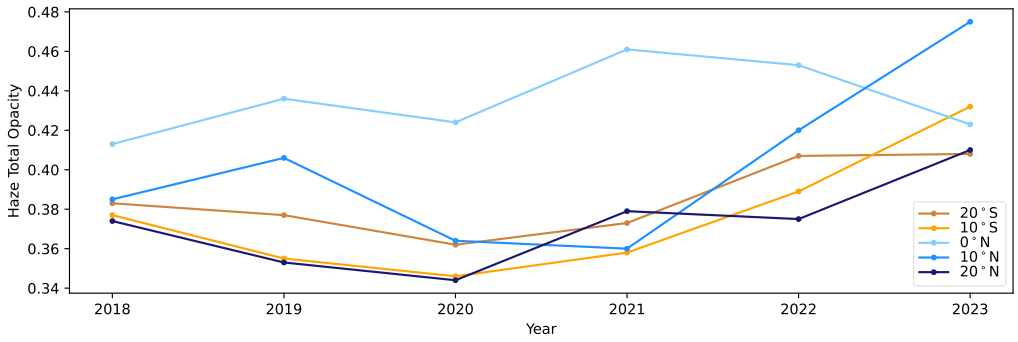
Figure 6.7.7 allows us to see how the aerosol is distributed through the vertical profile. For all years we have a very thin but dense haze layer, whereas the cloud layers are far more diffuse (but with a higher total opacity). Above the zonal regions, which correspond to the highest total opacity, we can also see they have higher opacity/bar in the haze layers. The Gaussian parameterisation of the aerosol layers means that they have symmetric distributions as we have a fixed peak pressure level. Within the main cloud layer we see that we have much more substantial opacity in the zonal regions, which peter significantly at the belts as expected with dynamical models of the circulation.

Figure 6.7.8 shows the variation of the total opacity for the cloud and haze layers for a selection of latitudes across all observation years. From this we can see that the cloud opacity is relatively stable for most locations over several years, with the equatorial cloud opacity increasing in 2018 and 2021 which are associated with the colouration events for this regions. The haze opacity is more variable.

We typically associate the Equatorial zone with having the most haze across the disc (except the GRS) however the peak within this region does move between years (as seen in Figure 6.7.6). In 2023 the 0°N no longer has the highest haze opacity due to the haze peak shifting north as seen in the 889nm observations (Figure 6.7.2) the peak is now 9°N, see through the 10°N being elevated for 2023 in Figure 6.7.8a. However, in this latitude region we have seen other errors associated with the large ammonia VMR changes, due to the high opacity retrieved for this narrow window, it is possible that there is also degeneracy occurring within the retrievals for this region around 9°N as the haze opacity is higher than would be expected from the 889nm appearance. However, since 2020 there is a general increase in the haze opacity away from the EZ, which is seen through 889nm observations, and a decrease in the brightness of the 889nm appearance of the EZ which is seen the decrease of the haze opacity at 0°N.



(a) Cloud

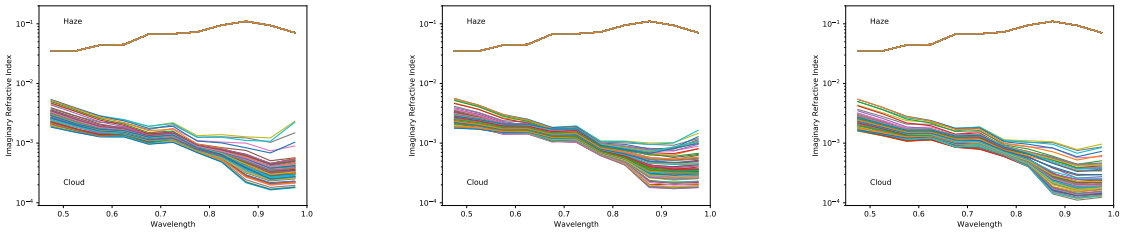


(b) Haze

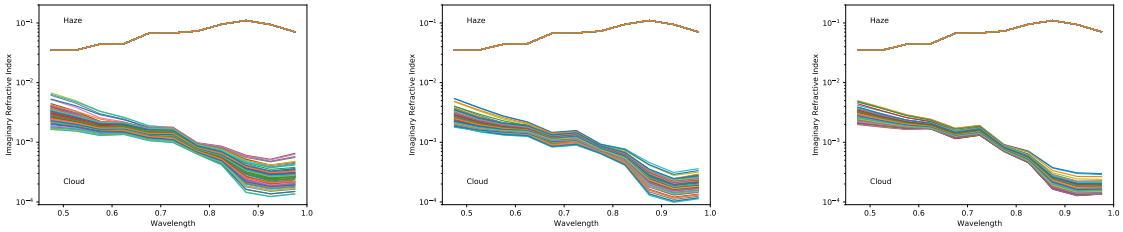
Figure 6.7.8: The total opacity of Cloud (top) and Haze (bottom) for a selection of latitudes (20°S, 10°S, 0°N, 10°N, 20°N) plotted for all observation years.

6.7.4 Imaginary Refractive Index

The parameterisation scheme only allows the cloud imaginary refractive indices to vary, with all other optical constant values fixed. Therefore, we expect variations in the values retrieved to account for the different colour and appearance of the cloud tops across observations. We assume that the main cloud layer contains both a spectrally flat material, such as NH_4SH, mixed with the chromophore material in some form. Each material has different imaginary RI values and what we retrieve is a mixture of both of these materials. Therefore, the retrieved RI depends on the ratio of chromophore to cloud material, with the indices assumed to add linearly, scaled with the mixing ratios. Further RI changes between regions may be caused by differences in the properties of the chromophore itself, as it is possible that differing exposure in each location, potentially caused by differing clouds conditions, leads to spectral variation. Differing dynamic conditions, due to the motion of air in each region, could lead to a range of over-turning times for cloud which would result in different exposure times for material. As chromophore material is exposed to different amounts of radiation it is theorised that the refractive indices may also change, seen in the Carlson et al. (2016) chromophore which produces a steeper blue absorption slope as it is irradiated for a longer duration. Differences retrieved for the cloud RI in different locations may capture a combination of these properties, leading to the different values retrieved in each region. The retrieved values for each observation are presented in Figure 6.7.9. The retrieved imaginary refractive index of the cloud at 525nm is shown in Figure 6.7.11, we also display the difference in RI value between 525nm and 625nm in Figure 6.7.12 which allows us to compare the blue slope for the retrieved cloud imaginary RI.

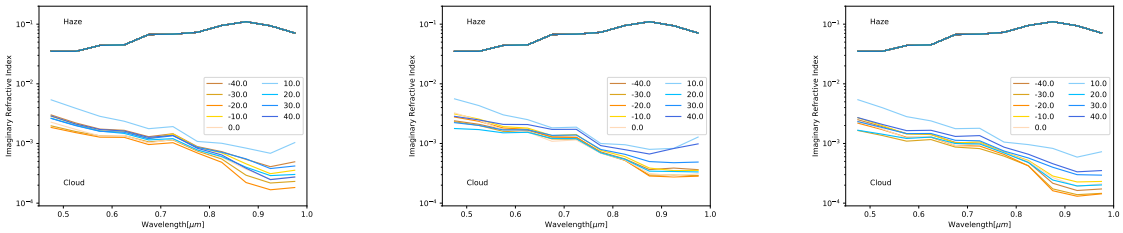


(a) 2018 (b) 2019 (c) 2020

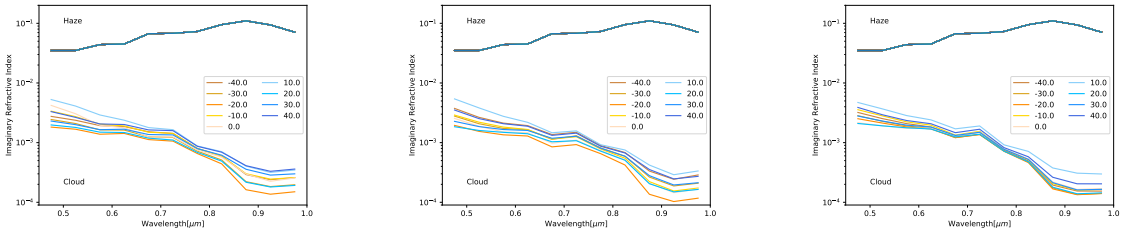


(d) 2021 (e) 2022 (f) 2023

Figure 6.7.9: The retrieved imaginary refractive indices retrieved for each observation, the top line is the fixed retrieval for the haze, then the cloud RI values for all latitudes below. (Figure 6.7.10 has labelled latitudes for a selection of latitudes.)



(a) 2018 (b) 2019 (c) 2020



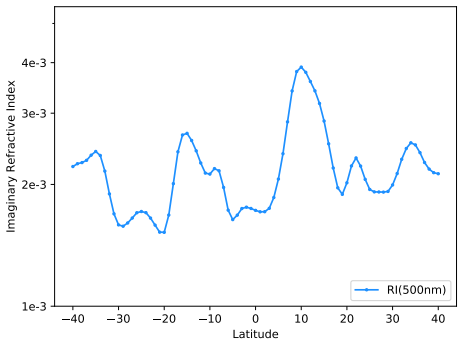
(d) 2021 (e) 2022 (f) 2023

Figure 6.7.10: The retrieved imaginary refractive indices retrieved for each observation for 40°N – 40°N with every 10° shown. The top line is the fixed retrieval for the haze.

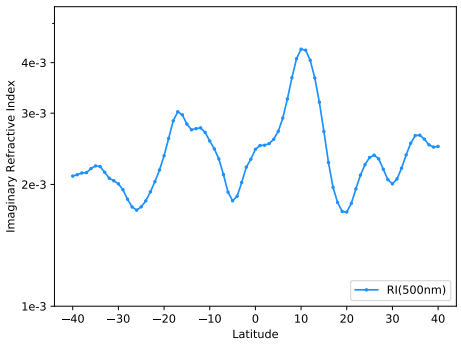
Due to the large number of latitudes being retrieved for each observation, we show a selected number of latitudes in Figure 6.7.10 to better see how the RI values change across the disc of Jupiter for all wavelengths. The variation in the values of the cloud imaginary refractive indices can be explained through two differences. First, as we expect the main cloud layer to contain both non-coloured, potentially spectrally flat material (e.g., NH_4SH as assumed with the real imaginary refractive), mixed with a chromophore substance which would have varied absorption across the wavelength range, difference between RI values for each latitude could be accounted for by differing mixing ratios of each material. This leads to brightening and darkening of the retrieved RI values, with the same RI shape but different values retrieved (Figure 6.7.11). We see that the redder regions in each observation have a greater retrieved RI value at 525nm. The peaks and troughs in Figure 6.7.11 relate closely to the variations in colour across the disc. Differences in imaginary RI can also occur due to variation in the properties of the chromophore material which alters its spectral properties, leading to different spectral slopes (which can be seen in Figure 6.7.12. Again, redder regions have greater slope values, indicating a steeper blue slope and more blue absorption. A combination of these two properties can produce the range of appearances across the disc of Jupiter.

For every observation the steepest blue slope of the retrieved RI and highest value of RI at 525nm is retrieved for the region around 10°N, corresponding to the NEB, the darkest shade of red on the disc (Figure 6.7.11, 6.7.12, Figure 6.7.13). In 2021 the colouration of the EZ is seen through an enhancement of both the RI retrieved at 525nm and also the RI slope, as shown in Figure 6.7.13. We can infer that we are adapting to the cloud top appearance through the properties of the cloud refractive indices due to a variation in the chromophore, rather than differences in the total opacity which has minimal changes between 2021 and 2023. We see that some reddening events require an increase in the imaginary RI as well as a steepening of the RI slope (Figure 6.7.13), such as the 2021 EZ colouration, both an increase in chromophore material (RI at 525nm value) and a change in the chromophore properties (steepening of the RI slope) is needed. However, for some years the variation is only represented through a change in the RI slope, such as the EZ from 2022 and 2023, where the imaginary RI at 525nm is similar value but the slope is shallower in 2023 when the region is paler indicating a more absorbing chromophore, giving the 2022 EZ its redder appearance despite

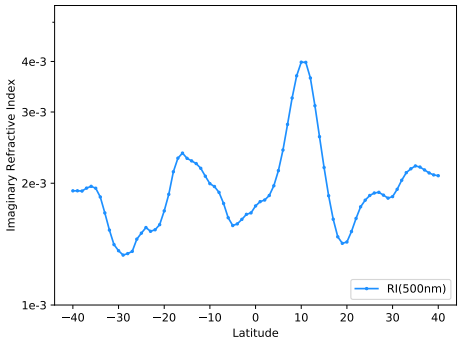
a similar mixing ratio for each year.



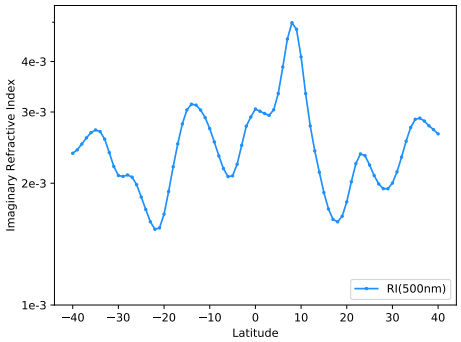
(a) 2018



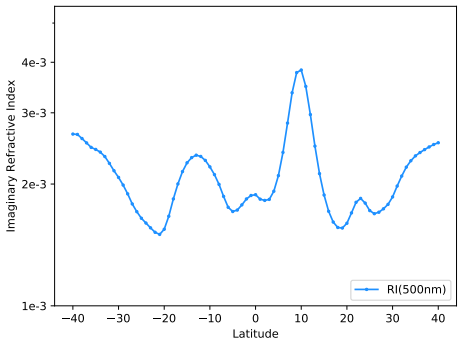
(b) 2019



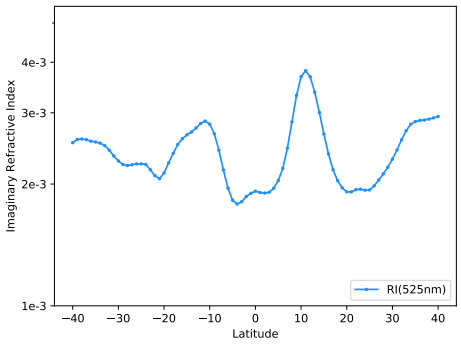
(c) 2020



(d) 2021

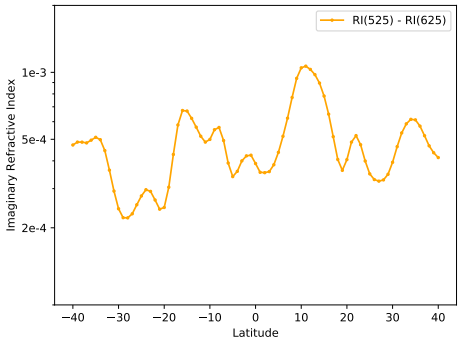


(e) 2022

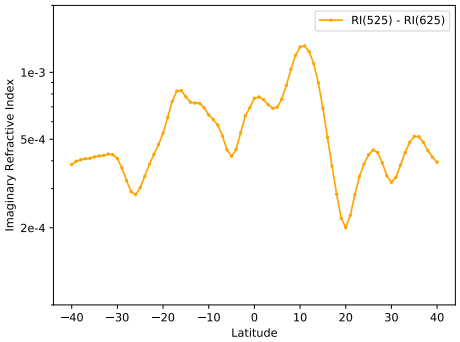


(f) 2023

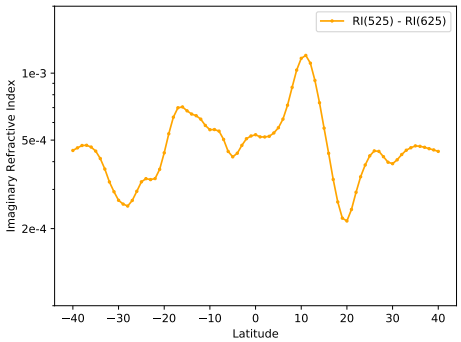
Figure 6.7.11: The imaginary refractive index value retrieved for the cloud at 525nm plotted for all observations across the latitude range. Larger values indicate a higher mixing ratio of the chromophore (with potential steepening of its slope) within the cloud layer.



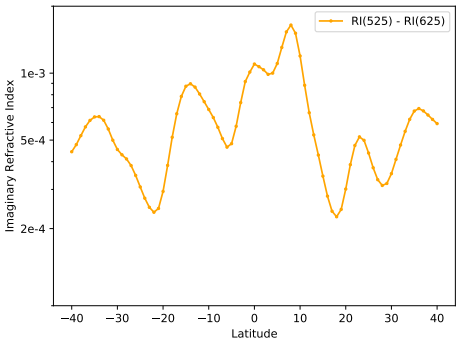
(a) 2018



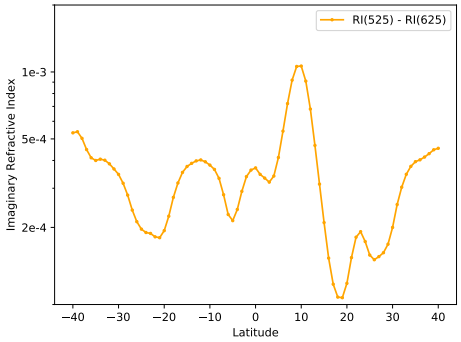
(b) 2019



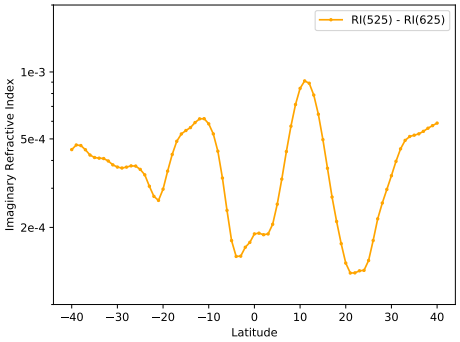
(c) 2020



(d) 2021

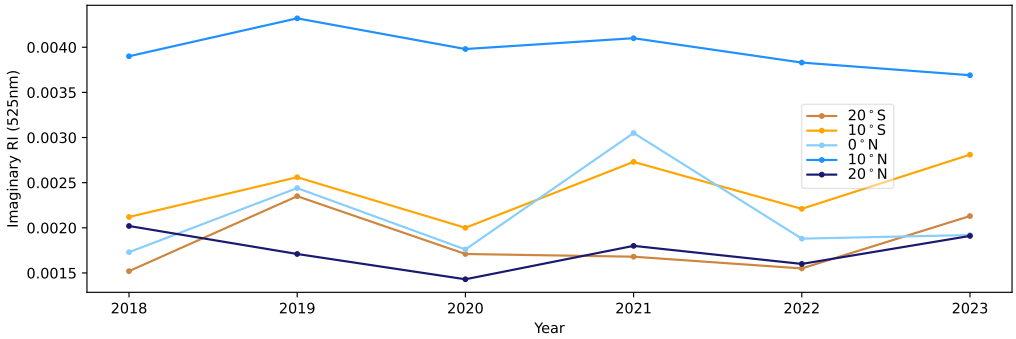


(e) 2022

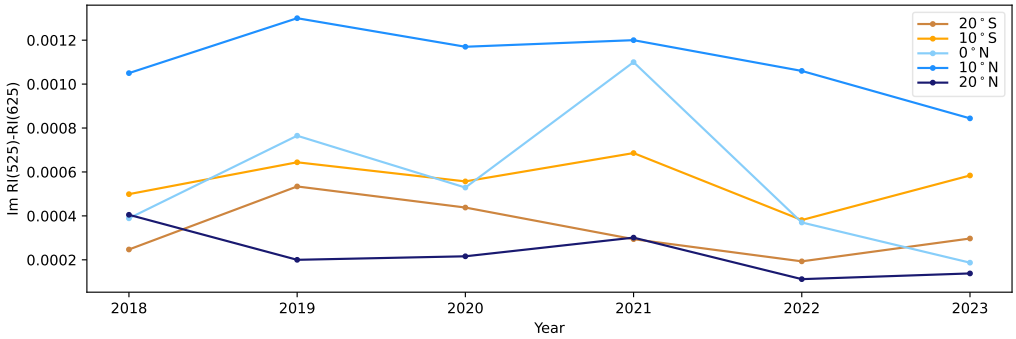


(f) 2023

Figure 6.7.12: Measure of the imaginary refractive index slope, the difference between retrieved values of imaginary refractive index at 525nm with the value at 625nm for all observations plotted across the disc. Larger values indicate a steeper blue slope for the chromophore indicating a redder appearance.



(a) Imaginary Refractive Index [525nm]



(b) Imaginary Refractive Index Slope [525nm-625nm]

Figure 6.7.13: The Imaginary Refractive Index values at 525nm (top) and imaginary refractive index slope, difference between 525nm and 625nm values (bottom) for a selection of latitudes (20°S, 10°S, 0°N, 10°N, 20°N) plotted for all observation years.

Similar RI values variations have been retrieved by Pérez-Hoyos et al. (2020), who have a tropospheric haze mixed with a chromophore material in their Model A, which has lower values around 500nm due to mixing with cloud material, but a similar RI slope to the Carlson et al. (2016) chromophore. Between two retrievals of the same region in subsequent years, Pérez-Hoyos et al. (2020) also see a variation in the RI slope among other parameter alterations to captures the changes in the NTB as it undergoes a colouration event. In addition an increase in the mixing ratio of chromophore material in the layer, from 190±30 part/cm^3 up to 280±70 part/cm^3 is also seen (Pérez-Hoyos et al., 2020).

Longer irradiation of the chromophore material could lead to an alteration of the spectral properties due greater UV exposure. This is seen in Figure 6.7.14 for the Carlson et al. (2016) chromophore,

where longer exposure times lead to a steeper blue absorption slope of the imaginary refractive index. As each region on Jupiter is likely to have varied dynamics, this would create different over-turning times across the disc, which could produce the different RI slopes which have been retrieved through our parameterisation. This was also seen in Dahl et al. (2021) (Figure 6.7.15), as the SEB, EZ and NEB had different retrieved RI values, which were similar in shape to both the Carlson et al. (2016) imaginary RI and each other, particularly for the slope gradient below 600nm. Despite the EZ and SEB regions being pale, Dahl et al. (2021) had retrieved a similar imaginary RI shape as for the NEB of darker colouration, even as a pure chromophore material layer. Therefore, the sloping cloud RI retrieved for all latitudes in our work agrees with the need for blue absorption even for paler regions, as can be seen in Figure 6.7.10, for 2023 when large swaths of Jupiter are bright white, the retrieved RI is still more absorbing at shorter wavelengths for even the palest regions (0°N, 20°N and 20°S).

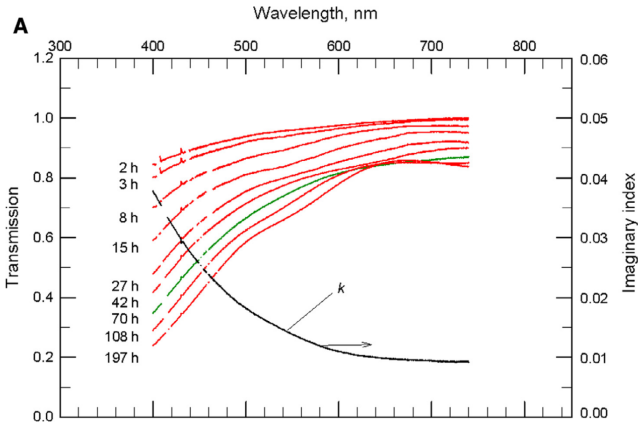


Figure 6.7.14: Transmission values for Carlson et al. (2016) chromophore material when exposed to radiation for differing amounts of time, the black refractive index line is taken for 70 hour radiation time (green).

The haze imaginary refractive indices are fixed for these retrievals, and are given in Table 5.3.1, having been predetermined before the main retrievals were undertaken. Having had no predetermined *a priori* for the RI values of the haze, instead fixing the values to what the spectral fits and χ^2/n values indicated as the best fit, we now need to compare these results to known substances. Optical constants can be identified through laboratory work, but the amount of data available for viable

species on Jupiter for both viable conditions and the correct wavelength range. Much of the work undertaken has been done for longer wavelengths than considered in the MUSE observations. This limits our ability to compare with real data to assess what species agree with our retrieved results. One suggestion which matches to the retrieved haze profile is a species which falls into the category of a tholin.

Tholins are complex compounds derived from carbon-containing molecules (such as methane or ethane) which have formed through photolysis of the starting molecule. They have been found across the solar system, notably on Titan, and have a range of imaginary refractive indices values which are comparable to those retrieved for our haze (He et al., 2022). Tholins tend to have a decreasing imaginary RI within our wavelength range, associated with their typically red hue, however, the steepest slope is at wavelengths shorter than $0.5\mu m$ (He et al., 2022). Another recent study, Grassi et al. (2024), assessing the aerosols of Jupiter, but using JIRAM observations around $5\mu m$, also found that tholins were able to best reproduce observations over species such as NH_3 and NH_4SH. However, we do not have the optical constants for all of these species within our wavelength range to be able to test the same conclusions. To better conclude what the haze particulates may be comprised of we need more laboratory data within our wavelength range.

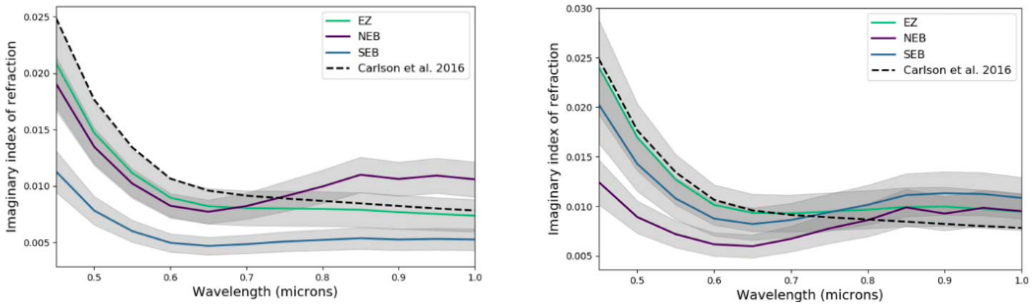


Figure 6.7.15: Retrieved imaginary refractive index values reproduced from Dahl et al. (2021) for the EZ, SEB and NEB. Left – Model 1 (similar to Crème Brûlée), Right – 2b (similar Braude et al. (2020)).

This is also the case for the cloud refractive index, as we are unsure of the normalised real RI values of the bulk cloud composition, however we expect it to be scattering with low imaginary RI values. Without the known properties we cannot fully calculate the mixing ratio of this material

with chromophore produces the retrieved imaginary RI. Therefore, any discussion on the material which is producing the cloud and haze imaginary refractive indices is hampered by the lack of visible laboratory data.

Despite our efforts to minimise the number of free parameters and thus the degeneracy within this parameterisation scheme, the free refractive indices of the main cloud layer will likely mean some error due to degeneracy remains. The ability of the imaginary RI values to alter the retrieval across the whole spectral range makes it an important parameter to retrieve, but it can also potentially account for variations which may be caused by other parameters, as seen in Figure 5.3.5. One such region where this could be an issue is $0.8\mu m$ onwards, as we see a greater range in the retrieved RI values, without a likely mechanism to drive these changes. We again could theorise changes in the chromophore material are due to differing amounts of irradiance, but there is no laboratory data in this wavelength range to provide evidence to support these changes. However, the increase in imaginary RI that we see for some regions, notably 10°N, has also been seen by others. Dahl et al. (2021) find for a pure chromophore layer, with the Carlson et al. (2016) chromophore as an *a priori* input, that an increase in imaginary RI around these wavelength greater than $0.8\mu m$ was retrieved for their NEB (Figure 6.7.15). Braude et al. (2020) also retrieves an increase in imaginary RI at $0.825\mu m$ onwards. We cannot compare these results to experimental data as it does not exist. Users of the Carlson et al. (2016) have to extrapolate values long-ward of $0.74\mu m$. Therefore, without further laboratory data with a wider wavelength range we cannot decipher what the variability of the imaginary RI values means with regards to our chromophore material or what may be causing these changes not seen for all regions. The longer irradiation times which steepen the blue absorption slope may also be altering the imaginary RI properties at longer wavelengths, however this cannot be known without further laboratory experiments.

The large amount of variability of the parameters, particularly due to us retrieving a mixed cloud, means direct comparison is difficult with other works. However, we still share similarities in our work with others. The slope of the Carlson et al. (2016) chromophore is similar to the retrieved values in our work, and it is also used with modifications for different regions (e.g., Braude et al. (2020), Pérez-

Hoyos et al. (2020), and Dahl et al. (2021) (Figure 6.7.15)). These variations occur both in the slope below $0.6\mu m$ but also through longer wavelength variations as values deviate from those extrapolated from Carlson et al. (2016) recorded values. The work of Pérez-Hoyos et al. (2020) also sees a decrease in the retrieved RI values for their mixed chromophore layer, indicative of mixing with other material. In addition, as the NTB region reddens, Pérez-Hoyos et al. (2020) retrieve a greater mixing ratio of the chromophore material within their layer to account for the variations in appearance. Although there are notable differences between past works, due to many having retrieved a pure chromophore layer unlike this work, we still retrieve similar variations in the retrieved imaginary refractive indices for the chromophore containing layers. These similarities between previous works include resemblance to the Carlson et al. (2016) when RI values are retrieved (rather than fixed to its values), but also through most models requiring modifications to the imaginary imaginary RI slope of the Carlson et al. (2016) chromophore in order to fit other regions or observations of Jupiter.

6.7.5 Fixed parameters

In addition to our retrieved parameters, we also wish to compare our fixed parameters with previous literature. There is a huge range of aerosol profiles in previous works with varying number of aerosol layers, different locations and composition. Several models (e.g., Crème Brûlée style models (Sromovsky et al. (2017), Baines et al. (2019), Dahl et al. (2021)), Pérez-Hoyos et al. (2020) Model A) had a high-level stratospheric haze located above 0.1 bar up to 0.01 bar, typically with very small optical depth of in the order of 0.001 (Pérez-Hoyos et al., 2020). We do not have a third layer in our model due to no indication of an aerosol layer at this level during our 'Snippet' analysis, plus the desire to simplify the parameter space. As we were able to fit to observed spectra without this layer, it seemed unnecessary to complicate the parameter space for no further improvement in fit.

The upper layer in our model is a haze layer centred at 0.2 bar, which ranges approximately 0.05 bar above and below the peak pressure. We have a relatively flat refractive index for this material, and with no slope below $0.6\mu m$, indicating a non-chromophore material. For Pérez-Hoyos et al. (2020) (both models), and Sromovsky et al. (2017) GRS and NEB models, this is the pressure level at which the chromophore layer has been placed. Simultaneously fitting to spectra at two viewing

angles gives us much more constraint on the location of the chromophore material which we find to be located deeper at the main cloud layer. However, our spectrally flat haze layer is located at a similar pressure level. Dahl et al. (2021) (using a model based on the Crème Brûlée model) finds a higher level for the chromophore layer, residing around 0.1 bar in the SEB and NEB, and 0.04 bar for the EZ, as with other Crème Brûlée models these chromophore layers are attached to the main cloud layer at the top. The low pressures to which the Dahl et al. (2021) clouds extend are not reproduced in our models, as we have no aerosol contribution above 0.1 bar. The Crème Brûlée style models then have a range of pressures for the base of the cloud for each location, ranging from 4.9 bar at the SEB (Sromovsky et al., 2017) to 2.1 bar at the EZ; the pressures of Dahl et al. (2021) lie within this range. Pérez-Hoyos et al. (2020) retrieve for their mixed chromophore model (A), a main cloud layer spanning 0.7 – 0.9 bar and for the Crème Brûlée model (B), a cloud base of 1 bar, chosen due to a lack of sensitivity deeper in the atmosphere in this work. These reside at the very tops of our main cloud layers, but the majority of our opacity lies below these levels, due to our peak opacity residing at 1.4 bar.

The free profile of the Braude et al. (2020) aerosol profile is defined as haze above 0.15 bar, meaning both aerosol layers in our model would be classified as cloud. Braude et al. (2020) also retrieved a stratospheric haze for the EZ above this point, with a constant opacity/bar of around 1, up to 0.01 bar (where it did not decrease, but lower pressures are not shown). In the cloud domain Braude et al. (2020) retrieve two enhancements to the opacity for the EZ and NTB, peaking around 0.25 bar, and then a deeper cloud at around 1.5 bar. These retrievals are very similar to the parameterisation used in this work. In the NEB Braude et al. (2020) retrieve a single peak in the opacity, with a block shape cloud from 0.2 – 1.5 bar, before decreasing with depth. The contribution to the opacity from the chromophore also varies in location between these regions ranging from a peak $\sim$ 0.3 bar in the EZ to 0.6 bar peak in the NEB with a pressure range of 0.4 bar. However, the retrievals for the GRS differ greatly with the contribution peaking around 0.2 bar and in a narrower region. The similar location retrieved by Braude et al. (2020) for the aerosol peaks as in this work helps provide further confidence on our retrieved aerosol layer locations. The different location of the chromophore in Braude et al. (2020) may again be due to the lack of constraint due to the single viewing angle

being fitted.

We also find similarities in our pressure levels to those retrieved using infrared observations from both Voyager/IRIS (Bézard et al., 1983) and Galileo/NIMS data (Irwin et al., 1998; Irwin et al., 2001; Irwin and Dyudina, 2002), which found main cloud layers based around 1.2-1.4 bar. These also agree with the only in situ observation of Jupiter's atmosphere, from the Galileo probe, where a peak in the nephelometer signal indicates a cloud layer extending from 0.76 – 1.34 bar (Ragent et al., 1998). Constraints at lower pressure levels are not possible as the probe only began reliable transmission below 0.46 bar. There is also an additional potential signal deeper in the atmosphere from 1.9 – 4.5 bar Ragent et al. (1998) (The profile can be seen in Figure 1.4.3). Unfortunately, the anomalous nature of the $5\mu m$ hotspot, which the probe descended into; has conditions which are unlikely to match closely to other regions on the disc. However, the similarity between the cloud layers seen by the probe nephelometer and those used in our parameterisation scheme, as well as those retrieved from other observations provides reassurance to the the cloud model used in this work.

No other previous study fixes the radius of both the cloud and haze across the disc, leading to a large range of values retrieved across different regions. Our values ($1.62\mu m$ cloud, $0.36\mu m$ haze) are within the huge range of values used in previous literature. We share similarities to some models, e.g., Braude et al. (2020), which had $1.5\mu m$ cloud radius in the NEB and typical values of 0.21 – $0.22\mu m$ for the haze across all regions in Sromovsky et al. (2017). However, there are also retrieved values for some regions which are not fully representative of our work, such as a larger cloud radius of $5\mu m$ used by Pérez-Hoyos et al. (2020) and retrieved by Dahl et al. (2021) and Braude et al. (2020) for certain regions. Our haze radii values are also often larger than those of others which can extend down to $0.02\mu m$ (Dahl et al., 2021). As we have a reasonable variance of our haze and cloud (0.31 and 0.35, respectively) size we are likely capturing a wide range of aerosol sizes. However, by keeping this parameter fixed we reduce degenerate pairings within our parameter space, reducing complexity which these cause, whilst still being able to capture variability through opacity and refractive indices, which we expect to vary, rather than masking these changes through degeneracy

with radius.

The Galileo probe nephelometer was able to extract particle size distributions from its descent, but the retrieved results are dependent on solution values (Mie scattering phase value, real and imaginary indices) which have to be selected in order to calculate the size distribution (Ragent et al., 1998). This can produce a large amount of variation in the retrieved particle size, with solutions sets ranging from $0.81\mu m$ – $7.9\mu m$ depending on chosen values at 1.22 bar. Our main cloud radius resides within these values again providing confirmation to the values selected.

The parameterisation scheme presented here is able to capture the variations which occur across the disc of Jupiter (40°N – 40°S), for more constraining observations simultaneously fitting dual viewing angles. This is done alongside a reduced number of free parameters by predetermining parameters, and yet we are still able to capture the variation in the aerosol profile on Jupiter, reproducing observed parameters such as the haze distribution (see at 889nm) as well as the ammonia distribution. We have been able to retrieve a $\chi^2/n < 1$ for the majority of the latitude regions across several observation dates, covering more latitudes and years than any previous work, all with the same *a priori* conditions.

There are still improvements which can be considered for the model. Degeneracies are still present within the parameter scheme, e.g., haze and ammonia variations around 10°N, and attempting to reduce these degenerate pairings further could improve the outcome of the retrieved spectra. However, the potential methods which could be used to achieve this are outside of the scope of this thesis but will be discussed further in Section 7.3. It is also possible that the simplistic scheme may not be able to capture all of the complexity of Jupiter's troposphere, and potentially could be combining multiple clouds, or species, within the main cloud layer retrieved, if similar to the Galileo probe (Ragent et al., 1998).

Overall, our retrieved parameter values typically lie within the ranges extracted by previous works and in-situ observations, and we share similarities with the profiles of these more complex works. Despite the reduced complexity of this model, with limited variable parameters, we have still been

able to reproduce a huge range of locations and observations, exceeding previous works for this model's adaptability. All this has also been achieved whist fitting to more constraining dual viewing angle observations which have more spatial and spectral resolution than many previous works.

6.8 Great Red Spot Minnaert Retrievals

The results presented below are from two retrievals of the GRS in 2018 and 2022. They use spectra produced from multiple individual observations of the GRS which have been combined to extract dual viewing angle spectra using the Minnaert approximation. From these spectra, we have undertaken a simultaneous dual-angle retrieval for the GRS in both 2018 and 2022. For the GRS we use the same parameter scheme as for the latitudinal retrievals, outlined in Table 5.3.2. The retrieved values for both 2018 and 2022 are given in Table 6.8.1. The retrieved spectra are shown in Figure 6.8.1, while the retrieved cloud imaginary RI are shown in Figure 6.8.2

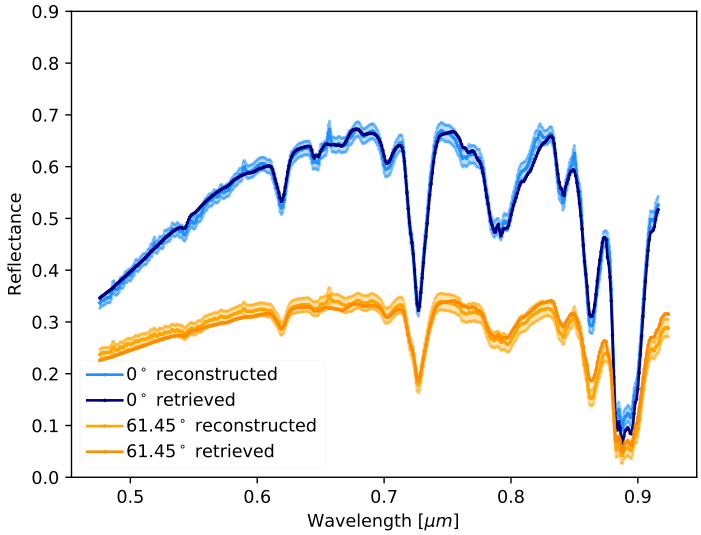
Parameter	*a priori*	error	2018	error	2022	error
Cloud Total Opacity (at $0.825\mu m$	10.0	10.0	8.16	0.179	7.851	0.180
Cloud Fractional Width	1.0	1.0	2.51	0.038	2.39	0.035
Haze Total Opacity	0.4	0.4	0.409	0.00590	0.446	0.00614
Haze Fractional Width	0.1	0.1	0.110	0.0109	0.102	0.0100
Ammonia VMR [$\times 10^{-4}$]	1.0	1.0	0.884	0.0845	1.06	0.0960
χ^2/n	–	–	0.780	–	0.472	–

Table 6.8.1: Retrieved parameters for the 2018 and 2022 observations of the GRS.

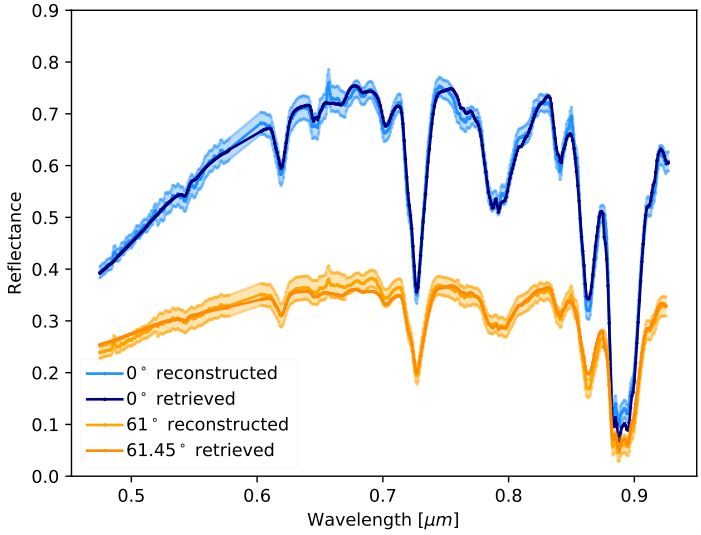
The parameterisation scheme which was developed for the zone and belt regions, with the GRS masked from the spectra, is still able to reproduce the GRS dual angle observations, both for 2018 and 2022, shown in Figure 6.8.1. The retrieved imaginary refractive indices are able to adapt the retrieved spectra to the steep blue slope below $0.6\mu m$, which can be seen through the steep imaginary RI values retrieved for both years in Figure 6.8.2. These retrieved values for the GRS are very similar to the NEB in 2022, however in 2018, they differ below $0.55\mu m$, potentially showing a shallower blue slope but with a greater mixing ratio of chromophore, which can be seen in Figure 6.7.12 as the slope value at 10°N is the lowest in 2018 out of all the observation years. Below $0.6\mu m$ the EZ has a shallower blue slope, as expected due to its paler appearance than the GRS.

One discrepancy between our retrieved values and our knowledge through observations is the amount of haze retrieved, with the retrieved haze opacity for both years being less than that retrieved in the EZ. However, in the 889nm observations, Figure 4.3.3, it is clear that the GRS is far brighter than the equatorial zone and therefore we would expect more haze to be retrieved. This may be due to our parameterisation scheme which fixes the haze imaginary refractive index, which although suitable for belted regions, may not be appropriate for the unique feature of the GRS. In Figure 6.8.1 at 889nm, the modelled reflectance is less than what is seen at 0° but greater than that seen at 61.45°. This indicates that the fixed imaginary RI values of the haze are less limb-darkened than what is needed to reproduce the haze over the GRS. This indicates that the material of the haze at the GRS is exposed to different conditions and/or has a different composition than the haze elsewhere on the disc due to the differing optical properties (more limb-darkened in the GRS).

The retrieved imaginary RI for the cloud which we expect to contain the chromophore material has a similar slope to the Carlson et al. (2016) at wavelengths less than $0.65\mu m$, but with smaller values indicative of the chromophore being mixed with cloud material. The RI values retrieved for the GRS are as large or larger than for any region or year in Figure 6.7.9, with the steepest blue slope. However, the slope is reasonably similar to the reddest regions, e.g., 10°N, indicating that both a higher ratio of chromophore, as well as different properties of the chromophore are needed at the GRS. At longer wavelengths there is no information about the Carlson et al. (2016) chromophore, therefore we cannot assess whether our material is similar at these wavelengths. Many other works (Baines et al. (2019); Sromovsky et al. (2017); Braude et al. (2020); Dahl et al. (2021) extrapolate beyond the data set with a steady value at longer wavelengths, seen as the grey dotted line in Figure 6.8.2. We see for our retrievals of the GRS that the retrieved RI values do not flatten as significantly as the chromophore extrapolated from the Carlson et al. (2016) values, and instead continue to decrease. However, this could be due to degeneracy with the haze RI values which we have determined are not as limb-darkening as needed for the GRS, so these decreasing cloud RI values for longer wavelengths may be compensating for this discrepancy.

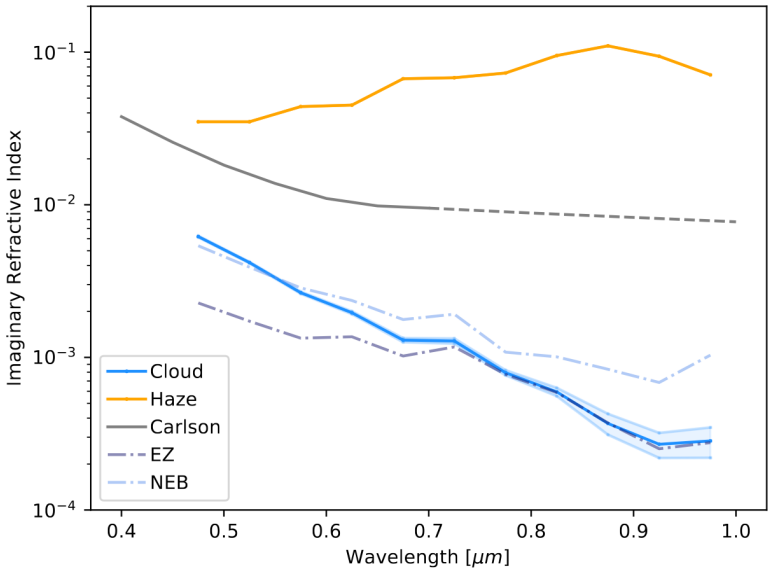


(a) GRS 2018

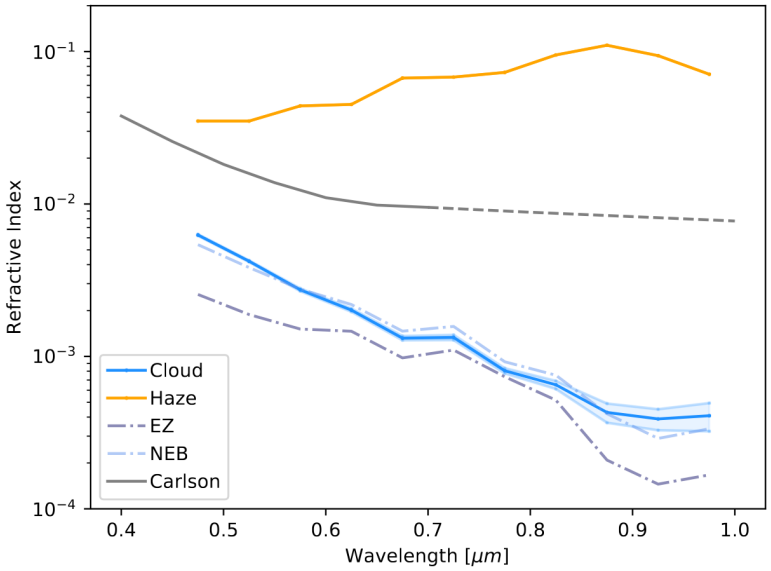


(b) GRS 2022

Figure 6.8.1: Retrieved spectra compared to observed reflectance for the GRS, produced using the Minnaert approximation, for both 2018 (top) and 2022 (bottom), fitting both viewing angles simultaneously.



(a) 2018



(b) 2022

Figure 6.8.2: Retrieved imaginary refractive indices for the 2018 and 2022 GRS retrievals. The orange haze RI is fixed and the blue cloud properties are allowed to vary. The grey profile is the Carlson et al. (2016) chromophore imaginary refractive indices included for comparison. Imaginary RI values for the EZ and NEB for each year are also included for comparison.

Although we believe that we are able to capture the variation across the disc with our parameterisation for zone and belt regions, adapting this to the GRS is not as simple as for other locations or observations. Due to it being an individual feature, the anti-cyclonic storm has very different dynamics from the larger belted structures which the parameterisation was developed for. It is probable that the GRS has a different aerosol profile than other regions. This was seen in Braude et al. (2020) where a free aerosol profile was used; the similar profile retrieved for the zone/belt regions as for our work: was not repeated for the GRS. Instead, larger opacity occurred higher in the atmosphere (around 0.2 bar) with a greater contribution to the opacity from chromophore material. The same variation between these regions could not be captured with our parameterisation because of the reduced range of free parameters, and the chromophore being located in the lower cloud. However, due to the steeper slope at wavelengths less than $0.6\mu m$, we still expect the majority of the chromophore to be located at depth. It is possible that chromophore also resides in the upper layer as well for the GRS, with some works e.g., Simon-Miller et al. (2001); Ordonez-Etxeberria et al. (2016) even suggesting two chromophores are needed to reproduce observations of the GRS. However, the chromophore material currently retrieved by both observations has very similar properties and is able to reproduce the absorption at blue slopes well.

The use of dual viewing angle spectra has provided greater constraint to our models of the GRS and has allowed us to determine that further improvements still need to be made for the model in this region. Further consideration of the pixels selected may be required: in this work, a large box was taken from the centre of the GRS (see Figure 4.3.3), to not capture the variation of the structure at the edge of the storm, but collecting as many pixels from the central GRS to perform the Minnaert fit. However, Anguiano-Arteaga et al. (2021) retrieve two different aerosol properties for regions (classed as GRS nucleus and GRS interior) which both lie in the pixel areas we selected for the Minnaert analysis, indicating that we may be averaging over different structures in our spectra. These structural differences within the centre of the GRS have been seen for JWST observations of the GRS (Harkett et al., 2024; Fletcher et al., 2024) as well as for dynamical models (Zhang and Marcus, 2024). An investigation into how much variation between these regions exists needs to be considered. As we are able to average over great swaths of zonal and belt regions successfully we

may not be as sensitive to these differences as the JWST and HST observations, which have much greater spatial resolution. Therefore, our assumption that the centre of the GRS has similar vertical structures may still be appropriate for the resolution of our observations.

The application of the Minnaert technique to the GRS is novel and the ability to extract and fit dual viewing angles simultaneously provides more constraint for our parameterisation scheme than for previous works. It can reproduce both GRS observations whilst retrieving reasonable estimates for the free parameters. Further investigation into the parameter space would be beneficial due to the potential differences of the GRS compared to other regions. This will allow us to ensure that the best representation of this region is found, but still with a simplified model in order to reduce degeneracy through a smaller variable parameter space.

6.9 Implication of Results for Jupiter's Atmosphere

The information which has been extracted by our retrievals for each observation allow us to build up a picture of how the atmospheric conditions of Jupiter alter over time and allow us to theorise how these changes are driven. As we have fewer variable parameters we are able to more clearly summarise the changes which are happening year on year in our observations, a summary of these changes for a selected number of latitude locations is shown in Figure 6.9.1.

The composition of the haze is not known, nor the source of the material, however, the ability of the discrete Gaussian layer to reproduce observations indicates that it is likely from a condensing source, as with the main cloud layer, rather than photochemical production. If it was comprised of material from a photochemical source, we would expect a more diffuse layer due to the production occurring over a wider range of pressure levels controlled by the depth of incoming radiation. Instead we see a thin dense layer which is more indicative of a condensing species. We do not expect the haze opacity to correlate with changes in colouration due to its fixed imaginary RI which is reasonably flat across the spectral range. We do not see strong enhancements in the haze opacity over the EZ during its colouration in 2019 or 2021 confirming this expectation. After 2020 we begin to see the haze opacity increase for other regions away from the EZ, this may be indicative of a change in the

circulation patterns for the zone belts. We can see in Figure 6.7.7f that the enhanced haze opacity is accompanied by less extended clouds being retrieved, with reduced cloud total opacities being retrieved Figure 6.9.1. This reduction in cloud opacity could indicate a weakened uplift of the air leading to reduced condensation, however, there is no notable reduction in ammonia VMR which would also be affected by circulation patterns.

As the chromophore material is within the cloud layer, any changes to the layer will also affect the visual appearance of the region. Therefore, when we have a large change in colouration in a region, there is likely a link to cloud opacity as well as refractive index properties of the chromophore within. An enhancement of cloud opacity could indicate a weakening of depletion mechanisms for the cloud layer, such as lack of overturning and/or downward motion of cloud. This occurred during the EZ colouration event in 2019, where there was an enhancement in the opacity of the cloud but also the value of the imaginary RI at 525nm, indicating a higher mixing ratio of chromophore, and a increase in the slope between 525nm and 625nm, indicating a more absorbing chromophore. The changes in the imaginary refractive indices lead to the colouration which we can see. However, the changes of these properties are likely driven by changes in the cloud. The change in spectral properties, i.e., change in RI slope, we believe is driven by further irradiation of the chromophore material, due to a similar effect seen by Carlson et al. (2016) for their chromophore under laboratory conditions. Therefore, if we are seeing an enhancement of cloud opacity due to a lower overturning rate then we would also expect chromophore material to be exposed on cloud tops for longer, changing the properties of the chromophore material. A similar pattern is also seen in 2019 for 10°N region when there is a redder NEB region, and also the EZ red colouration in 2021 (though a RI property change is seen in this year).

When the EZ becomes more pale in 2023, we see a reduction in the cloud opacity and a decrease in the RI metrics in Figure 6.9.1, indicating an decrease in the overturning time of the cloud layer meaning that the chromophore material is exposed for less time, leading to a shallower blue slope and a paler appearance. Through this mechanism it allows us to explain the vast colour changes experienced by different zones and belts, without losing characteristic properties, such as cloud and

haze width and opacity and ammonia VMR, which remain reasonably consistent for each location, but instead explaining the visual changes through variation in the atmospheric dynamics which link to chromophore RI properties.

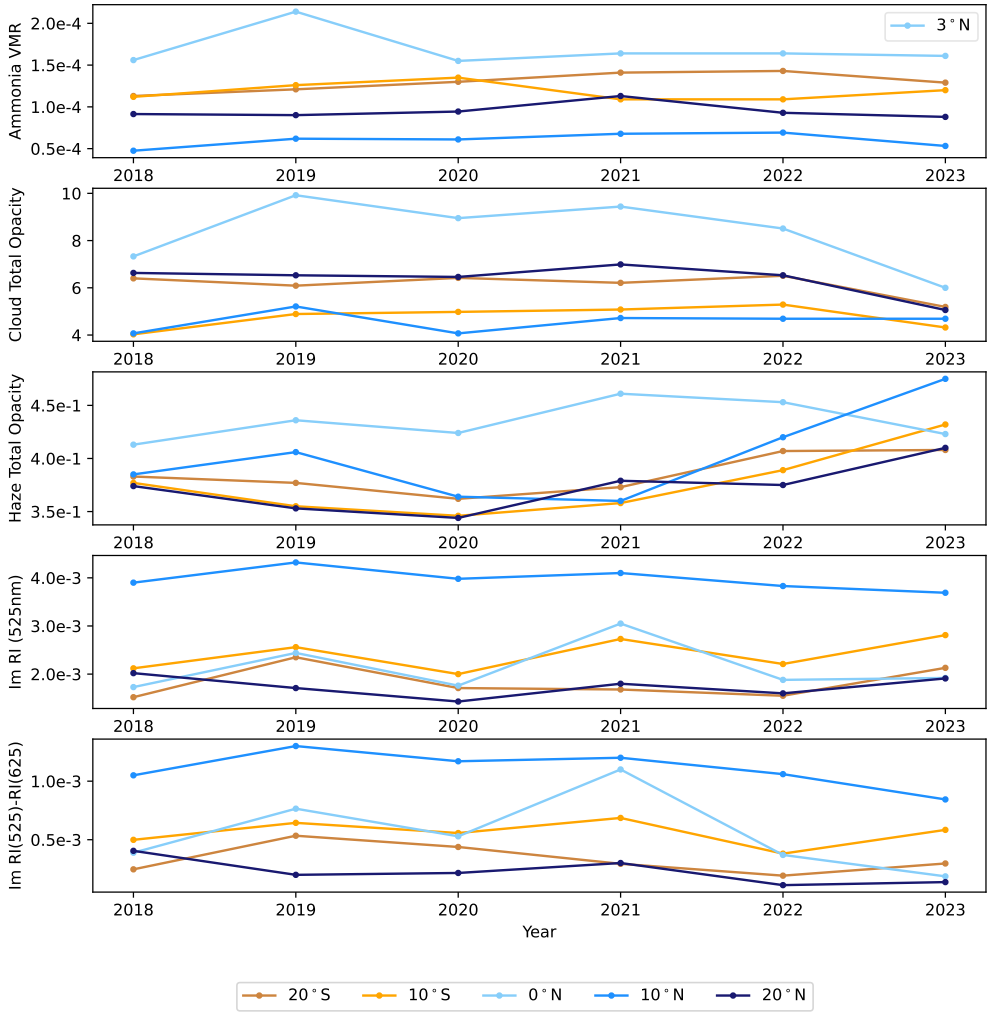


Figure 6.9.1: Retrieved values of NH_3 Volume Mixing ratio, Cloud total opacity, haze total opacity, imaginary refractive index at 525nm and the imaginary refractive slope, calculated as the difference between the RI at 525nm and 625nm, for a range of latitudes (20°S, 10°S, 0°N (3°N for NH_3 VMR as peak lies at this latitude), 10°N, 20°N) for each observation year.

The dynamical explanation for the variation of chromophore properties also extends to the GRS as the anticyclonic structure will cause different atmospheric properties when compared to the large overturning zonal and belt regions. The anticyclonic structure is likely to have slower overturning of its cloud tops due to the cyclonic motion dominating, therefore the cloud top material will be exposed for longer, leading to the steeper imaginary RI slope retrieved for the GRS. The differing structure of the GRS would also allow for different conditions for the haze, which could provide the variation to fit the increased limb darkening seen for GRS observations.

Overall, the application of the simplified parameter scheme, with a minimum number of free parameters has been able to reproduce our VLT/MUSE observations of Jupiter very well. Through the fixing of parameters, we have been able to minimise the number of degenerate pairs in the parameters space whilst still being able to capture variations across the disc and for multiple observations. By fitting dual viewing angles simultaneously we have been more constraining on our retrieved vertical profiles and have incorporated limb darkening effects into our work. Our results have also consistently found good spectral fits across a wide range of latitudes on Jupiter (with most $\chi^2/n < 1$ for the majority of latitudes), ranging from 40°N – 40°S. The fine latitude sampling rate of 1°, captures the transition between neighbouring regions.

The results we have retrieved across multiple observations, spanning six years, reproduce the realistic conditions seen for the haze and ammonia, matching both direct observations in our wavelength range (haze) and retrieved values through different wavelengths (ammonia). Providing confirmation that the values found are representative of the true atmospheric conditions. We have also extracted expected general trends, such as cloud opacity and imaginary RI, which cannot be directly measured but have been theorised, with cloudier zones and increased RI values in redder regions. In addition to the success for the belted regions, the parameterisation was also able to fit to the dual viewing angle observations of the GRS. Adapting to the steep blue absorption slopes seen at these locations. In conclusion, reducing the complexity of the parameterisation scheme has been shown to not impact the ability to reproduce observations and characteristics of Jupiter, and in fact removes a huge amount of degenerate pairings which has previously plagued past results. With only 6 variable

parameters we have been able to successfully reproduce over 970 spectra taken across a wide range of latitudes and observations of Jupiter, highlighting the strengths of our model presented in this thesis.

Chapter 7

Conclusions and Future Work

7.1 Summary

Jupiter is a dynamic planet. Its ever-changing appearance is linked to its evolving atmospheric state. For hundreds of years, we have been monitoring this planet in an attempt to better understand its vast atmosphere. With long-running observational history, we are aware of the scale, both temporal and spatial, to which this planet can undergo colouration events, such as the entire Equatorial zone changing from white to red in a matter of months. Improvements to our collective scientific ability means that we have progressed from only being able to note these variations: we can now attempt to model these changes and understand what drives them. Observations in the visible/near IR wavelengths reveal the cloud-top appearance as well as vertical aerosol and ammonia distribution of the planet. The range of colours on Jupiter, ranging from crisp white to a deeper red hue, are caused by a colour-causing chromophore material. The nature of this material, both its make up and distribution is elusive, and has been the focus of much atmospheric investigation for several decades. The striped appearance of the zone and belt regions follows a general pattern where we expect zonal regions to be cloudier, and belts to have smaller cloud opacities. However, the appearance of these regions does not follow a regular pattern. Despite zones often being paler, it is not a steadfast rule, since they undergo a wealth of colour variations. The ability to model both appearances and determine the changes between the atmospheric states which cause them is of importance on Jupiter,

as only then is an atmospheric model adaptive enough.

In order to better study Jupiter a range of missions and telescopes have been directed at the planet. The Galileo mission and associated descent probe provided a wealth of information about Jupiter. The descent probe still provides the only direct measurements of the atmosphere of Jupiter. Despite the unfortunately anomalous entry point in a hotspot, it provides in-situ measurements which created a basis in which to compare modelled aerosol profiles. The current Juno mission around Jupiter is providing an abundance of observational data, with excellent spatial resolution but with a limited field of view; hence, we have been part of ground-based support to extend the field of view and wavelength range of observations to provide context to the Juno observations. In Chapter 2 we discuss the VLT/MUSE observations undertaken, both as part of the ground-based support, but also to further the atmospheric modelling which can be undertaken for Jupiter. The MUSE instrument has an excellent spectral resolution within the visible/near IR wavelength range (0.125nm spacing) as well as a field of view which can fit the entire disc of Jupiter inside, producing spectral cubes where every observed pixel is also a spectrum covering the entire disc. This combination of spectral and spatial resolution produces remarkable observations for atmospheric modelling of Jupiter. The instrument also has an incredibly short exposure time (0.1s), eliminating observational effects often introduced to observations by the rapid rotation time of Jupiter. The combined high spatial and spectral resolution moves the goal posts for what is possible when modelling observations of Jupiter, increasing both the spectral constraint alongside the level of spatial detail it is possible to resolve by ground-based visible instruments.

Many previous works have been able to successfully reproduce observations of Jupiter for a collection of regions and wavelength ranges, as discussed in Chapter 1. These models can typically be separated by the location of their main cloud, around 1.4 bar as with Galileo probe location, or 0.7 bar as with the ECCM predicted ammonia layer. As the Galileo probe descended into an anomalous region, and the ECCM models use simplifications for the dynamics as well as predicting enhanced cloud abundances, neither can be used to decidedly confirm the main cloud location. We often find when models are applied to other locations or observations that they are unable to maintain the same

level of fit to observed spectra. However, adapting these models can be difficult due to the large number of free parameters needed to match observations. This leads to large variations in the retrieved parameter values across regions which can be hard to relate to physical processes. These aerosol models also allow us to retrieve the location and properties of chromophore material. Further information has been provided through laboratory work, which has been able to produce potential chromophore candidates and measure their optical properties.

One such work, Carlson et al. (2016) led to a large number of modelling studies which used this chromophore (or modified version). One model; Crème Brûlée, found it possible to model the GRS as well as selected regions across the disc with this single chromophore (Baines et al., 2019; Sromovsky et al., 2017; Dahl et al., 2021). However, it was also found by others that it could not reproduce some observations as well (Braude et al., 2020; Pérez-Hoyos et al., 2020), and instead other models of aerosol distribution were needed to match observations better. Attempting to determine which model best captures the atmosphere is difficult since they both match observations well despite different set-ups, revealing the degeneracy which exists between the parameters at these wavelengths.

Through the use of the Minnaert approximation (Chapter 4) we have been able to extract idealised spectra at the viewing angles desired (0.0° and 61.45°). Fitting to multiple viewing angle spectra simultaneously helps provide additional constraint to observations with more sensitivity to the vertical profile. Through this constraint, we can reduce the effect of degeneracy within the parameter space. Assuming each latitude region is homogeneous, we can fit the Minnaert approximation and extract coefficients which allows us to generate equivalent spectra at any viewing angle we wish to specify. This allows us to simultaneously produce dual viewing angles which provides further constraint on observations by incorporating limb darkening into the retrievals, without overly slowing down retrieval times. For our retrievals, we use the NEMESIS radiative transfer algorithm (Irwin et al., 2008), discussed in Chapter 3. We have extracted spectra from 40°N to 40°S across a range of observations, which will allow us to better characterise the cloud structure across the disc. In addition, through the use of multiple observations where its location has varied across the disc, we have also been able to apply this approximation to the Great Red Spot. We applied previously

modelled atmospheric solutions to these dual angle spectra but we found that they were unable to fit both viewing angles simultaneously, typically struggling to reproduce the blue absorption slope, short-ward of $0.6\mu m$. The inability of these models to reproduce our observations suggests that they do not fully capture the atmospheric profile, and highlights the degeneracy which plagues the parameter space of these models. To reduce the effects of the degenerate pairs we then introduced methods to predetermine parameters before undertaking full retrievals, explained in Chapter 5.

Through the use of methods such as 'Snippet' retrievals we were able to determine the location of the clouds without any *a priori* constraints, we were able to determine two separate clouds, one at 0.2 bar, and a deeper cloud at 1.4 bar. We then began to reduce the complexity caused by degeneracy in the further parameter space by determining and fixing values using grid searches, which reduces the number of pairings which can be causing said degeneracy. We were able to locate the chromophore material in the cloud, through inspection of the blue slope (below $0.6\mu m$) of the spectra. In addition to minimising the χ^2/n values we also ensured that known distributions, such as haze seen through the use of 889nm observations, were retrieved when selecting these parameters. In total, the final parameterisation scheme contains only 6 variable parameters (cloud and haze total opacity and fractional width, ammonia VMR and cloud imaginary refractive index spectra (for 11 wavelengths)). The low number of parameters minimised the degeneracy whilst still enabling us to capture the observed variation across the disc of Jupiter.

7.2 Conclusions

Our goals in this thesis were simple and focused on a single problem, improving the atmospheric aerosol parameterisation of Jupiter, outlined in the steps below.

- **Create an atmospheric model of Jupiter**
  - with high spectral constraint
  - utilising limb darkening constraint through multiple viewing angles
  - reducing degeneracy through the predetermination of parameters

- **Extend across the disc of Jupiter**
  - regular sampling beyond single samples in zones/belts
- **Expand across observation years**
  - see how parameters change year on year
- **Apply to the Great Red Spot**

Through the work outlined in this thesis, we have been able to produce a parameterisation scheme which has been able to reproduce observations over a range of years and locations of Jupiter, as well as the GRS. The parameter values retrieved have been realistic, producing the expected distributions of haze, cloud and ammonia across the disc. This has all been achieved whilst fitting the more constraining dual viewing angle spectra which incorporates limb darkening into our retrievals as well as more vertical constraint on the aerosol profile. We will discuss the further advancements that could be undertaken to extend the potential of the work achieved for this thesis below.

The VLT/MUSE observations which have been used for this work provide unprecedented spatial and spectral resolution for this wavelength range. For radiative transfer modelling of Jupiter in the visible/near IR this region provides sensitivity to the aerosol profile as well as methane and ammonia absorption. Alongside the huge potential for work undertaken here, the MUSE observations also contribute to ground-support for the Juno mission, providing spatial context to the spatially limited observations from the orbiter. Therefore, scheduling regular observations has not only benefited the range of observations we have to undertake retrievals for but has also been part of a global effort to gain simultaneous observations of Jupiter in a range of wavelengths to aid analysis of the Juno results. We have been successful with three observing proposals over three years, providing a wealth of new observations to continue the analysis of Jupiter.

Once reduced, aligned and calibrated we were able to extract spectra from the MUSE cubes, using the Minnaert approximation (Minnaert, 1941), introduced for Jupiter in Pérez-Hoyos et al. (2020). Through this approximation we are able to generate synthetic measured spectra at two viewing angles of the spectra, selecting 0.0° and 61.45°, chosen to capture the limb darkening effects whilst

not being too computationally expensive. We can do this for any latitude band on the disc of Jupiter. We used these spectra to test the previous works of Baines et al. (2019); Sromovsky et al. (2017); Braude et al. (2020) and to see whether their retrieved models, developed for a single viewing angle, can fit dual viewing angle spectra simultaneously. We use the NEMESIS radiative transfer code (Irwin et al., 2008) throughout this work. We found that none of the previous works were able to fit both viewing angles satisfactorily, often ill-fitting to the blue slope absorption at wavelengths less than $0.6\mu m$. Indicating that they were not representative of the atmosphere of Jupiter due to their inability to capture both viewing angles.

Due to the huge amount of degeneracy between the parameters and the lack of ability to determine improvements to a widely varying model it was deemed necessary to attempt to simplify the parameterisation scheme. This was achieved by fixing a greater number of parameters than done in previous works, leaving us with only 6 variable parameters. The model consists of cloud and haze layers with a Gaussian distribution of opacity/gram with respect to log(pressure), with fixed peak pressure, particle size and size variance. Alongside a simple knee profile for the ammonia mixing ratio, with a fixed knee pressure and fractional scale height whilst being limited to not exceed the saturated vapour pressure of ammonia. The real imaginary refractive index of both aerosol layers was fixed, as was the imaginary refractive index spectrum of the haze. We finalised the parameterisation scheme with only the cloud and haze total opacity and fractional cloud widths, ammonia deep volume mixing ratio and the cloud imaginary refractive indices allowed to vary. These variable parameters are needed to reproduce the variation we see across the disc of Jupiter, as well as adapting to multiple observations over several years. We have fixed as many parameters as possible, creating a model with minimal degenerate pairings through its simplicity.

As the parameterisation scheme was developed for the 2018 observation it was first applied to this observation. We found that it was able to fit the varied spectra across the disc, through changes in the total opacity of each aerosol layer and fraction width, alongside changes in the cloud imaginary RI. Combining retrievals from $40°\text{N} - 40°\text{S}$, we were able to reproduce the expected zone and belt opacity variations, with enhanced aerosol amounts in the main cloud layer within the zones and depleted

levels for the belts. The retrieved haze opacity was able to reproduce the observed distribution seen at 889nm, with significant enhancement in the haze above the equator. Through fitting the variable deep mixing ratio of ammonia we reproduce observations of the ammonia distribution found through radio observations, with a peak in abundance at 5°N followed by a depletion at 10°N, with a roughly consistent value retrieved elsewhere on the disc. Alongside these parameter retrievals we were able to adapt to the blue slope absorption, seen in observations below $0.6\mu m$, through the variation of the cloud imaginary refractive indices. As the chromophore is located in the cloud, we are retrieving the mixed RI values of both cloud material and the chromophore; this leads to variation in both the value at each wavelength due to the ratio of these constituents, but also the slope of values less than $0.6\mu m$ where we adapt to the properties of the chromophore. We expect the chromophore blue slope to vary as it is exposed to different conditions, likely caused by increased exposure driven by varying dynamics of different latitudes on the disc. Through the combination of very few variable parameters, we have been able to reproduce the latitudinal variation across the disc of Jupiter for the year the model was derived for, 2018.

As the parameterisation scheme is able to successfully model observations from 2018, we expanded to multiple observations up to 2023. For each year we fitted from 40°N – 40°S. Again the model was successful for each year, being able to adapt to latitudinal variance over several years. For example, we capture the EZ as it varies from white to red and back again. Across all observations, we have retrieved a χ^2/n value less than 1 for most latitudes. There are a few latitudes (e.g., 8 — 11°N in 2018) where we have not fully minimised these values, due to degeneracy between the haze abundance and ammonia, however, the fits to observations are still satisfactory in these limited regions. Despite the traces of error due to degeneracy still remaining, we have been able to retrieve realistic latitudinal distributions for cloud, haze and ammonia for six years of observations because we have removed so much complexity caused by degenerate pairings by fixing parameters. Having a model which has been able to adapt so easily across multiple latitudes and observations, whilst using the more constraining dual viewing angle observations, suggests that it provides a good representation of the atmospheric profile on Jupiter.

In addition to retrievals of the main zone and belt regions we were also able to apply the Minnaert method to the Great Red Spot through the use of multiple observations. The different viewing angles across the observations (two for 2018 and six for 2022) provided enough information to fit the Minnaert limb-darkening coefficients and extract dual viewing angle spectra for both years, 2018 and 2022. We then applied the parameterisation scheme and were able to reproduce the observations at both viewing angles simultaneously for both years, this is the first successful application of the Minnaert method for the GRS. Further investigation into the GRS may be beneficial to see whether differences in the parameterisation scheme are needed due to potential differences in haze properties highlighted through the fit around 889nm (indicating a more limb-darkened material may be needed), as well as the lower than expected haze opacity retrieved. However, the ability to reproduce the observations of the GRS, with the constraint of the dual viewing angles, indicates that the GRS aerosol profile is still well represented by our parameterisation scheme.

We believe that these visual changes to appearance are driven through dynamical variation of the air movement within these regions. We believe that the changes to the chromophore imaginary refractive index properties are linked to cloud dynamics. The majority of the visual changes are coming from an increase in the chromophore imaginary RI slope. This change is likely caused due to a slow down in the overturning rate of the cloud tops, leading to chromophore material to be irradiated for longer resulting in a steeper blue slope and a more red appearance for the region. The slow down of overturning may also lead to a reduction in the rate of depletion of the cloud layer and can be seen in the slight increase in cloud total opacity accompanying colouration events. The dependence of the exposure time of the chromophore on the cloud tops as a control of the material's optical properties, can also explain the differing RI properties retrieved for the GRS. Due to the anticyclonic nature of the storm, rather than the zone belt overturning patterns expected elsewhere, this would lead to different overturning time scales leading to different chromophore properties than expected elsewhere.

The success of our model in reproducing a wealth of observations, adapting across huge cloud-top appearances, demonstrates the importance of reducing degenerate pairings within the parameterisa-

tion scheme. The Minnaert approximation, allowing us to produce idealised viewing angle spectra, provides a useful tool to differentiate between aerosol profiles. The ability of our model to simultaneously fit dual angles, unlike many previous works, verifies its similarities to the true atmospheric conditions. Its viability for use with the GRS also opens new possibilities and improvements to research across the whole disc, including individual features, of Jupiter.

7.3 Further Work

7.3.1 Observational

- Although we have applied this parameterisation to observations over 6 years, with a single observation each year, we could benefit from applying the model to every observation night we have observed. This would extend the time period to 2014 for the VLT/MUSE instrument. Through more frequent observations we could see how the retrieved values vary between observed states. We would also benefit from continued observations to extend the time series to which we can apply this parameterisation. From this, we would be able to see how the atmosphere varies with further changes in appearance.

- As observing time has become more competitive to secure, particularly due to the recent success leading to significant observing time having been acquired 2018-2023, we should adapt our future telescope proposals. Having used the Adaptive Optics system for several observations we see minimal improvement to the observations for our with compared to the additional time for readouts. Removing the AO requirement and having very short observing blocks would be more beneficial for scheduling. We would also benefit from streamlining our observing pattern (currently 5 observations of Jupiter with 2 sky cubes for calibration). Typically we only use the best observation from each night for analysis and do not undertake the co-adding of cubes nor additional calibration from the sky cubes. Therefore reducing our proposals to 4 observations of Jupiter would reduce our observation blocks below 20 minutes, making our proposals more competitive. Continued alignment with the Juno Perijoves is beneficial to the wider community, but the inclusion of the GRS regularly is beneficial for our analysis. As we

have not been successful in gaining observation time for Jupiter on the VLT/MUSE since 2023, it is crucial to ensure our next proposal is successful to reduce the gap in our observations, through a very small time requirement with maximum flexibility in the observing period. We should prioritise observations where Juno Perijove longitudes also mean the GRS is included on the disc, to maximise the scientific return for each observation.

- Extending the wavelength range of the used observations for our retrievals could provide further constraint to our aerosol model. Attempting to fit wavelengths which are sensitive to different parts of the atmosphere would allow us to confirm that we have derived the aerosol profile successfully. Infrared observations are sensitive to thermal emissions and allow us to probe deeper into the atmosphere. Juno Perijoves provide an ideal timing as many telescopes are viewing Jupiter as part of the ground-based support, but using past observations would allow us to complement our large catalogue of MUSE observations. One instrument with simultaneous observations is VLT/VISIR, unfortunately, this instrument is now due to be decommissioned in the near future. It is a spectrometer which covers the three mid-infrared atmospheric windows ($5\mu m$, 8–$13\mu m$ and $17 - 20\mu m$) whilst covering the majority of Jupiter's disc. There have already been simultaneous observations of Jupiter by MUSE and VISIR on the same night, 25/05/2018, and other nearby observations may already exist. Many instruments are unable to cover the entirety of Jupiter in a single observation due to its large size. As the Minnaert fitting uses the full width of Jupiter, using instruments which are able to fit all of Jupiter in their FOV would reduce observational errors from tiling observations, which would be beneficial for our analysis. Other instruments such as IRTF/SpeX (0.7–$5.3\mu m$) or IRTF/TEXES ($8 - 26\mu m$) provide great spectral resolution but have a smaller field of views requiring tiling to cover enough of Jupiter for Minnaert approximations. Onboard Juno, the JIRAM instrument records infrared observations of the planet during Perijoves, which would align with several MUSE observations, but will be spatially limited in the belted regions. In addition, Cassini/VIMS observations provide both an extended wavelength range, 0.3 — $1.05\mu m$ and 0.85 — $5.1\mu m$, as well as full disc observations. Therefore, assessment of these datasets would also be beneficial.

7.3.2 Spectra extraction

- The ability of our parameterisation scheme to reproduce spectra for the GRS provides confidence in its ability to be applied successfully to other discrete features. Applying the parameterisation scheme to features, such as the Oval BA, brown barges, and $5\mu m$ hotspots, could provide important new constraints on their vertical aerosol profiles.

- To apply the Minnaert approximation to the GRS we need two observations which are reasonably spaced across the disc of Jupiter in order to reconstruct the limb-darkening/limb-brightening. Although we planned observations for 2022 that had longitudes of focus including the GRS at different viewing angles, we also have 'accidental' pairs of GRS observations which allow fits to be extracted. The 2018 observations in this work are one such pair. Therefore, the current observations should be assessed to see if any such pairs exist for further years. In addition, we could attempt to find other features which have also been captured in this way. Then we will be able to fit the Minnaert approximation, producing spectra for more years allowing us to assess the changes which the GRS has undergone, as we have done for the latitudinal variations studied in this work.

- High spatial resolution maps of the Great Red Spot reveal the difference in structure across the storm, e.g., Harkett et al. (2024). As MUSE has reasonable spatial resolution we may be able to extract pixels from similar structural regions of the GRS and fit the Minnaert approximations for smaller regions to capture this variation within the GRS. From this, we may be able to retrieve different parameter values representing the variety of structures across the feature better.

- When producing GRS spectra, using the Minnaert approximation, we have tried to use as many observations of the GRS to get the largest range of viewing angles to minimise fitting errors. An investigation could be done to see the minimum spacing of the GRS location on the disc that is needed to extract spectra that reproduce the observed reflectance of the GRS accurately. This would be beneficial as it may increase the number of past observational pairs which could be used to extract spectra. It could also reduce the observational demand for extracting limb-darkening spectra of the GRS (and other features) using the Minnaert

technique by reducing the number of observation blocks needed to get the required viewing angles.

- We assume that latitude bands are homogeneous across all longitudes. Whilst this approximation is typically correct there are some regions where this is not true, for example, the colouration eastward of the GRS. Separating pixels in the regions where different parts of a latitude band have clear differences, and undertaking two retrievals would allow us to better characterise all parts of the atmosphere. It would also eliminate error which could be introduced through a Minnaert approximation of regions with different characteristics. For regions where these asymmetries are related to larger events, such as the colouration of a belt, we may be able to retrieve parameter differences caused by these large-scale events, indicating some of the atmospheric changes which cause these events.

- Current retrievals only extend from 40°N – 40°S, extending this latitude range would provide information at more polar latitudes. As we move further towards the poles we have less zenith angle information to extract the Minnaert approximation for, leading to an increase in error needed for the produced spectra. However, attempting to extend the latitude range would be beneficial for the information it can reveal for the vertical profiles as the belted region ceases and transitions into the polar structuring.

7.3.3 Parameterisation Scheme

- Through the $\chi^2/n > 1$ retrieved for a small latitude region in 2018 (8 –11°N) we are aware of potential error caused by degeneracies still remaining in the model. We believe that the decrease in ammonia occurring in these regions partly leads to a retrieval of enhanced haze, to account for the limited absorption at higher altitudes, which is not seen for observations at 889nm. Therefore deploying methods to counteract this effect would be beneficial. One such method could be retrieving ammonia first, fixing the values then retrieving the aerosol parameters separately. Additionally, testing of different ammonia profile parameterisations could be done to see if a different model can break this degeneracy, as our current profile may be an oversimplification.

- When fitting to the GRS spectra, we find that the total haze opacity is lower than expected (as smaller values than the EZ were retrieved despite the GRS being brighter at 889nm). Additionally, we find that we are retrieving radiances smaller than those observed in the 889nm methane absorption region at 0.0°, and larger values at 61.45°, indicating that the fixed haze RI values are not limb-darkened enough to reproduce observations of the GRS. Therefore, the haze values need to be reassessed for the GRS to improve the observational fit, and hopefully the subsequently retrieved haze opacity.

- As we assume the main cloud layer contains the chromophore alongside the main cloud component, it is the combined imaginary refractive indices which are being retrieved. Determining how to disentangle these values to retrieve both the cloud properties and the chromophore properties could allow us to extract more information about each material separately. If we could determine the amount of chromophore material present in the cloud layer we would be able to test whether the mechanisms exist to produce the correct amount of material in that region, and thus how viable it is in our parameterisation. This would also allow us to better extract parameters which may differ between the two species, such as particle size and variance.

- An investigation into how the species are mixed in the main cloud layer could also be of interest, as it may affect how the retrieved values are affected by the materials being in different states. Baines et al. (2019) attempted this when creating the Crème Brûlée model, testing chromophore coated ices as well as mixed clouds alongside the thin chromophore layer. A similar investigation could be done, either as a parameterisation scheme run through NEMESIS or analysis after retrievals have been undertaken. It would be of interest to test if properties, such as imaginary refractive indices vary depending on the state of the materials, such as mixed solid particles, a chromophore coating (parameterisation scheme exists in NEMESIS already) or a chromophore nuclei.

7.3.4 Laboratory Improvements

- We are reliant on external line data to calculate k-tables for use in NEMESIS. Currently, the methane line data is not pure laboratory data and also uses observational data to calculate the absorption coefficients. The best methane line data from Rey et al. (2014) only extends down to 746nm, and this is theoretical rather than measured. The Karkoschka and Tomasko (2010) data used in this thesis, currently has the best coverage and resolution for our wavelength range. However, a new line data set, consisting of either laboratory-derived methane line data, or an extension of the theoretical Rey et al. (2014) data would improve the accuracy of our methane absorption during retrievals and would help to reduce a source of error in our retrievals.

- Laboratory measurements of potential chromophore materials are limited, but the advancements which they give through physical evidence to compare retrieved values are great. Having more information about this substance, or other theorised chromophores, including a wider wavelength range, as well as values for different exposure times would be beneficial. This would allow us to see if retrieved values are appropriate at longer wavelengths and whether the variations in the retrieved imaginary RI are truly realistic compared to a real substance.

- Additional optical properties of other potential cloud materials at Jupiter, such as NH_3 ice or NH_4SH, in the visible wavelength range would also be beneficial. Especially if further improvements are made de-tangling the species present in the cloud layer as accurate values for the cloud species are needed to do this accurately.

The application of the improvements suggested here could increase the impact of our parameterisation scheme even further, allowing us to successfully model more of Jupiter to an even greater level of accuracy across an even wider range of atmospheric features. The work presented here demonstrates that pre-determining parameters, creating a more simplistic atmospheric model, has allowed us to better represent the atmosphere across a wider range of locations and observations than possible before, whilst fitting more constraining dual viewing angle observations.

Bibliography

Adriani, A., Filacchione, G., Di Iorio, T., Turrini, D., Noschese, R., Cicchetti, A., Grassi, D., Mura, A., Sindoni, G., Zambelli, M., Piccioni, G., Capria, M. T., Tosi, F., Orosei, R., Dinelli, B. M., Moriconi, M. L., Roncon, E., Lunine, J. I., Becker, H. N., Bini, A., Barbis, A., Calamai, L., Pasqui, C., Nencioni, S., Rossi, M., Lastri, M., Formaro, R., and Olivieri, A. (2017a). Jiram, the jovian infrared auroral mapper. *Space Science Reviews*, 213(1):393–446. 58

Adriani, A., Mura, A., Moriconi, M. L., Dinelli, B. M., Fabiano, F., Altieri, F., Sindoni, G., Bolton, S. J., Connerney, J. E. P., Atreya, S. K., Bagenal, F., Gérard, J.-C. M. C., Filacchione, G., Tosi, F., Migliorini, A., Grassi, D., Piccioni, G., Noschese, R., Cicchetti, A., Gladstone, G. R., Hansen, C., Kurth, W. S., Levin, S. M., Mauk, B. H., McComas, D. J., Olivieri, A., Turrini, D., Stefani, S., and Amoroso, M. (2017b). Preliminary jiram results from juno polar observations: 2. analysis of the jupiter southern h3+ emissions and comparison with the north aurora. *Geophysical Research Letters*, 44(10):4633–4640. 5, 58

Anguiano-Arteaga, A., Pérez-Hoyos, S., Sánchez-Lavega, A., Sanz-Requena, J. F., and Irwin, P. G. J. (2023). Temporal Variations in Vertical Cloud Structure of Jupiter's Great Red Spot, Its Surroundings and Oval BA From HST/WFC3 Imaging. *Journal of Geophysical Research (Planets)*, 128(9):e2022JE007427. 24

Anguiano-Arteaga, A., Pérez-Hoyos, S., Sánchez-Lavega, A., Sanz-Requena, J. F., and Irwin, P. G. J. (2021). Vertical distribution of aerosols and hazes over jupiter's great red spot and its surroundings in 2016 from hst/wfc3 imaging. *Journal of Geophysical Research: Planets*, 126(11):e2021JE006996. e2021JE006996 2021JE006996. 37, 193

Arsenault, R., Madec, P. Y., Hubin, N., Paufique, J., Stroebele, S., Soenke, C., Donaldson, R., Fedrigo, E., Oberti, S., Tordo, S., Downing, M., Kiekebusch, M., Conzelmann, R., Duchateau, M., Jost, A., Hackenberg, W., Bonaccini Calia, D., Delabre, B., Stuik, R., Biasi, R., Gallieni, D., Lazzarini, P., Lelouarn, M., and Glindeman, A. (2008). ESO adaptive optics facility. In Hubin, N., Max, C. E., and Wizinowich, P. L., editors, *Adaptive Optics Systems*, volume 7015 of *Society of Photo-Optical Instrumentation Engineers (SPIE) Conference Series*, page 701524. 55

Atkinson, D. H., Pollack, J. B., and Seiff, A. (1998). The galileo probe doppler wind experiment: Measurement of the deep zonal winds on jupiter. *Journal of Geophysical Research: Planets*, 103(E10):22911–22928. 3

Atreya, S., Wong, M., Owen, T., Mahaffy, P., Niemann, H., de Pater, I., Drossart, P., and Encrenaz, T. (1999). A comparison of the atmospheres of jupiter and saturn: deep atmospheric composition, cloud structure, vertical mixing, and origin. *Planetary and Space Science*, 47(10):1243 – 1262. 12, 13, 27, 28, 29, 32

Atreya, S. K. and Romani, P. N. (1985). Photochemistry and clouds of Jupiter, Saturn and Uranus. In Hunt, G. E., editor, *Recent Advances in Planetary Meteorology*, pages 17–68. Cambridge University Press. 27

Atreya, S. K., Wong, A. S., Baines, K. H., Wong, M. H., and Owen, T. C. (2005). Jupiter's ammonia clouds – localized or ubiquitous? *Planetary and Space Science*, 53(5):498–507. 10, 16

Atreya, S. K., Wong, M. H., Owen, T. C., Niemann, H. B., and Mahaffy, P. R. (1997). Chemistry and Clouds of the Jupiter's Atmosphere: A Galileo Perspective. In Barbieri, C., Rahe, J., Johnson, T. V., and Sohus, A. M., editors, *The Three Galileos the Man, the Spacecraft the Telescope*, volume 220 of *Astrophysics and Space Science Library*, page 249. 9, 15

Bacon, R., Accardo, M., Adjali, L., Anwand, H., Bauer, S., Biswas, I., Blaizot, J., Boudon, D., Brau-Nogue, S., Brinchmann, J., Caillier, P., Capoani, L., Carollo, C. M., Contini, T., Couderc, P., Daguisé, E., Deiries, S., Delabre, B., Dreizler, S., Dubois, J., Dupieux, M., Dupuy, C., Emsellem, E., Fechner, T., Fleischmann, A., François, M., Gallou, G., Gharsa, T., Glindemann, A., Gojak, D., Guiderdoni, B., Hansali, G., Hahn, T., Jarno, A., Kelz, A., Koehler, C., Kosmalski, J.,

Laurent, F., Le Floch, M., Lilly, S. J., Lizon, J. L., Loupias, M., Manescau, A., Monstein, C., Nicklas, H., Olaya, J. C., Pares, L., Pasquini, L., Pécontal-Rousset, A., Pelló, R., Petit, C., Popow, E., Reiss, R., Remillieux, A., Renault, E., Roth, M., Rupprecht, G., Serre, D., Schaye, J., Soucail, G., Steinmetz, M., Streicher, O., Stuik, R., Valentin, H., Vernet, J., Weilbacher, P., Wisotzki, L., and Yerle, N. (2010). The MUSE second-generation VLT instrument. In McLean, I. S., Ramsay, S. K., and Takami, H., editors, *Ground-based and Airborne Instrumentation for Astronomy III*, volume 7735 of *Society of Photo-Optical Instrumentation Engineers (SPIE) Conference Series*, page 773508. 54

Baines, K., Sromovsky, L., Carlson, R., Momary, T., and Fry, P. (2019). The visual spectrum of jupiter's great red spot accurately modeled with aerosols produced by photolyzed ammonia reacting with acetylene. *Icarus*, 330:217–229. 20, 21, 36, 38, 39, 40, 41, 42, 45, 47, 48, 50, 116, 117, 141, 185, 190, 201, 204, 211

Baines, K. H., Carlson, R. W., and Kamp, L. W. (2002). Fresh Ammonia Ice Clouds in Jupiter. I. Spectroscopic Identification, Spatial Distribution, and Dynamical Implications. *Icarus*, 159(1):74–94. 15, 16

Ballester, P., Banse, K., Castro, S., Hanuschik, R., Hook, R. N., Izzo, C., Jung, Y., Kaufer, A., Larsen, J. M., Licha, T., Lorch, H., Lundin, L., Modigliani, A., Palsa, R., Péron, M., Sabet, C., and Vinther, J. (2006). Data reduction pipelines for the Very Large Telescope. In Silva, D. R. and Doxsey, R. E., editors, *Society of Photo-Optical Instrumentation Engineers (SPIE) Conference Series*, volume 6270 of *Society of Photo-Optical Instrumentation Engineers (SPIE) Conference Series*, page 62700T. 61

Banfield, D., Gierasch, P., Bell, M., Ustinov, E., Ingersoll, A., Vasavada, A., West, R. A., and Belton, M. (1998). Jupiter's cloud structure from galileo imaging data. *Icarus*, 135(1):230 – 250. 35

Becker, H. N., Alexander, J. W., Atreya, S. K., Bolton, S. J., Brennan, M. J., Brown, S. T., Guillaume, A., Guillot, T., Ingersoll, A. P., Levin, S. M., Lunine, J. I., Aglyamov, Y. S., and

Steffes, P. G. (2020). Small lightning flashes from shallow electrical storms on jupiter. *Nature*, 584(7819):55–58. 59

Bézard, B., Baluteau, J. P., and Marten, A. (1983). Study of the deep cloud structure in the equatorial region of jupiter from voyager infrared and visible data. *Icarus*, 54(3):434–455. 35, 187

Bjoraker, G. L., Wong, M. H., de Pater, I., Hewagama, T., Ádámkovics, M., and Orton, G. S. (2018). The gas composition and deep cloud structure of jupiter's great red spot. *The Astronomical Journal*, 156(3):101. 36

Bolton, S. J., Lunine, J., Stevenson, D., Connerney, J. E. P., Levin, S., Owen, T. C., Bagenal, F., Gautier, D., Ingersoll, A. P., Orton, G. S., Guillot, T., Hubbard, W., Bloxham, J., Coradini, A., Stephens, S. K., Mokashi, P., Thorne, R., and Thorpe, R. (2017). The Juno Mission. *Space Science Reviews*, 213(1-4):5–37. 57

Borysow, A., Borysow, J., and Fu, Y. (2000). Semi-empirical model of collision-induced absorption spectra of h2–h2 complexes in the second overtone band of hydrogen at temperatures from 50 to 500 k. *Icarus*, 145(2):601–608. 98

Borysow, A. and Frommhold, L. (1989). Collision-induced Infrared Spectra of H 2-He Pairs at Temperatures from 18 to 7000 K. II. Overtone and Hot Bands. *The Astrophysics Journal*, 341:549. 98

Braude, A. S. (2019). *Colour and Cloud Structure in the Atmospheres of the Giant Planets*. PhD thesis, University of Oxford, AOPP, University of Oxford, Oxford. 11, 110

Braude, A. S., Irwin, P. G., Orton, G. S., and Fletcher, L. N. (2020). Colour and tropospheric cloud structure of jupiter from muse/vlt: Retrieving a universal chromophore. *Icarus*, 338:113589. 37, 39, 42, 43, 44, 45, 46, 48, 49, 50, 76, 96, 98, 100, 115, 116, 117, 119, 121, 131, 141, 169, 170, 183, 184, 186, 187, 190, 193, 201, 204

Carlson, R., Baines, K., Anderson, M., Filacchione, G., and Simon, A. (2016). Chromophores from photolyzed ammonia reacting with acetylene: Application to jupiter's great red spot. *Icarus*,

274:106–115. v, 10, 19, 20, 21, 36, 37, 38, 39, 40, 41, 42, 43, 45, 46, 48, 49, 55, 176, 181, 182, 184, 185, 190, 192, 195, 201

Clark, R. N. and Lucey, P. G. (1984). Spectral properties of ice-particulate mixtures and implications for remote sensing. 1. Intimate mixtures. *JGR:Solid Earth*, 89:6341–6348. 16

Coles, P. A., Ovsyannikov, R. I., Polyansky, O. L., Yurchenko, S. N., and Tennyson, J. (2018). Improved potential energy surface and spectral assignments for ammonia in the near-infrared region. *Journal of Quantitative Spectroscopy and Radiative Transfer*, 219:199–212. 97

Conrath, B. J. and Gierasch, P. J. (1986). Retrieval of ammonia abundances and cloud opacities on jupiter from voyager iris spectra. *Icarus*, 67(3):444–455. 35

Dahl, E., Orton, G., Chanover, N., Baines, K., Carlson, R., Braude, A., Sinclair, J., Momary, T., Voelz, D., Alexander, C., and Irwin, P. (2023). Analysis of Jupiter's Disturbed Equatorial Zone from APO/NAIC and IRTF/SpeX. In *AAS/Division for Planetary Sciences Meeting Abstracts*, volume 55 of *AAS/Division for Planetary Sciences Meeting Abstracts*, page 326.05. 21

Dahl, E. K., Chanover, N. J., Orton, G. S., Baines, K. H., Sinclair, J. A., Voelz, D. G., Wijerathna, E. A., Strycker, P. D., and Irwin, P. G. J. (2021). Vertical structure and color of jovian latitudinal cloud bands during the juno era. *The Planetary Science Journal*, 2(1):16. 37, 39, 42, 44, 45, 46, 55, 71, 93, 149, 170, 182, 183, 184, 185, 186, 187, 190, 201

De Pater, I. and Lissauer, J. J. (2015). *Planetary sciences*. Cambridge core. Cambridge University Press, Cambridge, second edition. edition. 68

Dinelli, B. M., Fabiano, F., Adriani, A., Altieri, F., Moriconi, M. L., Mura, A., Sindoni, G., Filacchione, G., Tosi, F., Migliorini, A., Grassi, D., Piccioni, G., Noschese, R., Cicchetti, A., Bolton, S. J., Connerney, J. E. P., Atreya, S. K., Bagenal, F., Gladstone, G. R., Hansen, C. J., Kurth, W. S., Levin, S. M., Mauk, B. H., McComas, D. J., Gèrard, J.-C., Turrini, D., Stefani, S., Amoroso, M., and Olivieri, A. (2017). Preliminary jiram results from juno polar observations: 1. methodology and analysis applied to the jovian northern polar region. *Geophysical Research Letters*, 44(10):4625–4632. 58

ESO CPL Development Team (2015). EsoRex: ESO Recipe Execution Tool. Astrophysics Source Code Library, record ascl:1504.003. 61

Feroz, F. and Hobson, M. P. (2008). Multimodal nested sampling: an efficient and robust alternative to Markov Chain Monte Carlo methods for astronomical data analyses. *Monthly Notices of the Royal Astronomical Society*, 384(2):449–463. 91

Ferraro, J. R., Sill, G., and Fink, U. (1980). Infrared intensity measurements of cryodeposited thin films of nh 3, nh 4 hs, h 2 s, and assignments of absorption bands. *Applied Spectroscopy*, 34(5):525–533. 133

Ferris, J. P. and Ishikawa, Y. (1987). HCN and chromophore formation on Jupiter. *Nature*, 326(6115):777–778. 19, 20

Fletcher, L., Orton, G., Teanby, N., and Irwin, P. (2009). Phosphine on jupiter and saturn from cassini/cirs. *Icarus*, 202(2):543–564. 4, 14, 96

Fletcher, L. N. (2017). Cycles of activity in the jovian atmosphere. *Geophysical Research Letters*, 44(10):4725–4729. 22, 23, 24, 25

Fletcher, L. N., Biagiotti, F., King, O. R., Roman, M. T., Melin, H., Harkett, J., de Pater, I., Fouchet, T., Mura, A., Grassi, D., Piccioni, G., Wong, M., Rodriguez-Ovalle, P., Irwin, P., Orton, G., Fry, P., Bjoraker, G., and Hueso, R. (2024). Structure of jupiter's great red spot and south polar domain from jwst/nirspec and juno/jiram. Technical report, Copernicus Meetings. 193

Fletcher, L. N., Kaspi, Y., Guillot, T., and Showman, A. P. (2020). How well do we understand the belt/zone circulation of giant planet atmospheres? *Space Science Reviews*, 216(30-2):1572–9672. 3, 4, 14, 167

Fletcher, L. N., Orton, G., Rogers, J., Giles, R., Payne, A., Irwin, P., and Vedovato, M. (2017). Moist convection and the 2010–2011 revival of jupiter's south equatorial belt. *Icarus*, 286:94–117. 23, 24

Fletcher, L. N., Orton, G. S., Rogers, J. H., Simon-Miller, A. A., de Pater, I., Wong, M. H., Mousis, O., Irwin, P. G. J., Jacquesson, M., and Yanamandra-Fisher, P. A. (2011). Jovian temperature and

cloud variability during the 2009-2010 fade of the South Equatorial Belt. *Icarus*, 213(2):564–580. 23

Fletcher, L. N., Orton, G. S., Sinclair, J. A., Donnelly, P., Melin, H., Rogers, J. H., Greathouse, T. K., Kasaba, Y., Fujiyoshi, T., Sato, T. M., Fernandes, J., Irwin, P. G. J., Giles, R. S., Simon, A. A., Wong, M. H., and Vedovato, M. (2017). Jupiter's North Equatorial Belt expansion and thermal wave activity ahead of Juno's arrival. *Geophysical Research Letters*, 44(14):7140–7148. 23, 24

Gierasch, P. J., Conrath, B. J., and Magalha, J. A. (1986). Zonal mean properties of jupiter's upper troposphere from voyager infrared observations. *Icarus*, 67(3):456–483. 35

Giles, R. S., Fletcher, L. N., and Irwin, P. G. (2015). Cloud structure and composition of jupiter's troposphere from 5-μm cassini vims spectroscopy. *Icarus*, 257:457–470. 36, 50

Goody, R., West, R., Chen, L., and Crisp, D. (1989). The correlated-k method for radiation calculations in nonhomogeneous atmospheres. *Journal of Quantitative Spectroscopy and Radiative Transfer*, 42(6):539–550. 98, 99

Gordon, I. E., Rothman, L. S., Hargreaves, e. R., Hashemi, R., Karlovets, E. V., Skinner, F., Conway, E. K., Hill, C., Kochanov, R. V., Tan, Y., et al. (2022). The hitran2020 molecular spectroscopic database. *Journal of quantitative spectroscopy and radiative transfer*, 277:107949. 83

Grassi, D., Mura, A., Adriani, A., Sindoni, G., Atreya, S. K., Fletcher, L. N., Orton, G. S., Plainaki, C., Tosi, F., Biagiotti, F., Olivieri, A., Castagnoli, C., D'Aversa, E., Migliorini, A., Moirano, A., Noschese, R., Piccioni, G., Sordini, R., and Bolton, S. (2024). Jupiter's Hotspots as observed by JIRAM-Juno: limb darkening in thermal infrared. *Monthly Notices of the Royal Astronomical Society*, 533(2):2185–2198. 183

Grassi, D., Mura, A., Sindoni, G., Adriani, A., Atreya, S., Filacchione, G., Fletcher, L., Lunine, J., Moriconi, M., Noschese, R., Orton, G S, P. C., Sordini, R., Tosi, F., Turrini, D., Olivieri, A., Eichstadt, G., Hansen, C. J., Melin, H., Altieri, F., Cicchetti, A., Dinelli, B. M., Migliorini, A., Piccioni, G., Stefani, S., and Bolton, S. J. (2021). On the clouds and ammonia in jupiter's upper

troposphere from juno jiram reflectivity observations. *Monthly Notices of the Royal Astronomical Society*, 503(4):4892–4907. 58

Guillemin, J. C., El Chaouch, S., Bouayad, A., and Janati, T. (2001). Partial pressures and nature of products. Application to the photolysis of PH $_3$ and NH $_3$ in the atmosphere of jupiter and saturn. *Advances in Space Research*, 27(2):245–253. 19

Guillot, T., Li, C., Bolton, S. J., Brown, S. T., Ingersoll, A. P., Janssen, M. A., Levin, S. M., Lunine, J. I., Orton, G. S., Steffes, P. G., and Stevenson, D. (2020). Storms and the depletion of ammonia in jupiter: Ii. explaining the juno observations. *Journal of Geophysical Research: Planets*, 125(8):e2020JE006404. 59, 166

Guillot, T., Rosenqvist, M., Wong, M., Orton, G., Eichstädt, G., Brueshaber, S., Keaveney, C., Hansen, C., Kelley, K., Momary, T., Lunine, J., Mayer, J., and Bolton, S. (2023). How high are jupiter's clouds? analysis of junocam images of the" nautilus". In *EGU General Assembly Conference Abstracts*, pages EGU–17178. 59

Hansen, J. E. (1971). Multiple Scattering of Polarized Light in Planetary Atmospheres Part II. Sunlight Reflected by Terrestrial Water Clouds. *Journal of the Atmospheric Sciences*, 28(8):1400–1426. 130

Harkett, J., Fletcher, L. N., King, O. R. T., Roman, M. T., Melin, H., Hammel, H. B., Hueso, R., Sánchez-Lavega, A., Wong, M. H., Milam, S. N., Orton, G. S., de Kleer, K., Irwin, P. G. J., de Pater, I., Fouchet, T., Rodríguez-Ovalle, P., Fry, P. M., and Showalter, M. R. (2024). The thermal structure and composition of jupiter's great red spot from jwst/miri. *Journal of Geophysical Research: Planets*, 129(10):e2024JE008415. e2024JE008415 2024JE008415. 193, 209

He, C., Hörst, S. M., Radke, M., and Yant, M. (2022). Optical Constants of a Titan Haze Analog from 0.4 to 3.5 μm Determined Using Vacuum Spectroscopy. *The Planetary Science Journal*, 3(1):25. 183

Henyey, L. G. and Greenstein, J. L. (1941). Diffuse radiation in the galaxy. *Astrophysical Journal, vol. 93, p. 70-83 (1941).*, 93:70–83. 99

Hill, S. M., Irwin, P. G., Alexander, C., and Rogers, J. H. (2024). Spatial variations of jovian tropospheric ammonia via ground-based imaging. *Earth and Space Science*, 11(8):e2024EA003562. 132

Ingersoll, A. P., Dowling, T. E., Gierasch, P. J., Orton, G. S., Read, P. L., Sánchez-Lavega, A., Showman, A. P., Simon-Miller, A. A., and Vasavada, A. R. (2004). Dynamics of jupiter's atmosphere. In *Jupiter: The planet, satellites and magnetosphere*, volume 105. Cambridge University Press Cambridge, UK. 4

Irwin, P. (2009). *Radiative transfer processes in outer planetary atmospheres*, pages 215–262. Springer Praxis Books, Springer Berlin Heidelberg. 98, 99

Irwin, P. and Dyudina, U. (2002). The retrieval of cloud structure maps in the equatorial region of jupiter using a principal component analysis of galileo/nims data. *Icarus*, 156(1):52–63. 35, 187

Irwin, P., Parrish, P., Fouchet, T., Calcutt, S., Taylor, F., Simon-Miller, A., and Nixon, C. (2004). Retrievals of jovian tropospheric phosphine from cassini/cirs. *Icarus*, 172(1):37–49. Special Issue: Cassini-Huygens at Jupiter. 10, 14

Irwin, P., Tice, D., Fletcher, L. N., Barstow, J., Teanby, N., Orton, G., and Davis, G. (2015). Reanalysis of uranus' cloud scattering properties from irtf/spex observations using a self-consistent scattering cloud retrieval scheme. *Icarus*, 250:462–476. 101

Irwin, P., Weir, A., Taylor, F., Calcutt, S., and Carlson, R. (2001). The origin of belt/zone contrasts in the atmosphere of jupiter and their correlation with 5-μm opacity. *Icarus*, 149(2):397–415. 35, 187

Irwin, P. G., Bowles, N., Braude, A. S., Garland, R., and Calcutt, S. (2018a). Analysis of gaseous ammonia (nh3) absorption in the visible spectrum of jupiter. *Icarus*, 302:426–436. 76, 96, 98

Irwin, P. G., Bowles, N., Braude, A. S., Garland, R., Calcutt, S., Coles, P. A., Yurchenko, S. N., and Tennyson, J. (2019). Analysis of gaseous ammonia (nh3) absorption in the visible spectrum of jupiter - update. *Icarus*, 321:572–582. 97

Irwin, P. G., Dobinson, J., James, A., Toledo, D., Teanby, N. A., Fletcher, L. N., Orton, G. S., and Pérez-Hoyos, S. (2021). Latitudinal variation of methane mole fraction above clouds in neptune's atmosphere from vlt/muse-nfm: Limb-darkening reanalysis. *Icarus*, 357:114277. 52, 107, 108

Irwin, P. G., Dobinson, J., James, A., Wong, M. H., Fletcher, L. N., Roman, M. T., Teanby, N. A., Toledo, D., Orton, G. S., Pérez-Hoyos, S., Sánchez-Lavega, A., Sromovsky, L., Simon, A. A., Morales-Juberias, R., de Pater, I., and Cook, S. L. (2023). Spectral determination of the colour and vertical structure of dark spots in neptune's atmosphere. *Nature Astronomy*, 7(10):1198–1207. 99, 107

Irwin, P. G., Toledo, D., Garland, R., Teanby, N. A., Fletcher, L. N., Orton, G. A., and Bézard, B. (2018b). Detection of hydrogen sulfide above the clouds in uranus's atmosphere. *Nature Astronomy*, 2(5):420–427. 99

Irwin, P. G. J., Dobinson, J., James, A., Teanby, N. A., Simon, A. A., Fletcher, L. N., Roman, M. T., Orton, G. S., Wong, M. H., Toledo, D., Pérez-Hoyos, S., and Beck, J. (2024). Modelling the seasonal cycle of Uranus's colour and magnitude, and comparison with Neptune. *Monthly Notices of the Royal Astronomical Society*, 527(4):11521–11538. 17, 69, 70

Irwin, P. G. J., Teanby, N. A., de Kok, R., Fletcher, L. N., Howett, C. J. A., Tsang, C. C. C., Wilson, C. F., Calcutt, S. B., Nixon, C. A., and Parrish, P. D. (2008). The NEMESIS planetary atmosphere radiative transfer and retrieval tool. *Journal of Quantitative Spectroscopy and Radiative Transfer*, 109:1136–1150. 34, 45, 52, 66, 78, 83, 84, 86, 87, 88, 201, 204

Irwin, P. G. J., Teanby, N. A., Fletcher, L. N., Toledo, D., Orton, G. S., Wong, M. H., Roman, M. T., Pérez-Hoyos, S., James, A., and Dobinson, J. (2022). Hazy blue worlds: A holistic aerosol model for uranus and neptune, including dark spots. *Journal of Geophysical Research: Planets*, 127(6):e2022JE007189. e2022JE007189 2022JE007189. 107, 122

Irwin, P. G. J., Weir, A. L., Smith, S. E., Taylor, F. W., Lambert, A. L., Calcutt, S. B., Cameron-Smith, P. J., Carlson, R. W., Baines, K., Orton, G. S., Drossart, P., Encrenaz, T., and Roos-Serote, M. (1998). Cloud structure and atmospheric composition of Jupiter retrieved from Galileo near-

infrared mapping spectrometer real-time spectra. *JGR:Planets*, 103(E10):23001–23022. 35, 50, 187

James, A., Irwin, P., Dobinson, J., Wong, M., Tsubota, T., Simon, A., Fletcher, L., Roman, M., Teanby, N., Toledo, D., and Orton, G. (2023). The temporal brightening of Uranus' northern polar hood from HST/WFC3 and HST/STIS observations. In *AAS/Division for Planetary Sciences Meeting Abstracts*, volume 55 of *AAS/Division for Planetary Sciences Meeting Abstracts*, page 409.06. 107

Janssen, M., Oswald, J., Brown, S., Gulkis, S., Levin, S., Bolton, S., Allison, M., Atreya, S., Gautier, D., Ingersoll, A., Lunine, J., Orton, G., Owen, T., Steffes, P., Adumitroaie, V., Bellotti, A., Jewell, L., Li, C., Li, L., and Wang, C. (2017). *MWR: Microwave Radiometer for the Juno Mission to Jupiter*, pages 123–169. Space Science Reviews. 58, 59

Karkoschka, E. (1994). Spectrophotometry of the Jovian Planets and Titan at 300- to 1000-nm Wavelength: The Methane Spectrum. , 111(1):174–192. 68

Karkoschka, E. (1998). Methane, Ammonia, and Temperature Measurements of the Jovian Planets and Titan from CCD-Spectrophotometry. *Icarus*, 133(1):134–146. 19, 45, 110

Karkoschka, E. and Tomasko, M. G. (2010). Methane absorption coefficients for the jovian planets from laboratory, huygens, and hst data. *Icarus*, 205(2):674–694. 97, 212

Kaspi, Y., Galanti, E., Hubbard, W. B., Stevenson, D. J., Bolton, S. J., Iess, L., Guillot, T., Bloxham, J., Connerney, J. E. P., Cao, H., Durante, D., Folkner, W. M., Helled, R., Ingersoll, A. P., Levin, S. M., Lunine, J. I., Miguel, Y., Militzer, B., Parisi, M., and Wahl, S. M. (2018). Jupiter's atmospheric jet streams extend thousands of kilometres deep. *Nature*, 555(7695):223–226. 3

Khare, B. N. and Sagan, C. (1975). Cyclic Octatomic Sulfur: A Possible Infrared and Visible Chromophore in the Clouds of Jupiter. *Science*, 189(4204):722–723. 19

Lara, L.-M., Bézard, B., Griffith, C. A., Lacy, J. H., and Owen, T. (1998). High-Resolution 10-micronmeter Spectroscopy of Ammonia and Phosphine Lines on Jupiter. *Icarus*, 131(2):317–333. 19

Larson, H. P., Bjoraker, G. L., Davis, D. S., and Hofmann, R. (1984). The Jovian atmospheric window at 2.7 μm: A search for H_2S. *Icarus*, 60(3):621–639. 19

Larson, H. P., Treffers, R. R., and Fink, U. (1977). Phosphine in Jupiter's atmosphere: the evidence from high-altitude observations at 5 micrometers. *The Astrophysical Journal*, 211:972–979. 19

Lewis, J. S. (1976). Equilibrium and disequilibrium. Chemistry of adiabatic, solar-composition planetary atmospheres. In *Chemical Evolution of the Giant Planets*, pages 13–25. Elsevier Science. 19

Li, C., Ingersoll, A., Janssen, M., Levin, S., Bolton, S., Adumitroaie, V., Allison, M., Arballo, J., Bellotti, A., Brown, S., Ewald, S., Jewell, L., Misra, S., Orton, G., Oyafuso, F., Steffes, P., and Williamson, R. (2017). The distribution of ammonia on jupiter from a preliminary inversion of juno microwave radiometer data. *Geophysical Research Letters*, 44(11):5317–5325. 13, 14, 59, 96, 132, 144, 148, 166, 168, 169, 170

Loeffler, M. J. and Hudson, R. L. (2018). Coloring jupiter's clouds: Radiolysis of ammonium hydrosulfide (nh4sh). *Icarus*, 302:418–425. 19, 20

Loeffler, M. J., Hudson, R. L., Chanover, N. J., and Simon, A. A. (2016). The spectrum of Jupiter's Great Red Spot: The case for ammonium hydrosulfide (NH_4SH). *Icarus*, 271:265–268. 19, 20

Matcheva, K. I., Conrath, B. J., Gierasch, P. J., and Flasar, F. M. (2005). The cloud structure of the jovian atmosphere as seen by the cassini/cirs experiment. *Icarus*, 179(2):432–448. 35

Melin, H., Fletcher, L. N., Irwin, P. G. J., and Edgington, S. G. (2020). Jupiter in the Ultraviolet: Acetylene and Ethane Abundances in the Stratosphere of Jupiter from Cassini Observations between 0.15 and 0.19 μm. , 159(6):291. 68

Minnaert, M. (1941). The reciprocity principle in lunar photometry. *The Astrophysics Journal*, 93:403–410. 47, 104, 203

Mishchenko, M. I., Travis, L. D., Kahn, R. A., and West, R. A. (1997). Modeling phase functions for dustlike tropospheric aerosols using a shape mixture of randomly oriented polydisperse spheroids. *Journal of Geophysical Research: Atmospheres*, 102(D14):16831–16847. 99

Moeckel, C., de Pater, I., and DeBoer, D. (2023). Ammonia abundance derived from juno mwr and vla observations of jupiter. *The Planetary Science Journal*, 4(2):25. 132, 166, 167, 168, 170

Moses, J. I., Fouchet, T., Yelle, R. V., Friedson, A. J., Orton, G. S., Bézard, B., Drossart, P., Gladstone, G. R., Kostiuk, T., and Livengood, T. A. (2004). The stratosphere of Jupiter. In Bagenal, F., Dowling, T. E., and McKinnon, W. B., editors, *Jupiter. The Planet, Satellites and Magnetosphere*, pages 129–157. Cambridge University Press. 10

Moses, J. I., Visscher, C., Keane, T. C., and Sperier, A. (2010). On the abundance of non-cometary HCN on Jupiter. *Faraday Discussions*, 147:103. 20

Mura, A., Adriani, A., Altieri, F., Connerney, J. E. P., Bolton, S. J., Moriconi, M. L., Gérard, J.-C., Kurth, W. S., Dinelli, B. M., Fabiano, F., Tosi, F., Atreya, S. K., Bagenal, F., Gladstone, G. R., Hansen, C., Levin, S. M., Mauk, B. H., McComas, D. J., Sindoni, G., Filacchione, G., Migliorini, A., Grassi, D., Piccioni, G., Noschese, R., Cicchetti, A., Turrini, D., Stefani, S., Amoroso, M., and Olivieri, A. (2017). Infrared observations of jovian aurora from juno's first orbits: Main oval and satellite footprints. *Geophysical Research Letters*, 44(11):5308–5316. 58

NASA/SwRI/MSSS/Aran Anderson (2019). Pj21 great red spot. [Online; accessed June 21, 2024]. 5

Niemann, H. B., Atreya, S. K., Carignan, G. R., Donahue, T. M., Haberman, J. A., Harpold, D. N., Hartle, R. E., Hunten, D. M., Kasprzak, W. T., Mahaffy, P. R., Owen, T. C., and Way, S. H. (1998). The composition of the jovian atmosphere as determined by the galileo probe mass spectrometer. *Journal of Geophysical Research: Planets*, 103(E10):22831–22845. 9, 26, 95

Oneil, W. and Mitchell, R. (1983). Galileo mission overview. In *21st Aerospace Sciences Meeting*, page 96. 32

Ordonez-Etxeberria, I., Hueso, R., Sánchez-Lavega, A., and Pérez-Hoyos, S. (2016). Spatial distribution of jovian clouds, hazes and colors from cassini iss multi-spectral images. *Icarus*, 267:34–50. 193

Ortiz, J. L., Orton, G. S., Friedson, A. J., Stewart, S. T., Fisher, B. M., and Spencer, J. R. (1998). Evolution and persistence of 5-μm hot spots at the Galileo probe entry latitude. *JGR:Planets*, 103(E10):23051–23069. 4

Orton, G., Ortiz, J. L., Baines, K., Bjoraker, G., Carsenty, U., Colas, F., Dayal, A., Deming, D., Drossart, P., Frappa, E., Friedson, J., Goguen, J., Golisch, W., Griep, D., Hernandez, C., Hoffmann, W., Jennings, D., Kaminski, C., Kuhn, J., Laques, P., Limaye, S., Lin, H., Lecacheux, J., Martin, T., McCabe, G., Momary, T., Parker, D., Puetter, R., Ressler, M., Reyes, G., Sada, P., Spencer, J., Spitale, J., Stewart, S., Varsik, J., Warell, J., Wild, W., Yanamandra-Fisher, P., Fazio, G., Hora, J., and Deutsch, L. (1996). Earth-Based Observations of the Galileo Probe Entry Site. *Science*, 272(5263):839–840. 31, 32

Orton, G. S., Fisher, B. M., Baines, K. H., Stewart, S. T., Friedson, A. J., Ortiz, J. L., Marinova, M., Ressler, M., Dayal, A., Hoffmann, W., Hora, J., Hinkley, S., Krishnan, V., Masanovic, M., Tesic, J., Tziolas, A., and Parija, K. C. (1998). Characteristics of the Galileo probe entry site from Earth-based remote sensing observations. *JGR:Planets*, 103(E10):22791–22814. 31

Owen, T. (1976). Chemical abundances in the atmospheres of the giant planets and their satellites. In *Chemical Evolution of the Giant Planets*, pages 49–58. Elsevier Science. 19

O'Donoghue, J., Moore, L., Bhakyapaibul, T., Melin, H., Stallard, T., Connerney, J., and Tao, C. (2021). Global upper-atmospheric heating on jupiter by the polar aurorae. *Nature*, 596(7870):54–57. 58

Perez-Hoyos, S., Sanz-Requena, J., Sánchez-Lavega, A., Wong, M., Hammel, H., Orton, G., de Pater, I., Simon-Miller, A., Clarke, J., and Noll, K. (2012). Vertical cloud structure of the 2009 jupiter impact based on hst/wfc3 observations. *Icarus*, 221(2):1061–1078. 36

Plass, G. N., Kattawar, G. W., and Catchings, F. E. (1973). Matrix operator theory of radiative transfer. 1: Rayleigh scattering. *Appl. Opt.*, 12(2):314–329. 82

Prinn, R. G. and Lewis, J. S. (1975). Phosphine on Jupiter and Implications for the Great Red Spot. *Science*, 190(4211):274–276. 19

Pérez-Hoyos, S., Sanz-Requena, J., Barrado-Izagirre, N., Rojas, J., and Sánchez-Lavega, A. (2012). The 2009–2010 fade of jupiter's south equatorial belt: Vertical cloud structure models and zonal winds from visible imaging. *Icarus*, 217(1):256–271. 23, 39

Pérez-Hoyos, S., Sánchez-Lavega, A., Sanz-Requena, J., Barrado-Izagirre, N., Carrión-González, O., Anguiano-Arteaga, A., Irwin, P., and Braude, A. (2020). Color and aerosol changes in jupiter after a north temperate belt disturbance. *Icarus*, 352:114031. 37, 46, 47, 48, 49, 50, 104, 174, 181, 184, 185, 186, 187, 201, 203

Ragent, B., Colburn, D. S., Rages, K. A., Knight, T. C. D., Avrin, P., Orton, G. S., Yanamandra-Fisher, P. A., and Grams, G. W. (1998). The clouds of Jupiter: Results of the Galileo Jupiter mission probe nephelometer experiment. *JGR:Planets*, 103(E10):22891–22910. 9, 30, 31, 32, 33, 187, 188

Rages, K. A. (1977). *Atmospheric red chromophores in the outer solar system.* PhD thesis, Cornell University, New York. 19

Rayner, J. T., Cushing, M. C., and Vacca, W. D. (2009). The Infrared Telescope Facility (IRTF) Spectral Library: Cool Stars. , 185(2):289–432. 68

Read, P. L., Gierasch, P. J., Conrath, B. J., Simon-Miller, A., Fouchet, T., and Yamazaki, Y. H. (2006). Mapping potential-vorticity dynamics on Jupiter. I: Zonal-mean circulation from Cassini and Voyager 1 data. *Quarterly Journal of the Royal Meteorological Society*, 132:1577–1603. 3

Rey, M., Nikitin, A. V., and Tyuterev, V. G. (2014). Theoretical hot methane line lists up to t= 2000 k for astrophysical applications. *The Astrophysical Journal*, 789(1):2. 212

Richard, J. and Bacon, R. (Accessed 27-01-2025). Muse user manual. Available at `https://www.eso.org/sci/facilities/paranal/instruments/muse/doc/ESO-261650_MUSE_User_Manual.pdf`,. 54, 55

Rogers, J. (2017). 2016-17, report no.3: New mid-seb outbreak. Available at `https://britastro.org/section_information_/jupiter-section-overview/jupiter-in-2016-17/2016-17-report-no-3-new-mid-seb-outbreak`. 24

Rogers, J. (2019a). Jupiter in 2019, report no.7: Continuing disruption of the grs. Available at https://britastro.org/section_information_/jupiter-section-overview/jupiter-in-2019/jupiter-in-2019-report-no-7-continuing-disruption-of-the-grs. 24

Rogers, J. (2019b). Jupiter's south temperate domain, 2015-2018. Available at https://britastro.org/section_information_/jupiter-section-overview/long-term-reports-publications/jupiters-south-temperate-domain-2015-2018. 24

Rogers, J. (2022). Jupiter in 2021/22, report no.7: Equatorial region update. Available at https://britastro.org/section_information_/jupiter-section-overview/jupiter-in-2021-22/jupiter-in-2021-22-report-no-7-equatorial-region-update. 24

Rogers, J. and Adamoli, G. (2021). Jupiter in 2020, report no.9; final numerical report: Northern hemisphere. Available at https://britastro.org/wp-content/uploads/2017/08/JBAA-129-1_NEB-I_published.pdf. 24

Rogers, J. H. (1995). *The Giant Planet Jupiter*. Cambridge University Press. 24

Rogers, J. H. (2019c). Jupiter's north equatorial belt and jet, i, cyclic expansions and planetary waves. Available at https://britastro.org/wp-content/uploads/2017/08/JBAA-129-1_NEB-I_published.pdf. 24

Roos-Serote, M. and Irwin, P. (2006). Scattering properties and location of the jovian 5-micron absorber from galileo/nims limb-darkening observations. *Journal of Quantitative Spectroscopy and Radiative Transfer*, 101(3):448–461. Light in Planetary Atmospheres and Other Particulate Media. 36

Rothman, L., Gordon, I., Babikov, Y., Barbe, A., Chris Benner, D., Bernath, P., Birk, M., Bizzocchi, L., Boudon, V., Brown, L., Campargue, A., Chance, K., Cohen, E., Coudert, L., Devi, V., Drouin, B., Fayt, A., Flaud, J.-M., Gamache, R., Harrison, J., Hartmann, J.-M., Hill, C., Hodges, J., Jacquemart, D., Jolly, A., Lamouroux, J., Le Roy, R., Li, G., Long, D., Lyulin, O., Mackie, C., Massie, S., Mikhailenko, S., Müller, H., Naumenko, O., Nikitin, A., Orphal, J., Perevalov, V., Perrin, A., Polovtseva, E., Richard, C., Smith, M., Starikova, E., Sung, K., Tashkun, S., Tennyson,

J., Toon, G., Tyuterev, V., and Wagner, G. (2013). The hitran2012 molecular spectroscopic database. *Journal of Quantitative Spectroscopy and Radiative Transfer*, 130:4–50. HITRAN2012 special issue. 98

Ruiz, H. G. V. and Rowland, F. S. (1978). Possible scavenging reactions of C2H2 and C2H4 for phosphorus-containing radicals in the Jovian atmosphere. *Geophysical Research Letters*, 5:407–410. 19

Sagan, C. and Salpeter, E. E. (1976). Particles, environments, and possible ecologies in the Jovian atmosphere. *Astrophysical Journal Supplement Series*, 32:737–755. 19

Sánchez-Lavega, A., Rogers, J. H., Orton, G. S., García-Melendo, E., Legarreta, J., Colas, F., Dauvergne, J. L., Hueso, R., Rojas, J. F., Pérez-Hoyos, S., Mendikoa, I., Iñurrigarro, P., Gomez-Forrellad, J. M., Momary, T., Hansen, C. J., Eichstaedt, G., Miles, P., and Wesley, A. (2017). A planetary-scale disturbance in the most intense Jovian atmospheric jet from JunoCam and ground-based observations. *Geophysical Research Letters*, 44(10):4679–4686. 24, 47

Sill, G. T. (1976). The chemistry of the Jovian cloud colors. In Gehrels, T. and Matthews, S., editors, *IAU Colloq. 30: Jupiter: Studies of the Interior, Atmosp here, Magnetosphere and Satellites*, pages 372–383. 19

Simon, A. A., Tabataba-Vakili, F., Cosentino, R., Beebe, R. F., Wong, M. H., and Orton, G. S. (2018). Historical and contemporary trends in the size, drift, and color of jupiter's great red spot. *The Astronomical Journal*, 155(4):151. 24

Simon, A. A., Wong, M. H., and Orton, G. S. (2015). First Results from the Hubble OPAL Program: Jupiter in 2015. *The Astrophysical Journal*, 812(1):55. 4, 11, 25, 60, 61, 70, 109

Simon-Miller, A. A., Banfield, D., and Gierasch, P. J. (2001). Color and the Vertical Structure in Jupiter's Belts, Zones, and Weather Systems. *Icarus*, 154(2):459–474. 4, 39

Simon-Miller, A. A., Banfield, D., and Gierasch, P. J. (2001). An hst study of jovian chromophores. *Icarus*, 149(1):94–106. 17, 18, 19, 193

Simon-Miller, A. A., Conrath, B., Gierasch, P. J., and Beebe, R. F. (2000). A Detection of Water Ice on Jupiter with Voyager IRIS. *Icarus*, 145(2):454–461. 15

Smith, P. H. (1986). The vertical structure of the jovian atmosphere. *Icarus*, 65(2):264–279. 39

Sromovsky, L., Baines, K., Fry, P., and Carlson, R. (2017). A possibly universal red chromophore for modeling color variations on jupiter. *Icarus*, 291:232–244. 22, 36, 38, 39, 41, 42, 45, 47, 48, 50, 116, 117, 141, 170, 185, 186, 187, 190, 201, 204

Sromovsky, L., Collard, A., Fry, P., Orton, G., Lemmon, M., Tomasko, M., and Freedman, R. (1998). Galileo probe measurements of thermal and solar radiation fluxes in the jovian atmosphere. *Journal of Geophysical Research: Planets*, 103(E10):22929–22977. 30

Sromovsky, L. A. and Fry, P. M. (2002). Jupiter's Cloud Structure as Constrained by Galileo Probe and HST Observations. *Icarus*, 157(2):373–400. 31

Sromovsky, L. A. and Fry, P. M. (2010). The source of 3-μm absorption in Jupiter's clouds: Re-analysis of ISO observations using new NH_3 absorption models. *Icarus*, 210(1):211–229. 15, 36

Sromovsky, L. A. and Fry, P. M. (2018). Composition and structure of fresh ammonia clouds on Jupiter based on quantitative analysis of Galileo/NIMS and New Horizons/LEISA spectra. *Icarus*, 307:347–370. 15

Ströbele, S., La Penna, P., Arsenault, R., Conzelmann, R. D., Delabre, B., Duchateau, M., Dorn, R., Fedrigo, E., Hubin, N., Quentin, J., Jolley, P., Kiekebusch, M., Kirchbauer, J. P., Klein, B., Kolb, J., Kuntschner, H., Le Louarn, M., Lizon, J. L., Madec, P. Y., Pettazzi, L., Soenke, C., Tordo, S., Vernet, J., and Muradore, R. (2012). GALACSI system design and analysis. In Ellerbroek, B. L., Marchetti, E., and Véran, J.-P., editors, *Adaptive Optics Systems III*, volume 8447 of *Society of Photo-Optical Instrumentation Engineers (SPIE) Conference Series*, page 844737. 55

Strycker, P. D., Chanover, N. J., Simon-Miller, A. A., Banfield, D., and Gierasch, P. J. (2011). Jovian chromophore characteristics from multispectral hst images. *Icarus*, 215(2):552–583. 39

Sánchez-Lavega, A., García-Melendo, E., Legarreta, J., Miró, A., Soria, M., and Ahrens-Velásquez, K. (2024). The origin of jupiter's great red spot. *Geophysical Research Letters*, 51(12):e2024GL108993. e2024GL108993 2024GL108993. 3

Taylor, F., Atreya, S., Encrenaz, T., Hunten, D., Irwin, P., and Owen, T. (2004). The composition of the atmosphere of jupiter. In Bagenal, F., Dowling, T. E., and McKinnon, W. B., editors, *Jupiter. The Planet, Satellites and Magnetosphere*, pages 59–78. Cambridge University Press. 8

Weidenschilling, S. J. and Lewis, J. S. (1973). Atmospheric and cloud structures of the Jovian planets. *Icarus*, 20(4):465–476. 15, 27

Weilbacher, P. M., Palsa, R., Streicher, O., Bacon, R., Urrutia, T., Wisotzki, L., Conseil, S., Husemann, B., Jarno, A., Kelz, A., Pécontal-Rousset, A., Richard, J., Roth, M. M., Selman, F., and Vernet, J. (2020). The data processing pipeline for the muse instrument. *Astronomy & Astrophysics*, 641:A28. 62, 63

West, R. A., Baines, K. H., Friedson, A. J., Banfield, D., Ragent, B., and Taylor, F. W. (2004). Jovian Clouds and Haze. In Bagenal, F., Dowling, T. E., and McKinnon, W. B., editors, *Jupiter. The Planet, Satellites and Magnetosphere*, pages 79–104. Cambridge University Press. 17

West, R. A., Orton, G. S., Draine, B. T., and Hubbell, E. A. (1989). Infrared absorption features for tetrahedral ammonia ice crystals. *Icarus*, 80(1):220–223. 15

West, R. A., Strobel, D. F., and Tomasko, M. G. (1986). Clouds, aerosols, and photochemistry in the jovian atmosphere. *Icarus*, 65(2):161–217. 17, 18, 21

Wildt, R. (1939). On the chemical nature of the colouration of Jupiter's cloud forms. *Monthly Notices of the Royal Astronomical Society*, 99:616. 19

Wong, M. H., Atreya, S. K., Kuhn, W. R., Romani, P. N., and Mihalka, K. M. (2015). Fresh clouds: A parameterized updraft method for calculating cloud densities in one-dimensional models. *Icarus*, 245:273–281. 27, 29, 32, 33

Wong, M. H., Bjoraker, G. L., Smith, M. D., Flasar, F. M., and Nixon, C. A. (2004). Identification of the 10-μm ammonia ice feature on Jupiter. *Planetary and Space Science*, 52(5-6):385–395. 15

Zhang, A. and Marcus, P. S. (2024). Stable three-dimensional vortex families consistent with jovian observations including the great red spot. *Journal of Fluid Mechanics*, 984:A61. 193

Zhang, X., West, R., Banfield, D., and Yung, Y. (2013). Stratospheric aerosols on jupiter from cassini observations. *Icarus*, 226(1):159–171. 11, 12